# Improved Quantification of Arterial Spin Labelling Images using Partial Volume Correction Techniques

*Ruth Abigail Oliver*

A thesis submitted to University College London
for the degree of Doctor of Philosophy
in Medical Physics and Bioengineering
2015

# Declaration

I, Ruth Abigail Oliver, confirm that the work presented in this thesis is my own. Where information has been derived from other sources, I confirm that this has been indicated in the thesis.

# Acknowledgements

First of all, I must thank two very important people. My sincere gratitude goes to Xavier Golay and David Thomas, I cannot imagine two better supervisors. I definitely won the supervisor lottery. Both were always available and inspiring, despite being tremendously busy people, even when I made it very difficult for them to supervise me by moving to the other side of the world in the final throes of my PhD.

Huge thanks also go to Enrico De Vita, who is a tour de force of energy and enthusiasm, and doesn't seem to sleep. Thank you so much for keeping me going to the end, for reviewing my thesis, for your international phonecalls and technical input to some key chapters.

Thanks also goes out to my peers who took this PhD journey with me and provided fun and companionship along the way; Magda Sokolska, Marilena Rega, Patxi Torrealdea, Raj Ramasawmy, Miguel Sanchez, Niral Patel and James Fairney. Conferences were a whole heap more fun than they might otherwise have been without you guys, especially with my conference buddy Holly Holmes.

Finally, it is no exaggeration to say that none of this would have been possible with the devotion and support of my husband, Dave, and children Charlie and Jonquil. There are no words to express the depths of my appreciation.

*For Dave, Charlie and Jonquil*

# Abstract

Arterial Spin Labelling (ASL) MRI suffers from a phenomenon known as the partial volume effect (PVE), which causes a degradation in accuracy of quantitative perfusion estimates. The effect is caused by inadequate spatial resolution of the imaging system. Resolution of the system is determined by point spread function (PSF) of the imaging process and the voxel grid on which the image is sampled. ASL voxels are comparatively large, which leads to tissue signal mixing within an individual voxel that results in an underestimation of grey matter (GM) and overestimation of white matter (WM) perfusion.

PV correction of ASL images is not routinely applied. When PVC is applied, it usually takes the form of correcting for tissue fraction only, often by masking voxels with a partial volume fraction below a certain threshold. There are recent efforts to correct for tissue fraction effect through the use of linear regression or Bayesian inferencing using high resolution tissue posterior probability maps to estimate tissue concentration.

This thesis reports an investigation into techniques for PVC of ASL images. An extension to the linear regression method is described, using a 3D kernel to reduce the inherent blurring of this method and preserve spatial detail. An investigation into the application of a Bayesian inferencing toolkit (BASIL) to single timepoint ASL data to estimate GM and WM perfusion in the absence of kinetic information is described. BASIL is found to rely heavily on the spatial prior for perfusion when the number of signal averages is less than three, and is outperformed by linear regression in terms of spatial smoothing until five or more averages are used.

An existing method of creating partial volumes estimates from low resolution data is

modified to use a voxelwise estimation for the longitudinal relaxation of GM, which improves segmentation estimates in the deep GM structures and improves GM perfusion estimates.

An estimate for the width of the PSF for the 3D GRASE imaging sequence used in these studies is made and incorporated into a complete solution for PVC of ASL data, which deblurs the data through the process of deconvolution of the PSF, prior to a correction for the tissue fraction effect. This is found to elevate GM and reduce WM perfusion to a greater extent than correcting for tissue fraction alone, even in the case of a segmented acquisition.

The new method for PVC is applied to two clinical cohorts; a Frontal Temporal Dementia and Posterior Cortical Atrophy groups. These two populations exhibit differential patterns of cortical atrophy and reduced tissue metabolism, which remains after PV correction.

# Contents

# List of Tables

# List of Figures

# Chapter 1

# Introduction

Perfusion is the delivery of nutritive arterial blood to the capillary bed. This supply is essential to maintain homeostasis and is an important indicator of tissue viability. In fact, abnormalities in perfusion are the underlying cause of neurovascular diseases such as stroke. Therefore, the study and measurement of perfusion is of great clinical utility [21].

Arterial spin labelling (ASL) MRI is a non-invasive method of measuring perfusion. ASL images are degraded by a phenomenon known as the partial volume effect (PVE), which is manifest as a loss of contrast at a structural boundary due to inadequate spatial resolution. The point spread function of the imaging system and the grid of voxels that the image is sampled on together determine the resolution [22].

ASL imaging is based on tracking the passage of a tagged bolus of blood that requires the use of fast imaging techniques such as echo planar imaging (EPI) or 3D (gradient and spin echo) GRASE. These rapid imaging techniques allow one to take a 'snapshot' of the brain magnetisation. An image is taken before the arrival of the tagged blood. A second image is taken after the arrival of inflowing tagged blood, which reduces overall magnetisation. A perfusion weighted image is created by subtracting one from the other [23]. ASL imaging suffers from an intrinsically low signal to noise ratio (SNR), as the volume of labelled blood is usually only about 1% of total cerebral blood volume. In order to maximise SNR and acquire an image in clinically acceptable time frames, voxel sizes are large, typically 60mm$^3$.

The extent to which an anatomical structure suffers from PVEs depends on its size, with smaller structures more severely affected than larger ones. Consequently, the PVE is a particular problem when using ASL techniques to measure cerebral blood flow (CBF) due to the spatial scale of the cortex. Studies show that the cortical thickness varies from 1 to 4.5 mm, with an average thickness of 2.5 mm [5].

Given the relative size of an ASL voxel to cortical thickness, it is apparent that a typical image will contain voxels with signal from more than one tissue type, i.e. grey matter (GM) and white matter (WM), or grey matter and cerebral spinal fluid (CSF). The actual measured signal will be a weighted signal from the structures contained therein, in proportion to their volume and rate of blood flow.

Neurodegenerative disease is typified by progressive dysfunction and neuronal loss. Atrophy, both through so called 'healthy ageing' and disease, causes thinning of cortical structures, which exacerbates the PVE.

Grey matter (GM) perfusion is approximately three times that of white matter (WM) perfusion in adults, and up to 4 or 5 times for children [9]. Hence, in voxels where both tissue types are present, GM perfusion will possibly be significantly underestimated, with a corresponding overestimation of perfusion in the WM.

Partial volume correction (PVC) techniques aim to improve quantitative accuracy by removing PVEs. This is a somewhat under-researched problem in ASL imaging, although there is a larger body of work investigating the phenomenon in positron emission tomography (PET).

The objective of this project was to and develop improved methods for PVC in ASL imaging of cerebral perfusion, with the emphasis on post-processing techniques. This has led to the final development, following a series of successive steps, of a new PVC technique for ASL which combines a correction for tissue fraction in addition to the incorporation of image deblurring techniques. This is analagous to PVC techniques for PET data, but it is the first time these techniques have been jointly applied to ASL data.

## 1.1 Structure of the thesis

The thesis is structured to build a sequential picture of the partial volume correction (PVC) strategies developed throughout my PhD. The thesis begins with a discourse on the theory of ASL and existing methodologies for PVC. From a foundation of these existing methods, I introduce novel developments in each chapter. Finally, the complete PVC strategy is applied to two cohorts of dementia patients.

Chapter 2 provides an overview of the origins and theory of the ASL technique. The pulsed and continuous methods of labelling and quantification methods are presented, as well as a description of techniques to improve image quality. The recommendations of the ISMRM perfusion study group for best practice with the ultimate goal of advancing the use of ASL in the clinic are outlined, before concluding the chapter with a brief description of the application of ASL perfusion imaging in neurodegenerative disease.

Chapter 3 is essentially a background chapter and begins with a description of the PVE problem in PET imaging and the techniques that have been developed for it. Thereafter follows a literature review of the current state of the art methods for PVC in ASL, with a detailed description of the linear regression method.

Chapter 4 is a methods chapter and provides a description of the data acquisition and image processing techniques used for what might be described as conventional PV correction strategies for ASL. There is an account of the segmentation, registration and parcellation methods used.

The previous four chapters described background, history and methods. Chapter 5 marks the start of the section of the thesis which describes original work. This chapter contains a novel extension to the existing kernel method for linear regression, before moving on to applying a Bayesian inferencing method for PVC to single timepoint ASL for the first time. Both techniques are investigated in a simulation study as well as applied to a cohort of healthy controls.

Chapter 6 describes the application of an existing method of fractional segmentation to a 3D GRASE saturation recovery sequence for the first time. The FRASIER (FRActional Segmentation of InvERsion recovery) [8] method is further developed to include a voxelwise estimation of the longitudinal relaxation of GM in order to improve partial volume estimates for GM. This new technique is given the name SEPARATE - SEPAration of Relaxation curves for ASL Tissue fraction Estimation.

Chapter 7 presents a derivation of the point spread function for the 3D GRASE read-out technique used throughout the experimental work in this thesis and demonstration of a deblurring technique to remove the degrading effect on ASL perfusion estimates.

Chapter 8 describes the application of a novel, complete PVC technique that corrects for tissue fraction effect as well as deblurring to clinical data from a multi-centre study of patients who are at risk for frontal temporal dementia and a posterior cortical atrophy cohort.

Finally, chapter 9 offers a summary of the entire thesis and suggests avenues for future investigation.

# Chapter 2

# Arterial Spin Labelling MRI: An Overview

The following chapter provides some background on the principles of creating a quantitative map of cerebral perfusion by arterial spin labelling techniques, and a discussion on current clinical imaging recommendations and their use within this thesis.

## 2.1 Blood flow to the brain

The delivery of blood to an organ is known as *perfusion* and is an essential factor in terms of maintaining tissue health and as an indicator of tissue viability. A constant delivery of nutritive arterial blood to the capillary bed is fundamental for homeostasis of the brain. Perfusion in the brain is termed *cerebral blood flow* (CBF) and is the rate of flow of arterial blood to brain tissue. CBF is defined as the volume of blood flowing to a mass of brain tissue per unit time and is measured in units of ml/100g/min.

Abnormalities in perfusion are the underlying cause of neurovascular disease and perfusion is irregular in many conditions of disease such as stroke and tumours. Therefore, the study and measurement of perfusion assists with understanding disease progression. Measurements of CBF can be used to generate quantitative maps of regional perfusion which can highlight vascular disorders (see figure 2.1).

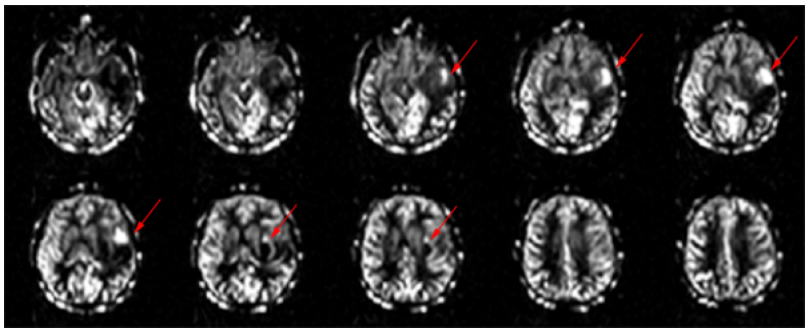

*Figure 2.1: Middle slices from a 3D perfusion weighted image showing a region of hyperperfusion (marked with red arrows) in the temporal lobe, indicative of a tumour. Images acquired by E. De Vita at the National Hospital for Neurology and Neurosurgery, London.*

## 2.2 Arterial Spin Labelling and Perfusion Imaging

Measuring perfusion using ASL techniques offers distinct advantages over other methods, such as Positron Emission Tomography (PET), Dynamic Contrast Enhanced (DCE) or Dynamic Susceptibility Contrast (DSC) MRI. All other imaging modalities are invasive, to a greater or lesser extent. In the case of PET imaging, a radioisotope is required which is expensive to produce and a source of ionising radiation to the patient.

DCE and DSC MRI require the use of a contrast agent, generally based on a Gadolinium chelate, the use of which must be limited in paediatric studies and avoided in patients with renal problems as this can lead to nephrogenic systemic fibrosis [21]. Both these techniques depend on the observation of a the passage of a bolus of contrast agent, with DCE using T1-weighted imaging and DSC using T2 or T2*-weighted imaging.

DCE MRI studies tend to focus on the measurement of $K^{trans}$ which is the *transfer constant* and characterises the diffusion of gadolinium chelates across the capillary endothelium. This is an important parameter in characterising tumour biology and response to treatment [24]. $K^{trans}$ in itself is not a measure of perfusion, but is sensitive to it and with the appropriate pharmacokinetic modelling, an estimation can be made, although this requires rapid imaging methods which are not widely available.

DSC MRI is the most popular MR perfusion technique in routine clinical practice. DSC tracks the first pass of a contrast agent through a large artery and tissue, and by choosing

voxels which are either in or close to a large vessel, such as the middle cerebral artery, it is possible to estimate an arterial input function (AIF). The AIF is used to recalibrate the experiment; meaning that CBF is measured relative to the AIF. These contrast based methods of estimating perfusion have the advantage that they are able to offer an estimation of cerebral blood volume (CBV), which ASL is unable to do. However, if the blood brain barrier (BBB) is not intact (such as in stroke and inflammatory disease), contrast agent can leak and care must be taken in interpreting results as contrast leakage will lead to quantification errors in both CBF and CBV.

ASL offers the unique advantage that perfusion is estimated using an endogenous contrast agent, which is totally non-invasive. ASL produces quantitative results and has better temporal and spatial resolution than nuclear imaging modalities. As a result, ASL is ideally suited to study healthy volunteers and poses no risk to patients taking part in longitudinal studies.

Despite these advantages, ASL remains an under-utilised imaging technique in the clinical arena. There has been an abundance of technical development in the twenty years since the birth of ASL methods and vast improvements in the quality of perfusion maps realised with them. However, this same cornucopia of labelling schemes, read-out options and quantification models has led to a lack of standardisation amongst researchers and scanner vendors, which has delayed acceptance in the clinical community.

## 2.3 Theory

Perfusion is observed by means of an endogenous contrast agent, which is created using a combination of radiofrequency (RF) and gradient pulses to invert or saturate the magnetisation of arterial blood water protons. The inverted arterial blood is delivered to the tissue bed at a rate that reflects the tissue perfusion and decreases the overall magnetisation of the tissue by an amount proportional to the delivery rate.

ASL perfusion imaging can be considered to be comprised of two parts. The first of these

is the *labelling*, in which arterial blood is tagged using an RF pulse to saturate or invert. The second component is the *readout*, in which the brain is imaged rapidly, using EPI or 3D GRASE. The labelling and readout portions of the sequence are quite independent.

The usual practice is to acquire two separate images, one that is known as the *labelled image* and is acquired after the inflow of labelled arterial blood. The other image is known as the *control image* and is acquired without any inversion of arterial blood. The two images are then subtracted to obtain a perfusion weighted image, as shown in figure 2.2.

The lifetime of the signal is dependent on the longitudinal relaxation of blood, which is usually within 1300 to 1750 ms at clinical field strengths of 1.5 or 3T [25]. This time duration is comparable to a quantity known as the *arterial transit time* or ATT, which is the time taken for the labelled protons to travel from the labelling plane to the tissue. A short delay between labelling and imaging means little T1 decay, and therefore a higher signal to noise ratio (SNR). However, a short interval may be insufficient for full arrival of the labelled protons to the capillary bed. Furthermore, the ATT varies between individuals and is known to increase with age. These considerations must be managed when choosing an implementation strategy.

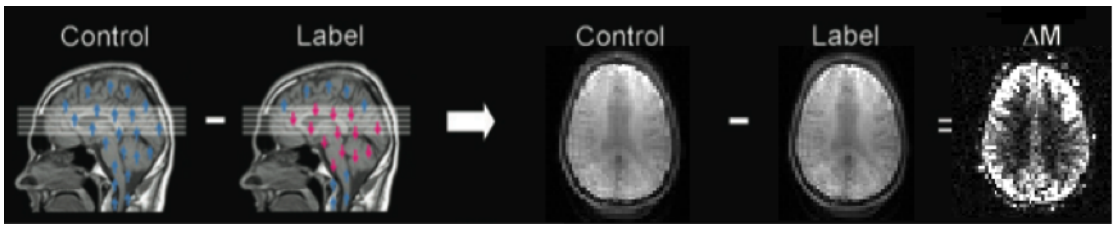


*Figure 2.2: A perfusion weighted image is created from the subtraction of a control image and a an image in which the arterial blood is magnetically labelled. The labelled image is acquired after a certain duration during which the blood is assumed to have travelled to the capillary bed. Adapted from [1].*

The difference in intensity between the control and labelled images is very small, typically only 1- 1.5% of the total signal. In order to increase the (SNR), it is usual to obtain multiple measurements and take an average. In order to make many measurements in an acceptable time frame, fast imaging techniques such as EPI or 3D GRASE are employed

[12].

ASL was first proposed in 1992 by Detre et al [26] using a spin echo sequence to acquire a single slice perfusion weighted image of a rat brain. Arterial blood was saturated with a slice selective RF pulse applied to a plane in the neck, which exchanged with bulk water in brain tissue upon reaching the capillary bed. A steady state between inflow and T1 decay was established. An image was then acquired in which the measured signal intensity within a voxel was attenuated according to the number of labelled protons that had travelled to that voxel, since the labelled protons act to reduce net longitudinal magnetisation.

However, this approach suffers from Magnetisation Transfer (MT) effects as the off-resonance pulses used to saturate blood water also saturate macromolecules within the imaging plane (or volume). This means that the acquired image is both perfusion and MT-weighted. In order to obtain an image that is purely perfusion weighted, the solution is to acquire an image with identical MT effects, but no perfusion weighting. This is easily achieved in the control acquisition by applying the saturation pulse outside the head, so that the imaging plane is equidistant between control and labelling planes. When the labelled image is subtracted from the control image, the MT effects are cancelled out, assuming identical MT weighting in both images. This is an effective solution, but does not lend itself to multi-slice acquisitions. MT is an important consideration is ASL imaging, as MT effects can considerably increase the apparent signal difference between control and label images, leading to an overestimation of perfusion.

## 2.4 ASL Implementations

There are two main camps that most ASL implementations belong to: continuous labelling or pulsed labelling. These approaches differ in the spatial extent and duration of the labelling pulse and both have their own strengths and weaknesses as a result.

### 2.4.1 Continuous ASL (CASL)

Also in 1992 Williams et al [27] developed and improved the technique further by using an adiabatic pulse to invert rather than saturate arterial blood, thus doubling the perfusion signal. This method came to be known as *continuous ASL* or CASL, due to the relatively long duration of the labelling pulse (2s). In an adiabatic pulse, the frequency of the pulse is swept from far off-resonance to resonance and beyond. This causes the effective field, $B_{eff}$ to sweep from +z to -z (provided the pulse is applied for sufficiently long enough).

If this is done slowly enough, the net magnetisation follows $B_{eff}$. Continuous inversion uses the same principle, other than that it is not the RF pulse which is varied. Rather, the resonant frequency of the spins is varied by the application of a gradient field in the inferior-superior direction. This means that the resonant frequency of a proton varies with position as it moves through the artery towards the head. The frequency of the RF pulse is selected to correspond to a certain transverse plane in the neck or head.

Essentially, when the proton is far from the resonance plane, the RF pulse is off resonance and the effective field is almost along the +z-axis. As the blood travels through the artery towards the resonance plane, the z-component of the $B_{eff}$ is eliminated and lies almost entirely along the x-axis. Further upstream from the plane, the proton is off-resonance in the other direction and $B_{eff}$ tips down to the -z-axis. Again, if the sweep of $B_{eff}$ is slow enough (driven by the velocity of the proton spins, rather than varying the pulse frequency, in this application), then the magnetisation is said to follow $B_{eff}$ and become inverted. This continuous labelling is very efficient at producing a steady stream of inverted blood as it is relatively insensitive to magnetic field inhomogenities, due to the off/on resonance sweep [2].

However, the implementation of CASL in humans proved challenging due to the need for specialist hardware to produce a continuous RF pulse, alongside specific absorption rate (SAR) restrictions. As such, CASL has not been routinely employed in clinical practice.

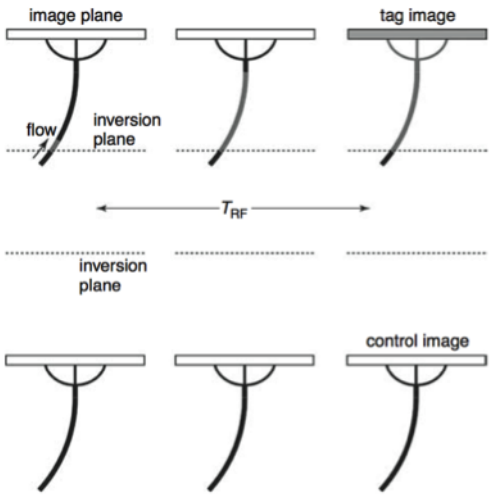


*Figure 2.3: CASL: the magnetisation of the arterial blood is inverted continuously while an RF pulse is applied in the presence of a magnetic field gradient in the direction of flow. As the blood passes through the inversion plane (where the RF pulse is on resonance), the magentisation is inverted. A continuous stream of labelled blood is created, as long as the RF field is applied. Adapted from [2].*

### 2.4.2 Pulsed ASL (PASL)

One of the first examples of a pulsed ASL experiment was that performed by Kwong et al in 1992 [28]. A slice selective inversion recovery image was acquired during a sensory activation paradigm in humans. An estimate of the qualitative changes in CBF between rest and activation was made by modelling the inflow of fully relaxed blood into the imaging slice during the inversion time. This imaging protocol was later adapted to provide quantitative measurements of CBF and termed *Flow Alternating Inversion Recovery*, or FAIR, by Kim et al [29].

The FAIR sequence is a symmetric method that automatically compensates for MT effects. A non-selective inversion pulse inverts all the blood in the transmitter coil that during a time interval flows into the imaging volume. This is the basis of the tagged blood signal. Conversely, the so-called slice-selective inversion inverts only the magnetisation within the imaging volume. Non-labelled, fully relaxed blood flows from outside of this volume into it, which means that an image acquired after this inflow of blood will have no perfusion weighting. Subtraction of the labelled and non-labelled

images produces a perfusion weighted image, which when scaled by the appropriate scale factor results in a voxelwise quantitative map of cerebal blood flow.

Additional developments in the field of pulsed ASL came in 1994 with the advent of the sequence developed by Edelman et al [30]. A 10-15 cm slab was labelled proximal to the imaging plane using a single 180 °pulse. A control image was acquired using an inversion slab sited outside the head to produce identical MT effects. This sequence was known as *Echo-Planar MR Imaging and Signal Targeting with Alternating Radio frequency* or EPISTAR (see figure 2.4). Due to the short duration of the tagging pulses (20-50 ms), *FAIR* and *EPISTAR* labelling techniques came to be known as *pulsed ASL*.

A continuous ASL (CASL) pulse is typically 2s long, whereas a PASL pulse is much shorter at around 20ms. This leads to CASL approaches offering a higher SNR due to the greater volume of blood that has been labelled due to the much longer labelling pulse, and contributing to the difference signal. However, PASL was the more popular imaging technique due to ease of implementation on standard hardware. This is no longer the case with the advent of *pseudo-continous ASL*, which is rapidly overtaking PASL in popularity.

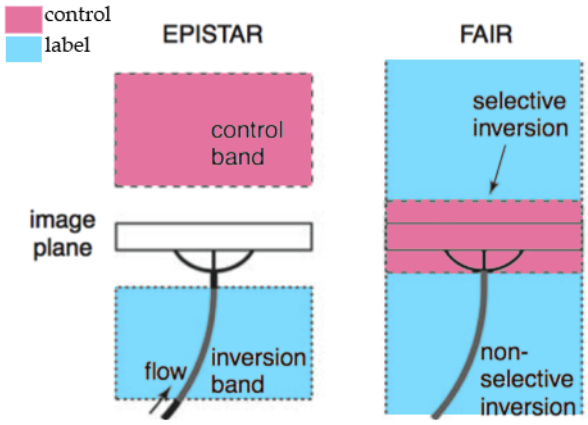


*Figure 2.4: PASL: EPISTAR and FAIR variations. In EPISTAR, the label is created with a spatially selective inversion slab below the imaging plane. The control image has a similar inversion slab above the imaging plane. In FAIR, the label is created with a non-selective inversion slab, with everything in the coil inverted. The control image is created from a selective inversion of the imaging plane.*

### 2.4.3 Pseudo-continuous ASL (pCASL)

In recent years, continuous ASL has enjoyed a renaissance with the advent of *Pseudo-Continuous ASL* (pCASL) developed in 2008 by Dai et al [31]. A train of short closely spaced RF pulses is used to invert arterial blood, which is comparable to the use of constant RF amplitude in CASL, but avoids the duty cycle constraints and additional hardware that is required for CASL. Thus pCASL sequences offer the advantages of CASL, such as high SNR and labelling efficiency, but are readily implemented on standard hardware.

pCASL combines the advantages of a CASL labelling scheme with the easier implementation of PASL imaging and is considered to be the state of the art. It is the labelling method of choice by the Perfusion Study Group (see section 2.7.2, although it was not readily available across all vendors at the start of this thesis.

## 2.5 Quantification Models

In order to obtain a quantitative measure of perfusion the perfusion weighted difference signal must be fitted to a suitable model. Two models in common use are discussed within this section.

### 2.5.1 Alsop-Detre Model

Early efforts to build a model to quantify perfusion utilised the nitrous oxide tracer clearance theory of Kety and Schmidt to produce a modified Bloch equation [26]:

$$\frac{dM_t(t)}{dt} = \frac{M_0 - M_t(t)}{T_{1,t}} + f\left(M_a(t) - \frac{M_t(t)}{\lambda}\right) \tag{2.1}$$

where $M_t$ is the longitudinal magnetisation of brain tissue water in arbitrary units, $M_0$ is the fully relaxed value of $M_t$, $\lambda$ is the blood brain partition coefficient, defined as

(quantity of tracer/gm of brain tissue)/(quantity of tracer/ml of blood), $T_{1,t}$ is the longitudinal relaxation time of brain water in the absence of flow or exchange between brain and blood water, $M_a$ is the magnetisation of arterial blood water in arbitrary units and $f$ is the cerebral blood flow in ml/g/s. This solution to the model assumes uniform plug flow, instantaneous exchange of blood and tissue spins, i.e. a single, well mixed compartment, and equal relaxation rates of arterial blood and tissue.

The original ASL experiments were in rats where the transit time of the tagged blood is negligible [26]. However, this is a parameter that can vary quite significantly in humans, both regionally within an individual brain and between subjects, even in a control population. The most accurate way to quantify transit time is to measure the perfusion signal at multiple time points and observe the wash in of the signal, although this increases the overall experiment length. This introduces other issues, such as a greater likelihood of motion artefact.

In order to reduce the dependency of the quantification model on variable transit time, Alsop suggested the inclusion of a post labelling delay (PLD) between the end of the tagged pulse and time of image acquisition, assuming the delay time is greater than the ATT ($\delta a$). Although the inclusion of the PLD will result in a reduced perfusion signal due to increased T1 decay, the benefit is that CBF estimates are relatively insensitive to variable transit times, provided that the PLD is greater than ($\delta a$). Studies suggest that in healthy volunteers the PLD should be selected to be around 1s and increased for patients with cerebrovascular disease [32].

The Alsop-Detre model was thus modified to include new parameters: $\delta a$, $\delta$ which is the tissue transit time and represents the time taken for labelled blood water to exchange into tissue, $T_{1a}$ the longitudinal relaxation of arterial blood water, $T_{1s}$ the longitudinal relaxation of tissue water during the control pulse, $T_{1ns}$ the longitudinal relaxation of tissue water after the control pulse, using the notation from [32] where *w* is the PLD:

$$f = \frac{-\lambda(M^{tag} - M^{ctrl})}{2\alpha M_b^0} C(T_{1ns}, T_{1s}, T_{1a}, \delta, \delta a) \tag{2.2}$$

where

$$\frac{1}{C} = T_{1ns}exp(-\delta/T_{1a})\Big[exp(min(\delta - w, 0/T_{1ns})(1 - \frac{T_{1s}}{T_{1ns}}\Big] + T_{1a}\Big[exp((min(\delta a - w, 0) - \delta a)/T_{1a}) - exp((min(\delta - w, 0) - \delta)/T_{1a})\Big] \tag{2.3}$$

### 2.5.2 General Kinetic Model

Buxton et al [33] took a somewhat different approach and proposed the *General Kinetic Model*. Within this model, Buxton describes the behaviour of the magnetisation difference signal, $\Delta M$, to be a function of delivery of magnetisation by arterial flow, clearance by venous outflow and longitudinal relaxation. Three separate functions are defined to described this behaviour:

$c(t)$**:** *delivery function* which is the normalised concentration of $\Delta M$ arriving at a voxel at a time *t*

$r(t, t')$**:** *residue function* which is the fraction of tagged water molecules that arrive at time $t'$ which still reside in the voxel at time *t*

$m(t, t')$**:** *magnetisation relaxation function* which is the fraction of the original longitudinal magnetisation carried by blood water to a voxel at time $t'$ which remains at time *t*

The evolution of $\Delta M$ is described by combining these three functions into a convolution integral:

$$\Delta M = 2M_{0B}f \int_0^t c(t')r(t - t')m(t - t')dt \tag{2.4}$$

$$\Delta M = 2M_{0B}f \left[c(t) \otimes r(t)m(t)\right] \tag{2.5}$$

where $M_{0B}$ is the equilibrium magnetisation of blood.

This forms the basis of the standard kinetic model, which applies equally to PASL and CASL, and in order to solve it one makes the assumption that the leading edge of a temporally defined labelled bolus of blood of duration $\tau$ with inversion efficiency $\alpha$ travels

to tissue in the imaging plane in a time $\Delta t$.

In order to solve equation 2.4, Buxton et al made the following assumptions:

1. Labelled arterial blood arrives as a uniform plug, such that before the transit time $\Delta t$, no labelled blood is present. Between $\Delta t$ and $\Delta t + \tau$ uniformly labelled blood arrives, with no labelled blood arriving after this time.

2. Tissue and blood exchange can be described by the single compartment model and depends on the blood brain partition coefficient $\lambda$, which is defined as the ratio between tissue and blood tracer (tagged blood) concentrations at equilibrium [34].

3. The longitudinal magnetisation of the labelled blood initially decays with the T1 of blood. It is assumed that all of the labelled water exchanges with tissue water instantaneously on arrival at the voxel, so that the label then relaxes with T1 of the tissue.

Thus, the PASL signal can be described as:

$$c(t) = \begin{cases} 0 & 0 < t < \Delta t \\ \alpha e^{-t/T_{1b}} & \Delta t < t < \Delta t + \tau \\ 0 & t > \Delta t + \tau \end{cases} \tag{2.6}$$

$$\Delta M(t) = \begin{cases} 0 & 0 < t < \Delta t \\ 2M_{0B} f (t - \delta t) \alpha e^{-t/T_{1B}} q_p(t) & \Delta t < t < \Delta t + \tau \\ 2M_{0B} f \tau \alpha e^{-t/T_{1B}} q_p(t) & \Delta t + \tau < t \end{cases} \tag{2.7}$$

where:

$$q_p(t) = \begin{cases} \frac{e^{kt}(e^{-k\Delta t} - e^{-kt})}{k(t - \Delta t)} & \Delta t < t < \Delta t + \tau \\ \frac{e^{kt}(e^{-k\Delta t} - e^{-k(\tau + \Delta t)})}{k\tau} & t > \Delta t + \tau \end{cases} \tag{2.8}$$

$$k = \frac{1}{T_{1B}} - \frac{1}{T_{1'}} \tag{2.9}$$

$$\frac{1}{T_{1'}} = \frac{1}{T_1} + \frac{f}{\lambda} \tag{2.10}$$

It is possible to quantify CBF from a measurement at a single time point or from measurements made from a series of acquisitions taken at increasing time intervals after labelling. For a single measurement, the appropriate equation listed above is solved for $f$ and calculated using the perfusion weighted image and relevant acquisition parameters, with $\tau$ and $\Delta$ t defined by the inclusion of additional saturation pulses. This is described further in section 2.5.3. For a multiple time point acquisition, the $\Delta M$ measurements are fitted to the appropriate PASL equation, which enables an estimation of $f$ and also transit time $\Delta t$ as depicted in figure 2.5.

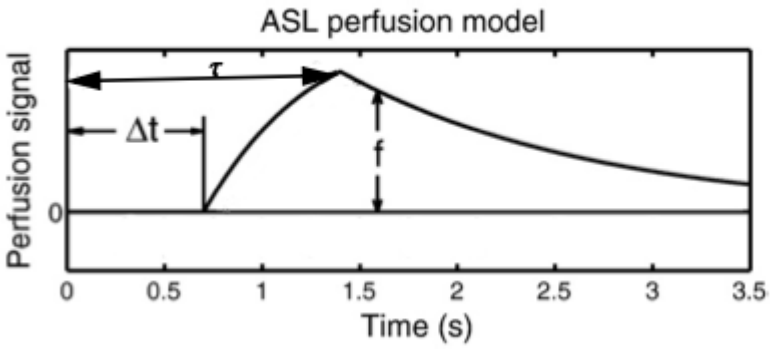


*Figure 2.5: Arterial spin labelling kinetic curve for an ideal difference signal as a function of acquisition time for a pulsed ASL labelling scheme. Labelled arterial blood arrives in voxels after a transit time, $\Delta t$, and continues to appear for the duration of the bolus $\tau$.*

Literature values are normally used for quantifying $\lambda$ and the relaxation time of blood. T1 and M0 maps of tissue can be created from fitting a model to a separate acquisition of inversion/saturation recovery data, which is the approach taken within this body of work.

### 2.5.3 Improved bolus definition using Q2TIPS

In PASL imaging there are two main causes of error in quantification; spatially varying transit times and signal arising from the vasculature. PASL imaging differs from CASL (where the duration of the tagged bolus is known) in that the tagged slab of blood has spatially varying transit times for a particular imaging region, along with an unknown duration for the bolus. Wong et al [35] sought to address these issues by using additional saturation pulses to improve definition of the labelled bolus. This technique is termed Quantitative Imaging of Perfusion using a Single Subtraction, and has two forms of implementation: QUIPSS I and QUIPSS II, which refers to whether the saturation pulse is applied to the imaging volume (QUIPSS I) or the labelling volume (QUIPSS II) after an inflow time TI1.

The QUIPSS II approach shares a common goal with the model of Alsop and Detre (discussed above) in that both techniques aim to define a tagged bolus of blood which is imaged after a sufficient time delay to ensure the bolus has reached the capillary bed. In theory, both approaches should make CBF quantification insensitive to transit time.

The imaging sequence used in this study makes use of a modification to QUIPSS II which is termed Q2TIPS [3]. In this method the QUIPSS II saturation pulse is replaced by a train of thin-slice saturation pulses at the distal end of the tagged bolus. This offers the advantage of producing a sharper edge for the bolus cut-off than using QUIPSS II, due to the thin sinc slice profile which better matched the sech inversion tagging pulse used in PASL (see figure 2.6).

In a PASL acquisition with Q2TIPS thin-slice saturation, the kinetic model can be simplified with certain assumptions.

For the condition $\Delta t + \tau < t$, from equation 2.7:

$$\Delta M = 2M_{0B} f \tau \alpha e^{-t/T_{1B}} q_p(t) \tag{2.11}$$

If we assume the $T_1$ of blood and tissue to be the same and that $f/\lambda \ll 1$, $q \approx 1$, we can write:

$$\Delta M = 2\alpha M_{0B} f \tau e^{-t/T_{1B}} \tag{2.12}$$

from which it follows, with $M_{0B} = M_0\lambda$ where $\lambda$ is the blood brain partition coefficient [34]:

$$f = \frac{\Delta M \lambda}{2\alpha M_0 TI1 e^{-\frac{TI2}{T_{1B}}}} \tag{2.13}$$

where *TI1* is the bolus duration, *TI2* is the inflow time, $\lambda$ is the blood brain partition coefficient, $\alpha$ is the labelling efficiency, $T_{1B}$ is the relaxation time of arterial blood at 3T. The sequence is shown in figure 2.6.

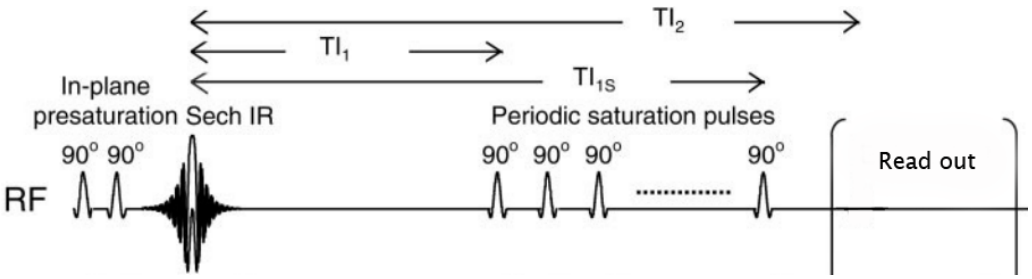


*Figure 2.6: Pulse sequence for Q2TIPS. Double in-plane presaturation pulses followed by a sech inversion tagging pulse. Periodic saturation pulses applied from TI1 to TI1s. 3D GRASE acquisition at TI2. Adapted from [3].*

## 2.6 Background Suppression

ASL is an inherently low SNR imaging modality due to the fact that perfusion typically replaces only 1% of brain water with inflowing blood water every second. This means that a 2s bolus of blood will alter only about 1% of tissue magnetisation is a tissue voxel, at best. Given arterial transit times and relaxation of the signal due to T1 decay, the difference between control and tagged images is usually much lower.

The most common source of artefact is patient motion, which can easily swamp the small perfusion signal. This can be countered by decreasing the signal intensity of the static tissue, without affecting the magnitude of the ASL difference signal, thus improving the overall SNR obtained.

It is possible to achieve this using a combination of saturation and inversion pulses and the technique is known as *background suppression* (BS), first demonstrated for ASL by Ye et al [36]. The methodology is as follows: a saturation pulse is applied to the imaging region, followed by one or more global inversion pulses (depending on how many tissue types are to be nulled). The inversion pulses are timed such that the longitudinal magnetisation is zero (or close to it) at the time of image acquisition.

The ASL signal is unaffected as the labelled blood does not experience the initial saturation pulse as it has yet to reach the imaging plane. It does experience the inversion pulses, but if the inversion is perfect and the pulse is instantaneous, merely the sign of the magnetisation difference will be affected, rather than the magnitude. Therefore, the signal from static tissue is suppressed whilst the perfusion signal is preserved.

In reality, the inversion pulses are not actually perfect: typically efficiency is about 95%. As such, the magnitude of the ASL signal is reduced by 5% for each inversion pulse experienced. This is an important consideration when selecting the number of tissue types (and therefore number of pulses) to be suppressed.

A further consideration is that BS suppresses the signal from static tissue at one point in time only. Therefore, BS is more suited to acquisition schemes that employ a single excitation for each TR. For schemes which do not, for example multi-slice EPI, the BS will only be optimal for a single slice. Hence, 3D volume acquisitions such as 3D GRASE [12], are ideally suited to the use of background suppression.

The imaging protocols employed in this project use two background suppression pulses in order to null the signal from static grey and white matter at the time of image acquisition. Using the notation from [12]:

$$\tau_1(TI) = TI + \frac{2}{R1_{opt}}.\ln((\frac{1}{2}+\frac{1}{4}) + (\frac{1}{2}-\frac{1}{4}).e^{1/2.TI.R1_{opt}}) \tag{2.14}$$

$$\tau_2(TI) = TI + \frac{2}{R1_{opt}}.\ln((\frac{1}{2}-\frac{1}{4}) + (\frac{1}{2}+\frac{1}{4}).e^{1/2.TI.R1_{opt}}) \tag{2.15}$$

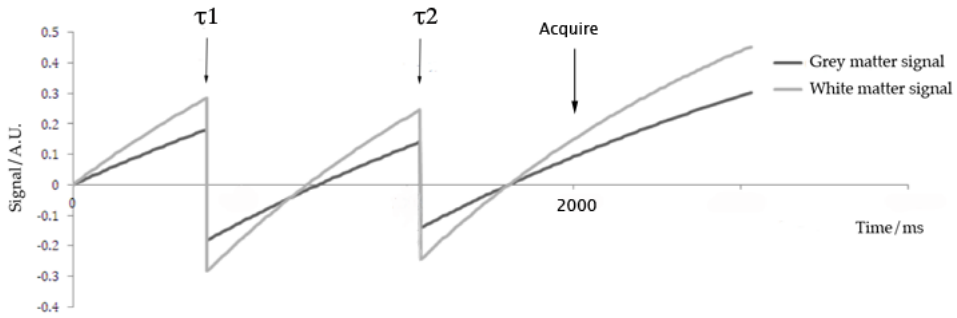


*Figure 2.7: Timing of background suppression pulses after initial saturation pulse. There are two inversion pulses to null grey and white matter, with the image acquisition occuring shortly after null points are passed for both tissues.*

Three inversion pulses are used in this acquisition (one to label and two for static tissue suppression). If a single inversion pulse efficiency is 95%, then the overall labelling efficiency will be:

$$\alpha = 0.95 * 0.95 * 0.95 = 0.86 \tag{2.16}$$

which must be factored into the model.

## 2.7 Readout Approach

In addition to choosing a suitable labelling protocol, a decision must be made about the readout module to be used. A rapid acquisition technique is required in order to capture multiple measurements in a short time for averaging data and improving SNR. Traditionally, either single or multislice single shot echo planar imaging (EPI) has been used. However, the use of 2D EPI techniques is non-ideal for a number of reasons, and there is a shift towards using segmented 3D sequences.

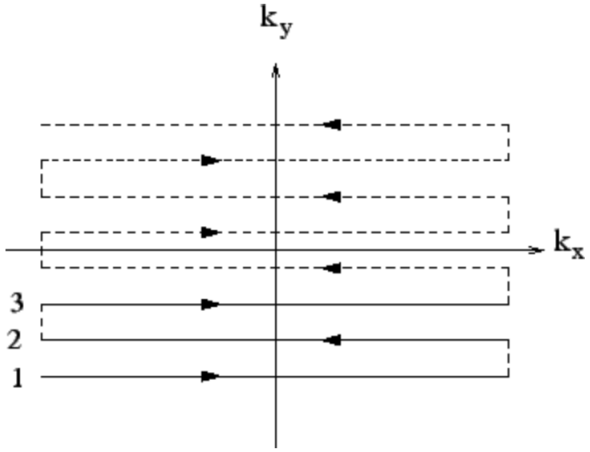


*Figure 2.8: k-space trajectory for single shot EPI sequences: the entirety of k-space is sampled after one RF pulse by blipping the signal along the phase-encoding axis.*

Multi-slice EPI is a 2D technique with slices acquired at different inflow times after labelling of the arterial blood. These slices are usually acquired in a sequential manner with an assumption that flow is from an inferior to superior slice. This is not necessarily true, as vascular physiology is somewhat variable. The general QUIPSS II condition is that TI2-TI1 should be longer than the longest bolus arrival time present in the slice. For a multi-slice acquisition, this timing is slice dependent. Additionally, background suppression (BS) is optimal at only one point in time, and therefore optimal only for one of the slices in a multi-slice acquisition.

### 2.7.1 3D GRASE

Gradient and Spin Echo (GRASE) imaging was developed in 1991 by K. Oshio and D. Feinberg as an alternative to EPI [4]. EPI uses the original k-space trajectory originally proposed by Mansfield et al [37], in which multiple lines of k-space are acquired in a single TR by rapid 'blipping' of the phase encoding gradient (see figure 2.8).

EPI places great demand on MR hardware systems due to the requirement for rapid switching of the gradient fields, as well as exhibiting chemical shift and signal dropout at the air/bone interface in the frontal lobe due to eddy current and susceptibility effects.

GRASE was designed to minimise the above limitations by alternating between gradient

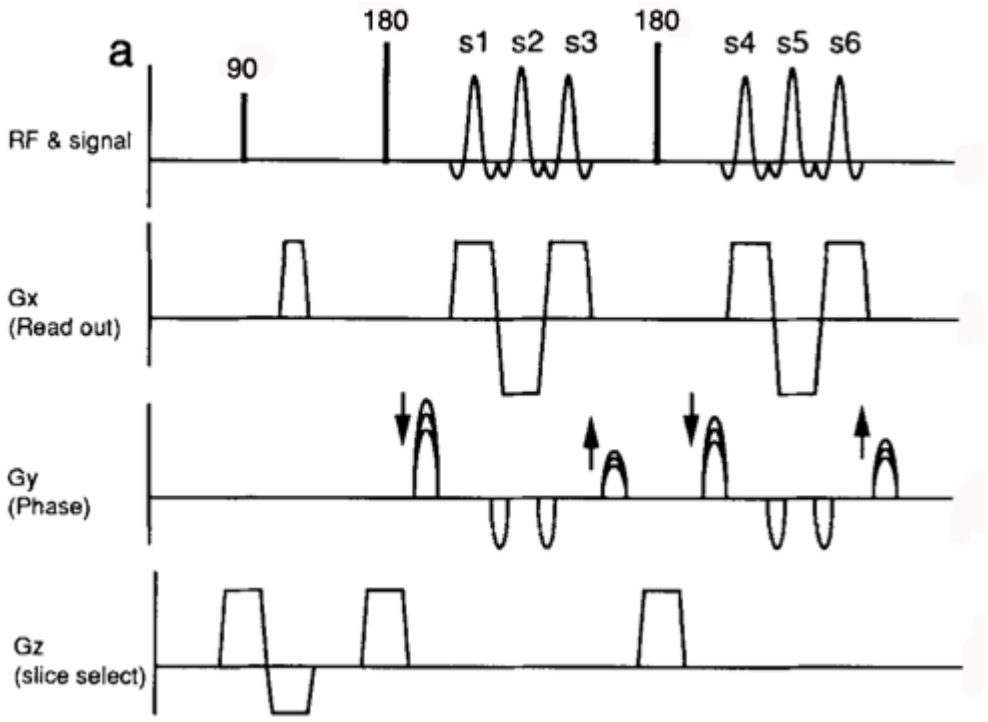


*Figure 2.9: GRASE pulse sequence adapted from [4]. s1, s2, s3 signals correspond to the lines of k-space labelled in figure 2.10.*

and RF pulses within the echo train. GRASE is in part based on the Carr Purcell Meiboom Gill (CPMG) spin echo pulse sequence, but is a hybrid of gradient and spin echo sequences. Multiple short duration gradient echo trains are created between successive 180 °pulses, which means that chemical shift and field inhomogeneity effects develop over a shorter time period between the 180 °pulses, compared to the greater time of the EPI echo train. This results in reduced phase errors which produces T2 decay of the echo train rather than the rapid T2* decay of EPI.

An RF-refocused echo train is formed, in which multiple lines of k-space are acquired using gradient reversals. Each k-space line is encoded differently by the phase encoding gradient pulses. The sequence is repeated with a different phase-encoding lobe, shown with arrows in figure 2.9, with s1, s2, s3 signals corresponding to the lines of k-space shown in figure 2.10. This trajectory scans over almost all of k-space within each RF-refocused echo train, with multiple excitation pulses populate k-space with interleaving.

Applying additional phase encoding gradients on a second axis means that the long echo train of GRASE imaging can be used to make single shot 3D images. This is known as the

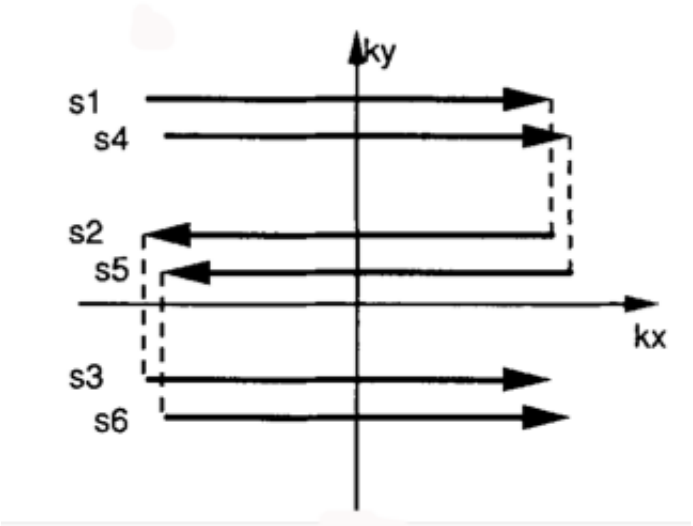


*Figure 2.10: Trajectory through k-space for a GRASE acquisition. A different starting place is used for each refocusing pulse.*

second phase encoding axis and runs along the inferior-superior direction. Consequently, 3D GRASE is a true 3D imaging technique and is able to offer a higher SNR than 2D EPI without the severe distortions or image quality problems which arise from attempting to use EPI in a 3D manner (EVI: echo volume imaging) [38].

### 2.7.2 Recommendations from the ISMRM Perfusion Study Group

With a view to simplifying and encouraging the use of ASL in the clinic, there is a drive to promote its use and standardise procedure, particularly in connection with applications in imaging dementia. Currently, FDG-PET imaging is considered to be the 'gold standard' for diagnosis of dementia. It is the expressed mission of a European-wide cooperative of scientists and clinicians [1] to develop ASL as a cost-effective non-invasive alternative to radiotracers in imaging dementia.

This has taken the form of a 'white paper', which is a consensus report written jointly by members of the ISMRM Perfusion Study Group and the European ASL in Dementia consortium [39]. The goal of the white paper is to document the current recommendations for optimal use of ASL imaging in the clinic and to encourage standardisation across

[1] http://www.cost.eu/COST_Actions/bmbs/Actions/BM1103

scanner vendors and sites. The hope is that this approach will encourage new scientists and clinicians to the field of ASL, rather than being overwhelmed by the vast array of implementations options, as well as facilitating comparison studies between sites.

For the most part, the ASL imaging used in this body of work is aligned with the recommendations from the white paper, other than where indicated. These are discussed in detail in chapter 3.

# Chapter 3

# Existing techniques for Partial Volume Correction in ASL

This chapter opens with a discussion of the origins of the partial volume effect in ASL and compares and contrasts correction strategies which are in existing use for another perfusion imaging modality, namely *Positron Emission Tomography*. PET imaging is a nuclear medicine modality for measuring metabolism, which is analogous to perfusion, and suffers from similar imaging degradations. A review then follows on how these PET techniques have been adapted for ASL, and what is the current state of the art in PV correction for ASL.

## 3.1 Partial Volume Correction in ASL

There is a factor which arises due to the nature of ASL imaging that is particularly relevant in studies where patient populations experience atrophy. This is the phenomenon known as the *Partial Volume Effect (PVE)*.

### 3.1.1 What is the PVE?

ASL suffers from an intrinsically low SNR, and in order to obtain an acceptable SNR, voxels are comparatively large. Voxels are much larger than is usually obtained in an

anatomical image, and typically around 60 $mm^3$, with in plane dimensions of around 4 mm and often larger in the slice direction.

Partial volume effects manifest themselves as a loss of contrast at a structure boundary. The PVE is caused by inadequate resolution of the imaging system, which is determined by the point spread function and the voxel grid on which the image is sampled.

#### 3.1.1.1 Spatial resolution

PV effects are a particular problem in neuroimaging due to the spatial scale of the cortex. Studies show that the cortical thickness varies from 1 to 4.5mm thickness, with an overall average thickness of 2.5mm. Cortical thinning is a hallmark of many neurodegenerative diseases, as well as a product of normal ageing.

Given the relative size of an ASL voxel to cortical thickness, it is apparent that a typical image will contain many voxels that have signal from more than one tissue type. As can be seen from the histogram of cortical thickness figure 3.1, there are few areas of the cortex that are thick enough that they will solely occupy the voxel volume.

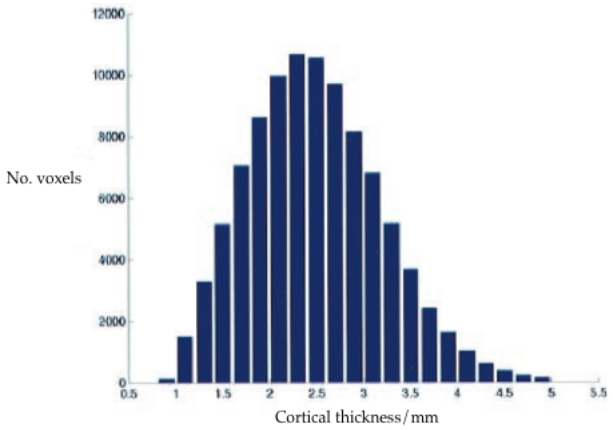


*Figure 3.1: Histogram of typical cortical thicknesses in a healthy subjected. Adapted from [5].*

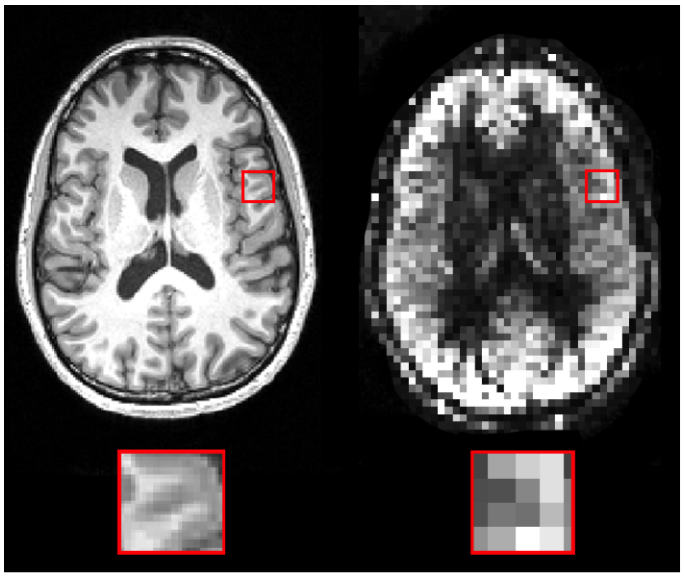

*Figure 3.2: The partial volume effect: when signal from more than one tissue type is contained within a voxel due to inadequate spatial resolution. A weighted average of two (or more) signals forms the voxel intensity. This is manifest as a loss of contrast at a tissue boundary. High resolution structural image at 1mm resolution clearly shows GM/WM interface. The same region from lower 4mm resolution ASL image suffers from PV effects.*

Figure 3.2 highlights the effect. The red squares show the same region of tissue from each image. The GM/WM boundary is clearly visible in the anatomical image due to the higher resolution the image was acquired at. The much larger voxels in the ASL image do not allow the tissue boundaries to be determined.

The actual measured signal in each voxel will be a weighted average of the signals from the structures contained therein. Grey matter perfusion is approximately three times that of white matter perfusion in adults, higher still in children [40]. Consequently, in voxels where both tissue types are present, the observed signal will be a weighted average of pure GM and WM perfusion levels. Studies on perfusion of WM are scarce, as the SNR is considered to be too poor to produce meaningful results, due to the longer transit time for the blood to reach the white matter and shorter T1 of WM [41].

Cortical atrophy exacerbates the PVE problem, and without appropriate partial volume correction, there will be an apparent decrease in perfusion when none is actually present. This is a serious confounding effect for longitudinal studies and it is of great importance that PV correction is performed on ASL data where atrophy is occurring.

#### 3.1.1.2 Point Spread Function

The second contributory factor to PVE is the *Point Spread Function*, or PSF. The PSF is a consequence of image formation and varies with the method of data acquisition. In short, the point spread effect causes blurring in the acquired image, with signals being displaced from their actual point of origin.

There appear to be no published articles addressing the impact of the PSF on the quantification of perfusion by ASL methods, although there is recent work to quantify the PSF in 3D GRASE imaging and remove the associated blurring.

This is discussed extensively in chapter 7.

## 3.2 PVC in PET studies

Positron Emission Tomography (PET) is an imaging modality that measures $\gamma$ rays that are produced from radioactive $\beta$ decay of a nucleus. As a nucleus decays, a positron is emitted. When the positron encounters an electron, both are annihilated and two $\gamma$ rays are produced. These $\gamma$ rays are then detected by the scanner apparatus and information about the location and intensity of radionuclide activity is acquired.

It is beyond the scope of this text to describe in detail PET image acquisition and reconstruction. However, given the parallels with ASL imaging, it is worthwhile to compare the partial volume effect and solutions that have been applied to this modality.

As in ASL imaging, the quantitative accuracy of PET measurements are degraded by the PVE, which is caused by blurring due to the point spread function which in turn is a consequence of the finite resolution of the imaging system and the rate at which the image is sampled. PET is an intrinsically low resolution imaging modality with a resolution typically between 5-6mm FWHM.

Factors which contribute to the PSF in PET are: the distance a positron travels before meeting an electron to annihilate with, non-colinearity of emitted $\gamma$ rays (due to

scattering), attenuation of $\gamma$ rays, detector configuration and reconstruction parameters.

Evaluation of the PSF usually involves imaging an object (point or line source of radioactivity) considerably smaller than the assumed system resolution and measuring the object width in the resultant image. As the PSF in PET imaging causes an underestimation in radioactivity concentration, it is common to define a recovery coefficient (RC), that is the ratio of the observed concentration in the observed image and the real radioactivity concentration. An alternative to direct measurement of the PSF is to simulate the RC for several PSF of different FWHM. Comparison of the measured RC with the suite of simulated PSF/RC pairs will yield the actual PSF. This method is particularly useful in situations where clinical reconstruction protocols do not meet the Nuclear Medicine standardisation body's requirement that voxel dimensions be one tenth of the expected PSF FWHM [42].

Of these two causes of PVE (blurring due to PSF and voxel grid size), it is the blurring caused by the PSF that is the primary target for PVC strategies in PET imaging. The PSF causes a displacement of activity between neighbouring regions in the brain, known as the 'spill in, spill out' effect, which is not necessarily balanced. The problem of multiple tissues existing within the same voxel due to inadequate voxel grid dimensions is very much a secondary consideration.

All existing PVC methods for PET images aim to correct for the spill-over effect caused by the PSF. From these, a subset also attempt to correct for the tissue fraction effect using structural information from a higher resolution MR or CT image. As such, PVC methods for PET can be divided into two categories.

The first category of techniques requires anatomical information, as described above. These include Meltzer's method [43], Muller-Gartner (MG) method [44] and the Geometric Transfer Method (GTM) of Rousset [45]. In general, methods which require anatomical information correct for both blurring and tissue fraction effect, with the exception of the GTM, which only corrects for blurring.

The second class of algorithms do not require anatomical data and are based on

deconvolution techniques and attempt to account for PVE during image reconstruction. However, these methods rely on an accurate estimation of the PSF, which in itself is a difficult quantity to measure, although they offer the advantage that no registration or segmentation of additional images is required. As no anatomical information is used, these methods are not able to account for the tissue fraction effect.

The first category of PVC methods can be further be subdivided into two classes – those which perform correction on a voxel-wise basis and those which are volume-based. As the terms suggest, these methods either correct for PV effects on a voxel-wise basis, or on a regional basis by segmenting the brain into non-overlapping regions. One method from each of these categories is briefly described next as a prelude to techniques in ASL. The Muller-Gartner method is described because of the parallels with an existing method for ASL PVC, namely linear regression [22]. The Geometric transfer method is described as this is an example of a technique which corrects for blurring, over 'spill over', as it tends to be called for PET imaging.

### 3.2.1 Muller-Gartner method

The Muller-Gartner (M-G) method [44] is a voxel-wise technique which corrects the PVE in the grey matter (GM) only. Correction is performed using the following equation:

$$f_{GM}(r) = \frac{f(r) - [A_{WM}P_{WM}(r)] \otimes h(r) - [A_{CSF}P_{CSF}(r)] \otimes h(r)}{P_{GM}(r) \otimes h(r)} \tag{3.1}$$

where, $f(r)$ is the observed image at voxel *r*, $f_{GM}(r)$ is the tracer uptake in the GM, $P_{GM}(r)$, $P_{WM}(r)$ and $P_{CSF}(r)$ are the tissue posterior probabilities of GM,WM and CSF. $A_{WM}$ is the estimated mean activity level in WM, $A_{CSF}$ is the estimated mean activity level in CSF (typically assumed to be zero) and *h* is the PSF of the scanner.

$A_{WM}$ can be estimated from a white matter region that is assumed to be free of partial volume effects. This assumes that WM activity is constant across all WM voxels, which may not be the case, and is a potential drawback. The posterior probability maps are

obtained from the segmentation of an anatomical MR image, which are then transformed to the same space as the PET data. In order to avoid a zero term in the denominator, it is usual to 'clip' $P_{GM}(r) > 0.05$, say, or use a binary mask for GM. A resultant image is produced which is a voxel-wise correction for GM only which corrects for blurring due to the PSF as well as tissue fraction effect.

### 3.2.2 Geometric Transfer Matrix method

The Geometric Transfer Matrix (GTM) method [45] operates on regions of the brain which have been defined from the segmentation of an anatomical scan into non-overlapping regions. This can be achieved using a tool like Freesurfer [1]. Each region is assumed to contain homogenous activity and a single value is produced for each ROI. As such, correction by the GTM method does not produce an image in the way that the M-G method does. The mean activity in each ROI is captured into a vector $r = [r_1, ..., r_n]$. The GTM is defined as an $n$ x $n$ matrix *G* such that $G_{ij}$ contains the fractional contribution of activity of region $r_j$ into $r_i$ . The reader is directed to [45] for further details on the calculation of the matrix elements of $G_{ij}$. Therefore, we can reason that the 'true' activity *T* can be obtained by solving the inverse problem:

$$T = G^{-1}r \tag{3.2}$$

The GTM method corrects for spill-over between regions, but does not address the issue of tissue fraction effect. A single activity value is obtained for each ROI, and it seems intuitive that the more regions that are defined, the more 'accurate' any correction is likely to be, and so the argument can be taken to the logical conclusion of there being one region per voxel. However, as the number of regions grows, so does the GTM, which is likely to become ill-conditioned and impossible to solve. Therefore, it is important to choose the ROI with care so as not to violate the assumption of homogeneous activity within the regions.

[1] http://surfer.nmr.mgh.harvard.edu

## 3.3 PVC in ASL studies

PVC is a more mature field area of research in PET studies than in ASL, so it is helpful to consider how the problems have been addressed using that modality.

Given that there is a significant degree of tissue signal mixing in an ASL image, it is apparent that some form of correction for the tissue fraction effect is required, and by implication, structural information in the form of a higher resolution anatomical image.

Broadly speaking, PET PVC methods are either applied as part of the image reconstruction process or as a post-processing technique. It is difficult to envisage an 'ASL parallel' with the former due to the differing methods of image formation.

Having said that, an investigation into removal of the point spread effect using deconvolution techniques has been undertaken in this thesis and is described in chapter 7. This differs from the deconvolution techniques used in PET as the application to ASL is a post-processing technique rather than incorporated during image reconstruction.

### 3.3.1 Existing methodology

There are few studies in which partial volume correction is performed on ASL data [46, 22, 6, 9, 15], with no known studies whatsoever in which blurring from the PSF is addressed as a contributory factor to the PVE. This is primarily because the PSF in MRI is much better than that of PET, particularly in a 3D segmented acquisition as used in this work. The dominating factor in causing partial volume effect in ASL is that of the tissue fraction effect. Recently, there have been preliminary efforts at characterising the PSF in 3D GRASE readouts and removal of associated blurring [47, 48]. Further details are provided in chapter 7.

The most common approach to dealing with PV effects is to circumvent the issue by only including voxels with a high GM content, typically over 80% [7]. The proportion of GM in a voxel is deduced from posterior probability maps obtained from high-resolution

anatomical images. This requires the probabilistic segmentation of the anatomical image and transformation of these estimations to perfusion space. This is a non-trivial step in itself, but moreover, this approach in general will still lead to an underestimation in perfusion. Any approach which selects candidate voxels based on their GM content makes comparisons between age groups difficult, as cortical thinning in elderly brains means that many voxels would be excluded from the analysis compared to a young person. Additionally, longitudinal studies where cortical atrophy is occurring are unreliable with a potential apparent decrease in perfusion due to tissue loss, rather than blood flow decreases.

At the start of this PhD, there existed two main methods for PVC in ASL; the linear regression method published by Asllani et al in 2008 [22] and the Bayesian inferencing method published by Chappell et al in 2011 [15].

### 3.3.2 Linear Regression

In 2008, Asllani [22] published a PVC method for ASL which borrowed some of the principles of PVC from the world of PET and shares some principles with the previously published Muller-Gartner method of PVC which is used for PET images [44]. A description of the method follows.

If we begin from the assumption that the magnetisation in a voxel, $M(r_i)$, can be described by the relationship:

$$M(r_i) = P_{GM}(r_i)m_{GM}(r_i) + P_{WM}(r_i)m_{WM}(r_i) + P_{CSF}(r_i)m_{CSF}(r_i) \tag{3.3}$$

where $P_j(r_i)$ are the posterior probabilities for the $j^{th}$ tissue type at voxel $r_i$, and $m_j$ are the separate tissue magnetisations sought after. The posterior probabilities of the three tissue types are obtained from the segmentation of high resolution anatomical data as described in section 4.2.3.

The relationship for cerebral blood flow is described as [2]:

$$CBF = \frac{\Delta M \lambda}{2\alpha M_0 T I_1 e^{-TI_2/T_{1B}}} \tag{3.4}$$

Re-writing as:

$$CBF = \frac{\Delta M}{M_0}.F_s \tag{3.5}$$

where:

$$F_s = \frac{\lambda}{2\alpha T I_1 e^{-TI_2/T_{1B}}} \tag{3.6}$$

As $F_s$ is composed of sequence and tissue specific constants, it is clear CBF is proportional to a ratio of two images, namely $\Delta M$ and $M_0$, both of which are affected by PV effects.

Assuming zero perfusion in CSF, the magnetisation in the difference image, $\Delta M$ can be written as"

$$\Delta M = P_{GM}(r_i)m_{GM}(r_i) + P_{WM}(r_i)m_{WM}(r_i) \tag{3.7}$$

For any particular voxel, whilst $P_{GM}$, $P_{WM}$ and $P_{CSF}$ are known quantities, there remain five unknowns - $\delta m_{GM}$, $\delta m_{WM}$, $m_{0,GM}$, $m_{0,WM}$ and $m_{0,CSF}$, which are the tissue specific contributions to the difference and equilibrium magnetisation images, respectively. It is not possible to solve for five unknowns with the two equations on hand.

As a solution to this, Asllani proposed that each voxel be the centre of a small region, called a kernel, such as the 5 x 5 kernel shown in figure 3.3. If the assumption is made that within this small region the GM, WM and CSF tissue signals are constant, (in both $\delta m$ and $m_0$), we are able to write a series of simultaneous equations that will enable us to solve for the unknown quantities.

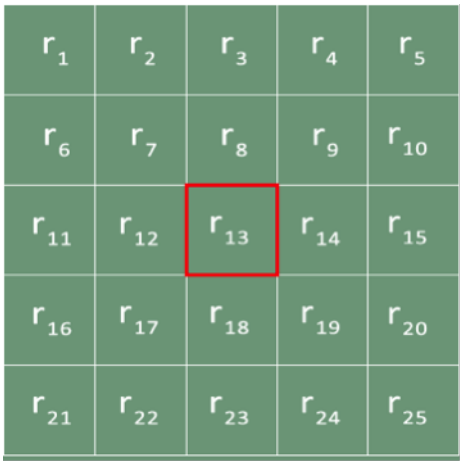


*Figure 3.3: A 5 x 5 kernel for linear regression: the centre voxel (outlined in red) is solved by assuming that GM, WM and CSF signals are constant over this region.*

Consider the 5 x 5 kernel depicted in figure 3.3 and that it is a portion of an $M_0$ image, with three unknowns to be found, $m_{0,GM}$, $m_{0,WM}$ and $m_{0,CSF}$. (If the difference image were being processed, the term representing CSF would be zero, with only two unknowns to be found). The voxel for which the partial volume contributions are going to be found is $r_{13}$ with a neighbourhood comprised of voxels $r_1$ to $r_{25}$.

In matrix form, these 25 simultaneous equations can be written:

$$\begin{bmatrix} M_{r_1} \\ \vdots \\ M_{r_i} \\ \vdots \\ M_{r_{25}} \end{bmatrix} = \begin{bmatrix} P_{GM}r_1 & P_{WM}r_1 & P_{CSF}r_1 \\ \vdots & \vdots & \vdots \\ P_{GM}r_i & P_{WM}r_i & P_{CSF}r_i \\ \vdots & \vdots & \vdots \\ P_{GM}r_{25} & P_{WM}r_{25} & P_{CSF}r_{25} \end{bmatrix} \begin{bmatrix} m_{GM} \\ m_{WM} \\ m_{CSF} \end{bmatrix}$$

The left hand side of the equation consists of a column vector of magnetisations for the entire kernel. The centre term is a 25 x 3 matrix containing the tissue posterior probabilities for tissue type in the $i^{th}$ voxel. The number of rows in the matrix is dependent on kernel size and is $n^2$ for a kernel of side *n*. The number of columns is dependent on how many different tissue types are being solved for (two or three, in our application).

More concisely, using $M(r_i)$ to denote either $\Delta M$ or $M0$, this can be written:

$$M(r_i) = P_j(r_i) \cdot m_j(r_i) \tag{3.8}$$

$m_j$ can be solved for using the standard least squares solution where $P^T$ is the transverse of $P$, and $((P^T \cdot P)^{-1} \cdot P^T)$ is the pseudo-inverse of P:

$$m = (P^T \cdot P)^{-1} \cdot P^T \cdot M \tag{3.9}$$

where *m* is a vector containing the separate tissue magnetisations for $r_{13}$.

By sliding the kernel across the entire image, it is possible to solve for GM/WM (and CSF) magnetisations in each voxel. The assumption that each tissue magnetisation is constant over the kernel region introduces a degree of spatial blurring, although it should be noted that this varies with kernel size and the data within in the kernel, which is changing on a voxel by voxel basis.

There is an inherent trade-off in this method; a large kernel will contain many equations with which to perform the regression and ensure that the matrix equations are not rank deficient. The matrix equations must be rank 2 for a difference image and 3 for an M0/control image. In order words, there must be at least two (or 3 for a control image) independent equations describing the magnetisation. The larger the kernel, the more likely this is to be true. However, spatial smoothing increases with kernel size as the assumption about constant magnetisation breaks down.

The linear regression method for PVC of ASL data shares shares some common features with the Muller-Gartner method used for PET, in that GM and WM tissue flows are derived from tissue fraction estimates. However, there are crucial differences. A single value is estimated for WM activity and used globally from an area of WM assumed to be free from PV effects. It is not necessarily the case that there is homogeneous activity in WM. As such, a correction is found only for GM regions. The linear regression method

does produce a voxelwise correction in both GM and WM, although it should be noted that it is matter of debate as to whether or not WM perfusion estimate obtained through ASL are reliable due to the low SNR and longer transit times for WM [49].

Additionally, the M-G method incorporates a deblurring of the PSF, which the linear regression method described here for ASL does not. In fact, no mention is made of the PSF in the original methods paper, or any of the papers which has since applied the method.

### 3.3.3 Studies applying Linear Regression for PVC

Although it is seven years since publication of the original linear regression method, it is not the case that PVC is in common use in ASL imaging. Asllani published a further paper in 2009 applying the correction method to ASL data obtained from a group of young and elderly subjects in an effort to decouple CBF and atrophy. In contrast to the findings reported in PET studies of perfusion that CBF does not decline with age after PVC, [50, 43] she reported PVE corrected GM CBF of $88.2 \pm 16.1$ and $107 \pm 17.5$ ml/100g/min in the elderly (mean age $68.0 \pm 6.2$) and young (mean age $26.4 \pm 2.9$) groups respectively.

A continuous labelling (2000 ms) and EPI readout scheme were used for the acquisition. The same post-labelling delay (800 ms) was used for the young and elderly group, although there is likely a longer transit time for the elderly subjects, which has the potential to cause an underestimation in CBF values for this group. However, the PVC GM CBF values are considerably higher than that reported in other studies. The study of Binnewijzend et al [46] reports a mean uncorrected CBF of $33 \pm 5$ ml/100g/min in the elderly control group, with a PVC GM CBF of $49 \pm 7$ ml/100g/min. Chappell et al [15] report a typical increase of 69-80% in GM CBF after correction in a young subject group. Asllani does not state the mean uncorrected global GM CBF value of either the young or elderly cohort, so it is impossible to assess the effect of the correction. However, these quoted values are unusually high, particularly for an elderly cohort, given that we are concerned with capillary and not vascular flow. An insufficient

post-labelling delay time could lead to vascular signal contaminating the perfusion signal, which is certainly possible given that a multislice EPI acquisition was used with inflow times ranging from 800 to 1696 ms.

### 3.3.4 Modified Least Trimmed Squares applied to LR

In terms of extensions to the published linear regression method, Liang et al [6], published an enhancement in late 2012 which applies a modified least trimmed squares (mLTS) [51] regularisation to the kernel as a means of discarding outliers before performing the regression to reduce the smoothing effect. Voxels from within the kernel are placed in ascending order in terms of absolute difference in intensity from the central voxel. A subset of voxels is selected from the original kernel, starting with those closest in intensity to the central voxel, until the rank of the subset is 2. An initial estimate of the partial volumes is obtained from this subset. The process is then refined further by computing the residuals using the partial volume estimates and sorting into ascending order in terms of difference from the central voxel once more. A subset of the voxels with the smallest residuals is selected based on a trimming parameter, $\alpha$, and the partial volumes re-estimated. This process is repeated for a number of iterations until convergence occurs.

Liang applies the PVC technique to the difference image alone and does not quantify CBF or the increase in GM CBF that this method offers. The paper focusses on varying the degree of trimming used for the cut-off of voxel difference and a comparison between the original method of Asllani. Both techniques are applied to simulated data like that used in [15] and in this thesis.

Satisfying results are observed in the simulation study, in terms of reduced edge blurring of two areas of hypo and hyper-perfusion, as compared to the original LR method. (See figure 3.4). There is clearly reduced blurring of these areas compared to the original LR, but this is not surprising, as the trimming has effectively reduced the size of the kernel to just contain voxels which are alike. With this simulated data, there is a clear demarcation

between voxels which are alike and which are not.

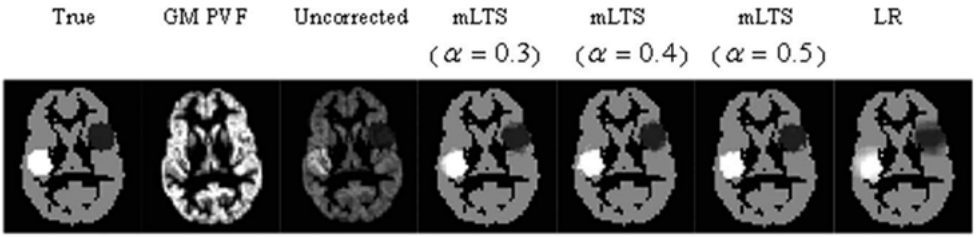


*Figure 3.4: PV correction using the modified least trimmed squares enhancement of LR for a simulation study, from [6].*

The results obtained from in vivo data are not as compelling and are displayed in figure 3.5. At the present time, it is believed that the hallmark of a good PV correction is that a relatively constant value is found for the GM CBF across all PV ranges, or GM $\Delta M$, as has been PV corrected in this case. The expectation is that there is a linear relationship between perfusion and partial volume which is removed after PV correction. Whilst it can be seen that there is an uplift in the perfusion values in the three subjects shown in Liang's paper, there appears to still be a linear dependency on PV fraction which has not been removed.

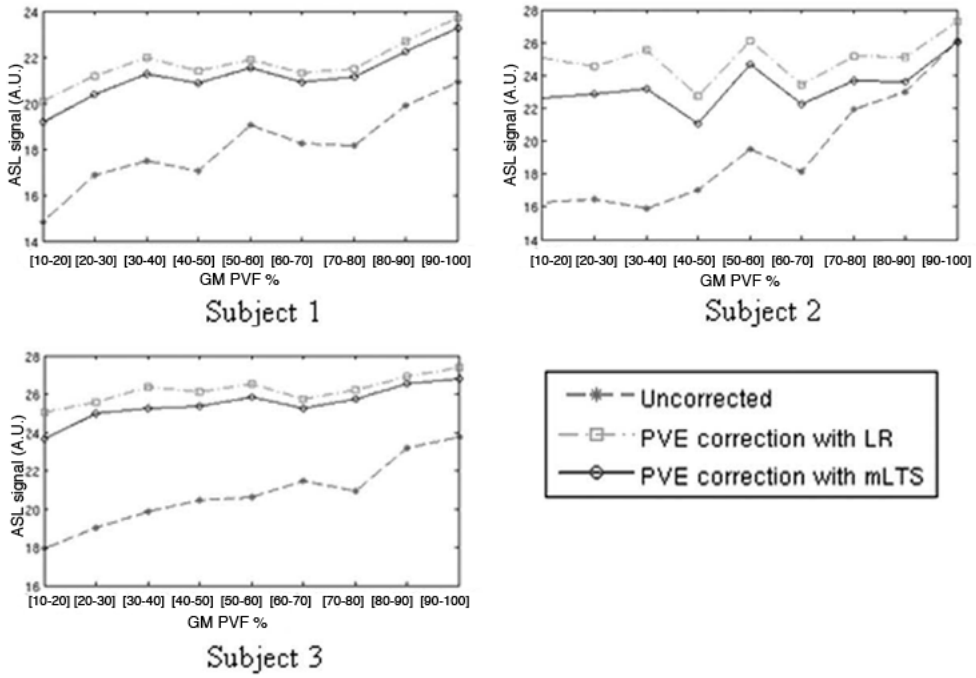


*Figure 3.5: Modified least trimmed squares method applied to in-vivo data, from [6]. The uncorrected CBF is not linear across the PV fractions, as the theory suggests it should be. For example, we expect the CBF to be higher in a 60-70% GM voxel, compared to a 50-60% one. The GM CBF results appear to mirror the uncorrected mean CBF values, which suggests a dependency on PV remains.*

These in vivo results are quite different to those published by other researchers using LR methods, albeit with the caveat that groupwise averages are quoted in those works [7, 46]. Figure 3.6 shows a groupwise PVC result for both a young and older cohort, with consistent GM CBF results across the PV fraction range for both cohorts.

It is possible that the data used in the Liang paper is particularly noisy, and that the smoothing 'side-effect' of linear regression has been negated somewhat by the reduced kernel size, as the PV corrected results seem to mirror the raw data across the PV fractions.

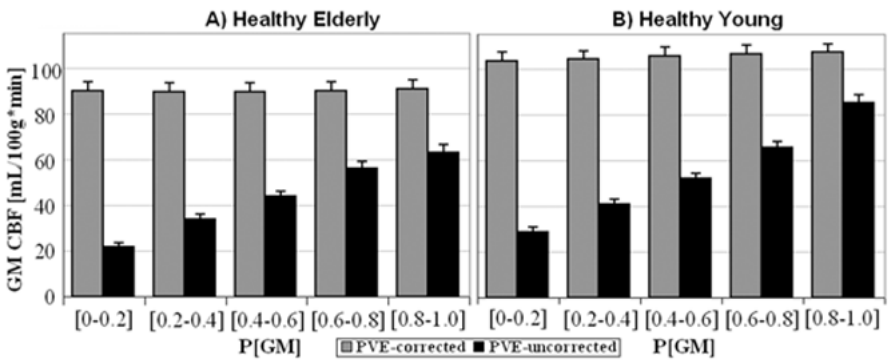


*Figure 3.6: GM CBF results for a young and an elderly healthy control cohorts. The uncorrected CBF shows a strong linear dependence on PV fraction, and a consistent result is found for GM CBF after correction [7].*

## 3.4 Partial Volume Correction by Bayesian Inference

The principal alternative to the linear regression method for PVC is Bayesian Inference for Arterial Spin Labelling (BASIL), a technique which uses Bayesian inferencing and is available from the FSL suite of tools from the FMRIB group [2]. This section provides an overview of BASIL.

### 3.4.1 BASIL

BASIL is a Bayesian inferencing framework for fitting perfusion data to the general kinetic model [33] and was primarily designed for processing multi-timepoint data. Acquisitions of this type sample the full time course of the kinetic curve (see figure 2.5.) This offers an advantage over single timepoint data in that the separate GM and WM tissue kinetics can be estimated, as well as bolus arrival time, which can be an important indicator in stroke patients.

In this application, the goal is to find the normal distribution for parameters GM and WM CBF and bolus arrival time having measured some data (perfusion at various time points). This is dependent on the likelihood - P(data | parameters) - of which perfusion and the

[2] http://fsl.fmrib.ox.ac.uk/fsl/fslwiki/BASIL

partial volume estimates contribute, multiplied by the prior probability (our beliefs about physiological ranges for the parameters). Essentially, an answer is sought to the question: if these values for perfusion are observed, given a set of partial volumes (from a high-resolution T1 segmentation) and spatial priors, what is the most likely value for separate GM and WM tissue perfusion?

#### 3.4.1.1 Spatial priors

It is usual practice to fit the kinetic model to the data using a non-linear least squares algorithm. BASIL makes use of spatial and non-spatial priors in a probabilistic non-linear least squares method to arrive at a fit for the general kinetic model. The non-spatial priors are the T1 of tissue, bolus arrival time and bolus duration, with these priors based on real *a priori* knowledge. Including these priors in the model effectively restricts the range of plausible values that these parameters can take. For example, in the case of bolus arrival time, most voxels will be in a certain range as a result of the distance from labelling to imaging location. Including this strong prior information will help make the estimates more robust in the case of poor SNR.

There is no sensible prior for perfusion (due to subject variability), so a spatial smoothness prior is used instead. The spatial prior provides a form of adaptive spatial regularisation by encoding the belief that the GM or WM perfusion in one voxel should not differ dramatically from its neighbours. Spatial priors are encoded in BASIL in the form of a Markov Random Field (MRF). It is beyond the scope of this report to discuss the implementation of MRF spatial priors in detail. The reader is directed to [52] for further detail. Suffice to say, the spatial homogeneity of a parameter is captured by the MRF and is adaptive, being determined from the data.

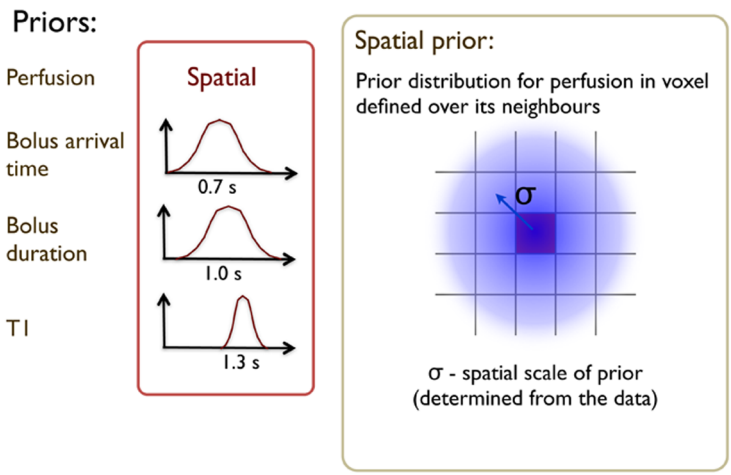


*Figure 3.7: Priors used in BASIL; non-spatial priors are on T1 of tissue, bolus arrival time and bolus duration, normal distribution assumed. Spatial priors are used for GM and WM CBF, with the spatial extent, σ, being defined from the data. Image courtesy of Michael Chappell.*

A schematic of the spatial and non-spatial priors is shown in figure 3.7. The scale of the spatial prior is the spatial extent, $\sigma$, which specifies how rapidly the spatial prior tails off with the distance; nearest neighbours exert the most influence and $\sigma$ can be considered to define the size of the neighbourhood. The spatial prior is adaptive in that the parameter which dictates the spatial extent of the smoothness is determined from the data. This means that smoothing effect is dependent on the data in any given region and can vary across the brain, depending on how informative the data is.

BASIL tries to explicitly model the noise in the data, which influences the smoothing effect. If BASIL is unable to form a good estimate for the noise, less reliance will be placed on the data and more on the prior. This results in more smoothing in the GM and WM estimates, as the spatial prior essential tells us that the each voxel is like its neighbour.

#### 3.4.1.2 PVC using Bayesian inferencing

In terms of partial volume correction, BASIL uses the tissue kinetics of blood flow to assist with separating perfusion into tissue type. GM CBF is known to arrive earlier than WM CBF, and this is modelled using the general kinetic model in tandem with the model

for PV:

$$\Delta M = P_{GM}\delta m_{GM} + P_{WM}\delta m_{WM} \tag{3.10}$$

Bayes' theorem states that the posterior probability for the parameters being modelled having observed some data, is proportional to the likelihood of observing that data with these parameters, multiplied by the prior information on the parameters.

In terms of perfusion:

$$P(parameters|data) = \frac{P(data|parameters)P(parameters)}{P(data)} \tag{3.11}$$

where:

P(data) = P($\Delta M$, t, PVF)

P(parameters) = P($CBF_{GM}$, $CBF_{WM}$, CBF, ATT, T1, $\epsilon$)

and *P(data|parameters)* is known as the *likelihood* term and *P(parameters)* represents the *prior* information. where $CBF_{GM}$, $CBF_{WM}$ are the separate GM and WM tissue flows, $CBF$ is the uncorrected perfusion, $ATT$ is the arterial transit time, $\epsilon$ is the noise in the data, $t$ is the time at which the kinetic curve is sampled, $T1$ is the tissue longitudinal relaxation time and $PVF$ represents the partial volume estimates for GM and WM in ASL space.

From equation 3.11, it can be seen that perfusion and the partial volume estimates are part of the likelihood term, which is a description of how the data is generated for a given set of parameters, subject to noise. This is weighted by the prior information, and the spatial prior information is exploited to separate perfusion into GM and WM components.

BASIL is an iterative algorithm and requires initialisation. To begin with, an estimate is made for GM flow only, with further parameters added as the algorithm proceeds. An initial estimate is made for the WM component based on a fixed ratio of the GM value (WM = 0.4 * GM [53]). Based on this initialisation, a further model fit occurs with the

full model. At each iteration, all the voxels are updated and then the spatial parameter of the spatial prior is updated before another voxelwise parameter update step. GM and WM voxelwise perfusion values are arrived at from a combination of the time series in a given voxel, the neighbouring perfusion values and the level of noise that has been observed in the data.

As an aside, BASIL is designed to operate on the difference signal alone, it does not PV correct an $M0$ or control image, as there is no third term for CSF in the model.

BASIL was designed for multi-timepoint ASL data and has not previously been applied to single timepoint data, which possess no kinetic information. An investigation of the utility of BASIL in this case was carried out and is described in chapter 5.

## 3.5 Fractional Segmentation from Inversion Recovery data: FRASIER

This section describes an alternative method of creating partial volume maps from data which is acquired at the same resolution as the perfusion data, thus removing the need for registration and resampling of high resolution anatomical data to perfusion space.

### 3.5.1 Issues with registration and ASL data

Within the limited number of papers published on PVC of ASL data, the second most recent is the paper by Petr et al published at the end of 2012 [9]. The PVC technique described within the paper uses the linear regression method of Asllani in its original form, albeit the PV correction is only applied to difference and not control images. The difference in approach lies in the creation of the PV estimates – these are created from saturation recovery data acquired using a Look-Locker read out, rather than from T1-weighted anatomical data, as is usually the case.

Within our own group, at the time that this paper was published, we were in discussion

about using saturation recovery data, rather than anatomical images, as the basis of a segmentation method. As saturation data is acquired as part of the existing protocol, using this data to create segmentation maps would not increase the scan time, provided the same sampling points are used.

Registration of high resolution anatomical data to low resolution ASL data can be problematic. PV correction methods usually require the registration of anatomical data to ASL space (normally a control image) in order to apply this transform to the partial volume estimates which are produced at anatomical imaging resolutions.

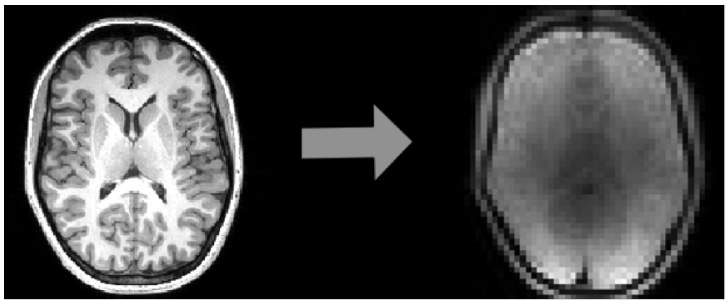

*Figure 3.8: Partial volume estimates are transformed to perfusion space by registering high resolution anatomical images to lower contrast and resolution ASL images. ASL on right, MPRAGE on left.*

As can be seen in figure 3.8, the low resolution ASL data is lacking in contrast and spatial detail. This lack of strong features creates difficulties for registration algorithms. The chances of success of this procedure can sometimes be improved by registering the ASL image to the anatomical image, and then applying the inverse transform. However, this cannot be guaranteed, and it fails sufficiently often that it is necessary to manually check each registration, and if necessary, tweak the registration parameters to improve the outcome. This is subjective, error prone and time consuming.

As the transformation obtained from this registration is then applied to the tissue segmentation maps, it is vital that the transformation is accurate. Any errors in registration will cause the transformed PV information contained in the maps to be inaccurate, which renders any PV correction performed using these maps to be unreliable.

A misalignment of even one voxel between the ASL data and the PV maps will have a

large effect on the quality of the PV correction given that the cortex is less than one voxel wide at the usual resolution of ASL data. The inherent spatial blurring introduced when using linear regression methods for PVC tends to mask registration errors to a certain extent, but it is likely that as techniques are developed to reduce spatial blurring, errors in registration will become more apparent.

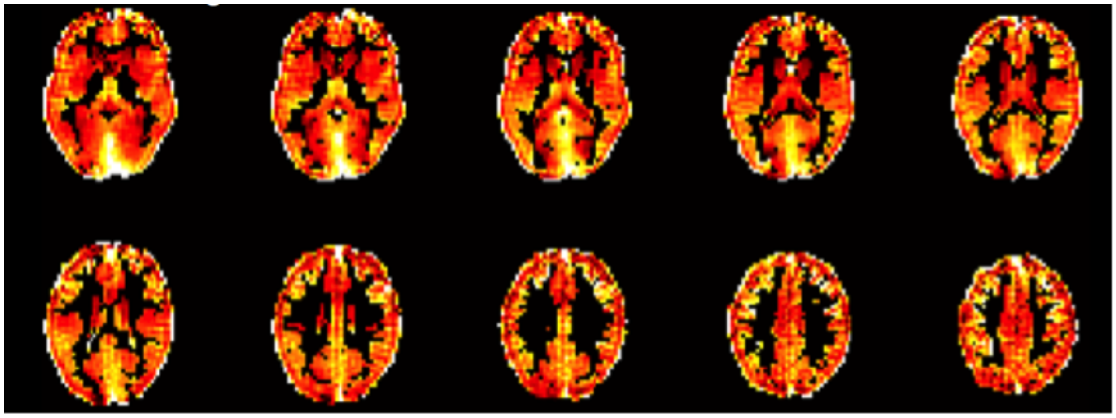

*Figure 3.9: Ten middle slices of a grey matter CBF map showing a 'ringing' effect caused at the brain boundary due to misalignment of partial volume maps and perfusion data. There is an overestimation of GM perfusion due to the PV maps as the GM/CSF interface is not correctly positioned.*

A registration error is usually most apparent at the brain boundary and is caused by the PV maps not being scaled correctly to the ASL data. An example of this is shown in figure 3.9. The brain boundary is a region where we expect to find PV effects due to voxels containing a mixture of CSF and GM. There is a 'blooming' effect due to the brain boundary voxels being scaled after correction to too high a value. This is due to the brain edge voxels having the incorrect PV estimates assigned to them in the linear regression. Voxels which actually contain a mixture of GM and WM are being treated as though they contain a GM/CSF mixture, which causes the GM estimation to be artificially high as there is no perfusion in CSF. A one voxel misalignment between the perfusion weighted image and the PV estimates will cause this to happen.

With regards to the creation of the PV maps themselves, the segmentation algorithms that are in general use rely on registering subject images to a standard atlas. These algorithms tend to fail quite rapidly once a patient population with atrophy is encountered, as is the case for either elderly or dementia patients – in fact the very groups where PVC is

valuable. Therefore, a method of creating partial volume estimates without relying on anatomical data is particularly useful in these cases.

Moreover, there is no consensus in the literature as to how the segmentations should be resampled from anatomical to perfusion space. Consider the GM partial volume maps in figure 3.10. Image (a) has been resampled using trilinear interpolation whilst (b) has been resampled using a spline interpolation. The differences between the two maps are subtle, but they are evident. Each map will produce a different weighting for tissue fractions in the model that ultimately affects the partial volume correction.

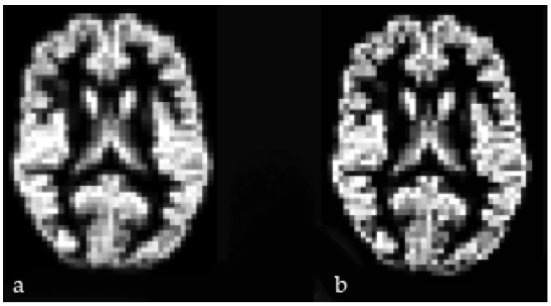


*Figure 3.10: Grey matter partial volume maps after resampling to perfusion space. (a) has been resampled using trilinear interpolation, and (b) resampled using spline interpolation.*

Producing partial volume estimates directly at perfusion resolution removes the requirement to resample, along with the associated decisions as to how to achieve the resampling.

## 3.6 The FRASIER segmentation method

The ability to segment MRI brain images into tissue types is of great utility in the study of structure and function. There are a number of packages which are freely available for performing this task, such as the FAST tool from the FMRIB group at Oxford [3], SPM from the Wellcome Trust Centre for Neuroimaging at UCL [4] and Freesurfer from the Harvard group [5] to name some of the most commonly employed algorithms.

It is usual for brain segmentation tools to require a high-resolution T1-weighted image as the input image, and thus rely on images with a single contrast. Whilst segmentation

[3] http://fsl.fmrib.ox.ac.uk/fsl/fslwiki/FAST
[4] http://www.fil.ion.ucl.ac.uk/spm/
[5] http://surfer.nmr.mgh.harvard.edu/

methods have been developed which make use of multi-contrast MR imaging and the associated additional information for voxel classification, the relatively long acquisition and additional processing times have meant that images with a single contrast remain the most widely used.

The primary issue with performing segmentations on single contrast images is that of partial volume. Whilst the resolution of single contrast high resolution MR anatomical images is considerably better than that used in ASL (1mm x 1mm x 1mm compared to 4mm x 4mm x 4mm typically), given the relatively small size of cortical folding and the fact that the cortex can be as thin as 2mm in places, there is still the issue of multiple tissue types occupying the same voxel.

Due to the limited information available with which to classify voxels from single contrast images, it is usual to rely on *a priori* templates. These templates are generally created from healthy controls, with limited relevance to elderly and or atrophied brains, which can lead to inaccurate segmentation results. A further complication when using T1-weighted images is that voxel intensity may be corrupted by a bias field (for further details see section 4.2.1).

Alternative brain segmentation methods which make use of quantitative MR parameters have been proposed, and in this vein, Shin et al [8] proposed a brain tissue classification method based on quantitative T1. Shin termed this method 'FRASIER', from 'FRActional Signal mapping from InvErsion Recovery'. The basis of this method is that the dynamic signal from an inversion recovery experiment is sampled at various time points, to which a curve can be fitted, and thus the signal modelled. This curve is considered to be the sum of three mono-exponential functions, which represent the recovery of GM, WM and CSF tissue signals. Through a linear least squares estimation process, an estimate is found for each of the tissue fractional signals, which is then converted to a *fractional volume* by scaling the signals for tissue density.

### 3.6.1 FRASIER algorithm

Shin used a Look-Locker inversion recovery EPI (IR LL-EPI) dataset in order to characterise the relaxation of the signal. In the original paper, the signal from an inversion recovery acquisition is fitted to a linear combination of three exponential functions, which represent the relaxation curves of GM, WM and CSF.

Shin proposed that a fit is made to the model:

$$S(t) = \sum_i S_i(1 - 2e^{-t/T1_i}) \tag{3.12}$$

where $S_i$ is the fractional signal of tissue i with relaxation time $T1_i$ .

Consider an inversion recovery sequence of n time points with voxelwise signals:

$$S_{obs} = [S_1 ... S_n]^T \tag{3.13}$$

and define for each time point *t* such that *X* is a *n* x 3 matrix where *n* is the number of time points,

$$X = \begin{bmatrix} (1 - 2e^{-t_1/T1_{GM}}) & (1 - 2e^{-t_1/T1_{WM}}) & (1 - 2e^{-t_1/T1_{CSF}}) \\ \vdots & \vdots & \vdots \\ (1 - 2e^{-t_n/T1_{GM}}) & (1 - 2e^{-t_n/T1_{WM}}) & (1 - 2e^{-t_n/T1_{CSF}}) \end{bmatrix} \tag{3.14}$$

$$F_s = [F_{S,GM}, F_{S,WM}, F_{S,CSF}]^T \tag{3.15}$$

one can write

$$S_{obs} = XF_s \tag{3.16}$$

$F_s$ contains the fractional signal for each tissue type, which can be calculated using a least

squares estimation, provided the T1 for each tissue type is known:

$$F_s = (X^T X)^{-1} X^T S_{obs} \tag{3.17}$$

The fractional signal can be converted to a fractional volume, $p_i$, by correcting for the variable water density using the relationship:

$$p_i = \frac{\frac{S_i}{\rho_i}}{\sum_i \frac{S_j}{\rho_j}} \tag{3.18}$$

where $\rho_j$ is the relative water density for GM, WM and CSF (0.89, 0.73 and 1.0 respectively[54].

### 3.6.2 Petr et al extension

Petr et al extended the work of Shin by using a Look-Locker saturation recovery EPI sequence, rather than an inversion recovery; more importantly this data is acquired at the same resolution as the perfusion weighted data. This adds some complexity to the calculation of tissue fractions.

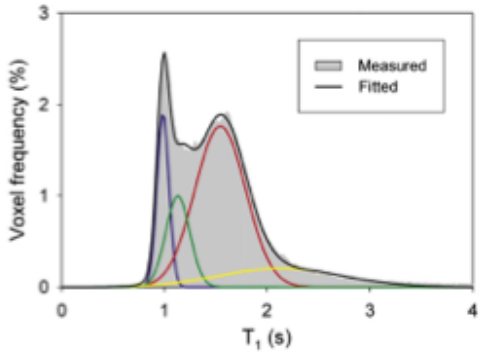


*Figure 3.11: Figure 1 from [8] which demonstrates how a histogram created from a quantitative T1 map can be used to estimate T1 of GM and WM. Four Gaussians are fitted to the histogram: blue is WM, green is WM + GM, red is GM and yellow is GM + CSF.*

The FRASIER method (though perhaps it is not quite correct to use the acronym 'FRASIER' when saturation recovery data is used) requires knowledge of the T1 of GM, WM and CSF. Shin estimated the T1 of GM and WM by fitting a Gaussian Mixture Model (GMM) to the histogram of a quantitative T1 map produced from the inversion recovery sequence. Four Gaussians were fitted to the histogram which represented

WM, GM, WM + GM, and GM + CSF. The average T1 values for WM and GM were determined as the means of the two highest distributions. Due to the relatively low volume of CSF compared to other tissues, a literature value of 4300ms was used for the T1 of CSF.

The resolution of the data used in the Shin paper is 1.7 x 1.7 x 4.0 $mm^3$ on a 128 x 128 matrix. At this resolution it is possible to discern a peak in the histogram for pure GM voxels (see figure 3.11). This is not possible at the usual resolution that ASL data is acquired at, as there are very few (if any) voxels which contain 100% GM.

If the T1 of GM cannot be measured from the T1 map, it must be estimated. Petr proposed an approach which estimates a global value for the T1 of GM by searching for the optimal value through a process of gradient descent and iterative minimisation.

The procedure can be summarised as:

1. Use a literature value for the T1 of GM as an initial starting point.
2. Calculate the PV fractions that are obtained with this T1 value.
3. Calculate the total signal that would be obtained from these PV fractions.
4. Calculate the error between the modelled signal and the observed signal.
5. Adjust T1 of GM in order to minimise error in step 4.
6. Repeat until no further reduction in error in step 4 is obtained.

From this process, PV maps for GM, WM and CSF are produced at the resolution of the perfusion data and without the need for resampling, although it is still necessary to co-register the PV maps and perfusion data as the two datasets are not necessarily aligned, as there may have been patient movement

Petr appears to obtain good results in terms of the PV maps produced in this way, although there is the usual difficulty in determining 'better' rather than 'different', when there is no gold standard for comparison.

In particular, he points out that the FRASIER WM PV map ( labelled (f) in figure 3.12) contains more structural details than the anatomical image derived PV map, (d). Likewise,

the deep GM regions in (e) are of a reduced intensity compared to (c). He claims that the WM is very thin in this region and that this structural detail is not realised from an anatomical segmentation resampled to ASL resolution.

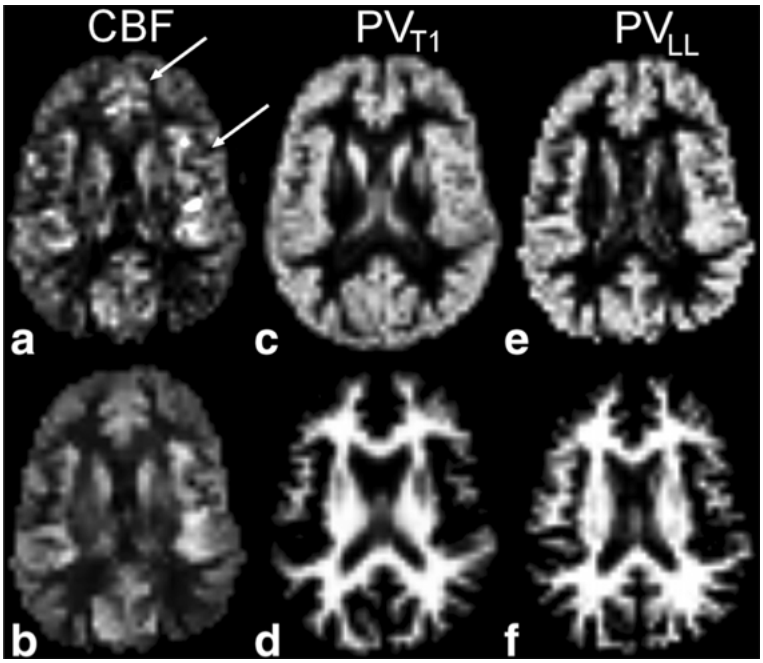


*Figure 3.12: (a) CBF map, no PV correction (b) CBF map, after recombining PV effects from FRASIER maps (c) GM PV from anatomical image (d) WM PV from anatomical image (e) GM PV using FRASIER (f) WM PV using FRASIER. Taken from [9].*

This paper is the first published instance of PV estimates being created from saturation recovery data obtained at ASL resolution, and applied in a PV correction. The limitations of this study are that there is quite clearly reduced GM tissue concentration in the deep GM areas compared with high resolution T1 segmentations, and also that a co-registration of the PV maps to the perfusion data is still required.

### 3.6.3 FRASIER applied to QUASAR

The most recent paper to apply PVC techniques to ASL data is that published in the second half of 2014 by Ahlgren et al [10].

In this study, the FRASIER technique is used as previously published by Shin [8], but differs from Petr et al referred to above, in that the QUASAR (QUantitative STAR

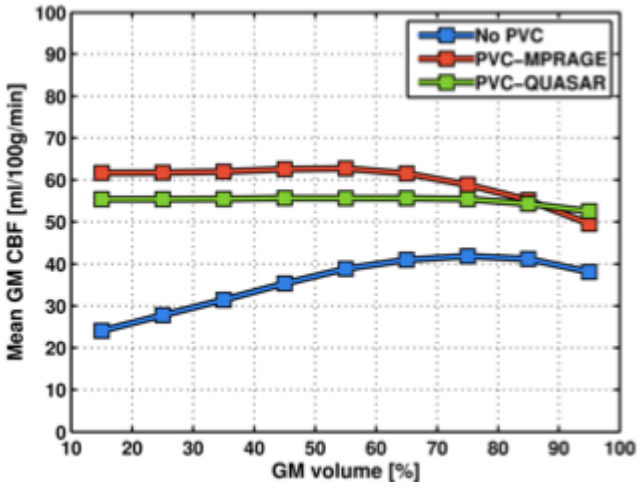


*Figure 3.13: GM CBF results obtained using FRASIER applied to QUASAR data (green), and also using T1 high resolution derived PV maps (red), uncorrected data (blue), from [10].*

Labelling of Arterial Regions) sequence [55] is employed for perfusion imaging. The advantage offered by using QUASAR is that the same sequence that is used for estimating perfusion forms the basis of the PV maps. This means that there is no need for registration of separate datasets, which will reduce a potential source of error. However, the QUASAR sequence is not in common use in the ASL community and only available on Philips scanners.

In terms of the linear regression, Ahlgren et al propose the use of a circular kernel, which effectively removes the voxels which are greater than a certain distance from the centre voxel. This is similar to the least trimmed squares method, except that voxels are removed from the regression based on their distance from the centre voxel, rather than difference in intensity from it.

A comparison is made of the GM CBF results obtained using the QUASAR-FRASIER and the QUASAR-T1 anatomical methods, with the result shown in figure 3.13.

It is not stated which PV maps were used to create the mean uncorrected CBF values, although it seems most likely that it was the MPRAGE derived maps, as there is a similar trend of decreasing CBF from the 80% GM range. The QUASAR-FRASIER method produces a consistent result across all PV fractions, in contrast to that with the MPRAGE maps.

## 3.7 Discussion

This chapter provides an account of the existing techniques and current state of the art methods for PV correction of ASL data. It begins with a brief summary of the methods used in PET studies, and how they may or not be applicable to ASL data.

A detailed description follows of the techniques currently in use for ASL, which can be separated into two categories; using PV maps from high resolution anatomical data or creating them from saturation recovery sequences using a Look-Locker read out. All of the described methods require PV estimates at the resolution of the ASL data.

There are two distinct methods of using PV maps in PVC. They are either used in a linear regression algorithm, or in a Bayesian inferencing iterative algorithm to produce separate GM and WM tissue flows.

Both PVC methods are explored in further detail in chapter 5.

# Chapter 4

# Image Processing Pipeline and General Methods

This chapter describes the data acquisition protocol and general image processing methods used in this thesis, before concluding with a detailed description of the processing pipeline.

## 4.1 Data Acquisition

This chapter describes the data acquisition techniques used for both the healthy controls imaged for the purposes of this study, and a study which is being conducted by the Dementia Research Centre (DRC), which is a clinical department within the UCL Institute of Neurology. This data is known as the 'GENFI' cohort [1] and the reader is directed to chapter 8 for a full description of the data and analysis.

For the most part, the imaging protocols and parameters used follow the recommendations of the ISMRM Perfusion Study Group 'white paper' [39], other than where indicated. These recommendations and the actual implementations used in this body of work are summarised in table 4.1.

The data acquisition can be considered to be comprised of two parts; the perfusion data and supporting parameter estimations, and the anatomical data used for partial volume

[1] (http://genfi.org.uk/)

correction.

### 4.1.1 Labelling Scheme

The scheme used throughout is single time point ASL with a QUIPSS II [35] saturation to define the bolus length. The inflow time (TI2) is 2000 ms and the first saturation pulse is applied at TI1 = 800 ms. The recommendations of the ISMRM Perfusion Study Group are that a single time point pCASL labelling scheme is used. However, that labelling implementation was not available on the Siemens Trio when our studies were performed. In this event, the workgroup recommends the use of a pulsed labelling scheme and QUIPSS II saturation pulses with the bolus cut-off at TI1 = 800 ms. This was the approach taken.

### 4.1.2 Background Suppression

Background suppression was used to null static tissue signal. The theory behind the technique is described in section 2.6. The study by Günther et al [12] recommends that the nulling of the static tissue occurs 100 ms before acquisition time. This results in a small static tissue signal at the time of acquisition, which assists with post-processing techniques. Accordingly, the nulling was calculated to occur at 1900 ms.

A relaxation rate, $R1_{opt}$, of 1/700 ms was used for the timing of the two inversion pulses, where were calculated according to equations 2.14 and 2.15. The two non-selective background suppression pulses were timed to occur at 754 ms and 1610 ms after the labelling and imaging volume saturation pulse. These inversion pulses coupled with the labelling pulse reduced the overall labelling efficiency to 0.86. $(0.95 * 0.95 * 0.95)$.

### 4.1.3 Read-out

The 3D GRASE sequence was originally developed as a one shot technique, but it is now common to use segmented acquisitions. A comprehensive description of 3D GRASE

imaging can be found in section 2.7.1. The volume was acquired in eight segments and was split such that one segment consisted of a 64 x 8 x 20 matrix, with the split along the first phase-encoding direction (see figure 4.1).

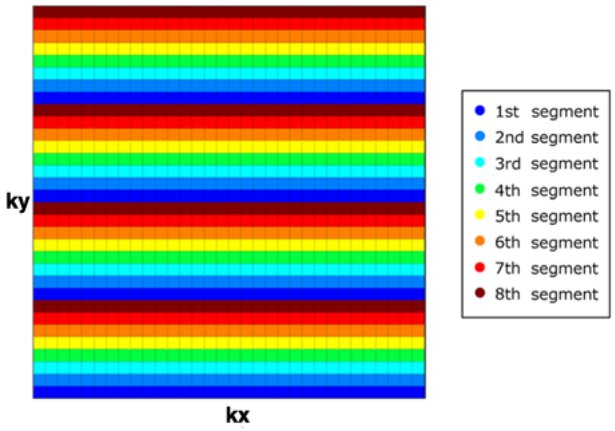


*Figure 4.1: 3D GRASE eight shot segmentation scheme. Each shot was 64 x 8 x 20 voxels, with the segmentation along the phase-encoding direction. Figure adapted from [11] and shows a 32 x 32 matrix for illustration of segmentation scheme.*

This was done to mitigate the effects of T2 decay along the partition direction, and therefore reduce blurring along this axis. This phenomenon is described and investigated in detail in Chapter 7.

Figure 4.2 shows the background suppression with 3D GRASE readout sequence used in this study.

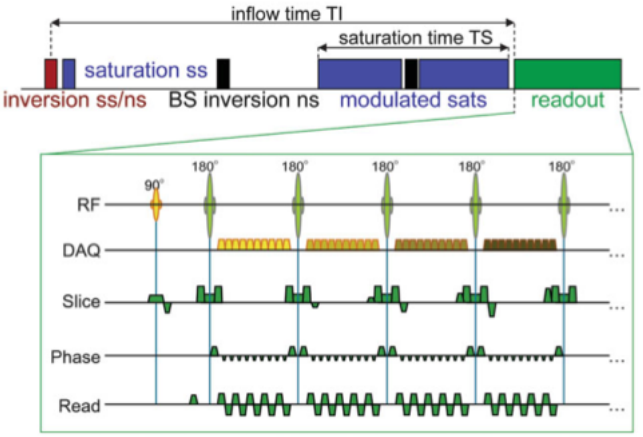


*Figure 4.2: Sequence incorporating pulsed ASL with background suppression and a 3D GRASE readout used in this thesis. The modulated saturation pulses produce two saturation bands on both sides of the imaging region, in order to suppress signal from inflowing venous blood. From [12].*

### 4.1.4 Summary of ASL imaging parameters

| Protocol/Parameter | PSG Recommendation | Used in this thesis |
|---|---|---|
| Field Strength | 3T | 3T |
| Receive Coil | 8 or more channels | 32 channels |
| Labelling | Single PLD pCASL | Single PLD PASL + QUIPSS II |
| PLD | 2000 ms | 2000 ms |
| Background Suppression | 2 inversion pulses | 2 inversion pulses |
| Read-out | Segmented 3D read-out | Segmented 3D GRASE |
| Quantification Model | General Kinetic Model | General Kinetic Model |
| Matrix | | 64 x 64 x 20 |
| Resolution | | 3.75 x 3.75 x 3.8 $mm^3$ |

*Table 4.1: Summary of important imaging parameter and recommendations of the joint ISMRM Perfusion Study Group (PSG) and European ASL in Dementia Consortium and those used in this thesis.*

An example of a perfusion weighted image obtained in this study using the above parameters is shown in figure 4.3. This image has been created by subtraction of the control and label images after registration.

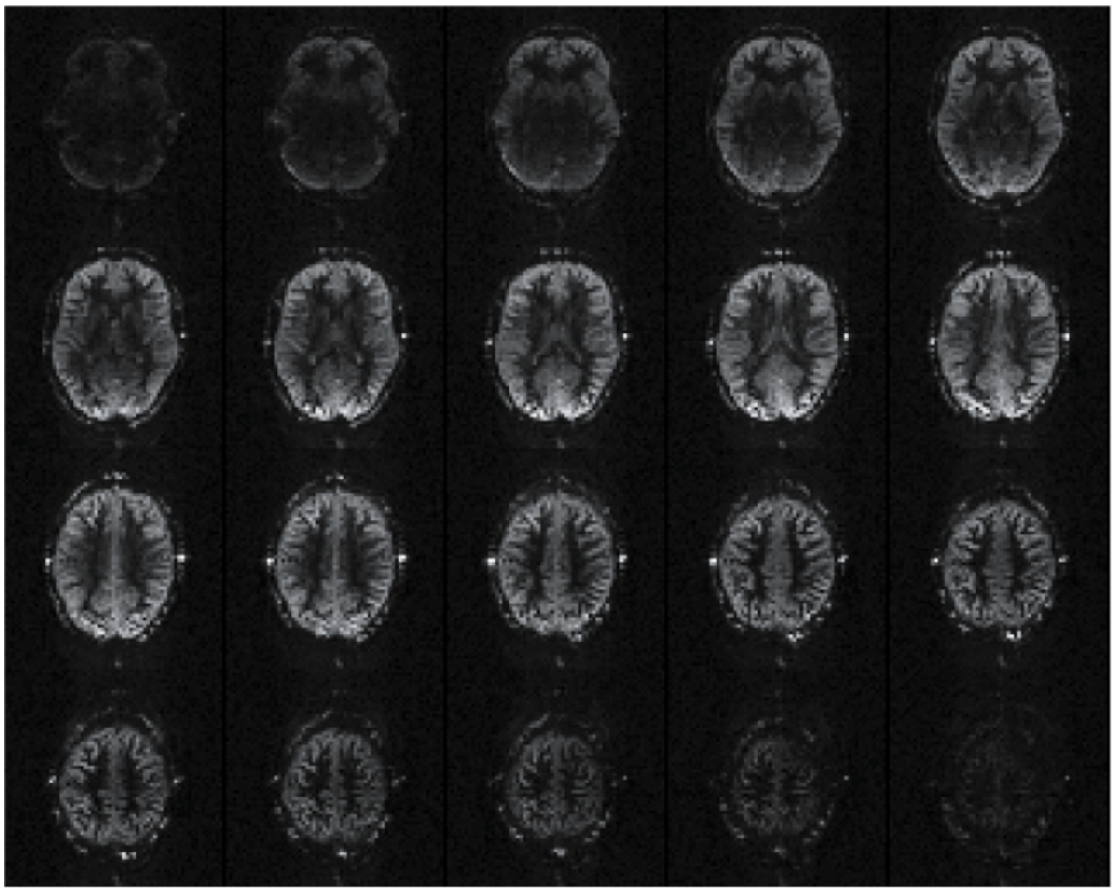

*Figure 4.3: A perfusion weighted image obtained from a healthy control using the imaging parameters in 4.1. The image consists of 20 slices of 64 x 64 voxels with a 3.75 x 3.75 x 3.8 $mm^3$ resolution.*

### 4.1.5 Anatomical data

As described in Chapter 3, PV correction methods usually require an estimate of the tissue concentration in the form of posterior probability maps. These maps are created from the segmentation of high resolution anatomical images and should be of as high a resolution as possible to assist the segmentation algorithms.

Throughout this project an MPRAGE image protocol is used for the anatomical data. The acquisition sequence is optimised to provide the best contrast between grey and white matter in the brain. Figure 4.4 shows an example of the quality of the anatomical data and the tissue probability maps obtained from segmenting that image SPM8 software, as described later in this chapter. The acquisition details of the MPRAGE sequence are shown in table 8.2.

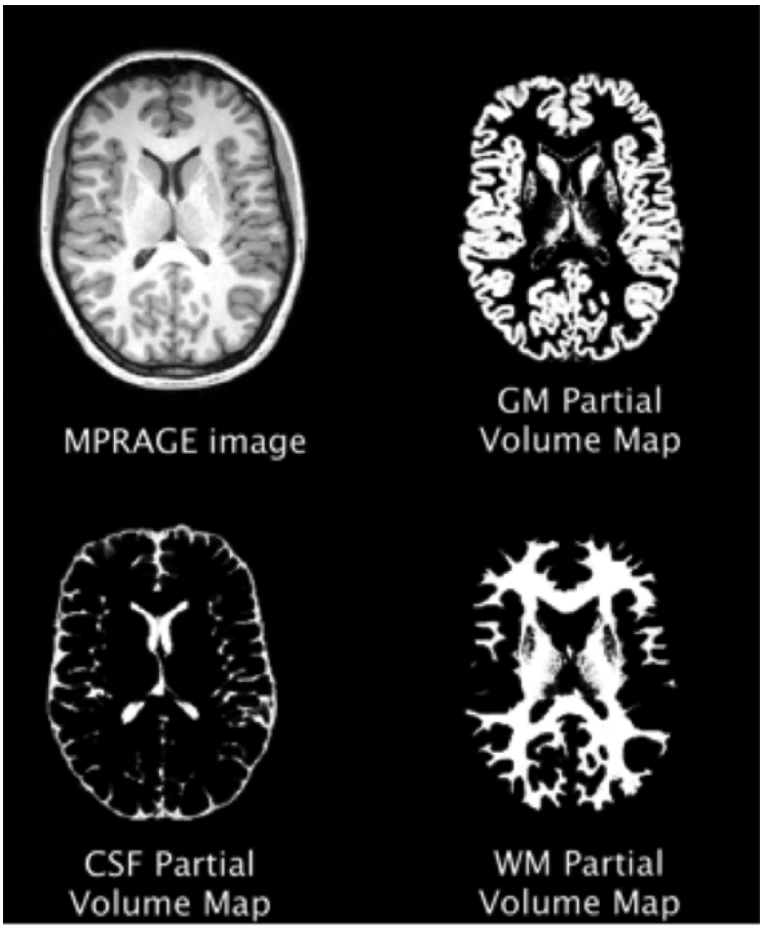


*Figure 4.4: Typical MPRAGE image and associated tissue fraction maps. These are grey scale images with intensities ranging from 0 to 1, which reflect the relevant tissue fraction within a voxel. For example, a voxel intensity of 0.5 represents a tissue partial volume of 50%.*

### 4.1.6 Summary of anatomical imaging parameters

| Parameter | Value |
|---|---|
| Acquisition matrix | 208 x 256 x 256 |
| Resolution | 1.1 x 1.1 x 1.1 $mm^3$ |
| TI | 900 ms |
| TR | 2200 ms |
| TE | 2.9 ms |
| Flip angle | 10 ° |

*Table 4.2: Summary of MPRAGE imaging parameters*

### 4.1.7 Saturation recovery data

As part of the CBF quantification, a proton density image is required for scaling of the data. To achieve this, a series of saturation recovery images were acquired at three time points and fitted to the following model:

$$M(t) = M_0(1 - e^{TR/T_1}) \tag{4.1}$$

where $M_0$ is the equilibrium magnetisation, $T_1$ is the tissue longitudinal relaxation, and $TR$ is the repetition time.

The images were acquired at $t = 1000, 3000, 5000$ ms for the control subjects. In order to produce maps of $T_1$ and $M_0$, each voxel was fitted to the above equation using a non-linear least squares method in Matlab. Example voxel-wise $T_1$ and $M_0$ maps are shown in figure 4.5.

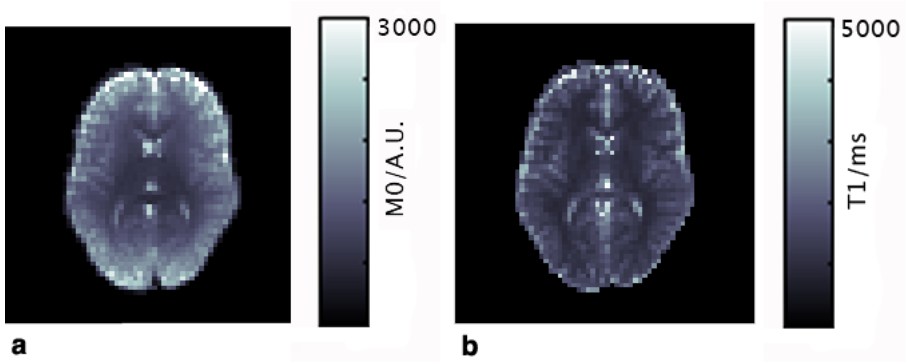


*Figure 4.5: Voxelwise (a) M0 and (b) T1 maps produced from fitting the saturation recovery sequence to equation 4.1.*

## 4.2 Image Processing

Most medical image analysis will require some form of image processing, either as a pre-processing step, to apply a correction to an image (noise removal, bias field correction, motion correction) or to aid analysis of the image itself. This is a vast area of research, so the following sections focus on the image processing techniques which are required to

perform the PVC techniques that are described within this thesis.

### 4.2.1 Bias field removal

Automated analysis of medical images using techniques from the computer vision domain is an ever growing area of research. In MR imaging, a frequently encountered problem for such tools is that of the *bias field*, which is a smooth, low frequency signal which corrupts the image and leads to non-structural intensity variations within the same tissue class.

If $I$ is the measured intensity in the image and $I^{'}$ is the 'true' intensity, then the bias field effect may be modelled by:

$$I = \alpha I' + \epsilon \tag{4.2}$$

where $\alpha$ and $\epsilon$ represent the bias field and additive noise respectively.

Figure 4.6 shows a proton-density image acquired on a 3T scanner, alongside an estimate of the bias field and its subsequent removal from the image. After removal, the image is more uniform in intensity and no longer exhibits the bright central region shown in the pre-correction image. Note that after filtering, the image histogram shows two clearly defined peaks, which are far less apparent before. This clearly illustrates the importance of bias correction for automomated image segmentation.

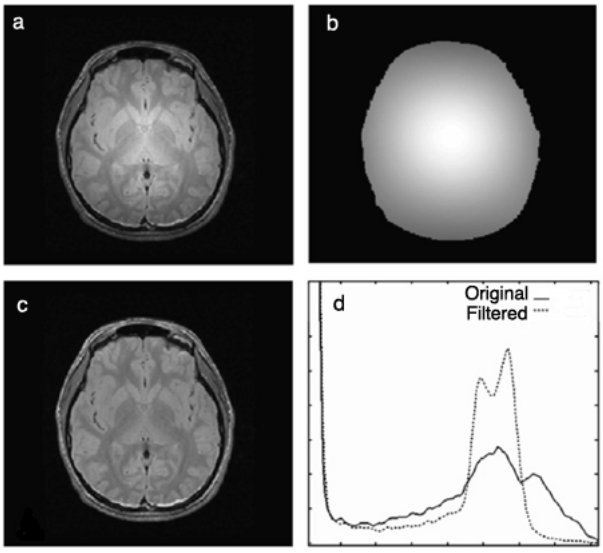


*Figure 4.6: (a) proton-density image acquired on a 3T scanner, (b) an estimate of the bias field, (c) the image after bias inhomogeneity removal, (d) image histogram before and after correction. Adapted from [13].*

The most common causes of this source of inhomogeneity are radio-frequency (RF) non-uniformity, caused by imperfections in the RF coils and interactions between the object being scanned and its environment . This is a particular problem in any type of MR imaging where surface coils are used, and is often apparent in neuroimaging due to the proximity of the head coil to the brain. The existence of a bias field can greatly reduce the accuracy of segmentation and registration techniques, and therefore the reliability of any derived measured. Bias field removal is therefore an essential pre-procesing step in the field of neuroimage analysis.

There are a number of techniques in existence to deal with the issue. If there is knowledge of the bias field in the image domain, perhaps by imaging a phantom, it is a simple matter to correct the image by division of the bias field. However, time constraints may make this impractical. Additionally, a bias field calculated from a phantom image will not necessarily be the same as that induced by a patient.

Another option is to acquire a body coil image and use that to generate coil sensitivity maps for the array coils, in order to account for this inhomogeneity ('pre-scan normalisation' option on the Siemens scanner).

It is also usual to derive the bias field retrospectively from the image, and there are a number of competing tools in the field of MR image analysis offering this service.

Broadly speaking, bias correction methods can be assigned to one of the following three models:

1. *statistical*: the bias field is assumed to be a random variable which can be estimated statistically
2. *low frequency*: the bias field is composed of low frequency oscillations which can be removed in the frequency domain using a low pass filter
3. *hypersurface model*: a map is fit to the bias field using a smooth function, the parameters of which are estimated by regression

Commonly used tools for the estimation and removal of the bias field are:

1. FSL BET [2] contains a bias field removal option
2. Non-parametric Non-uniform intensity Normalization (N3) from Freesurfer [3]
3. SPM bias correction [4]

### 4.2.2 Brain extraction

Perfusion images, by the very nature of their creation, contain little non-brain tissue, such as skin, muscle, fat and eyeballs. High resolution anatomical images of course contain all of these things. Registration between perfusion and anatomical images can be made more robust by the automatic removal of these features from the higher resolution image prior to performing the registration.

In the literature, there are numerous approaches to the task of segmenting the brain into brain and non-brain regions. It seems we can separate the various methodologies into three distinct groups.

[2] http://fsl.fmrib.ox.ac.uk/fsl/fslwiki/BET
[3] http://surfer.nmr.mgh.harvard.edu/fswiki
[4] http://www.fil.ion.ucl.ac.uk/spm

#### 4.2.2.1 Manual segmentation

The first of these methods is manual segmentation by a trained neuroimaging analyst. Interestingly, the author of the tool which is used extensively throughout the world (FSL BET), Stephen Smith of FMRIB, states that manual segmentation of the whole brain from non-brain tissue (as distinct from the segmentation of the brain into tissue classes) is 'probably more *accurate* than fully automated methods are ever likely to achieve' [14]. He states the reasons for this are that the size of the 'image neighbourhood' is essentially the entire brain image, with global information assisting with differentiation between the cerebellum and neighbouring veins, unusual pathology, removal of optic nerves, the external contours of gyri. A manual operator is able to take a somewhat holistic approach to the task in a way that an automated algorithm cannot. However, manual segmentation is non-ideal for the usual reasons of time involved and intra- and inter- operator variability.

#### 4.2.2.2 Thresholding

The second class of whole brain segmentation is based on a simple thresholding of the brain in order to separate the image into foreground and background. Upper and lower thresholds are selected such that the image is separated into bright parts (scalp and eyeballs) and less bright parts, namely brain tissue, skull and air. Thresholding generates a binary image, and theoretically, the largest contiguous non-background cluster should represent the brain. This binary image is then applied as a mask to then original image.

The problems with this somewhat simplistic approach is that the voxel clusters representing the brain are usually remain connected to other non-brain parts of the image by high intensity voxels, effectively 'linking' what should be two disparate portions of the image. These connections must be broken and this process is often carried out using morphological operators to erode and break the connections and then dilate the brain back to its original size.

This 'thresholding plus morphology' technique is really a semi-automated method, as it requires user intervention in the form of threshold selection, which may necessitate a trial and error approach until a good segmentation is found.

#### 4.2.2.3 Surface models

The final class of techniques is that of deformable surface models. A surface model of the brain is constructed from a mesh of shapes, such as a tessellated mesh of triangles, see figure 4.7. This mesh is then deformed to fit the brain by an iterative process which applies two principal constraints to the fitting. Firstly, there is a smoothness condition that is applied so that the mesh surface matches the smoothness of the actual brain surface. Secondly, there is a constraint which matches the model to the relevant part of the brain image, namely, the surface. This method offers an advantage over thresholding techniques in that a large neighbourhood of information is considered for any point of interest, which makes the technique more robust and easier to automate than thresholding methods.

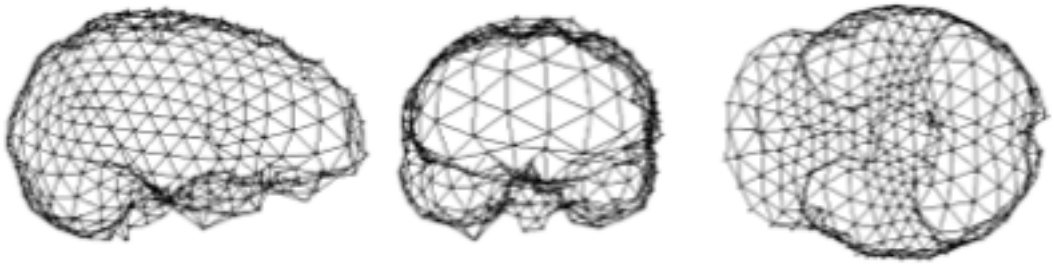

*Figure 4.7: A typical mesh surface used in surface model techniques for brain segmentation. From [14].*

#### 4.2.2.4 Brain Extraction Tool - BET

By far and away, the most widely used automated whole brain segmentation tool is FSL's Brain Extraction Tool (BET). This tool is a hybrid of the two automated techniques described above, and a comprehensive description is provided in [14].

An important parameter which affects the quality of the segmentation is the *fractional*

*intensity threshold*, known as the '-f flag'. This sets the intensity threshold for separating brain and non-brain tissue. Larger values produce smaller brain volumes, and vice versa. A study by Popescu et al systematically investigated a range of values for *f*, coupled with other BET options, against manual segmentation methods. The conclusion of the study was that values of $0.1 < f < 0.3$ coupled with the bias correction facility and removal of neck slices worked best, albeit applied to MS brains, which exhibit atrophy [56]. The lower end of the range is more suited to atrophied brains; interestingly the default value if $f = 0.5$, which is designed for healthy controls.It was found for this cohort of young, healthy brains that the optimal value for f was 0.25.

### 4.2.3 Segmentation

*Segmentation* refers to the process of separating a whole brain volume into its GM, WM and CSF components. Manual segmentation of brain volumes by a trained analyst is the gold standard, but this is very labour intensive and can be subjective. Therefore, there is a high demand for reproducible, accurate, automated brain segmentation algorithms.

Historically, approaches to automated brain segmentation have tended to fall into one of two categories; either *tissue classification* or *registration to a standard template* based.

In the latter approach, a template brain is warped via a process of nonlinear registration to match the brain image which requires segmentation. Prior to warping, regions or segments of interest are defined on the template, which after registration are then overlaid on the brain image to automatically identify structures.

Tissue classification algorithms aim to assign a voxel to a tissue class on the basis of intensity. This approach requires that the intensity distribution for each tissue class is defined. This is usually achieved by modelling the intensity distributions as a *Gaussian mixture model*, or GMM.

The tissue classes (GM, WM and CSF) can be modelled using a histogram of the brain image to be segmented. For this approach to be successful, it is essential that the image is

preprocessed to remove bias field inhomogeneities and other sources of artefact, otherwise it is likely that there will be no clear separation of the tissue classes.

An intensity distribution can be modelled by a mixture of *K* Gaussians. The $k_{th}$ Gaussian is modelled by a mean $\mu_k$ and variance ${\sigma^2}_k$ and mixing proportion $\gamma_k$ where $\sum_{k=1}^{K} \gamma_k = 1$ with constraint $\gamma_k \geq 0$.

For a GMM, the probability of observing voxel intensity $y_i$ given it is a member of the $k_{th}$ Gaussian cluster and that the $k_{th}$ Gaussian has parameters $\mu_k$ and ${\sigma^2}_k$ is:

$$P(y_i)|\mu, \sigma, \gamma) = \sum_{k=1}^{K} P(y_i, c_i = k|\mu_k.\sigma_k, \gamma_k) \tag{4.3}$$

If we assume that all the elements are independent, then the probability of all voxels $\mathbf{y}$ is:

$$P(\mathbf{y}|\mu, \sigma, \gamma) = \prod_{i=1}^{I} \left( \sum_{k=1}^{K} \frac{\gamma_k}{(2\pi\sigma_k^2)^{(1/2)}} exp\left( -\frac{(y_i - \mu_k)^2)}{2\sigma_k^2} \right) \right) \tag{4.4}$$

This probability is then maximised with respect to $\mu$, $\sigma$ and $\gamma$ by minimising an appropriate cost function. The reader is directed to [57] for full details of the derivation.

Figure 4.8 depicts an intensity histogram for a typical brain image. A voxel from that image is selected (in red box) and has intensity = 17203. Three tissue classes are modelled for the GMM, with a class representing GM, WM and CSF. The GMM suggests relative proportions of GM, WM and CSF for that voxel intensity. In this case, we can see that the voxel is almost entirely composed of WM, based on purely on information about voxel intensity.

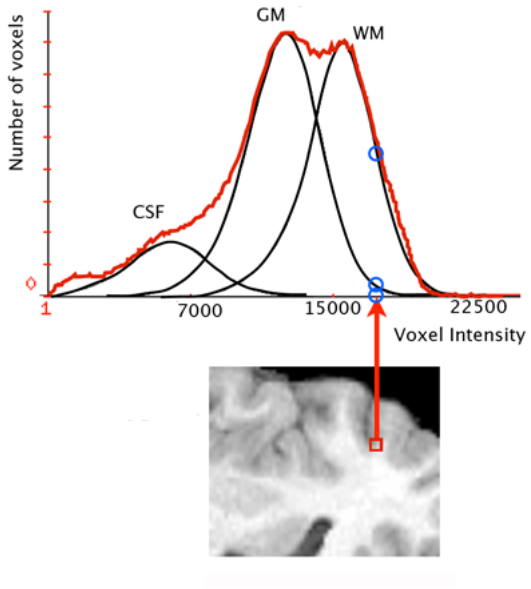


*Figure 4.8: A Gaussian mixture model fitted to an image histogram. Three classes are fitted, to represent GM, WM and CSF. The voxel seleced from the image has an intensity of 17203, which would suggest that the voxel is composed almost entirely of WM.*

However, if the only information from the intensity distribution is used, this can lead to misclassification of voxels, for example scalp has a similar intensity to GM and can be classified as such. Two of the most widely used brain segmentation techniques will be briefly discussed, and their approaches to improving tissue segmentation using a GMM.

#### 4.2.3.1 Statistical Parametric Mapping (SPM8)

More recent developments in neuroimaging analysis have seen a move towards an 'integrated generative modelling approach' in which tissue classification and nonlinear warping are combined within the same framework [57]. This is the approach taken for the tool *Statistical Parametric Mapping version 8*, known as 'SPM8' [5].

SPM8 is a well established tool in worldwide use developed at the Wellcome Trust Centre for Neuroimaging at University College London and runs within a Matlab installation. SPM8 uses an iterative procedure in which bias correction, spatial normalisation and tissue segmentation are all part of the same GMM.

[5] http://www.fil.ion.ucl.ac.uk/spm/

SPM8 improves tissue classification by incorporating *spatial priors* in the form of tissue probability maps. These spatial priors are derived from a modified version of the ICBM Tissue Probabilistic Atlas [6], and give the prior probability of a voxel in a registered image belonging to one of the tissue classes, with the key point being that this probability is irrespective of voxel intensity.

This additional *a priori* information can be factored into the model alongside voxel intensity to aid in assigning a particular voxel to a class. SPM8 estimates tissue partial volumes by using more than one Gaussian per tissue class in its model and iteratively registering to the spatial priors to produce a highly accurate segmentation.

#### 4.2.3.2 FMRIB Automated Segmentation Tool (FAST)

It could be said that the main competitor in the neuroimaging marketplace to SPM8, is *FAST*, developed by the FMRIB group at Oxford University [7]. FAST also models the voxel intensities as a Gaussian mixture model, but does not register to spatial priors. Instead, FAST uses spatial neighbourhood information in the form of a Markov random field (MRF) to offer a likelihood about the class that a voxel belongs to [58].

The MRF encodes information which suggests the class that a voxel may belong to on the basis of the class of the neighbouring voxels, by allowing voxel intensity to vary smoothly, such that if a neigbouring voxel is GM, say, this would tend to suggest the voxel under investigation is also GM.

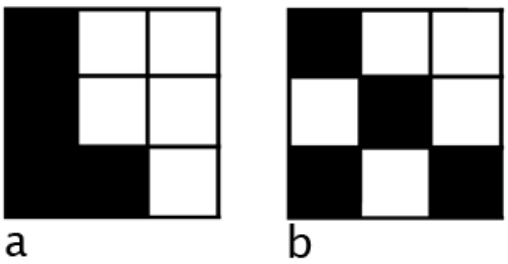


*Figure 4.9: Two possible voxel configurations for a segment of a brain image. Image (b) is an unlikely configuration and would be assigned a low probability. Image (a) is more likely, and would receive a higher prbability, given what is known about brain anatomy.*

To illustrate this point, in figure 4.9 two potential voxel configurations are shown.

[6] http://www.loni.ucla.edu/ICBM/ICBMprobabilistic.html
[7] http://fsl.fmrib.ox.ac.uk/fsl/fslwiki/FAST

The image on the right would be assigned a low probability, as this is an unlikely configuration given what is known about brain anatomy. The left hand image would be assigned a high probability, as a contiguous structure is shown which aligns with our beliefs about brain structure.

This probability estimate can be combined with the GMM to incorporate spatial information into the tissue classification, which makes the algorithm robust to noise. It is then a matter for the user to tune the algorithm so that the correct balance is struck between using voxel intensity and belief about tissue type based on the neighbouring voxels to make a classification:

$$logP(c_i) = logP(y_i) + \beta P(MRF) \tag{4.5}$$

where $P(c_i)$ is the probability of belonging to class $c_i$ for a voxel of intensity $y_i$, plus some weighting $\beta$ of the likelihood offered by the MRF [58].

Both FAST and SPM8 actually produce partial volume estimates, that is, they do not produce hard segmentations of tissue classes, but produce an estimation of what fraction of each voxel belongs to a particular class.

### 4.2.4 Image Registration

The process of spatially aligning two or more images of the same object is known as *image registration*. Image registration is the technique of transforming one image to the coordinate system of the other, with the images then said to be *registered*. Registration between images can be of the same type, known as *mono-modal*. These images may have been taken at different times in a longitudinal study to track disease progression, for example, tumour growth or suppression after a therapy, tissue atrophy in neurodegenerative disease. Other instances where mono-modal registration might be required are motion correction and comparison of pre- and post-operative images.

Multi-modal registration is the technique of registering images from different image

modalities, such as PET and CT, or PET and MRI. This is commonly done for the purposes of using information from one modality to quantify a parameter in the other. For example, using segmentations or regions obtained from a high resolution MRI overlaid on a PET image to assess regional activity. Multi-modal registration is also used in PET PVC techniques which correct for the tissue fraction effect.

The majority of ASL PVC techniques (with the exception of the FRASIER technique) require high resolution MR images to be registered to perfusion images. As such, this is a mono-modal registration, albeit a registration between images created by different MR sequences, which creates some challenges, as will be discussed in this chapter.

The set of parameters which define the registration of one image to another is known as a *transformation* and it is usual to speak of *transforming* one image to the space of another. There three types of transformation which are commonly in used in medical image analysis are: affine, rigid and non-rigid. It is helpful to define some terminology which is in general use. A *source* image is the image which is deformed so as to resemble as closely as possible the *target* image. The target image is fixed, with the source image undergoing deformations (depending on the constraints imposed) until it matches the target as much as is possible using a particular registration algorithm. A brief description of the three types of transformation follows.

#### 4.2.4.1 Rigid transformation

A rigid transformation rotates and translates the source image only. Using homogeneous coordinates which are frequently used in projective geometry, this transformation can be written as:

$$\begin{bmatrix} x' \\ y' \\ z' \\ 1 \end{bmatrix} = \left[\begin{array}{ccc|c} & R & & \begin{matrix} t_x \\ t_y \\ t_z \end{matrix} \\ \hline 0 & 0 & 0 & 1 \end{array}\right] \begin{bmatrix} x \\ y \\ z \\ 1 \end{bmatrix}$$

$$R_x = \begin{bmatrix} 1 & 0 & 0 \\ 0 & cos\alpha & -sin\alpha \\ 0 & sin\alpha & cos\alpha \end{bmatrix}$$

$$R_y = \begin{bmatrix} cos\beta & 0 & sin\beta \\ 0 & 1 & 0 \\ -sin\beta & 0 & cos\beta \end{bmatrix}$$

$$R_z = \begin{bmatrix} cos\gamma & -sin\gamma & 0 \\ sin\gamma & cos\gamma & 0 \\ 0 & 0 & 1 \end{bmatrix}$$

where *x*, *y* and *z* are the coordinates of the voxel to be transformed, $t_x$, $t_y$, and $t_z$ denote the translation to be applied to each axis, with $R_x$, $R_y$ and $R_z$ representing the rotation matrices around the three axes with $R$ = $R_x.R_y.R_z$ and $\alpha$, $\beta$ and $\gamma$ the angles of rotation around them [59].

A rigid transformation is appropriate for registering images of the same subject together, such as in motion correction for a series of images, or images of different MR sequences.

#### 4.2.4.2 Affine transformation

An affine transformation is as a rigid transformation, but with the additional possibilities of shearing and scaling. As such, a rigid transformation is a special case of an affine transformation.

A voxel or pixel is scaled from one image to another in the following way:

$$\begin{bmatrix} x' \\ y' \\ z' \\ 1 \end{bmatrix} = \begin{bmatrix} S_x & 0 & 0 & 0 \\ 0 & S_y & 0 & 0 \\ 0 & 0 & S_z & 0 \\ 0 & 0 & 0 & 1 \end{bmatrix} \begin{bmatrix} x \\ y \\ z \\ 1 \end{bmatrix}$$

where $s_x$, $s_y$ and $s_z$ are the scaling factors for the three axes.

Shearing can be applied when an image is known to suffer from a distortion, such as may occur in MR images in the presence of non-linear gradient fields.

Using the same notation, shearing can be described by:

$$\begin{bmatrix} x' \\ y' \\ z' \\ 1 \end{bmatrix} = \begin{bmatrix} 1 & k_{xy} & k_{xz} & 0 \\ k_{yx} & 1 & k_{yz} & 0 \\ k_{zx} & k_{zy} & 1 & 0 \\ 0 & 0 & 0 & 1 \end{bmatrix} \begin{bmatrix} x \\ y \\ z \\ 1 \end{bmatrix}$$

where $k_{xy}$ represents the shear due to *x* along the *y* axis, and so on.

#### 4.2.4.3 Non-rigid transformations

In brain imaging, the rigid body constraint is satisfied to a good approximation. Consequently global, rigid transformations are the most common type of registration used in neuroimaging applications. Having said that, a correction for an EPI distortion can commonly include a non-rigid registration.

A *non-rigid* or *elastic* registration describes a transformation in which local warping takes place in order to align the source with the target image. Such a transform is non-linear and not able to be described by a matrix operation. A non-rigid transformation may be applied to an image to warp it into the space of a common template (e.g. MNI) in order to make inter-subject comparisons.

In this body of work, affine and rigid transformations are used.

## 4.3 Methods used in this thesis

This section focuses on the details of the implementations used from the available array of image processing tools and techniques.

### 4.3.1 Brain extraction

As previously described, FSL's *BET* is commonly used for the purpose of extracting brain tissue from the head. This tool also has an in-built bias correction facility and outputs a binary mask of the extracted brain. It was found for this cohort of young, healthy brains that the optimal value for the thresholding parameter $f$ was 0.25.

### 4.3.2 Segmentation

The PVC method requires estimates of the proportion of GM, WM and CSF within a voxel. These estimates take the form of tissue posterior probability maps obtained from the segmentation of a high resolution anatomical image.

After the application of *BET*, SPM8 was used to further segment the extracted brains into GM, WM and CSF tissue probability maps. These are partial volume estimates where the fraction of the voxel occupied by a particular tissue type is given. Three maps are produced, one for each tissue type, with the data in the range 0 to 1 and the three maps summing to 1 for each voxel. SPM8 is widely used throughout the medical imaging community and was chosen as the segmentation tool as it has been used by others in PV correction work [7, 40, 6]. Additionally, in a direct comparison between SPM8 and FAST, SPM8 was found to outperform FAST on both simulated data from *Brain Web* and an array of challenging clinical data in terms of the Dice coefficient overlap with the automated method and a manually segmented reference image [60].

*Tool used: SPM8 - tissue segmentation*

### 4.3.3 Registration

#### 4.3.3.1 Target image

The target space for the partial volume correction is perfusion space, at the resolution of the ASL data. This requires transformation of the anatomical data to perfusion space, and also potentially, motion correction of the ASL and saturation recovery sequence images.

Registration of perfusion data is non-trivial as it is usually low resolution and low contrast. The saturation recovery images are not background suppressed, unlike the control/tag images, and contain more static tissue signal and stronger features for registration algorithms to lock on to. As such, the TR = 5000 image was chosen as the target image in perfusion space.

#### 4.3.3.2 Perfusion image

Three averages were acquired for each subject for the control/tag pairs in order to increase SNR. Difference images (subtraction of control and tag pair) are produced automatically on our scanner. The three difference images were rigidly registered to the target image and a mean difference image created from these three. Registering control/tag pairs to the mean control image and creating difference images from the subtraction of the registered pairs was also investigated, but this was found to be less reliable than registration of the scanner-created difference images.

This is somewhat surprising, as the control and tag images have considerably better SNR than the difference images and so one would expect registration of the former to be more easily accomplished than that of the latter. Most likely, the scanner created difference images are a straight subtraction without registration as they are acquired in quick succession. As for registering to the target image, it may be that the background suppression has reduced image contrast to the point that the difference image register better. In any case, the difference images from the scanner were registered to the target

image.

*Tool used: FSL FLIRT - rigid registration*

#### 4.3.3.3 Partial volume estimates

The GM, WM and CSF partial volume maps are created in high resolution anatomical space and it is necessary to transform these to perfusion space.

A mean control image was created by registering the three acquired control images to the target image and taking the mean. The mean control image was registered to the MPRAGE 'BET' image using a rigid transform. This transform was then inverted to provide the transformation from anatomical to perfusion space. This was done because it was found that results were more robust in registering the lower resolution image to the higher one.

The inverted transform was then used in a resampling algorithm to transform the GM, WM and CSF probability maps to perfusion space. This is an important step and care must be exercised when choosing the tool with which to perform this task. At present, the only freely available tool which correctly transforms anatomical information to perfusion space is *FSL applywarp*. This is the only resampling tool which does not use a linear or nearest neighbour (NN) interpolation. Neither of these approaches will transform the PV information correctly.

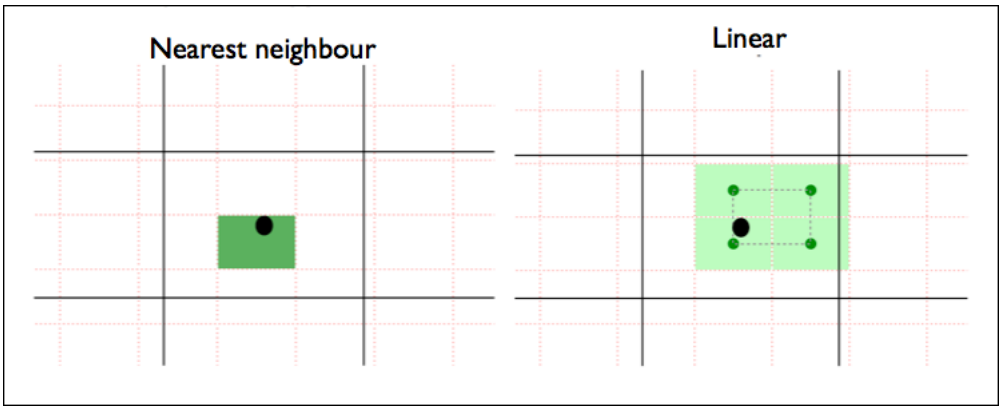


*Figure 4.10: Interpolation schemes. The black lines represent the larger ASL voxels and the red dotted lines the smaller MPRAGE voxels. Nearest neighbour will assign the value of the voxel nearest to new, smaller voxel. This will assist with preserving sharp edges in an interpolated image. A linear interpolation will calculate a new value that lies between the existing voxel values.*

Figure 4.10 shows the larger ASL voxels from perfusion space overlaid on the smaller anatomical image voxels. We require a single value for the ASL voxel (black outline) based on the underlying values from the smaller voxels underneath. A NN interpolation scheme will choose the value of the voxel coloured in dark green, and a linear interpolation scheme will calculate a value that lies between the four highlighted voxels. Neither of these schemes will reflect the entire partial volume information that underlies the ASL voxel, as no information is taken from the other voxels in the region.

To ensure that the PV maps at ASL resolution reflect the PV information across the entire higher resolution region, the transformation (rotation and translation) is first applied to the PV maps, with the target (ASL) image at a four times super-sampled resolution of the ASL data. A spline interpolation of the high resolution PV maps to the super-sampled ASL image is employed, with the PV maps in the lower resolution ASL space derived by integration over the appropriate region. In essence, this amounts to calculating the mean PV of the smaller voxels in anatomical space that equate to a large ASL voxel. This sounds a rather tortuous procedure; fortunately it is achieved in one step using the FSL tool 'applywarp'. As an aside, it should be noted that spline interpolation was used with *applywarp*, in a like manner to the work in [15] and [9]. Given that the most accurate method of interpolation is apodised sinc, it may be appropriate to make use of the sinc interpolation option available with *applywarp*, as inaccurate registration is likely to result

in artefacts in the transformed PV maps [61].

The use of *applywarp* underpins the use of *FLIRT* as the registration algorithm. *applywarp* is only compatible with *FLIRT*, so it is not possible to use another registration tool. Nonetheless, *FLIRT* is a well-established registration tool in worldwide use.

*Tool used: FSL applywarp - resampling*

### 4.3.4 Partial Volume Correction

Following the above steps results in motion-corrected perfusion data and PV maps in perfusion space. It is then possible to apply a PV correction method (e.g.BASIL, linear regression) which will produce separate GM and WM perfusion maps. It should be noted that the common pre-processing step of smoothing is not applied to the perfusion data, as the linear regression method for PVC introduces an inherent spatial smoothing.

The initial paper proposing the use of linear regression for PV correction by Asllani et al stressed the importance of applying the method to both the difference image *and* the control or M0 image. This of course doubles the processing time, and moreover, the M0 or proton density scaling image is not always available from a clinical scanner. An investigation into the difference between applying the correction to $\Delta M$ and M0 or directly to the CBF map is provided in section 5.5.

The PV correction results are presented in this thesis in such a way that two separate perfusion maps are produced, one for GM and one for WM CBF. These maps present the perfusion as though each voxel contained 100% GM or WM. Note, the values are not scaled by tissue fraction, as is sometimes the case [9, 7]. This is a detail that can lead to confusion, so for the sake of clarity, an example is given here.

Consider a voxel of intensity 40 A.U. with partial volumes of 0.5 GM and 0.5 WM within an uncorrected image. After partial volume correction, separate GM and WM maps are produced with intensities of 60 and 20 respectively for that voxel. These values represent the unscaled intensity for GM and WM. If these maps were then scaled by the partial

volume fraction, the same voxel would have values of 30 and 10 respectively in the GM and WM maps; the product of the corrected intensity and the partial volume for each map. This approach allows one to readily envisage the contribution oof each tissue to the observed voxel value (e.g. for the 40 A.U. voxel, 30 A.U comes from GM and 10 A.U. from WM), but it does offer any information about the pure actual tissue flow, so is not the methodology used in this thesis.

## 4.4 Regional Analysis

It can be appropriate to consider mean regional values rather than global mean values, in order to assess the impact of deblurring and PV correction algorithms on a local basis.

### 4.4.1 Parcellation using FreeSurfer

Regions of interest (ROI) were obtained by performing a *parcellation* of a subject anatomical scan using the FreeSurfer package [8]. FS is an automated software suite for analysis of anatomical MR data. *Parcellation* is the process of dividing an anatomical image into a set of labelled regions which provide some sort of description of the image. In the application used in this work, parcellation has been used to divide the brain into volumes of interest which represent anatomical areas and is distinct from a *segmentation*, in which only three tissue regions (GM, WM and CSF) are produced.

Like segmentation, parcellation is achieved by registering the subject anatomical image to a standard space, such as the MNI or Talairach space. It is beyond this scope of this thesis to provide a detailed description of FreeSurfer; suffce to say, the parcellation takes place in standard space, but is propagated back to subject space, so that a subject specific parcellation is produced.

FreeSurfer produces a very detailed parcellation containing several hundred individual regions. These have been combined into a superset of larger regions, as this level of detail

[8] Martinos Centre for Biomedical Imaging, Harvard, MA, USA

is not required. Parcellation is an incredibly intensive process, which takes on the order of 24 hours for a single subject, even for quad core machines.

The parcellations must be transformed to ASL space. This is done in the same way as for the transformation of the PV maps, which one notable difference. As the labelled regions produced by FreeSurfer need to be transformed in such a way that their integer values are preserved, that is, the integer label of region, as they are in fact masks. A linear or spline interpolation would produce non-integer values, so a 'nearest neighbour' interpolation is used.

### 4.4.2 Regions of Interest

The detailed FreeSurfer parcellations were combined into larger ROI for analysis. These took the form of 9 masks, consisting of 9 GM regions and 1 WM region. It was considered sufficient to combine all WM voxels into one region and consider them as a whole for two reasons. Firstly, whether or not it is possible to measure WM perfusion using CBF is still a matter of debate, given the low SNR due to long transit times compared to T1 relaxation of blood, so is of questionable utility.

Secondly, the PVC correction methods developed in this thesis were applied to a cohort of patients who are either at risk of cortical atrophy, or are diagnosed as suffering from dementia, so the ROIs were chosen with this application in mind. These are the same ROI as used in [16] and were chosen by clinicians as relevant regions in terms of propensity for atrophy in dementia patients, such as the frontal, parietal and temporal lobes.

One of the FreeSurfer outputs is a file called *aparc+aseg.mgz*, which is where the parcellation results can be found. This file contains the FreeSurfer labels which have been combined to produce the larger region masks as detailed in table 4.3.

## 4.5 Processing pipeline

This chapter describes the image processing and general methods which constitute the ASL PVC processing pipeline. A schematic can be seen in figure 4.11. The elements coloured yellow represent high resolution images, the low resolution images are pink, with processes coloured blue.

The partial volume correction pipeline is essentially a post-processing technique, and is heavily reliant on a successful registration of high resolution anatomical data to much lower resolution perfusion space. The pipeline involves segmentation, registration, resampling and linear regression. Numerous options exist for each step of the pipeline, and a successful outcome is dependent on choosing the correct tool. This chapter describes the tools used in this thesis along with the rationale for doing so.

Chapters 5, 6, and 7 describe novel developments to the pipeline which improve the accuracy of GM and WM perfusion estimations.

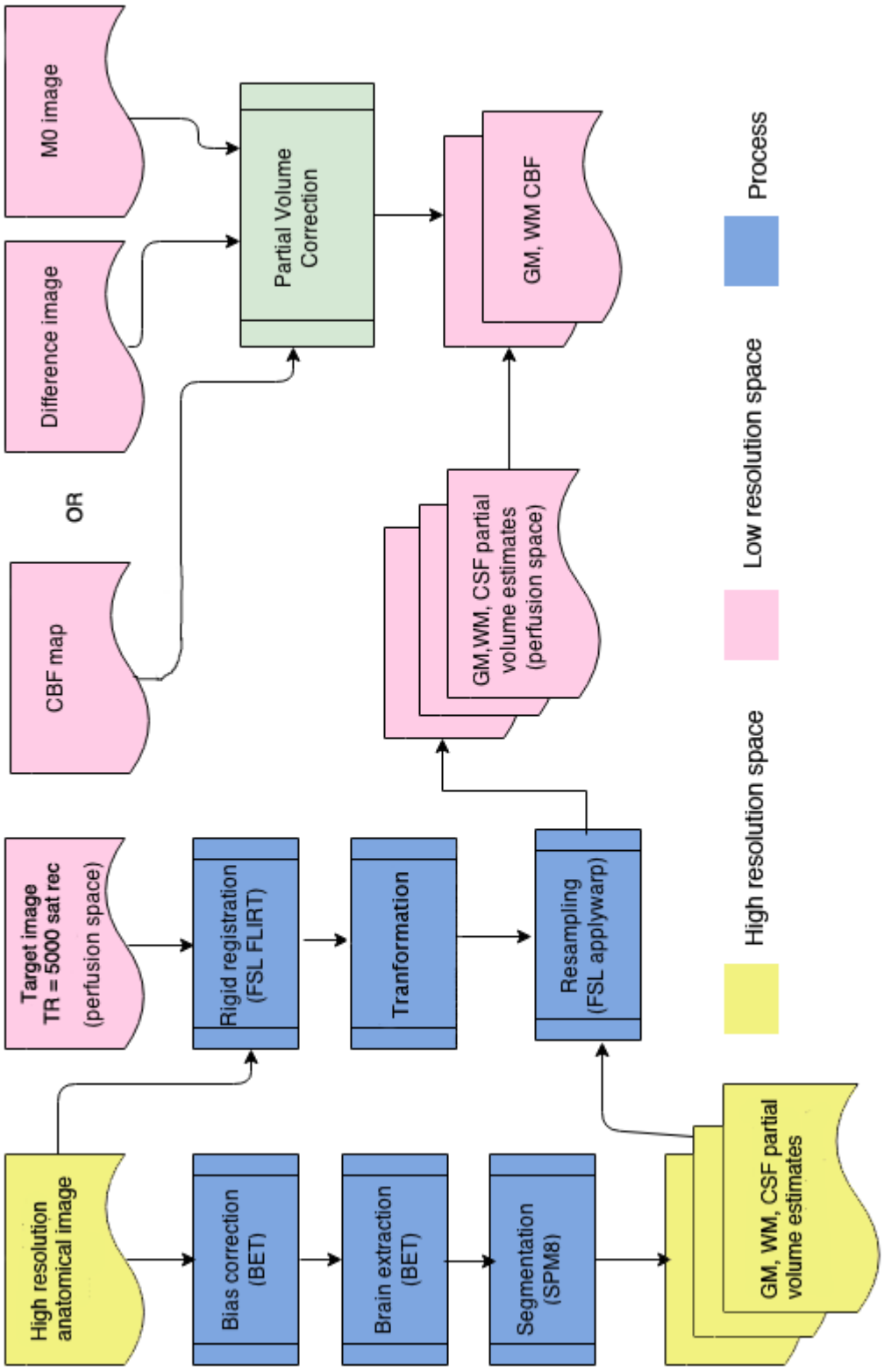


*Figure 4.11: Schematic of the processing pipeline for the image processing techniques used for pre-processing prior to PV correction.*

| Region | FreeSurfer labels in region |
|---|---|
| Frontal | 1028 2028 1027 2027 1003 2003 1018 2018 1019 2019 1020 2020 1012 2012 1014 2014 1032 2032 |
| Central | 1024 2024 1017 2017 1022 2022 |
| Parietal | 1029 2029 1008 2008 1031 2031 1025 2025 |
| Temporal | 1030 2030 1015 2015 1009 2009 1007 2007 1034 2034 1006 2006 1033 2033 1016 2016 1001 2001 |
| Occipital | 1011 2011 1013 2013 1005 2005 1021 2021 |
| Cingulate | 1026 2026 1002 2002 1023 2023 1010 2010 |
| Insula | 1035 2035 |
| Deep GM | 10 49 11 50 12 51 13 52 18 54 26 58 27 59 |
| Hippocampus | 17 53 |
| WM | 7 46 1004 2004 2 41 77 78 79 250 251 252 253 254 255 |

*Table 4.3: Regions of interest defined from FreeSurfer parcellation labels contained in aparc+aseg.mgz.*

# Chapter 5

# Improvements on Linear Regression method for Partial Volume Correction

This chapter presents a novel extension to the 2D kernel linear regression method for PVC published by Asllani et al [22]. An investigation into a Bayesian inference model for PV correction is applied to single time point ASL data for the first time, and a comparison made between that and the improved LR method.

This work was the subject of oral presentations at ESMRMB 2012 and 2013 and a poster at ISMRM 2013.

## 5.1 Introduction

The linear regression method for PV correction causes an inherent blurring in the produced GM and WM CBF maps due to the assumption that magnetisation and perfusion is constant over the linear regression kernel region. The larger the kernel, the greater the smoothing effect; the smoothing is equivalent to the application of a Gaussian smoothing kernel of FWHM 5mm and 9mm for a 5 x 5 and 15 x 15 kernel respectively for voxels of in-plane resolution 3.4 x 3.4 $mm^2$ [22]. Nonetheless, a larger kernel results in more equations being available, and so there is a trade-off between these considerations.

## 5.2 Development of 3D kernel applied to PVC

### 5.2.1 Theory

The linear regression method of PV correction is designed to solve a system of linear equations for two or three unknowns. It would seem reasonable that a 3 x 3 square kernel would provide sufficient information to solve the inverse problem, as this offers nine equations for the regression. In practice, there are boundary conditions which mean that a kernel containing so few voxels is not suitable.

Recall the equation from chapter 3 for separating the voxelwise magnetisation signal into GM, WM and CSF components:

$$M(r_i) = P_j(r_i) \cdot m_j(r_i) \tag{5.1}$$

where $M(r_i)$ is the total voxel magnetisation, $P_j(r_i)$ is a vector containing the posterior probabilities for all 3 tissue types and $m_j(r_i)$ is the tissue specific magnetisations.

Solving for $m_j$ is accomplished using the standard least squares solution:

$$m_j = (P_j^T \cdot P_j)^{-1} \cdot P_j^T \cdot M \tag{5.2}$$

where $(P_j^T \cdot P_j)^{-1} \cdot P_j^T$ is the pseudoinverse of $P$.

If either of the following situations is encountered:

1. The Moore-Penrose pseudoinverse of $P_j$ is singular
2. The LR kernel contains less than 3 non-zero voxels (as can occur at the brain boundary)

then some form of special case handling must be applied.

Asllani handled these cases by imposing the condition that the central voxel in the kernel

(i.e. the one that is being PV corrected) be set to zero when either of these two situations occur. It was found that in the case of a 3 x 3 kernel these two situations are frequently encountered on the brain boundary. Asllani reports that the smallest useful kernel is 5 x 5, although there is one instance in the literature where the authors describe using a 3 x 3 kernel without any reported problems [9]. The authors do not state whether they used the same criteria as above, or how they handled these cases.

### 5.2.2 From a 2D to a 3D kernel

It is proposed that the radius of the linear regression kernel may be reduced, yet retain sufficient information, by moving from a 2D form to a 3D embodiment. Theoretically, this novel idea facilitates a reduction in the radius of the kernel whilst retaining the number of voxels and therefore information within the kernel.

This idea is depicted in figure 5.1. The image on the LHS shows a 2D 5 x 5 kernel, which is the smallest kernel recommended by Asllani and the one usually implemented for LR PVC. It is proposed to replace this with the 3D 3 x 3 x 3 kernel on the RHS.

*Figure 5.1: Comparison of 2D and 3D kernel. An equivalent number of voxels are contained within each kernel, although the 3D kernel has a smaller radius than the 2D kernel.*

Minimising kernel radius reduces the associated blurring effect of PVC by LR, which is important to preserve spatial detail. From table 5.1 it can be seen that in a 3 x 3 x 3 kernel, there are 27 voxels with a kernel radius (at the furthest point) of $\sqrt{3}$ compared to $\sqrt{8}$ for a 2D 5 x 5 kernel. Therefore, there are a comparable number of voxels (and thus equations), but the kernel has a smaller radius that will translate to reduced blurring in the PVC images.

| Kernel size | 2D voxels | 2D Max radius (A.U.) | 3D voxels | 3D Max radius (A.U.) |
|---|---|---|---|---|
| 3 | 9 | $\sqrt{2}$ | 27 | $\sqrt{3}$ |
| 5 | 25 | $\sqrt{8}$ | 125 | $\sqrt{12}$ |
| 7 | 49 | $\sqrt{18}$ | 343 | $\sqrt{27}$ |
| 11 | 121 | $\sqrt{50}$ | 1331 | $\sqrt{75}$ |

*Table 5.1: Comparison of the number of voxels and subsequent kernel radius for 2D and 3D kernels.*

The use of a 3D kernel is particularly suited to isotropic 3D data, as has been acquired in the studies presented in this thesis. It is not uncommon for voxels to be larger in the slice direction; if a 3D kernel is used in these cases, it is likely that a greater amount of blurring will occur in this direction, than in-plane. Additionally, as each image slice has a different inflow time for 2D EPI data, this means that a 3D kernel will require a more complex treatment when applied to this type of data. (A potential solution to this problem is to perform the PV correction directly to a CBF map; the validity of this approach is discussed in section 5.5).

It should be noted that the use of a 3D kernel does not impose any additional computational load over that of the original linear regression method. With the advent of 3D image acquisitions, it is a simple matter to apply a 3D kernel to the perfusion images.

## 5.3 Application of the 3D kernel for PV correction

### 5.3.1 Simulation study

In order to properly assess the performance of an algorithm, a ground truth is required. A simulated data set was based on vivo data in order to quantify the performance of the PVC algorithm using the existing method of a 2D kernel and compare it to the new method using a 3D kernel.

#### 5.3.1.1 Creation of simulated data

GM and WM posterior probability maps from a subject from the in vivo data were transferred to ASL space and resolution as previously described in chapter 3. The resolution of these maps after transformation was 3.75 x 3.75 x 3.8 $mm^3$ on a 64 x 64 x 20 voxel grid. The creation of the simulated data was modelled on that in [15, 6]. The GM voxels intensities were set to 60 A.U. in GM, 20 A.U. in WM, with a hyper- and hypo- intense spherical regions (radius = 5 voxels) of 100 A.U. and 20 A.U. located in GM.

Previous studies investigating the noise characteristics of CBF images suggest that there is little to no autocorrelation in the noise and that it can essentially considered to be white [62]. More recently, researchers investigating image blurring caused by the point spread function (PSF) propose that it is possible to determine the PSF from the autocorrelation of the residuals obtaining from fitting perfusion data to a model, which would suggest that the noise is correlated [15, 47]. This work is discussed in section 7.2.3.2.

However, for the purposes of this simulation study where the data is generated from structural data without any blurring, it is appropriate to assume a Gaussian noise model. Accordingly, white noise of amplitude = 5 was generated using the Matlab function *randn* which generates a pseudorandom number from a normal distribution with mean of 0 and standard deviation of 1. This was added to the image, such that the SNR was 20 for a 100% GM voxel of intensity 100. Partial volume effects were introduced according to:

$$\Delta M = P_{GM}(r_i)m_{GM}(r_i) + P_{WM}(r_i)m_{WM}(r_i) \tag{5.3}$$

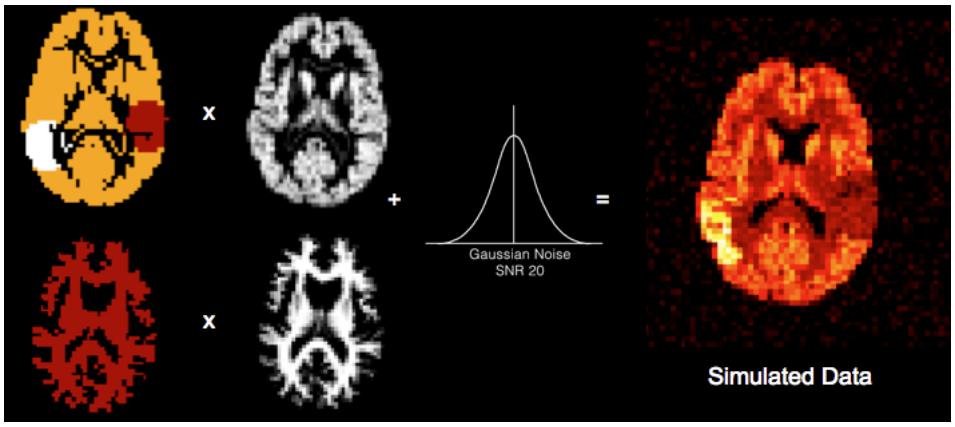


*Figure 5.2: Creation of simulated data. Ground truths for GM and WM were created with simulated hypo- and hyper-perfusion lesions of radius 5 voxels in the GM ground truth. Partial volume fractions were applied to the ground truths and the images combined along with Gaussian noise of SNR = 20 for the hyperperfused lesion.*

#### 5.3.1.2 Method

In the model (see equation 5.3), the perfusion in CSF was set to zero, therefore the GM and WM intensities are the only unknown quantities. Kernel sizes of 3,5,7 and 11 in both 2D and 3D format were used to PV correct the simulated data. The root mean square error (RMSE) between the PV corrected result for GM and the GM ground truth was calculated for all pixels.

To assess the level of smoothing introduced by the smallest kernels, 3 x 3 x 3 and 5 x 5, a line profile was taken through the hypo- and hyper-perfusion regions and compared to the line profile through the same regions in the ground truth.

#### 5.3.1.3 Results

| Kernel size | 2D voxels | RMSE for 2D | 3D voxels | RMSE for 3D |
|---|---|---|---|---|
| 3 | 9 | 4.16 | 27 | 3.96 |
| 5 | 25 | 4.04 | 125 | 4.08 |
| 7 | 49 | 4.15 | 343 | 4.23 |
| 11 | 121 | 4.35 | 1331 | 4.60 |

*Table 5.2: Root mean squared error between simulated GM ground truth and PVC results using a 2D and 3D kernels of sizes 3,5,7 and 11.*

In table 5.2, the 'Kernel size' column indicates the kernel side length in number of voxels and columns 2 and 4 show the total number of voxels that would be contained in the kernel, if the kernel was 2D or 3D. It can be seen that the lowest RMSE, that is difference between the ground truth and recovered GM image is for the 3D 3 x 3 x 3 case. Broadly speaking, as the kernel size grows, whether 2D or 3D, the RMSE increases. However, there is a decrease in RMSE in moving from the 2D cases of 3 x 3 to 5 x 5, despite an increase in kernel size. The reason for this is that the boundary conditions are invoked frequently for the 3 x 3 case, which has the effect of stripping away voxels at the brain edge, as the value of the voxel is set to 0.

The smallest RMSE is observed for a 3D 3 x 3 x 3 kernel, as predicted by the hypothesis. The 3D 3 x 3 x 3 kernel contains 27 voxels, which is comparable to the 25 voxels in the 2D 5 x 5 kernel, yet the kernel radius is smaller, which leads to less in-plane smoothing in the PV corrected images and therefore a closer recovery to the ground truth values.

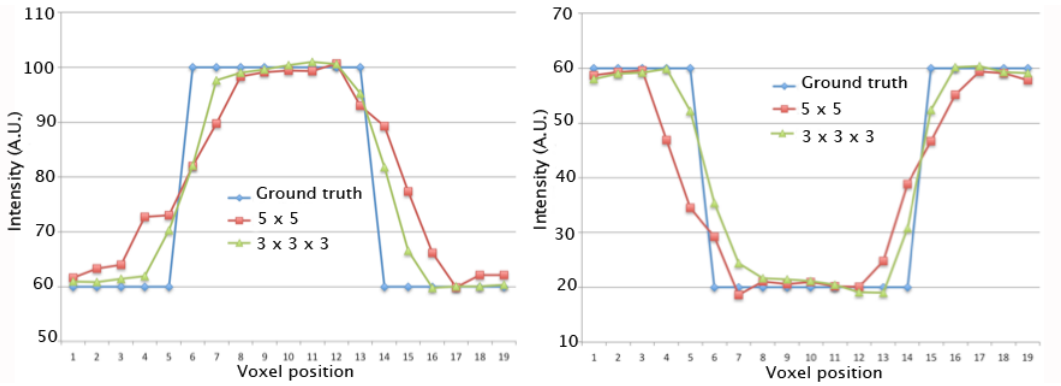


*Figure 5.3: Profiles taken through the hyperperfused lesion (RHS) and hypoperfused lesion (LHS) of the simulated data. The ground truth data is shown by the blue line and is a step function. The 3D kernel PVC result is shown in green, with the 2D in red. The 3D kernel result is closer in profile shape than the 2D kernel.*

Line profiles through the hyper- and hypo-intense regions for both the ground truth and the GM recovered regions are shown in figure 5.3. The ground truth is marked in blue and shows a step change in intensity associated with the simulated lesions. It can be seen that the 3 x 3 x 3 is closer in profile to the ground truth than the 5 x 5 kernel, which translates to reduced blurring of edges.

This finding is also demonstrated in figure 5.4 which shows the same middle slice through

the ground truth, the GM PV fraction map, the simulated data and the attempts to recover the ground truth using a 3 x 3 x 3 and 5 x 5 kernel. It can clearly be seen that by using the 3 x 3 x 3 kernel the edges of the simulated lesions are better preserved. This difference can be quantified by considering the FWHM of the intensity profile for the slice shown. The lesion diameters at FWHM for the hyperperfused region are: ground truth = 28.1 mm, 2D kernel = 31.9 mm, 3D kernel = 29.4 mm. For the hypoperfused region: ground truth = 31.9 mm, 2D kernel = 33.8 mm, 3D kernel = 30.6 mm. Both PVC methods overestimate the lesion diameters for the hyperperfused lesion, but at the FWHM, the 3D kernel slightly underestimates for the hyperperfused one, compared to the 2D case. This result is a consequence of the reduced blurring with the higher intensity region around it in the 3D case.

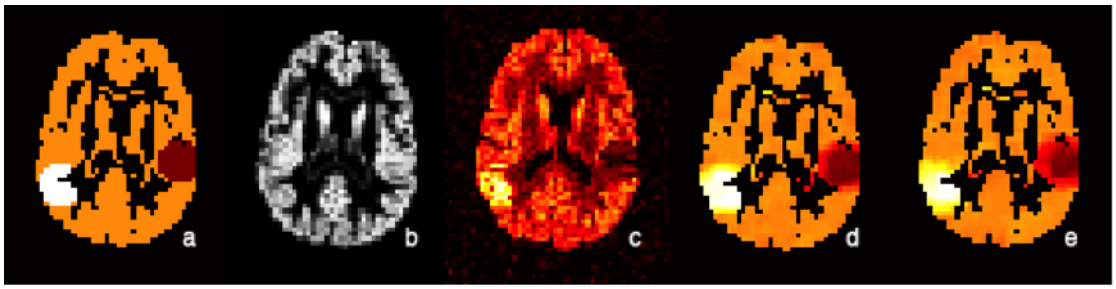


*Figure 5.4: Simulated data and result. (a) Ground truth (b) Partial volume fraction GM (c) Simulated data (d) 3x3x3 kernel PVC GM result (e) 5x5 kernel PVC GM result.*

#### 5.3.1.4 Discussion

This piece of work focused on an attempt to modify an established method of partial volume correction for ASL data in order to reduce the inherent spatial blurring which occurs as a consequence of the assumption that perfusion is constant over the linear regression kernel. It has been shown that the smallest viable 2D kernel is 5 x 5, although this still introduces blurring in the recovered pure tissue maps equivalent to smoothing with a 5mm FWHM Gaussian kernel.

Use of a 3D kernel allows the kernel radius to be reduced whilst preserving total voxel numbers, and therefore equations for the linear regression method. A 3D 3 x 3 x 3 kernel offers 27 equations, compared to 25 for the nearest 2D equivalent. The smaller radius of

the 3D 3 x 3 x 3 kernel compared to the 2D 5 x 5, which results in reduced blurring in the recovered GM and CBF pure tissue maps.

Consequently, the 3D kernel is better at preserving spatial detail, in particular high contrast edges. This is a useful and important finding, which has potential applications in patient groups. If PV correction techniques are to be applied to pathological cases, it is important that disease features are not smoothed away during post-processing techniques.

For example, Multiple Sclerosis (MS) patients present with lesions throughout the brain that are a result of inflammation and demyelination. Studies have shown decreased perfusion in cortical lesions compared to normally appearing GM [63, 64, 65]. As an additional feature of MS is brain atrophy, it is important for longitudinal studies that a PV correction is performed in order to compare perfusion across time points. Lesion volume is used as a surrogate marker of disease progression. Clearly, it is also important that the boundary of these lesions is preserved, rather than blurring any significant changes in perfusion out into the surrounding healthy tissue.

### 5.3.2 In vivo study

Previous studies have demonstrated the efficacy of the linear regression method in correcting for the tissue fraction effect [6, 9, 22, 7, 46]. This investigation sought to characterise the difference, if any, between recovered GM CBF maps using a 2D and a 3D kernel, and to assess how the reduced smoothing effect seen using a 3D kernel on simulated data, translates to in vivo data.

#### 5.3.2.1 Theory

The simulation and theoretical considerations suggest that less smoothing will be present in PV corrected maps of GM CBF using a 3D kernel. When using in vivo data, no ground truth is available, which makes the assessment of results obtained using different

methods difficult. That being said, there is a parameter that we wish to optimise (level of smoothing) and it is possible to make a comparison study between the two methods which assesses this.

With this goal in mind, the *spatial gradient* is introduced. This can be regarded as a measure of retained spatial detail in the image and borrows from the field of computer vision with its gradient edge detectors [66].

Edge detection is a mathematical technique which is applied to an image in order to detect regions where the image intensity changes rapidly, such as at a boundary or some strong image feature and be accomplished using first or second order derivatives.

The mathematical tool of choice for detecting both edge strength and direction at a particular location $(x, y, z)$ in an image $I$ is the *gradient*, denoted $\nabla I$ and is defined as the vector:

$$\nabla I = grad(f) = \begin{bmatrix} g_x \\ g_y \\ g_z \end{bmatrix} = \begin{bmatrix} \frac{\partial I}{\partial x} \\ \frac{\partial I}{\partial y} \\ \frac{\partial I}{\partial z} \end{bmatrix} \tag{5.4}$$

where $\frac{\partial I}{\partial x}$, $\frac{\partial I}{\partial y}$, $\frac{\partial I}{\partial z}$ are the numerical gradients along the first, second and third dimensions of the image.

As $\nabla I$ is a vector quantity, it offers information about direction and magnitude of the greatest change of image intensity. For the purpose of assessing retained spatial detail in a image, it is sufficient to be concerned with the magnitude of $\nabla I$:

$$G = mag(\nabla I) = \sqrt{{g_x}^2 + {g_y}^2 + {g_z}^2} \tag{5.5}$$

which represents the rate of change of intensity in the gradient vector. *G* is a voxelwise representation of the gradient of image $I$ and as such is an image the same size as $I$.

If the GM CBF image obtained using a 3D kernel contains a larger magnitude of spatial

gradient than that from a 2D kernel, this suggests that there is more retained detail in the image.

#### 5.3.2.2 Method

Perfusion and anatomical data were collected using the imaging protocol described in chapter 4. The control group consisted of 4 females and 2 males with ages ranging from 23 to 31 years (mean age 26.3 $\pm$ 3.1 years).

The processing pipeline as described by figure 4.11 was utilised to produce separate maps of GM and WM perfusion. The PV correction algorithm was applied to the $M0$ and $\Delta M$ images separately, before combining to a single image of either GM or WM perfusion. The images were PV corrected using a 2D 5 x 5 and 3D 3 x 3 x 3 kernel.

The mean CBF prior to correction and mean GM CBF, using a 2D and 3D kernel for correction were calculated across the whole brain, after masking at GM PV fraction 0.1. It is commonly accepted practice to exclude voxels with PV fractions less than 0.1, as there is too little tissue within the voxel for the LR to be reliable [15, 6].

In order to quantitatively assess the correction using the 2 kernels, the consistency of the mean GM CBF was calculated across the range of GM PV fractions, in a manner like that described in [22, 15]. The GM probability map was split into nine binary masks containing 10-20%,20-30%.....90-100% GM PVF. As the GM PV maps are quite heterogeneous, these masks represent a pseudorandom sample across the brain. The mean CBF and GM CBF was calculated within each 10% range.

Additionally, the GM was separated into 9 regions using a Freesurfer parcellation, representing frontal, central, parietal, temporal, occipital, cingulate, insula, deep GM, and hippocampal regions. The mean CBF and corrected GM CBF was calculated in these contiguous regions.

To make a quantitative comparison of smoothing resulting in the PV corrected maps, the magnitude of the spatial gradient of the GM CBF maps was calculated for each voxel

using equation 5.5. The large gradient obtained at the brain boundary was removed by image erosion, prior to masking at GM PV fraction > 0.1 to exclude low GM regions. The mean spatial gradient and standard deviation was calculated over the remaining voxels for both the 2D and 3D cases.

#### 5.3.2.3 Results

The global mean of the standard, uncorrected CBF map, and 2D and 3D kernel PV corrected GM CBF maps is listed in table 5.3. Comparing the GM CBF after PV correction using both a 2D and 3D kernel, there is little difference between the mean values, calculated across all voxels after excluding voxels which have less than 10% GM, in accordance with the recommendation in [15]. The ratio of PV corrected GM CBF to uncorrected CBF ranged from 1.2 to 1.6 for 2D, and 1.3 to 1.6 for 3D.

| | | 2D | 3D | 2D | 3D |
|---|---|---|---|---|---|
| Subject | CBF (ml/100g/min) | GM CBF (ml/100g/min) | | Spatial Gradient (/voxel) | |
| AA | $49.6 \pm 22.6$ | $61.3 \pm 14.4$ | $62.9 \pm 17.1$ | $12.7 \pm 11.1$ | $13.7 \pm 10.4$ |
| HH | $43.1 \pm 24.6$ | $62.3 \pm 20.8$ | $62.0 \pm 22.5$ | $10.7 \pm 7.3$ | $12.0 \pm 7.8$ |
| MS | $39.5 \pm 16.9$ | $55.8 \pm 17.3$ | $55.8 \pm 19.0$ | $9.0 \pm 7.1$ | $10.2 \pm 7.5$ |
| MV | $37.6 \pm 18.5$ | $61.3 \pm 22.0$ | $60.8 \pm 22.6$ | $14.0 \pm 10.9$ | $14.7 \pm 11.5$ |
| RR | $39.4 \pm 21.7$ | $62.7 \pm 21.1$ | $61.9 \pm 19.3$ | $11.2 \pm 8.9$ | $12.4 \pm 9.4$ |
| SK | $34.9 \pm 15.2$ | $53.4 \pm 16.2$ | $53.0 \pm 18.2$ | $9.3 \pm 7.6$ | $10.5 \pm 7.9$ |

*Table 5.3: In vivo data results: Uncorrected CBF, PV corrected GM CBF and spatial gradient using a 2D and 3D kernel for the PV correction. All values are mean of the remaining voxels after excluding GM PV fraction < 0.1.*

The correction on a regional basis is shown in figure 5.5 and table 5.4. Of the six subjects, four had greatest perfusion both before and after correction in the occipital region (AA, HH, MV, RR). Of the remaining two, MS showed greater perfusion in the hippocampal region both before and after correction, with SK showing greater perfusion in the occipital region prior to correction, but marginally greater perfusion in the hippocampus after correction with a 3D kernel. The correction using a 2D kernel was greatest in the occipital region.

The correction across the GM PV fractions relative to the uncorrected CBF can be seen

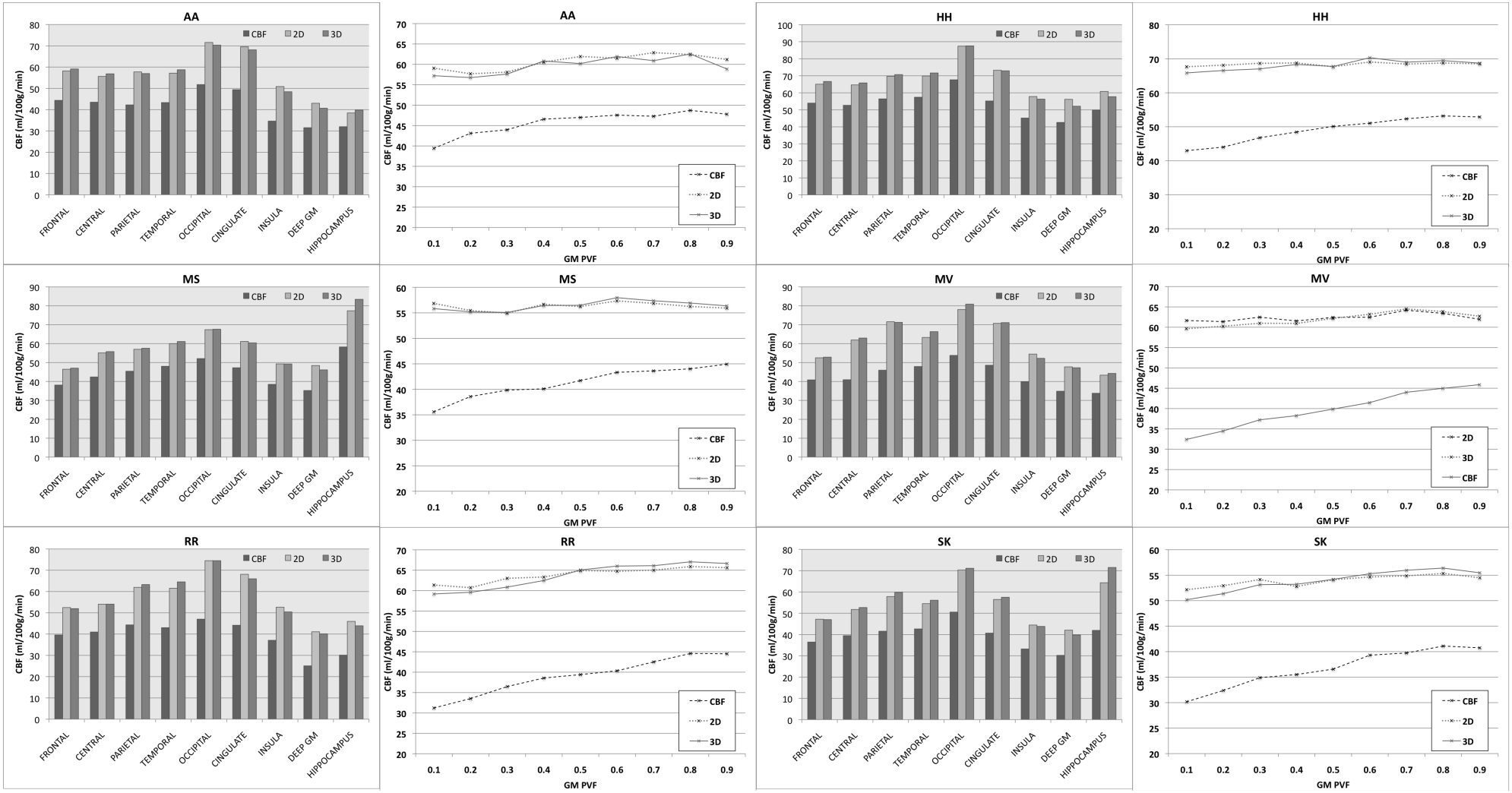


*Figure 5.5: Bar charts: regional mean CBF, and 2D and 3D kernel GM CBF for six control subjects. Line graphs: dependency on CBF and GM CBF after correction by 2D and 3D kernel for LR over the partial volume range.*

| | AA | | | HH | | | MS | | | MV | | | RR | | | SK | | |
|---|---|---|---|---|---|---|---|---|---|---|---|---|---|---|---|---|---|---|
| Region | CBF | 2D | 3D | CBF | 2D | 3D | CBF | 2D | 3D | CBF | 2D | 3D | CBF | 2D | 3D | CBF | 2D | 3D |
| Frontal | 44.4± 21.4 | 58.2± 19.2 | 59.1± 20.3 | 53.9± 16.0 | 65.0± 15.4 | 66.6± 17.0 | 38.1± 16.9 | 46.5± 15.2 | 47.0± 16.8 | 40.8± 17.6 | 52.5± 17.2 | 52.9± 17.7 | 39.6± 19.7 | 52.5± 17.7 | 52.0± 17.9 | 36.5± 11.9 | 47.2± 11.9 | 47.0± 13.2 |
| Central | 43.5± 20.7 | 55.6± 19.2 | 56.8± 17.3 | 52.7± 13.9 | 64.6± 11.8 | 65.8± 12.4 | 42.2± 11.9 | 55.±1 11.2 | 55.8± 11.8 | 40.9± 16.5 | 62.0± 21.9 | 63.0± 20.9 | 41.0± 20.8 | 54.0± 16.6 | 54.1± 16.9 | 41.0± 20.8 | 54.±0 16.6 | 54.1± 16.9 |
| Parietal | 42±.2 18.3 | 57.7± 15.3 | 57.0± 16.2 | 56.4± 13.7 | 69.7± 10.2 | 70.7± 11.6 | 45.4± 10.2 | 57.0± 6.8 | 57.6± 7.7 | 46.0± 15.1 | 71.6± 17.7 | 71.2± 17.3 | 44.3± 20.0 | 62.0± 17.0 | 63.3± 17.7 | 39.5± 11.5 | 51.8± 12.0 | 52.7± 13.1 |
| Temporal | 43.3± 14.9 | 57.2± 14.7 | 58.8± 16.3 | 57.4± 11.0 | 69.9± 9.0 | 71.6± 9.1 | 48.0± 10.5 | 60.0± 7.2 | 61.1± 7.9 | 47.9± 13.0 | 63.3± 12.8 | 66.3± 13.4 | 43.0± 18.0 | 61.5± 16.6 | 64.5± 16.8 | 43.0± 17.9 | 61.5± 16.6 | 64.5± 16.8 |
| Occipital | 51.8± 20.4 | 71.6± 21.2 | 70.3± 22.5 | 67.6± 21.4 | 87.4± 18.2 | 87.6± 19.8 | 52.1± 12.5 | 67.4± 10.5 | 67.6± 11.3 | 53.8± 19.7 | 78.0± 21.7 | 80.9± 23.8 | 47.0± 21.8 | 74.5± 18.4 | 74.5± 20.1 | 42.6±8.8 | 54.5± 8.2 | 56.1± 9.1 |
| Cingulate | 49.4± 14.9 | 69.6± 10.8 | 68.1± 14.2 | 55.2± 10.2 | 73.2± 10.6 | 72.9± 12.8 | 47.2± 11.4 | 61.2± 11.9 | 60.4± 11.4 | 48.6± 13.0 | 70.6± 15.4 | 71.1± 16.1 | 44.2± 17.6 | 68.1± 17.9 | 66.0± 17.4 | 40.7± 9.4 | 56.5± 9.0 | 57.5± 11.0 |
| Insula | 34.6± 10.2 | 50.9± 10.9 | 48.4± 10.9 | 45.2± 14.7 | 57.8± 6.8 | 56.3± 8.0 | 38.5± 9.2 | 49.3± 6.5 | 49.3± 6.9 | 39.9± 8.2 | 54.5± 11.0 | 52.3± 8.8 | 37.1± 15.8 | 52.6± 15.9 | 50.4± 13.8 | 33.2± 6.5 | 44.5± 6.4 | 43.8± 6.8 |
| Deep GM | 31.5± 13.6 | 43.0± 17.2 | 40.7± 18.0 | 42.6± 14.7 | 56.2± 20.8 | 52.1± 18.1 | 35.2± 20.0 | 48.4± 23.7 | 46.3± 21.7 | 34.9± 15.5 | 47.7± 20.9 | 47.3± 22.2 | 25.1± 19.0 | 41.1± 22.1 | 40.1± 25.0 | 30.2± 16.9 | 42.1± 21.7 | 39.8± 19.8 |
| Hippocampus | 32.0± 10.7 | 38.5± 10.5 | 39.8± 15.4 | 49.8± 10.4 | 60.8± 5.7 | 57.5± 4.6 | 58.2± 15.4 | 77.4± 6.3 | 83.4± 15.5 | 33.8± 17.2 | 43.4± 23.4 | 44.3± 23.7 | 30.1± 21.6 | 58.4± 30.5 | 43.9± 30.1 | 42.0± 11.5 | 53.2± 30.6 | 51.1± 27.6 |

*Table 5.4: Mean and S.D. uncorrected CBF and GM CBF created using a 2D and a 3D kernel for the LR PVC method across brain regions defined from a Freesurfer segmentation. All measurements in ml/100g/min.*

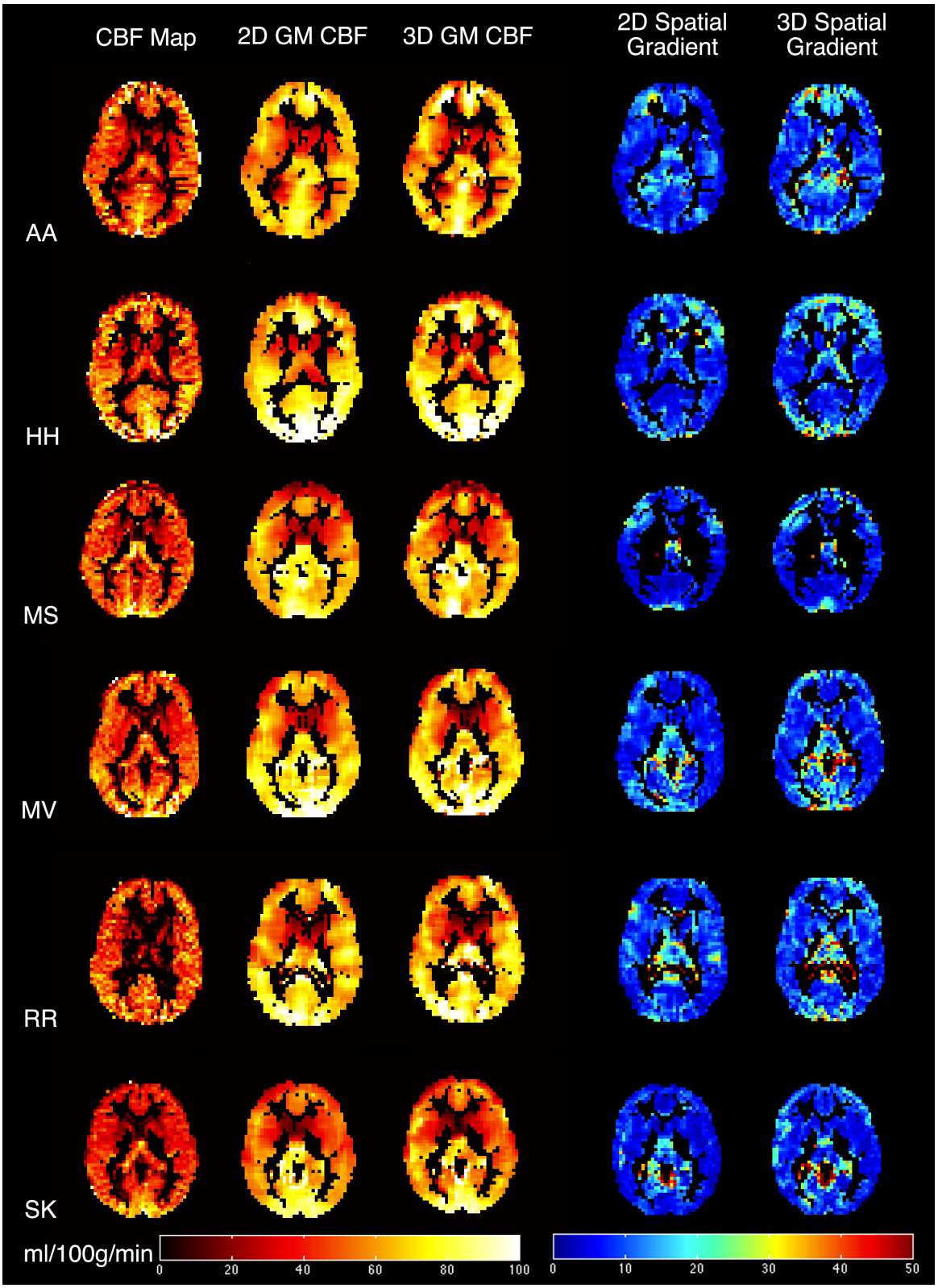


*Figure 5.6: Axial middles slices from six control subjects of the uncorrected CBF map, GM CBF PV corrected maps using a 2D and 3D kernel. Also shown is the spatial gradient magnitude image for the 2D and 3D kernel GM CBF maps. The 3D kernel case shows less blurring, which is supported by the greater intensity in the spatial gradient image.*

in the line graphs in 5.5. The dependency on PV fraction for the uncorrected CBF map is apparent for all subjects, with CBF increasing as GM PV fraction increases. The greatest increase post-correction is of course seen at the lower end of the PV range. Both 2D and 3D kernels follow the same trajectory in terms of correction, although it can be seen that the 2D kernel offers a slightly larger estimation than the 3D one in the 10-20% GM PV range.

Subject AA showed a slight difference from the other subjects in that the uncorrected CBF was fairly stable from GM PV 40% onwards. The increase in CBF from GM PVF 40-50% to 90-100% was 1.2 ml/100g/min, which was not observed in the other subjects, and cannot be readily explained.

Figure 5.6 shows a middle slice from the uncorrected CBF map, alongside the same slice from the PV corrected GM CBF maps for the 2D and 3D kernel correction methods, as well as the corresponding spatial gradient maps for all six subjects.

Whilst the mean GM CBF results may not differ much depending on whether a 2D or 3D kernel is used, visual inspection of the resultant GM CBF maps does show a variation in signal distribution. There appears to be less blurring or smoothing, and therefore more retained spatial detail in the maps produced using a 3D kernel.

This can be quantified by comparing the spatial gradients of the GM CBF maps, which are reported in table 5.3. It can be seen that the 3D case has a consistently higher spatial gradient than the 2D case, which supports the hypothesis and visual inspection of the PV corrected maps.

#### 5.3.2.4 Discussion

The effectiveness of the linear regression method for PV correction is accepted, and indeed it is seen that the application of the method has resulted in mean GM CBF measurements 1.2 to 1.6 times greater than mean CBF values obtained without PV correction. There is an inherent trade-off in the linear regression method which results in

spatial smoothing of the recovered GM CBF maps, and the goal of this project was to reduce the smoothing and provide more accurate quantitative results for GM perfusion.

It can be seen that the mean GM CBF values obtained after PV correction obtained using a 2D or 3D kernel are consistent with each other, both when the means are calculated on a regional, contiguous basis and also on a pseudorandom sample of voxels with the same GM PVF.

The difference in results produced by the 2 kernel types is shown in the distribution of signal. The larger 2D kernel causes greater blurring in the PV corrected maps than the 3D kernel and this is manifested by the greater mean spatial gradient obtained from the 3D kernel case. This suggests that the 3D kernel is better suited to preserving spatial detail.

All subjects show a comparatively high perfusion in the occipital region, both before and after correction. The fact that it is common across all subjects would suggest that it is a feature of the imaging sequence.

A finding of note is that shown in figure 5.5, which charts the dependency of uncorrected CBF on GM PVF, and also the GM CBF post-correction. The assumption that perfusion is relatively constant throughout the brain leads to a conclusion that the corrected GM perfusion will show consistency across all GM fractions after correction, and indeed this general trend is displayed in the aforementioned figure.

Theory suggests that as the GM PVF approaches 100%, the mean uncorrected CBF value for voxels which contain this proportion of GM will approach the GM CBF corrected value. That is, that the uncorrected CBF value rises to meet the corrected GM CBF value, for voxels which are close to 100% GM. Chappell et al [15] performed a simulation study using three differing datasets, the results

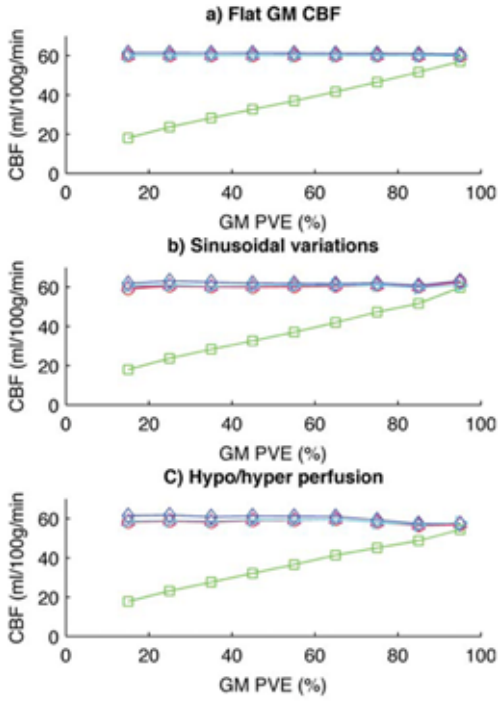

of which can be seen in figure 5.7. The uncorrected CBF (called 'standard' in this figure) for GM PVF 90-100% coalesces with the corrected GM CBF value, which is constant across all PV ranges. This is not seen on the in vivo data presented in our study, which shows a definite offset due to the uncorrected CBF not meeting the GM CBF value. This same finding is observed for all six subjects, and throughout the reported studies of other researchers, including the in vivo data used in Chappell's paper, which is discussed in the next section [22, 6, 7].

Given that Chappell finds perfect agreement in his simulation study, at first glance this would suggest that the mismatch at high PVF is due to an imperfect registration between the perfusion images and PV estimates. For the simulation, the 'perfusion' data is generated from the PV estimates, and as a consequence is perfectly registered with the PV estimates, which are used in the linear regression.

Registration of perfusion and anatomical data is notoriously problematic due to the low contrast and spatial detail in perfusion images. Add into the mix the requirement to downsample high resolution tissue partial volume estimates to the much lower resolution of perfusion images, it is to easy to attribute the offset to these problems.

The same pattern of consistently higher GM CBF is seen whether the $\Delta M$ and M0 are both PV corrected, or just the $\Delta M$ image, (or for that matter the CBF map) which would rule out an explanation based on elimination of the CSF signal in the M0 image causing GM CBF to be elevated. Misregistration of high PV fraction GM voxels by displacing them to overlap regions of CSF would result in lower GM CBF values (as these would be voxels in the perfusion image with low intensity), whereas low fraction GM voxels displaced to the CSF receive a 'boosting' of their true value, which is very obvious in a

PV corrected image (see figure 3.9).

What is clear is that the issue affects GM CBF across the entire PV range, as evidenced by the constant value of GM CBF. Whilst it is difficult to hypothesis as to what exactly is causing the problem, Chappell's simulation study shows that the offset is not there when simulated data which is created from perfectly registered PV maps is used. Along with the perfect registration, constant values were used for GM and WM perfusion, for which the assumption that perfusion is constant within the kernel is true. It is possible that a violation of this assumption is occuring with in vivo data, which is elevating GM CBF estimates.

Having said that, it is also the case that registration challenges contribute to this problem, with difficulties in registering the different imaging modalities and creating reliable PV estimates being the motivation behind the work of Shin [8] and Petr's application of it to PV correction using linear regression [9]. This is discussed in chapter 3 and a novel extension to these ideas in described in chapter 6.

## 5.4 Bayesian Inference applied to single time point ASL

As described in chapter 3, BASIL was designed for multiple timepoint data acquisitions and uses kinetic information to infer values for GM and WM flow and bolus arrival time. In a single timepoint experiment, the kinetic curve is sampled at one time point only; as such, the full time course cannot be characterised. However, it is still possible make use of the spatial prior information which encapsulates the belief that voxels near to each other are likely to be alike to estimate separate GM and WM flow. The aim of this study was to investigate whether using the spatial prior alone without tissue kinetic information would offer any advantage over the use of linear regression for PVC. This study is believed to be the first to apply BASIL to single timepoint ASL data.

### 5.4.1 Simulation study

#### 5.4.1.1 Methods

The same digital phantom as previously described in section 5.3.1 was used to quantify the performance of BASIL on single timepoint data. The required format for the input data to BASIL is in the form of a 4D time series, ordered in ascending time points. It is possible to present BASIL with data that has been averaged to a single image per time point, or with each measurement at each time point, should more than one have been acquired.

Essentially, BASIL requires PV maps at ASL resolution, an ASL difference image and a calibration for M0 to correctly scale the perfusion maps. There are a number of tools which sit on top of BASIL to assist the user with getting the data to this state, and development is ongoing.

In order to test the effect of the presentation of the data to BASIL, the simulated data was inputted to BASIL as a series of n = 1 to 9 averages at the same time point, with a different random noise pattern for each 'average'. It is usual practice to acquire more than one signal average at a timepoint, whether the experiment is a multiple or single timepoint study. Thus, it is appropriate to investigate the output of BASIL as a function of the number of averages provided as input.

The RMSE between the PV corrected result and the ground truth for GM were calculated and plotted against number of volumes, or signal averages, in the stack. For comparison purposes, the result obtained using linear regression with a 3 x 3 x 3 kernel is shown as a flat line across all volumes. The LR method must be applied to a single image, and requires a mean image to be created from all multiple measurements.

#### 5.4.1.2 Results

The RMSE between the GM CBF PV corrected result and the input ground truth is shown in table 5.5 and figure 5.8. BASIL does not produce a lower RMSE than that of the LR method between the PV corrected result and the ground truth until five averages are presented to it. The RMSE continues to decrease with increasing averages, but the rate of decline falls sharply after three volumes and plateaus after five.

| | BASIL | LR |
|---|---|---|
| No. of averages/volumes | RMSE | RMSE |
| 1 | 11.5 | 3.6 |
| 2 | 9.2 | 3.6 |
| 3 | 4.3 | 3.6 |
| 4 | 3.7 | 3.6 |
| 5 | 3.5 | 3.6 |
| 6 | 3.4 | 3.6 |
| 7 | 3.3 | 3.6 |
| 8 | 3.2 | 3.6 |
| 9 | 3.1 | 3.6 |

*Table 5.5: Root mean squared error between simulated GM ground truth and PVC results for BASIL using an increasing number of averages. BASIL does not outperform LR until 5 image averages are presented to it.*

The images in figure 5.8 are revealing; BASIL requires three images as input before the PV corrected result begins to capture what are actually extremely coarse spatial features. With one volume, BASIL largely fails to recover the hyper- and hypointense simulated lesions. If two volumes are used, the spatial variation in intensity for the lesions starts to appear, but the edges are ill-defined and the result is somewhat blurred. In line with the RMSE result, BASIL requires a three-volume input before an output is observed which is comparable to that obtained using the LR method.

#### 5.4.1.3 Discussion

The oversmoothing of the PV corrected output for BASIL was an unexpected result which had not previously been observed when applied to multiple timepoint data. The reason for this is tied up in the way BASIL estimates the noise component of the ASL signal.

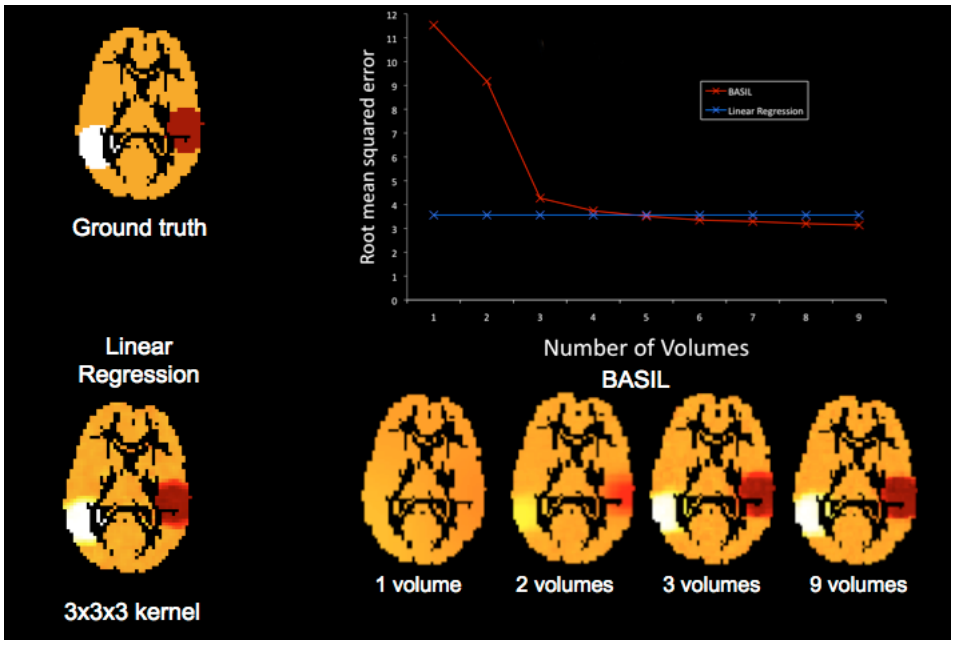


*Figure 5.8: Comparison between BASIL and linear regression on a simulated dataset. BASIL does not recover gross spatial detail until 3 or more averages are used.*

When less than three volumes of data are inputted to the Bayesian algorithm, BASIL is not able to estimate the noise contained within the signal and relies heavily on the spatial prior, rather than the data, which states that voxels near to each other are like each other, which produces a very smooth result, losing spatial detail. The simulated lesions in the ground truth have a five voxel radius, so can be considered to be a large spatial feature, given that a voxel is of side length just under 4mm.

With single-TI data, it is quite possible that a user may present BASIL with one volume of perfusion data (it is unusual to have only one measurement in perfusion experiments, but multiple measurements at the same TI may have been averaged to produce a single image for a particular time point). With multi-TI data, even averaging the multiple measurements at the same TI to a single image (although this is not recommended, as BASIL is able to infer more about the noise content of the data if it is unaveraged), it is likely that there will be multiple image volumes for BASIL to operate on as it is entirely normal to acquire multi-TI data at more than three timepoints; notably, Chappell [15] acquired perfusion data at ten timepoints throughout the kinetic curve.

This is clearly a feature of BASIL that researchers using single timepoint ASL

acquisitions need to be aware of. The main claim, as it were, of BASIL is that the resulting estimates of tissue perfusion are *adaptively smoothed*, with the level of smoothing very much related to the amount of spatial detail in the input images [15].

Additionally, BASIL is more complicated than LR methods for PVC, both conceptually and practically, as well as more time consuming in execution. These factors should be considered alongside the finding that BASIL relies heavily on prior information when low numbers of data volumes are available, when making a decision about what method of PVC to apply.

### 5.4.2 In vivo study

Armed with the knowledge that at least three data volumes are required to recover gross spatial detail, a comparison was made of the performance of BASIL and LR on in vivo data.

#### 5.4.2.1 Method

BASIL was designed for the specific ASL sequences used at the FMRIB lab at Oxford University; namely, pulsed labelling with a multiple time point 3D GRASE readout with a global value used for the M0 calibration based on the CSF signal. As such, BASIL incorporates a PVC correction for the difference images only. This is contrary to the approach of Asllani in [22], where it is stated that the voxelwise measurements of perfusion are a ratio of two images, each of which are affected by voxel heterogeneity.

For comparison purposes, BASIL was applied to a stack of three difference images, and LR using a 3D 3 x 3 x 3 kernel was applied to the difference and M0 images. It might be argued that a fair comparison would be to apply the LR only to the difference images; however, we wished to investigate the differences between the full application of the method published by Asllani et al and BASIL.

#### 5.4.2.2 Results

Table 5.6 shows the global mean CBF before PV correction and after using BASIL and a 3D kernel for LR. The difference between the two GM CBF groups is not significant (p = 0.26), with the difference between BASIL and LR mean GM CBF usually only a 1-2 ml/100g/min apart. The difference was more pronounced for subject AA, with the BASIL result some 9.6 ml/100g/min lower than for the LR method.

| Subject | Mean CBF | GM CBF (3D kernel) | GM CBF (BASIL) |
|---|---|---|---|
| AA | $49.6 \pm 22.6$ | $62.9 \pm 17.1$ | $53.3 \pm 30.1$ |
| HH | $43.1 \pm 24.6$ | $62.0 \pm 22.5$ | $60.8 \pm 30.3$ |
| MS | $39.5 \pm 16.9$ | $55.8 \pm 19.0$ | $56.1 \pm 22.4$ |
| MV | $37.6 \pm 18.5$ | $60.8 \pm 22.6$ | $58.0 \pm 31.3$ |
| RR | $39.4 \pm 21.7$ | $61.9 \pm 19.3$ | $58.4 \pm 22.0$ |
| SK | $34.9 \pm 15.2$ | $53.0 \pm 18.2$ | $55.7 \pm 24.5$ |

*Table 5.6: Mean CBF, GM CBF after PV correction using a 3D kernel with linear regression, GM CBF using BASIL. All measurements in ml/100g/min after masking at GM PVF > 0.1.*

Table 5.7 shows a comparison between the 3D kernel LR method for PVC with BASIL, with the mean value given for the same Freesurfer brain segmentation regions as in the 2D and 3D kernel comparison.

Global and region mean GM CBF values alone do not reveal the full story. Figure 5.9 shows middle slices from the six subjects in a like manner to the comparison that was made for the LR method between 2D and 3D kernels. Clearly, the BASIL results are more heterogeneous than the LR ones, which is evidenced in the mean GM CBF results by the greater standard deviation for BASIL. Visual inspection of the data supports this, with a less smooth appearance in the images.

Moving on the comparison across the GM PVF range, the same pattern is observed for all subjects; the mean GM CBF BASIL result appears to peak in the 40-60% GM range. There is an upward trajectory from the lower PV fractions of 10-20%, rising to the highest GM CBF values at the mid-range, before decreasing and dropping to a mean GM CBF which is consistently below that of the LR method at 90-100% GM. The LR method is more consistent across all PV fractions, as can be observed in the graphs in figure 5.10.

| | AA | | | HH | | | MS | | | MV | | | RR | | | SK | | |
|---|---|---|---|---|---|---|---|---|---|---|---|---|---|---|---|---|---|---|
| Region | CBF | BASIL | 3D | CBF | BASIL | 3D | CBF | BASIL | 3D | CBF | BASIL | 3D | CBF | BASIL | 3D | CBF | BASIL | 3D |
| Frontal | 44.4± 21.4 | 58.8± 29.5 | 59.1± 20.3 | 53.9± 16.0 | 74.2± 26.2 | 66.6± 17.0 | 38.1± 16.9 | 47.6± 19.1 | 47.0± 16.8 | 40.8± 17.6 | 53.8± 25.9 | 52.9± 17.7 | 39.6± 19.7 | 54.3± 25.2 | 52.0± 17.9 | 36.5± 11.9 | 49.9± 18.4 | 47.0± 13.2 |
| Central | 43.5± 20.7 | 55.0± 28.6 | 56.8± 17.3 | 52.7± 13.9 | 72.7± 23.5 | 65.8± 12.4 | 42.2± 11.9 | 55.3± 16.0 | 55.8± 11.8 | 40.9± 16.5 | 56.3± 26.0 | 63.0± 20.9 | 41.0± 20.8 | 56.2± 25.7 | 54.1± 16.9 | 39.5± 11.5 | 49.9± 18.4 | 47.0± 13.2 |
| Parietal | 42.2± 18.3 | 53.5± 27.1 | 57.0± 16.2 | 56.4± 13.7 | 74.6± 19.4 | 70.7± 11.6 | 45.4± 10.2 | 56.3± 12.7 | 57.6± 7.7 | 46.0± 15.1 | 62.3± 23.5 | 71.2± 17.3 | 44.3± 20.0 | 62.7± 23.1 | 63.3± 17.7 | 41.6± 9.8 | 55.5± 14.6 | 59.8± 10.8 |
| Temporal | 43.3± 14.9 | 53.0± 23.3 | 58.8± 16.3 | 57.4± 11.0 | 73.8± 18.1 | 71.6± 9.1 | 48.0± 10.5 | 60.7± 18.4 | 61.1± 7.9 | 47.9± 13.0 | 60.1± 19.6 | 66.3± 13.4 | 43.0± 18.0 | 61.9± 19.5 | 64.5± 16.8 | 42.6± 8.8 | 56.5± 14.7 | 56.1± 9.1 |
| Occipital | 51.8± 20.4 | 64.6± 28.5 | 70.3± 22.5 | 67.6± 21.4 | 86.5± 26.4 | 87.6± 19.8 | 52.1± 12.5 | 67.1± 18.4 | 67.6± 11.3 | 53.8± 19.7 | 68.4± 28.5 | 80.9± 23.8 | 47.0± 21.8 | 71.6± 22.0 | 74.5± 20.1 | 50.6± 12.1 | 67.9± 17.3 | 71.1± 14.2 |
| Cingulate | 49.4± 14.9 | 61.1± 20.8 | 68.1± 14.2 | 55.2± 10.2 | 74.3± 18.7 | 72.9± 12.8 | 47.2± 11.4 | 56.8± 13.6 | 60.4± 11.4 | 48.6± 13.0 | 61.4± 18.4 | 71.1± 16.1 | 44.2± 17.6 | 56.9± 17.3 | 66.0± 17.4 | 40.7± 9.4 | 50.5± 11.6 | 57.5± 11.0 |
| Insula | 34.6± 10.2 | 43.2± 17.1 | 48.4± 10.9 | 45.2± 14.7 | 55.8± 14.1 | 56.3± 8.0 | 38.5± 9.2 | 46.0± 12.4 | 49.3± 6.9 | 39.9± 8.2 | 49.6± 13.6 | 52.3± 8.8 | 37.1± 15.8 | 46.5± 16.5 | 50.4± 13.8 | 33.2± 6.5 | 40.7± 11.5 | 43.8± 6.8 |
| Deep GM | 31.5± 13.6 | 40.2± 20.7 | 40.7± 18.0 | 42.6± 14.7 | 59.0± 22.6 | 52.1± 18.1 | 35.2± 20.0 | 45.7± 24.8 | 46.3± 21.7 | 34.9± 15.5 | 45.4± 24.4 | 47.3± 22.2 | 25.1± 19.0 | 34.5± 18.9 | 40.1± 25.0 | 30.2± 16.9 | 39.6± 24.1 | 39.8± 19.8 |
| Hippocampus | 32.0± 10.7 | 37.6± 18.2 | 39.8± 15.4 | 49.8± 10.4 | 60.2± 13.7 | 57.5± 4.6 | 58.2± 15.4 | 74.1± 21.2 | 83.4± 15.5 | 33.8± 17.2 | 43.2± 21.4 | 44.3± 23.7 | 30.1± 21.6 | 43.5± 21.8 | 43.9± 30.1 | 34.9± 22.6 | 54.0± 17.0 | 71.5± 9.2 |

*Table 5.7: Mean and S.D. uncorrected CBF and GM CBF created using a 2D and a 3D kernel for the LR PVC method across brain regions defined from a Freesurfer segmentation. All measurements in ml/100g/min.*

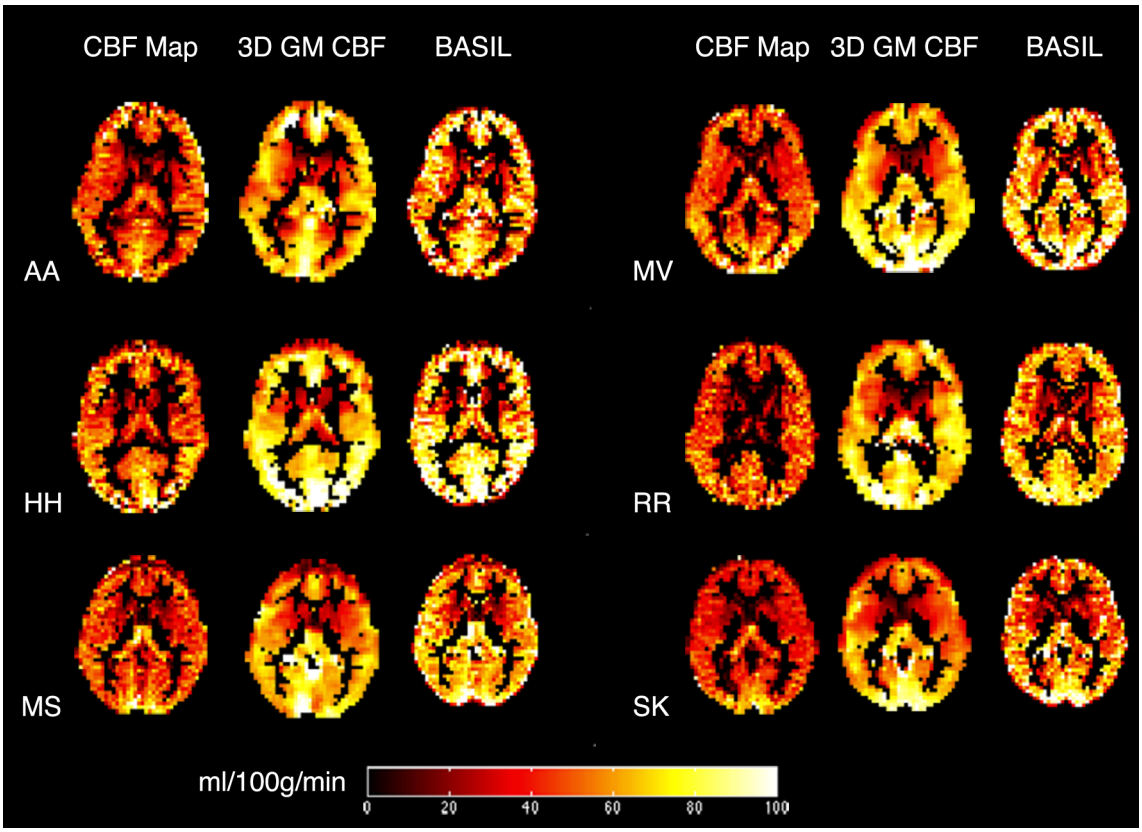


*Figure 5.9: Middle slices from six control subjects showing a comparison between the GM CBF obtained by using the 3D kernel LR method and BASIL. Whilst global mean values for GM CBF are in agreement between the two methods, the BASIL method produces GM CBF maps with more spatial variability.*

Finally, as for LR, it is noted that BASIL also does not converge to the uncorrected CBF result at high GM PV fractions, despite the downward trajectory mentioned above.

#### 5.4.2.3 Discussion

This section focused on a comparison between the LR method for PV correction using a 3D kernel and an alternative method, BASIL, which uses Bayesian analysis to infer a result for GM CBF.

BASIL claims to be able to 'provide PV corrected GM CBF estimates whilst maintaining underlying spatial structure...the new method is shown to protect spatial features in the CBF images, avoiding the introduction of added smoothness to the boundaries of regions of hypo or hyper perfusion' [15]. It is proposed that this is achieved by applying an adaptive smoothing to the CBF and GM CBF estimation which is derived from the data

itself, which may offer an advantage over LR methods at regions of high spatial variation, such as tissue boundaries or pathology.

However, the simulation study described within this chapter has shown that the output of BASIL is strongly weighted by spatial priors when the data input is less than three images, which actually leads to a result which smoothes away large spatial features. The study offered three input volumes to BASIL, to avoid this oversmoothing 'feature', and it can be seen in the results that the BASIL GM CBF images are indeed more heterogeneous than the LR. As to to whether or not the increased spatial variation in the GM CBF BASIL images represents true spatial features is open for debate. The images appear to contain more noise than the original CBF images, unlike LR, where one useful side-effect of the inherent spatial smoothing is noise removal. Could it be that the BASIL outputs simply contain more noise than the LR images, rather than an increase in retained spatial detail?

In terms of a comparison between LR and BASIL, whilst the mean GM CBF values for both are in broad agreement, it can be seen in the pseudorandom samples across the GM PVF ranges shown in figure 5.10 that the BASIL result is not linear, showing a distinct rise around the mid PVF ranges.

There is only one other published paper to date which uses the BASIL method for PV correction, and this is Chappell's original paper describing the technique [15]. The in vivo data section presents the same result as observed here, shown in figure 5.11, where the 'Spatial PV' method referred to is BASIL.

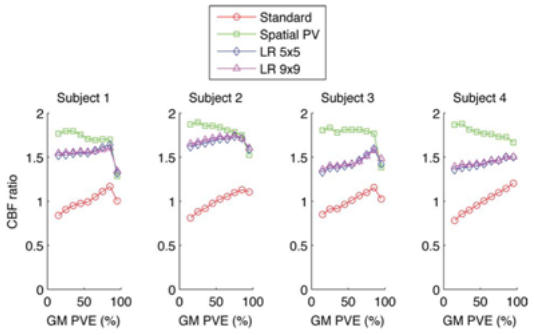


*Figure 5.11: Variation in GM CBF across PV range obtained using BASIL published in [15].*

Chappell does remark on the in vivo data results within his paper, which are notably worse

than those observed in his simulation study. He suggests that the differences may be 'due to inaccuracies in the PVE and residual effects of the T2 blurring'. As to the former suggestion, of course the LR method has been executed using the same PV estimates as BASIL, so one would expect the LR result to follow a similar pattern if that were the reason. The LR result is not flat across all PV fractions, and in three out of four cases the mean GM CBF drops sharply in the 90-100% range mirroring the BASIL result. However, in contrast to the BASIL result, the LR result appears to be more consistent across most of the PV range.

Towards the suggestion that T2 blurring is causing some kind of 'residual effect', the data used within our study uses 3D GRASE data obtained in eight segments which minimises T2 blurring. The through plane blurring observed with this kind of acquisition is explored in chapter 7 and it can be seen that it is greatly reduced compared to the one-shot acquisition used by Chappell. However, the same pattern of non-linearity for the BASIL GM CBF results across the PV range are observed in our study with segmented data, so this hypothesis is not supported by our data.

Chappell makes the point that BASIL is highly dependent on the accuracy of the PV estimates obtained from a segmentation of a T1-weighted structural image, which is likely to be poor in highly myelinated and deep GM areas. Of course, the same is true for LR and any method which relies on a correction using structural information.

This is an inherent weakness of both these methods, and there is recent work to move away from using structural data to inform about PV estimates. Petr et al [9] present an alternative method for obtaining these estimates which is described in chapter 3 and a novel extension to that is presented in chapter 6.

In conclusion, BASIL does not appear to offer any advantage over LR for PV correction of single timepoint data, and in the case of limited image volumes for input, may be at a distinct disadvantage. Given the complexity and increased computational running time of BASIL, it is recommended that BASIL be reserved for multiple timepoint data, where is can generally be guaranteed that there will be sufficient input data to prevent

oversmoothing.

## 5.5 PV correction applied to CBF maps

This remainder of this chapter is devoted to an investigation of the feasibility of applying the LR PV correction method directly to a CBF map, rather than separately to the difference and control images. Asllani's assertion is that perfusion images are actually a ratio of a difference and a magnetisation image, both of which are affected by partial volume and a correction must be applied to both.

The need for this investigation arose from being presented with some data from a General Electric (GE) scanner, for which the protocol at the time produced scaled CBF maps as its output, rather than difference and control data. This is non-ideal for a few reasons. It poses issues for motion correction, lack of transparency as to the assumptions which have gone into calculating the CBF map, as well as not providing access for PV correction to the component image inputs to the CBF map. GE now provide the difference and $M0$ images by default.

It is also worthwhile to perform this investigation as there is a lack of consensus amongst researchers. Asllani's approach has not been widely adopted by others in the field. In some cases, [15, 6, 9] the PV correction is applied only to the difference image, as a voxelwise magnetisation image is not acquired and a global value based on CSF is used to scale perfusion values. Another group have applied the correction directly to CBF maps [46]. In short, there is no standard recommended procedure and no investigation has previously been undertaken to ascertain the effect of applying PV correction to difference and equilibrium images and combining them, compared to directly applying the correction to CBF maps.

### 5.5.1 Method

A CBF map was calculated using the general kinetic model for the same six subjects previously described. As with all the data used within this thesis, the voxel dimensions are 3.75 x 3.75 x 3.8 $mm^3$, so a significant PV effect can be expected.

In this instance there is no mean control image to act as the target for registration of the higher resolution PV estimates, so the PV maps were registered to the CBF map. For the difference and M0 images, the PV estimates were registered to the mean control image as previously described.

The CBF map, difference and M0 images were PV corrected using a 3D 3 x 3 x 3 kernel for LR. The difference and M0 images wee combined along with the appropriate scale factors to produce separate maps of GM and WM tissue flow. No scaling was required for the flow maps produced from the CBF map.

### 5.5.2 Results

Table 5.8 shows a global mean GM CBF produced by applying PV correction to the difference and control magnetisation images, compared with applying it directly to the CBF map. In all but one case, applying the correction solely to the CBF map resulted in a lower mean GM CBF value.

| Subject | Mean CBF | GM CBF ($\Delta$ M/M0) | GM CBF (CBF) |
|---|---|---|---|
| AA | 49.6 $\pm$ 22.6 | 62.9 $\pm$ 17.1 | 58.7 $\pm$ 20.1 |
| HH | 43.1 $\pm$ 24.6 | 62.0 $\pm$ 22.5 | 63.9 $\pm$ 17.6 |
| MS | 39.5 $\pm$ 16.9 | 55.8 $\pm$ 19.0 | 53.9 $\pm$ 15.0 |
| MV | 37.6 $\pm$ 18.5 | 60.8 $\pm$ 22.6 | 59.9 $\pm$ 14.4 |
| RR | 39.4 $\pm$ 21.7 | 61.9 $\pm$ 19.3 | 57.8 $\pm$ 16.3 |
| SK | 34.9 $\pm$ 15.2 | 53.0 $\pm$ 18.2 | 49.7 $\pm$ 13.3 |
| Groupwise mean | 38.4$\pm$ 19.7 | 57.2 $\pm$19.9 | 53.9 $\pm$ 18.6 |

*Table 5.8: Comparison between applying PV correction to difference and control magnetisation images with applying directly to CBF map. All measurements in ml/100g/min with GM CBF maps masked at PVF > 0.1 prior to calculations.*

A two-sample paired t-test of the two groups of PV corrected data showed there to be no significant difference in the means at the 5% significance level.

### 5.5.3 Discussion

Registration of the PV maps to the CBF map was found to be problematic. Normally, the control image (or TR = 5000 ms saturation recovery sequence in our study) would act as a target for the registration of anatomical data to perfusion space (or vice versa, with the inverse matrix applied), which contains more spatial detail. However, one group which applied the LR method directly to CBF maps report registering the PV maps directly to the CBF maps with success, although the CBF maps were at a higher in-plane resolution (1.7 x 1.7 $mm^2$ ) than that used in our study, which may account for this [46].

A misregistration which causes high GM PV fraction voxels to be displaced to CSF region smay account for the reduction in global mean GM CBF values observed with this 'single image' method of PV correction. Whilst the mean values for GM CBF are lower in five out of the six cases, the difference is not found to be significant. From this it may be concluded that it is legitimate to apply the LR PVC method directly to a CBF map, rather than to separate images of $\Delta M$ and $M0$, if they are not available. However, given the difficulty with registering CBF or difference images, it is clearly preferable to have access to control and tagged images.

## 5.6 Conclusion

In summary, this chapter has presented an extension to the LR method for PVC of ASL data proposed by Asllani et al, with the stated aim of reducing the inherent blurring which is produced in the separate tissue maps. This method has been termed the '3D kernel' and is found to be effective at reducing blurring, whilst not increasing computational intensity.

An investigation was made into the use of a Bayesian inferencing method for PV correction of ASL data applied to single timepoint data and whether there was any

advantage in using this tool when kinetic information is unavailable, as the case for single timepoint data. This tool, BASIL, was found to be heavily dependent on the volume of data presented to it, with fewer than three volumes causing the algorithm to rely heavily on priors and smooth away spatial detail in the output images. It is concluded that BASIL be reserved for scenarios where multiple measurements are available, either for single or multiple timepoint acquisitions.

Finally, given the lack of consensus about which component images should be PV corrected, a study was undertaken to ascertain the effect of applying PVC to difference and control images, as Asllani suggests is the correct approach, or directly to just the difference or CBF map. It would seem that applying the correction directly to the CBF map may result in a small underestimation compared to the two image correction technique, but that the discrepancy is not significant.

It is evident that any PVC will only be as good as the data allows; both BASIL and LR methods are heavily dependent on the registration of high resolution anatomical data to low resolution perfusion space. This is error prone and difficult to achieve.

Chapter 6 proposes an alternative method for acquiring PV estimates in perfusion space, obviating the need for troublesome registrations.

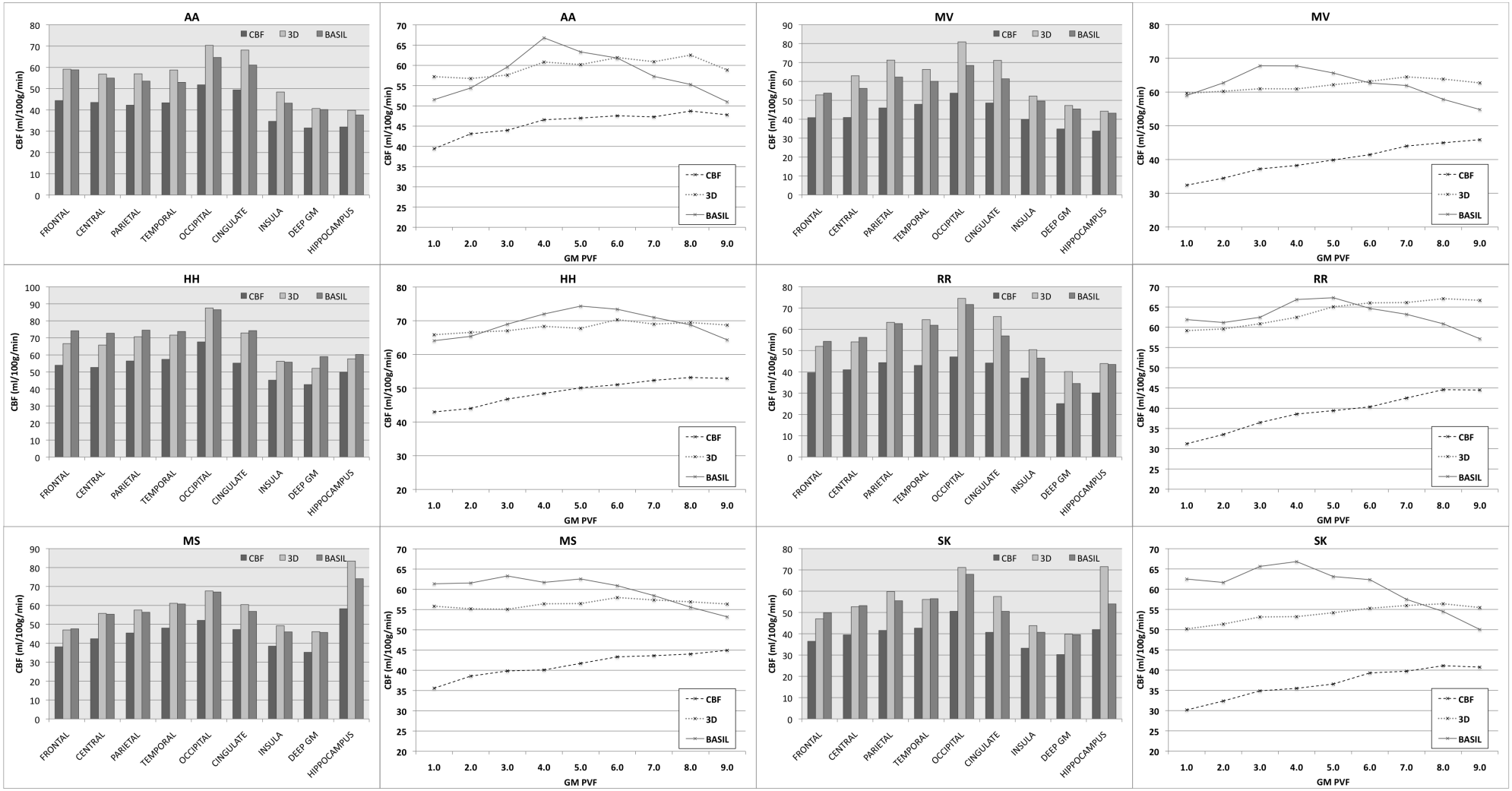


*Figure 5.10: Comparison between uncorrected CBF and GM CBF obtained by 3D LR and BASIL methods. Bar charts show a regional mean for the Freesurfer derived contiguous regions. Line graphs show variation is uncorrected CBF and GM CBF across the PV fraction range. Regional mean values are in close agreement, but the pseudorandom sampling by GM PVF shows BASIL results peak around 40-60% GM.*

# Chapter 6

# Separation of relaxation curves for ASL tissue fraction estimation: SEPARATE

This chapter describes a novel extension to the ideas originally proposed by Shin and Petr [67, 8, 9] to create partial volume estimates from low resolution inversion or saturation recovery data. This work formed the basis of an oral presentation at ISMRM 2014 [68].

## 6.1 Introduction

The FRASIER method for creating partial volumes estimates from inversion recovery data using a Look-Locker readout was originally proposed by Shin et al [67, 8], and adapted for use with saturation recovery data at standard ASL resolution by Petr et al [9]. The basis of the FRASIER method has been described in detail in chapter 3, along with Petr's method for estimating the T1 of GM, for which it is not possible to apply the Shin method of estimating this value from a Gausssian mixture model of a T1 map due to the low resolution of the data.

### 6.1.1 Fractional segmentation using 3D GRASE data

Previous researchers utilised Look-Locker inversion or saturation recovery EPI sequences for data collection. In contrast, we suggest the use of a saturation recovery 3D GRASE

sequence, which simplifies matters considerably. The Look-Locker data must be acquired at two different flip angles to compensate for B1-field inhomogeneity; this correction is not required for 3D GRASE data, which is one of the advantages of acquiring the data in this way.

The second advantage of using 3D GRASE for data sampling is that Lock-Locker sequences impose restrictions on the sampling intervals that can be used. Typically, regularly spaced sampling determined by the image acquisition time is used. This is not the case with a 3D GRASE readout, where each time point is independent of the others, which offers the advantage that the relaxation curve can be sampled more densely when the signal is changing rapidly. In addition, it allows us to use the same readout for both ASL and PV correction.

We believe this is the first time that 3D GRASE data has been used to produce partial volume estimations.

### 6.1.2 Voxelwise estimation of the T1 of GM applied to fractional segmentation

Petr uses a process of iterative minimisation to arrive at a global value for the T1 of GM. This would seem a reasonable approach, given that a global value is used for the T1 of WM and a literature value for the T1 of CSF. However, it is important that the values for GM, WM and CSF are as accurate as possible in order to get a correct fractional segmentation. Having said that, since the volume of CSF is substantially smaller than that of the GM or WM, it is usual practice to use a literature value and not estimate from a Gaussian mixture model.

Petr achieves plausible results, and claims to visualise structure in the WM partial volume map which does not survive the transformation and resampling from a high resolution structural image. Figure 6.1 shows an extract from the Petr paper with the GM and WM PV maps marked as $PV_{T1}$ and $PV_{LL}$ for the maps created from high resolution and Lock-

Locker sampled data, respectively. For the WM, there is more structural detail in the $PV_{LL}$ map at the locations marked with red arrows. However, for the GM PV map, the $PV_{LL}$ map clearly shows deep grey matter adjacent to the ventricles of lower intensity, and therefore lower GM tissue fraction, than that in the $PV_{T1}$ map, also labelled with red arrows. [1]

Whilst Petr's hypothesis about the increased WM structure in the Look-Locker data is reasonable, this cannot explain the reduced intensity seen in the deep GM.

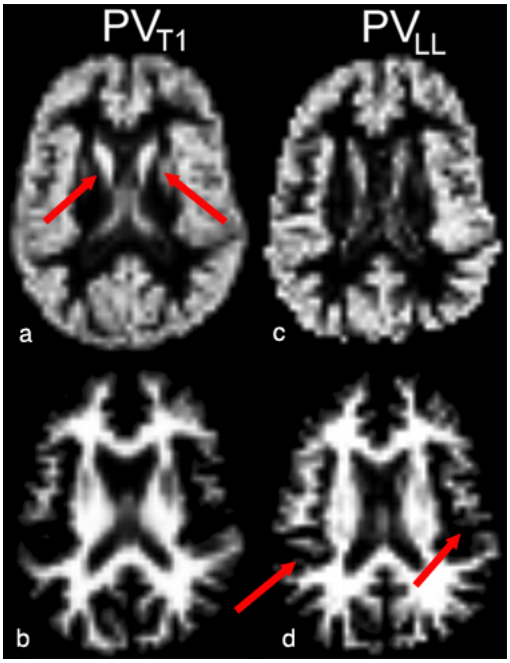


*Figure 6.1: PV maps produced from a high resolution anatomical segmentation downsampled to ASL resolution ($PV_{LL}$) and from a Look-Locker saturation recovery sequence, acquired at ASL resolution ($PV_{T1}$), from [9]. Red arrows mark regions of greater intensity in the deep GM for $PV_{T1}$ and more structural detail for the WM in $PV_{LL}$.*

It is useful to refer to a high resolution anatomical image to obtain an insight into which GM PV map is accurate. Consultation with neuroanatomy texts would suggest that these voxels represent the head of the caudate nucleus, and are rightly identified as GM in the $PV_{T1}$ map . This is depicted in figure 6.2, with the caudate nucleus marked in red.

This would suggest that the PV maps which are derived from an anatomical image are more accurate for this particular structure. It is hypothesised that the lower intensity

[1] It should be noted that $PV_{T1}$ and $PV_{LL}$ is the notation used by Petr et al and is replicated in this section to be consistent with that paper. The equivalent notation used in this chapter is to $PV_{MPRAGE}$ and $PV_{ASL}$, respectively.

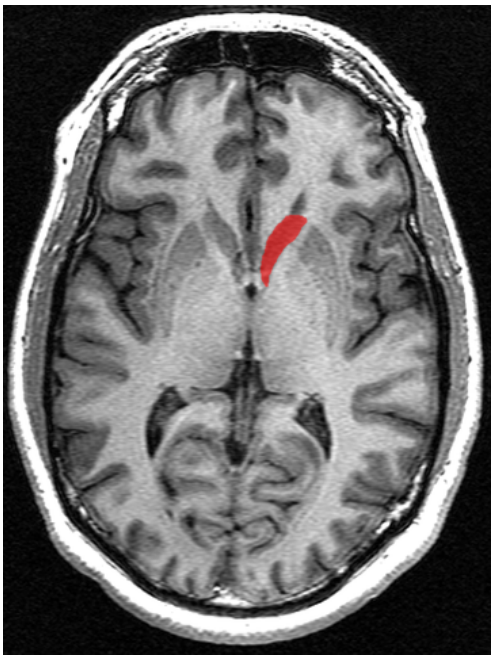

*Figure 6.2: Transverse view of the caudate nucleus (highlighted in red) in a structural MRI. Image credited to Geoffrey Hall, McMaster University, Canada.*

observed in the fractional segmentation derived PV maps is due to the fact that a global value for the T1 of GM has been used to derive the segmentations. The T1 of GM is know to vary, particularly between the cortex and the basal ganglia, of which the caudate nucleus is part [69].

As such, we sought to improve the fractional segmentation method by utilising a voxelwise measure of the T1 GM, rather than estimating and applying a global value of T1 GM. We propose the acronym *SEPARATE* to describe this novel technique: **SEPA**ration of **R**elaxation curves for **A**SL **T**issue fraction **E**stimation.

## 6.2 Method

Eight healthy controls ranging in age 25 to 43 years with mean age 34.9 $\pm$ 5.7 took part in the study. The same high resolution anatomical image and perfusion data was acquired as in described in chapter 3.

In terms of solving equation 3.12 by the fractional segmentation method, there are six unknowns; the T1 of GM, WM and CSF and the partial volume fractions ($F_{S,GM}$, $F_{S,WM}$,

$F_{S,CSF}$). The T1 of WM will be estimated directly from the T1 map as there are sufficient 100% WM voxels to ensure this estimate is reliable, and a literature value will be used for the T1 of CSF. This leaves four unknowns which must be solved for.

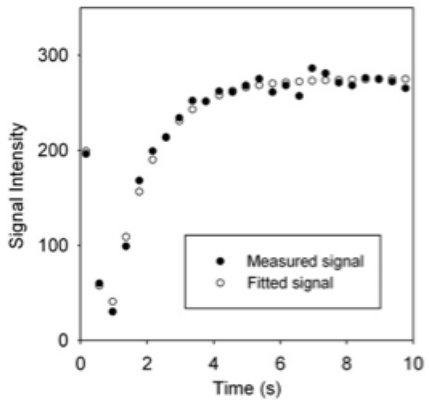


*Figure 6.3: Figure 3(B) from [8]. Shin et al sampled the recovery curve over a 10s period, with 25 time points. Conversely, Petr et al used 13 time points and sample to 3640 ms only.*

Our original acquisition paradigm for the saturation recovery sequence for calculating whole voxel M0/T1 maps consisted of sampling the data at TI = 1000, 3000, 5000 ms. At least one additional time point is needed to be added to the acquisition strategy in order to solve for the four unknown quantities.

Petr used 13 time points, beginning at TI = 40 ms with intervals of 300 ms. In contrast, Shin sampled over a 10 s period, with intervals of 400 ms providing 25 time points. Theoretically, only four time points should be required, but both groups used a much larger number to improve the accuracy of the estimations.

For this study, we acquired a data set was acquired with time points at TI = 100, 200, 300, 400, 500, 600, 700, 800, 900, 1000, 1100, 1200, 1300, 1400, 1500, 1600, 1700, 1800, 1900, 2000, 2200, 2400, 2600, 2800, 3000, 3500, 4000, 4500, 5000, 6000, 8000 ms. The images at these time points were acquired in a pseudo-random, rather than sequential, order.

A higher density of sampling is used at the early stage of recovery (100 - 2000 ms) with larger intervals between the time points as the relaxation progresses. A saturation recovery curve for one of the subjects from the study is shown in figure 6.4 for all 31 time points as detailed above. Compared to the regular 40 ms sampling used by the Shin group shown in figure 6.3, it can be seen that there is a greater sampling density in the rapidly changing part of the curve. The increased sampling density does of course increase overall scan time, but this was carried out in a comprehensive manner as a proof of principle and is

not necessarily optimally efficient.

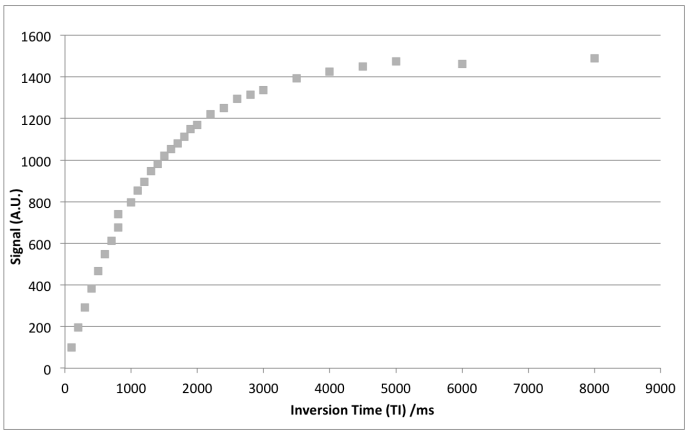


*Figure 6.4: Tissue relaxation after saturation recovery inversion for one voxel through the full 31 time points, ranging from 100 ms to 8000 ms. The curve is more densely sampled during the rapid recovery portion than in previous studies.*

### 6.2.1 Voxelwise estimation of T1 GM

Petr estimated the T1 of WM by making an *a priori* assumption about the likely range of acceptable T1 WM values at 3T and thresholding the T1 map to include only voxels with these values. The mean was then found from these candidate voxels and used alongside a literature value of T1 CSF of 4300 ms to jointly estimate a global value for the T1 of GM and voxelwise fractional segmentations.

We propose an alternative to this method of T1 WM and GM estimation, which does not rely on any *a priori* assumptions for WM, and produces a voxelwise estimation for the T1 of GM, for which it is hypothesised will produce more accurate GM PV maps.

T1 and M0 maps were calculated from the saturation recovery sequence as described in equation 3.12. A three Gaussian mixture model was fitted to a histogram of the T1 map, under the assumption that there are no pure GM voxels at this resolution and the mixtures represent WM, GM + WM and GM + CSF. The peak of the Gaussian with the lowest mean value represents the T1 of WM.

A voxelwise value for T1 GM is estimated by adapting Petr's method of alternate estimation of the PV fractions and T1 GM by selecting a 3 x 3 x 3 kernel from the

saturation recovery sequence and performing the estimation over this neighbourhood only, rather than estimating a global T1 GM value which minimises the objective function. This kernel is slid over the entire image, with the central voxel being the one for which the T1 of GM is found.

A form of regularisation was used on the estimation of T1 GM by applying boundary conditions from the Gaussian mixture model step, described above. The lower bound for T1GM was set to the T1 of WM and the upper bound set to the mean value of the GM/CSF mixture. In regions of the image where there is no GM (for example in 100% WM regions) the algorithm is unable to estimate the T1 for GM and these voxels are flagged for the subsequent processing step. This GM T1 map is then refiltered by using a 3 x 3 x 3 kernel and any voxels which were flagged in the proceeding step are replaced by the mean of a neighbourhood of 'good' values which fall in the range defined above. This step is repeated until all flagged voxels are replaced. If this second pass failed to replace any remaining flagged voxels, the kernel size was increased ( 5 x 5 x 5 ). In practice, it was only necessary to repeat this step for one of the subjects (JF).

Equation 3.12 is then solved to produce tissue fractional signals using a linear least squares fit with global values of T1 WM and CSF, and a voxelwise value for T1 GM. The tissue fractional signals are converted to fractional volumes by applying equation 3.18 in order to correct for the water density of the different tissue types. These maps are denoted as $PV_{sat\_rec}$.

Partial volume maps were also created from the segmentation of anatomical MPRAGE data transformed to ASL space as previously described. These are denoted $PV_{MPRAGE}$.

### 6.2.2 PV correction of CBF maps

Cerebral blood flow (CBF) maps for the eight subjects were calculated using the Buxton model (see equation 2.7) for pulsed ASL data; these are referred to as 'acquired CBF maps'. These CBF maps were partial volume corrected using a 3 x 3 x 3 kernel for linear regression in order to separate the signal into GM and WM components, as described

in chapter 5. The PV correction was applied directly to the calculated CBF maps in accordance with the finding in chapter 5 that this approach is legitimate. The partial volume correction was performed twice; using the $PV_{sat\_rec}$ and $PV_{MPRAGE}$ maps.

### 6.2.3 Validation

After PV correction, the separate GM and WM CBF maps were recombined by multiplying by the partial volume fractions and summing them to attempt to recover the CBF map which was the input to the PVC procedure, as in equation 6.1

$$CBF_{recomb}(r) = \Delta CBF_{GM}(r).P_{GM}(r) + \Delta CBF_{WM}(r).P_{WM}(r) \tag{6.1}$$

where $\Delta M_{GM}$, $\Delta M_{WM}$ are the partial volume corrected flows for GM and WM, and $P_{GM}$ and $P_{WM}$ are the partial volume fractions for GM and WM at voxel *r*.

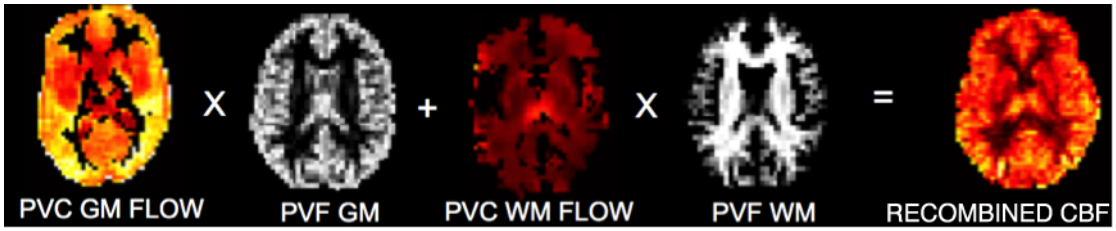


*Figure 6.5: Validation of PVC results: the pure GM and WM flows are recombined with their respective partial volume fraction maps to recreate the CBF map. Any differences between the 'recombined' CBF and calculated CBF are attributed to errors in the partial volume fraction maps.*

The basis of this validation is that any departure between the CBF values obtained from recombining the separate GM and WM flows and the actual CBF values will be attributable to errors in the PV maps. The linear regression method for PVC does introduce spatial blurring, but an assumption is made that this effect will be similar for both the $PV_{sat\_rec}$ and $PV_{MPRAGE}$ maps.

Accordingly, the correlation between the recombined CBF maps and the acquired CBF maps was calculated. In this case, as a one to one correspondence between the recombined

CBF and the acquired CBF is the desired result, the sum of absolute difference (SAD) between the two over all voxels was also computed.

Both sets of PV maps were used to created pseudorandom regions of interest of GM % as previously described in order to investigate the dependency of GM CBF on GM PVF.

## 6.3 Results

### 6.3.1 T1 relaxation times

The mean global T1 relaxation times derived from the saturation recovery data were 1150 $\pm$ 53 ms for WM and 1608 $\pm$ 51 ms for GM, respectively. It was found that using these global values for T1 GM produced GM PV maps much the same as those of Petr, that is, that there is reduced intensity in the deep GM structures compared to the GM PV map from segmentation of a high resolution MPRAGE image.

Figure 6.6 shows three sets of tissue partial volume maps for one of the subjects. The top row shows PVF maps derived from an MPRAGE segmentation and registration to perfusion space, as has been used previously in this thesis. The middle row shows those from a 3D GRASE saturation recovery sequence, assuming a single global value for GM T1 and those deep GM structures which have a lower PVF value as described above are marked with red arrows. Using a voxelwise T1 GM value increases the PV estimate for these regions, making them consistent with high resolution anatomical imaging. This is shown in the bottom row.

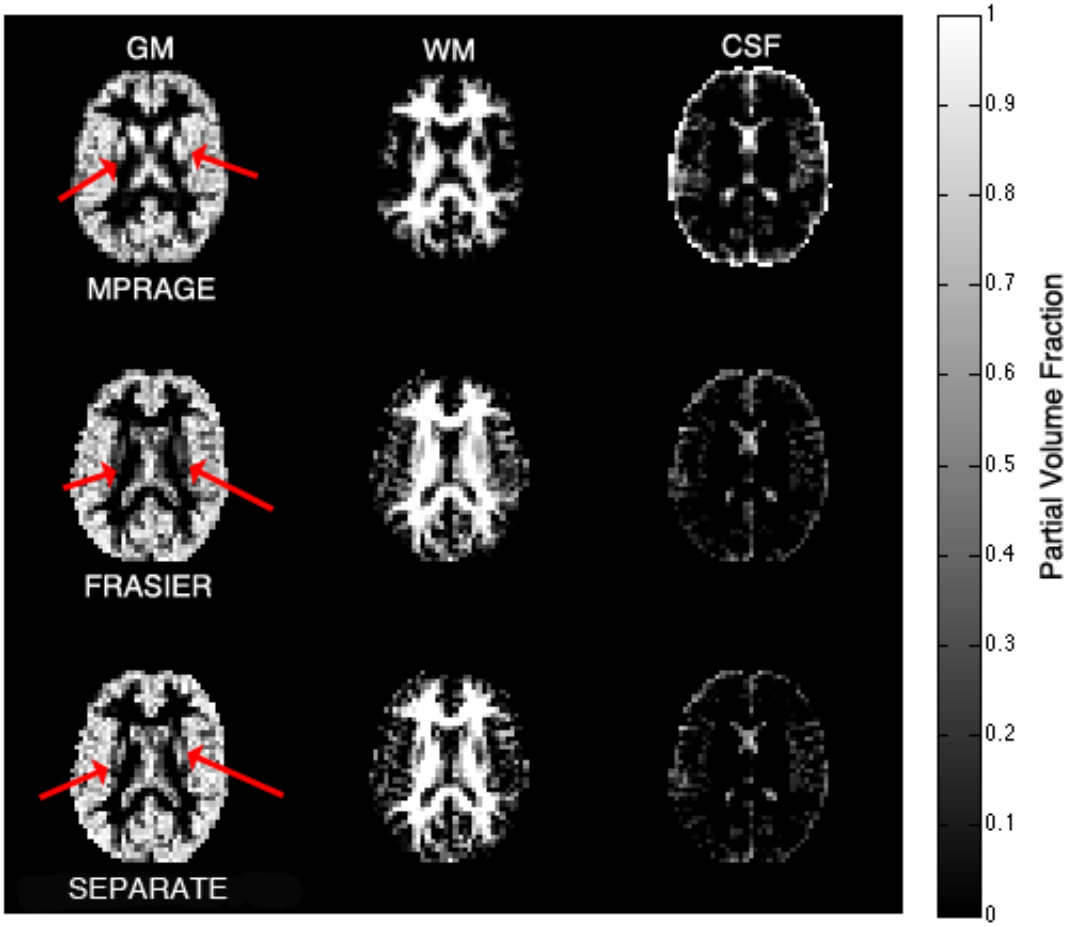


*Figure 6.6: Top row: PV fractions derived from MPRAGE segmentations. Middle row: PV maps from a saturation recovery sequence using a 3D GRASE acquisition and original FRASIER segmentation method. Bottom row: PV maps from same saturation recovery sequence as middle row, but voxelwise T1 GM values are used in the fractional segmentation. Red arrows mark regions where FRASIER and MPRAGE differed on GM maps. The SEPARATE method produces greater PVF in these regions.*

### 6.3.2 Validation of PV maps

Figure 6.7 shows the voxelwise correlation for the same subject between the acquired CBF maps and the recombined CBF maps after PV correction for the $PV_{sat\_rec}$ and $PV_{MPRAGE}$ maps. There is a wider scatter for the $PV_{MPRAGE}$ maps, along with a systematic offset, evidenced by points lying along the x-axis. These points represent voxels which have a non-zero value for the acquired CBF map, but after recombination from the $PV_{MPRAGE}$ maps, the equivalent voxel has a zero value. This is strongly suggestive of a misalignment between the two CBF maps, indicative of a registration error in the PV maps. This is not

seen in the recombined 3D GRASE maps.

However, for both scatter plots, the line of best fit does not go through the origin, in fact there is an intercept of similar magnitude on the recombined CBF axis in both cases. This would suggest that the recombined CBF voxels, measured over all voxels, are of a higher value than the counterpart acquired CBF voxels. Figure 6.8 shows a middle slice from the acquired CBF and recombined CBF maps. Blurring is evident in both of the recombined maps, compared to the acquired CBF map, which is a possible explanation for the offset on the correlations plot.

Table 6.1 shows both the correlation and sum of absolute differences (SAD) of the recombined CBF maps as compared to the acquired CBF maps calculated according to the Buxton model. There is better correlation ($R^2$) and lower SAD using the 3D GRASE data for all subjects, with a mean ($R^2$) of 0.80 and 0.44 for the 3D GRASE and MPRAGE groups, respectively. The mean SAD are 2.39 x $10^5$ and 3.87 x $10^5$ for 3D GRASE and MPRAGE. This is indicative of a better registration between the 3D GRASE derived PV maps and the perfusion data, than with the MPRAGE derived PV estimates.

| | Correlation ($R^2$) | | SAD (x$10^5$) | |
|---|---|---|---|---|
| Subject | GRASE | MPRAGE | GRASE | MPRAGE |
| ED | 0.84 | 0.59 | 1.98 | 3.25 |
| JF | 0.73 | 0.35 | 3.54 | 5.48 |
| JM | 0.81 | 0.24 | 2.28 | 4.26 |
| JT | 0.81 | 0.52 | 1.82 | 2.81 |
| KL | 0.80 | 0.44 | 2.33 | 4.09 |
| NZ | 0.83 | 0.37 | 2.44 | 4.61 |
| RL | 0.79 | 0.38 | 2.94 | 5.10 |
| RO | 0.82 | 0.64 | 1.82 | 1.38 |
| Mean | 0.80 | 0.44 | 2.39 | 3.87 |

*Table 6.1: Voxelwise correlation between CBF maps generated after recombining GM and WM CBF flows with acquired CBF maps. Sum of absolute difference (SAD) reflects difference between these recombined maps and the acquired CBF map.*

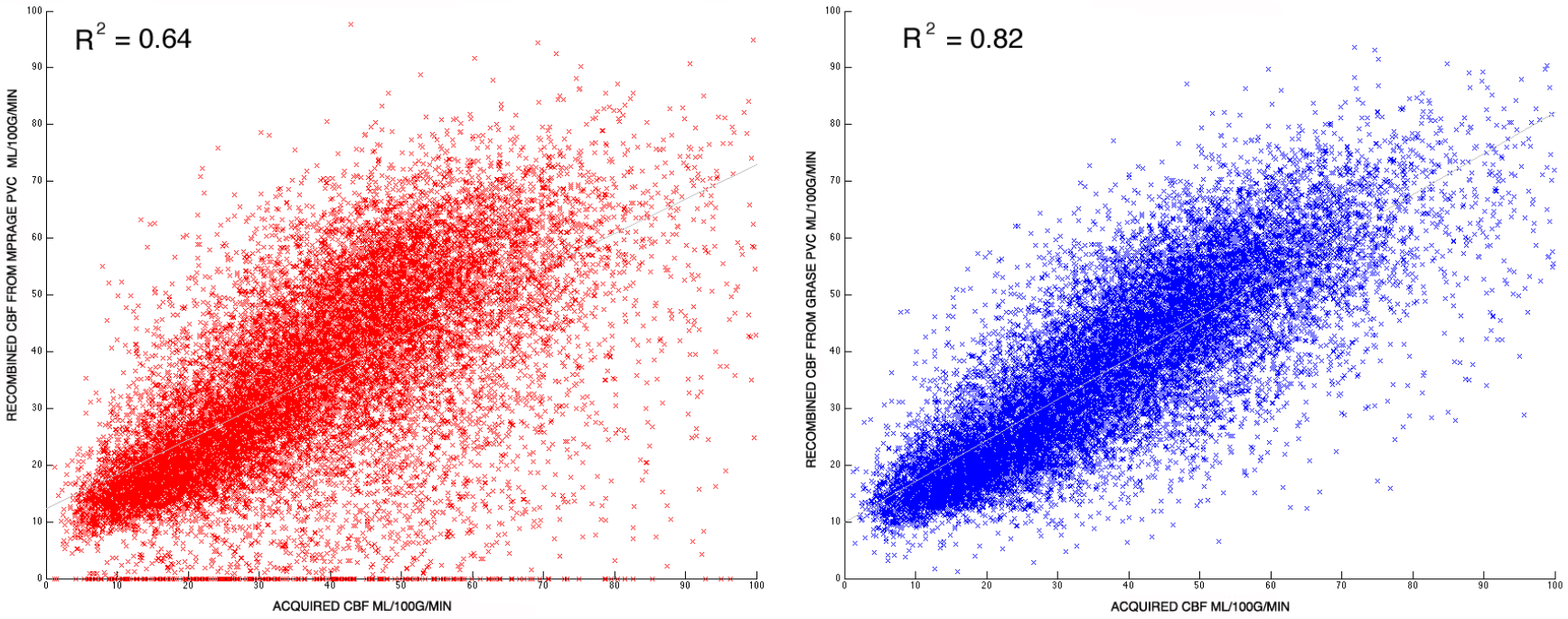


*Figure 6.7: LH image: Voxelwise correlation between acquired CBF map and recombined CBF map after PV correction with MPRAGE derived PV maps. RH image: Voxelwise correlation between acquired CBF map and recombined CBF map after PV correction with saturation recovery 3D GRASE derived PV maps. A better correlation is seen with the 3D GRASE data, denoting less misalignment between the perfusion data and the PV maps.*

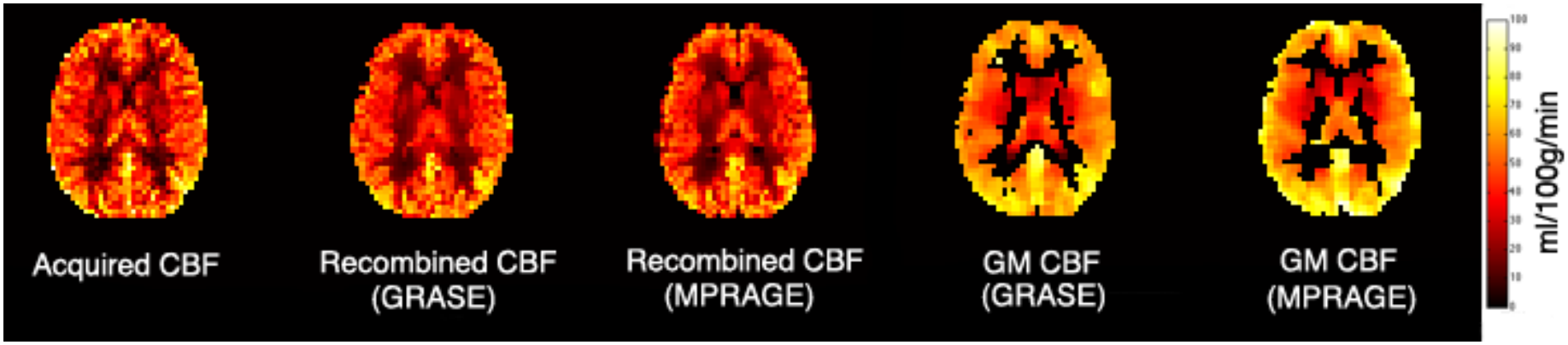


*Figure 6.8: Validation of PV maps: comparison between recombined CBF maps after applying PV corrections using the PV maps derived from 3D GRASE and MPRAGE data. GM CBF maps after PV correction and masking at PVF > 10% GM.*

| | Gradient | | Offset % | |
|---|---|---|---|---|
| Subject | GRASE | MPRAGE | GRASE | MPRAGE |
| ED | -0.0065 ± 0.0049 | 0.054 ± 0.061 | 7.8 | 9.2 |
| JF | -0.085 ± 0.0051 | 0.040 ± 0.013 | 11.7 | 36.7 |
| JM | 0.036 ± 0.010 | 0.017 ± 0.011 | 14.3 | 42.1 |
| JT | 0.040 ± 0.013 | 0.0070 ± 0.016 | 11.3 | 25.7 |
| KL | -0.088 ± 0.0047 | 0.037 ± 0.0063 | 12.9 | 29.4 |
| NZ | -0.010 ± 0.0043 | 0.051 ± 0.012 | 25.1 | 37.3 |
| RL | 0.030 ± 0.011 | 0.060 ± 0.012 | 14.3 | 37.7 |
| RO | 0.026 ± 0.0084 | 0.035 ± 0.017 | 12.2 | 24.5 |

*Table 6.2: Gradient of line of best fit with 95% confidence intervals for the GM CBF mean values across the PV 10% GM bin ranges, shown in figures 6.11 and 6.12.*

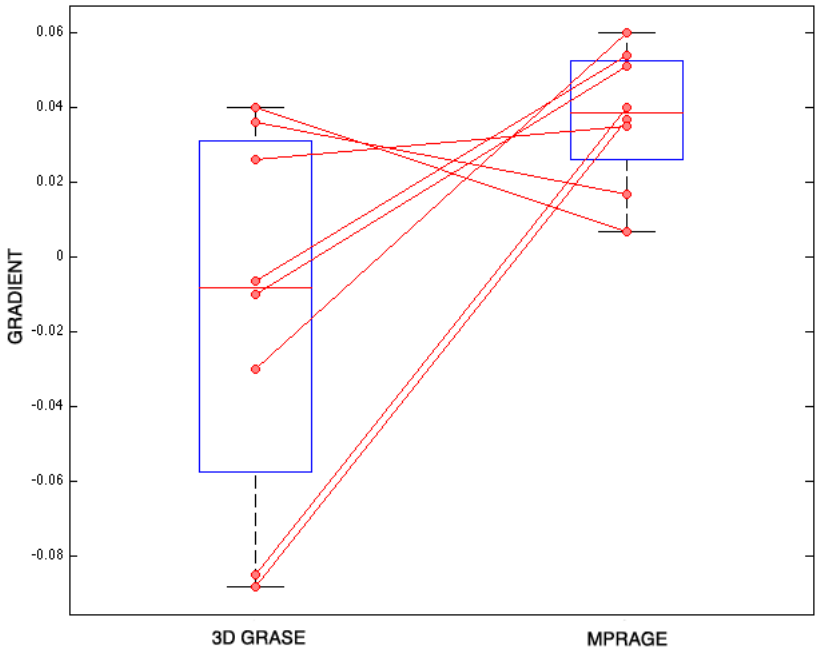


*Figure 6.9: Box plot of the gradient of GM CBF best fit line for two groups; using 3D GRASE PV maps and MPRAGE PV maps. Lines link same subject in each imaging group. The box plot shows a greater spread in gradients for the 3D GRASE imaging compared to MPRAGE, but the mean gradient is closer to zero. The median values are -0.0083 and 0.039 for 3D GRASE and MPRAGE respectively.*

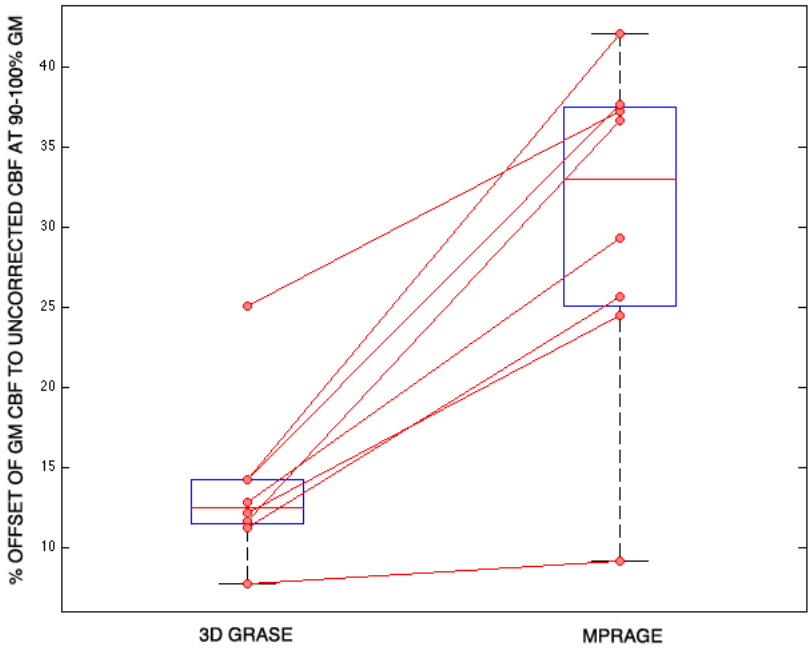


*Figure 6.10: Box plot of the percentage offsets of the 90-100% GM CBF and uncorrected CBF values as a fraction of uncorrected CBF. Lines link same subject in each imaging group. The mean % offset for the MPRAGE data is more than twice that obtained using 3D GRASE data, with individual % offsets higher with MPRAGE imaging in every case. Median values are 12.6% and 33.1% for 3D GRASE and MPRAGE respectively.*

### 6.3.3 Partial volume correction of CBF maps

Figures 6.11 and 6.12 show the dependency of mean uncorrected CBF and mean GM CBF after PV correction across the PV range, as seen in chapter 5. There are two graphs for each subject in this case, as the PV fractions differ depending on which GM PVF map they were generated from.

As expected, the uncorrected CBF shows a dependency on partial volume fraction, as calculated from both sets of PV fractions. There is a theoretical expectation that the dependency is linear, and that as the GM PVF approaches 100%, the mean CBF value will overlap that of the PV corrected GM CBF, which is expected to be constant across all PV ranges. There are therefore two metrics to consider in assessing the quality of the PV correction; gradient of line of best fit of the GM CBF and the offset at 90-100% GM

PVF between uncorrected CBF and GM CBF.

It was shown in chapter 5 that close agreement between uncorrected CBF and GM CBF mean values is not observed, even at high GM PV fractions, unless simulated data is used. This suggests that the cause of the offset is mis-registration between the perfusion data and PV maps. Therefore, it follows that a smaller offset between the two means for the 90-100% GM PVF bin is indicative of an improved registration. The offset between the GM CBF and uncorrected CBF for the 90-100% range as a fraction of the uncorrected CBF value in the same range, as a percentage, is shown in table 6.2, alongside the gradient of the line of best fit of the GM CBF.

This information is displayed graphically in the box plots in figures 6.9 and 6.10 and . For the offsets, the median values are 12.6% and 33.1% for the 3D GRASE and MPRAGE respectively. There is one outlier for the 3D GRASE group, (NZ (3D GRASE) = 25.1%) and whilst this greater than the rest of the cohort, it is still reduced compared to the MPRAGE offset (NZ(MPRAGE) = 37.3%). The other offset values fall into the range 7.8 - 14.3% for 3D GRASE and 9.2 to 42.1% for the MPRAGE.

In terms of the gradient across the GM CBF, there are three subjects for whom the gradient is closer to zero for the MPRAGE maps; JF, JM and KL. For the cases of JF and JM, the uncorrected CBF maps are somewhat flat across the entire PVF range, with the corrected GM CBF lines lying almost parallel. This is symptomatic of misalignment of the data and PV maps. To a lesser extent, the same is true for all subjects using the MPRAGE maps, whereas a linear rise for mean uncorrected CBF is seen when using the 3D GRASE maps.

Therefore, when assessing the quality of the PV correction, it is appropriate to consider the gradient and offset metrics in tandem; the hallmark of a good PV correction is a consistent value for GM CBF across all PV ranges, as well as this value being close to the mean uncorrected CBF value at the 90-100% GM PVF range. From this small sample size, it would seem that an offset of around 10% is reasonable.

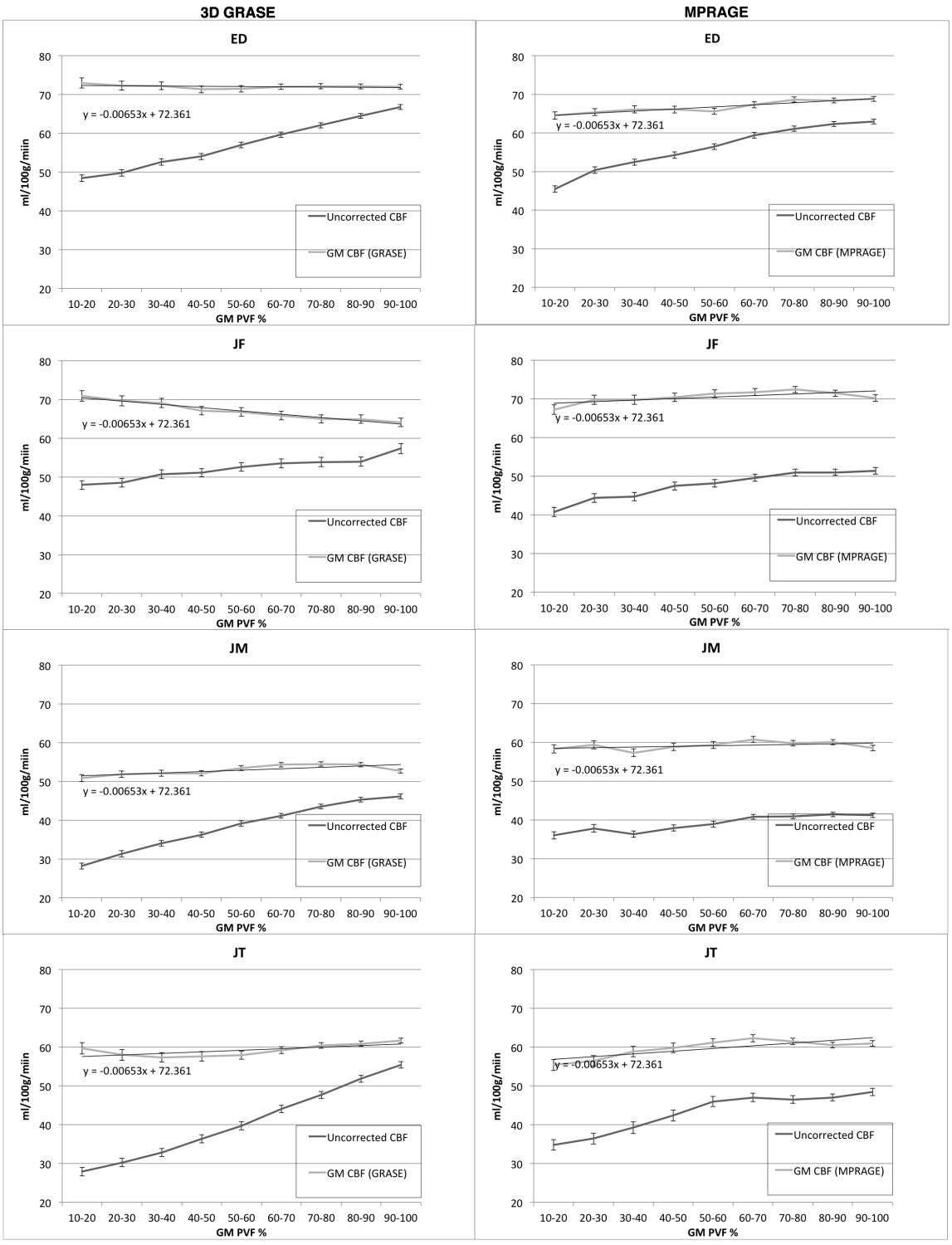


*Figure 6.11: Subjects ED, JF, JM, JT : Mean uncorrected CBF and GM CBF binned into GM partial volume fractions. The left hand side shows PV corrections using PV estimates generated from 3D GRASE data, whilst the right hand side shows corrections using MPRAGE derived partial volume estimates. Lines of best fit and associated equation for the GM CBF are shown. Error bars are 95% confidence intervals on mean estimation.*

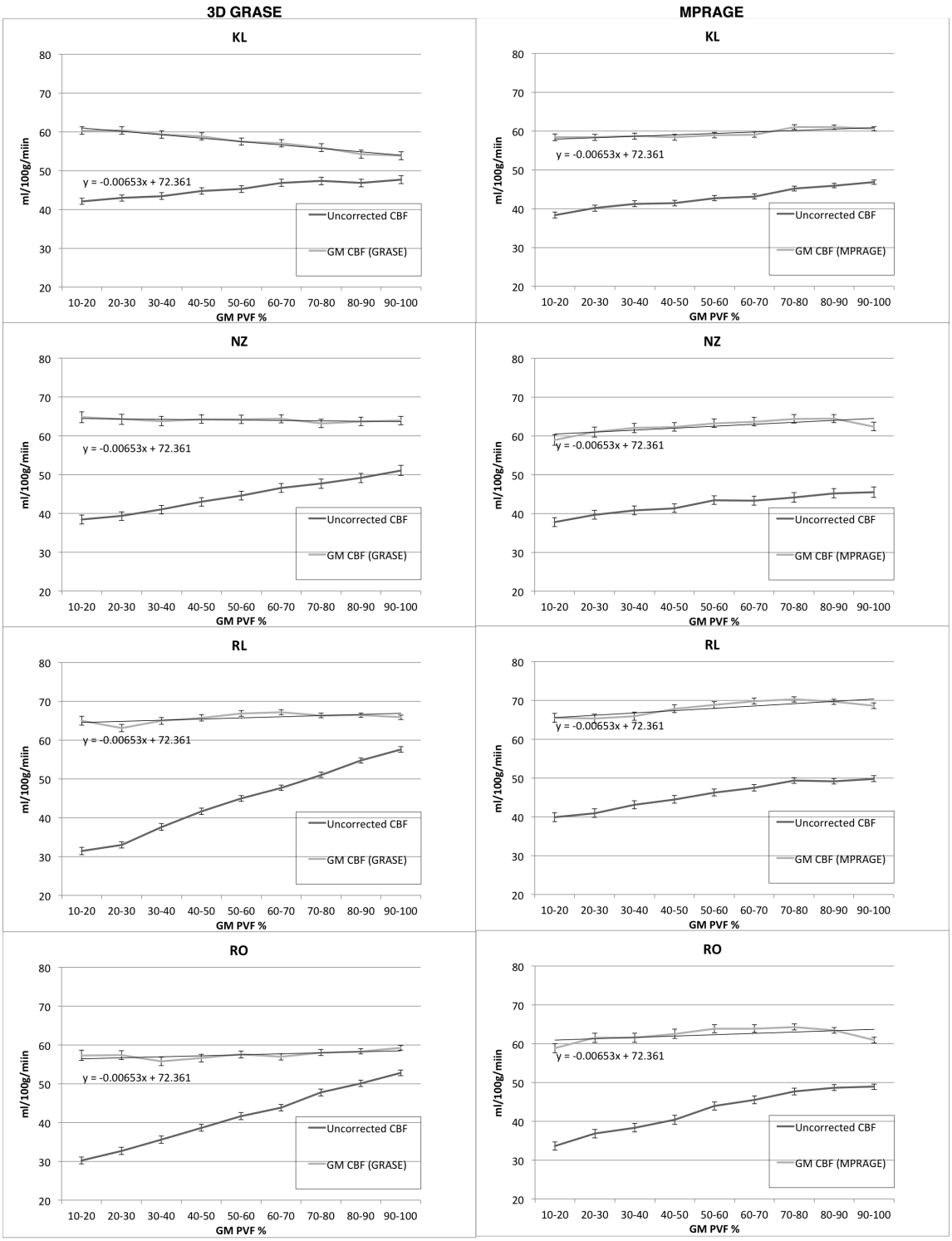


*Figure 6.12: Subjects KL, NZ, RL, RO : Mean uncorrected CBF and GM CBF binned into GM partial volume fractions. The left hand side shows PV corrections using PV estimates generated from 3D GRASE data, whilst the right hand side shows corrections using MPRAGE derived partial volume estimates. Lines of best fit and associated equation for the GM CBF are shown. Error bars are 95% confidence intervals on mean estimation.*

## 6.4 Discussion

This study has demonstrated that it is possible to use 3D GRASE saturation recovery data in a fractional segmentation algorithm to produce PV maps. The FRASIER method has been adapted to estimate the T1 of GM on a voxelwise basis, which improves the estimation of the PV of GM in the basal ganglia, compared to the original FRASIER method. This is the first reported study to apply 3D GRASE data to this technique and to use a voxelwise estimation for the T1 of GM.

The goal of a partial volume correction algorithm is to remove the dependency of the voxel intensity on tissue fraction. If the assumption that separate GM and WM perfusion are constant holds true, it is expected that the a best fit line as shown in figures 6.11 and 6.12 would have a zero, or close to zero, gradient. Additionally, there should be in agreement between the uncorrected and GM CBF maps at the 90-100% GM PV fraction. Therefore, the hallmark of a successful PV correction is a consistent value across all tissue fractions, which the uncorrected CBF values tend towards. Conversely, for PV maps which are well registered to the perfusion data, there will be a smooth linear increase in CBF across the PV range.

The PV corrections performed using the 3D GRASE data showed a median gradient closer to the zero and a smaller median offset between the GM CBF and uncorrected CBF means for the 90-100% GM PVF. This means that, in general, the PV maps obtained from 3D GRASE data are better registered to the perfusion data than the MPRAGE maps and produce results which better fit the model.

For the three subjects where the gradient of best fit of the GM CBF is closer to zero in the MPRAGE case, the offset at 90-100% GM PVF is still lower for the 3D GRASE case. Moreover, the voxelwise correlations and SAD between the acquired CBF maps and recombined CBF maps are significantly better for the $PV_{sat\_rec}$ maps ($R^2$ = 0.73, 0.81, 0.80 (3D GRASE) and 0.35, 0.24, 0.44 (MPRAGE) ), so it would seem that even in the case of a poor or difficult registration, saturation recovery derived PV maps are still the

superior choice.

The voxelwise correlation between the acquired CBF and recombined CBF maps demonstrate the difficulty in registering the high resolution MPRAGE PV maps to the much lower resolution ASL space. The correlation for the $PV_{MPRAGE}$ maps is consistently poorer, with the scatter plots (see example in 6.7) indicating a misalignment between the acquired and recombined CBF maps.

Whilst the $PV_{sat\_rec}$ maps are generated from data which also needs registering to perfusion weighted data, the two datasets (saturation recovery and perfusion weighted) are of the same resolution so no resampling is required, which eliminates one potential source of error.

Thirty-one time points were used for sampling the saturation recovery data in order to estimate the PV fractions. This invites an investigation into the optimal number of data points and sampling interval, with a view to minimising scan time. More sample points not only increases acquisition time, but increases the possibility of motion artefact and registration misalignment. This is an avenue for future work.

Unlike in the study of Petr et al, fat suppression was not used during the saturation recovery sequence acquisition. The result of this is that as fat has a longitudinal relaxation time close to that of WM, for some of the subjects (see figure 6.6 WM PV map from 3D GRASE data), there is a ring of voxels encircling the brain in the WM PV map. In terms of PV correction, this does not affect the results as these fat voxels are outside of the brain; however, the resultant WM PVF map is not accurate and it would be an improvement on the technique if fat suppression was incorporated.

In all cases, the CSF PV map from the saturation recovery sequence is of a lower intensity than that for the MPRAGE derived maps. For practical purposes, this is not important as the CSF PV map is not used as part of the PV correction. This is most likely a reflection of the literature value of 4300 ms which was used not being accurate for the 3D GRASE sequence. There are not enough voxels containing 100% CSF at the resolution used in this study for direct measurement of the T1 of CSF, so would be beneficial to obtain an

estimate of the T1 of CSF acquired under the same conditions as that of WM and GM in order to assess if T1 of CSF being used in the estimation is accurate. This is most important if a PV correction is being performed on an M0 image, for which there is a contribution from CSF.

## 6.5 Conclusion

The importance of a good registration for reliable PV correction cannot be overstated, yet is difficult to achieve, particularly when trying to register images of greatly differing contrast and resolution, as is the case with perfusion and anatomical images. Moreover, segmentations of anatomical data usually rely on registration to a healthy template atlas, which can be inappropriate for cohorts which exhibit atrophy.

The SEPARATE segmentation method offers a reliable alternative, which does not rely on registration and resampling of high resolution anatomical data. However, the SEPARATE (or FRASIER) method requires multiple data points from a saturation or inversion recovery acquisition, which may not be acquired as part of a routine clinical examination, whereas it is usual to acquire an anatomical image. This will produce difficulties for retrospective analysis and post-processing.

The inclusion of the voxelwise estimates for the T1 of GM improves the PV estimates obtained from a fractional segmentation method compared to using a global T1 for GM and produces PV maps with fewer registration errors than those from an anatomical segmentation. This in turn produces more accurate partial volume corrections.

# Chapter 7

# Image Deblurring

This chapter describes the origin of the point spread effect in 3D GRASE imaging and the use of a theoretical derivation of the point spread function (PSF). Image restoration through a process of deconvolution of the PSF is incorporated into a complete and novel solution for PV correction of ASL 3D GRASE data.

## 7.1 The Point Spread Function

In both PET and ASL perfusion imaging, PV effects are caused by inadequate spatial resolution, which is a consequence of the voxel grid the image is sampled on and some degree of blurring due to the PSF of the imaging process.

The PSF of an imaging system describes the mapping of a perfect representation of a point object to the actual observed image. In a linear, shift invariant system, knowledge of the PSF can be used via the process of convolution to predict the image of an object. The PSF determines the smallest resolvable object, and therefore the sharpness of an image.

In ASL, the PSF has the undesired effect of tissue signal blurring which impacts perfusion quantification due to cross contamination of the higher GM signal with the much lower adjacent WM signal and vice versa. This phenomenon contributes to increased partial volume effects.

The fact that there are two contributory elements to the PV effect is well understood and explored in PET imaging [44, 43, 70, 71]. State of the art PET scanners have a PSF of around 2-3 mm, but historically this has been much larger; typically around 5-6 mm full width at half maximum (FWHM) and known to adversely affect perfusion quantification [72]. Consequently, all PV correction methods for PET data involve a correction for the effect . This is not the case with ASL perfusion imaging. It remains uncommon to account for PV effects at all, and if any correction attempt is made, this usually takes the form of correcting for tissue fraction only.

One of the possible reasons for this may be that as the PSF in MR imaging is usually narrower than that of PET imaging, it is assumed that its effect can be ignored. However, as will be discussed later in the chapter, when fast imaging techniques are employed, it is appropriate to consider the effect of the PSF.

### 7.1.1 Definition

The standard definition of the PSF, $H(r; r_0)$, follows from the image appearance at *r* due to an ideal point source $\delta(r_0)$. If we make the assumption that the system is shift-invariant, we may write $H(r - r_0)$, so that *H* is strongly dependent on $r - r_0$ rather than just on $r_0$ [73].

Provided linearity and shift-invariance are both true, the observed image, $I_{observed}(r)$, is described as a convolution of the actual image, $I_{actual}(r)$, with the PSF, ***H(r)***:

$$I_{observed}(r) = \int_{allspace} I_{actual}(r')H(r - r')dr' \tag{7.1}$$

or more concisely,

$$I_{observed}(r) = I_{actual}(r) * H(r) \tag{7.2}$$

where $*$ denotes convolution.

In the frequency domain, or k-space as it is known in MR imaging, the PSF transforms

as the modulation transfer function (MTF), and can be considered to act as a weighting function on the acquired signals, given that the Fourier transform (FT) of convolution in the spatial domain is multiplication in the frequency domain.

As such the ideal PSF is a delta function, which will cause all acquired frequencies to be equally weighted. However, in practice this is never the case, and the width of the PSF is sequence dependent (see figure 7.1).


*Figure 7.1: The ideal PSF is a delta function, which has a constant value in k-space. In reality, this is never the case, and the acquired frequencies do not experience equal weighting.*

Whilst it is the case that the tissue fraction effect can be mitigated by sampling on a smaller voxel grid, there is a trade-off in terms of SNR, which is especially problematic for estimating the lower WM perfusion. Moreover, blurring in the partition direction is a feature of 3D GRASE imaging which cannot be alleviated by this approach.

This investigation was undertaken to ascertain whether blurring due to the PSF in ASL perfusion imaging is a significant cause of quantification error, as with PET imaging. Whilst there are a very limited number of articles investigating the effect of blurring due to the PSF on image quality [15, 47], there are no published articles addressing the role of the PSF in ASL partial volume correction.

### 7.1.2 Blurring Effect

The degree to which a structure is affected by the PSF depends on its size. Brain structures which are smaller than twice the FWHM of the PSF are most strongly affected [70].

As the cortex ranges in thickness from 2 to 4 mm in a healthy brain, and can be less than

half this in an atrophied brain, PV effects caused by the PSF are a significant cause for concern in PET imaging and a potential source of error in ASL imaging.

The relationship between PSF and structure size is shown in figure 7.2. Two structures of width (a) 10 mm and (b) 30 mm are convolved with a Gaussian PSF of FWHM 10.5 mm figure 7.2. The smaller structure is on the order of the PSF and suffers more attenuation in maximum value than the larger structure.

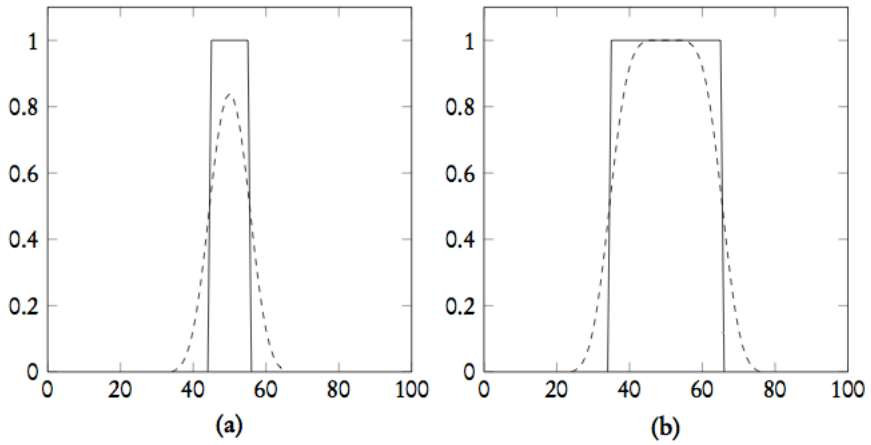


*Figure 7.2: Ilustration of relationship between structure size and PSF width. The same PSF (FWHM = 10.5 mm) is convolved with two structures of different widths. Plot (a) shows the effect on a structure of width 10 mm and (b) shows the effect on a structure of 30 mm. The smaller structure suffers a greater reduction in intensity. Taken from [16].*

The implication of this is that the cortical ASL signal will suffer some attenuation, the extent of which will depend on the tissue thickness and the width of the PSF, while the WM signal will be largely preserved.

## 7.2 The PSF in MR imaging

Measurement of the PSF of an imaging system can be accomplished by imaging a 'test object', for example a fluorescent bead in microscopy, which is considered to be a point source object. However, in MR imaging, determination of the PSF is more complicated as it is dependent on the object, the sequence parameters and post-processing methods. Care is usually taken to try and minimise the width of the PSF and therefore preserve image

resolution.

Nevertheless, attempts to characterise the PSF in MR using test objects have been made. Such an example is shown in figure 7.3. A perspex object is filled with an aqueous solution or gel to provide a source of protons. A pattern of bars of decreasing separation is used to determine the minimum spatial frequency which can be resolved by the system.

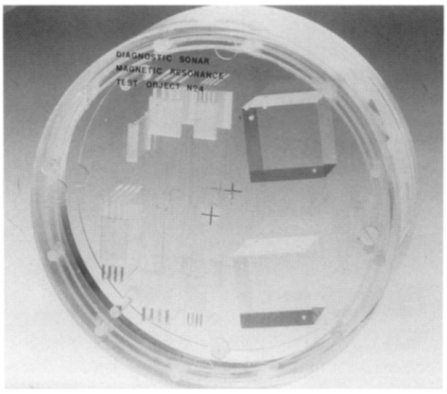


*Figure 7.3: Perspex block filled with an aqueous solution and a 'comb' pattern of varying spatial frequency in order to assess the minimum resolvable distance by the imaging system. Taken from [17].*

However, this method only offers a rough estimation of spatial resolution and it must be noted that the test object being used to measure the PSF may actually influence it (susceptibility effects, T2 rate alterations) [17]. These considerations mean that actual measurement of the PSF in MR imaging is non-trivial.

### 7.2.1 The PSF in ASL perfusion imaging

ASL imaging requires the use of fast acquisition methods such as EPI or 3D GRASE. Knowledge of the PSF is particularly important for fast imaging techniques in order to produce images of good quality.

EPI is of lower resolution than conventional imaging and more prone to artifacts due to susceptibility effects at air/bone interfaces, eddy currents from rapidly switching gradients and $T2^*$ relaxation which takes place during the acquisition period.

Like EPI, 3D GRASE imaging is usually acquired at comparatively low resolution. For 3D GRASE, we are concerned with the effect of the PSF in the partition direction due to the length of the echo train that is employed relative to T2 decay times. This manifests itself as an echo train which follows a smooth T2 decay throughout k-space and appears as blurring in the partition direction in the image.

It has been found that measurements of mean GM CBF using EPI acquisitions for the read-out are higher than those obtained using a single-shot 3D GRASE sequence, and vice-versa for WM CBF. It has been proposed that the discrepancy is due to PV effects caused by the wide PSF along the partition direction for single-shot 3D GRASE [74].

The decay of the echo train signal is exponential, which means the 1D PSF along the z-axis for 3D GRASE imaging has a Lorentzian form, with literature values ranging from 1.5 to 1.9 voxels FWHM for a single shot acquisition [15, 74]. The width of the PSF depends on how long the acquisition takes, with longer echo trains producing more blurring.

### 7.2.2 Segmented acquisitions

Through-plane blurring in 3D GRASE can be reduced be using a segmented acquisition, which is the recommended acquisition strategy of the ISMRM Perfusion Study Group [39], although the greater the number of segments, the higher the risk of artifact due to subject motion during the overall longer period required to acquire a full k-space data set.

Boscolo Galazzo et al [47] recently published work investigating an optimisation of the number of the segments used to acquire the whole brain and the time taken to do so, how many averages it was possible to acquire as a consequence of the number of segments, versus a deblurring post-processing method. For a field of view 240 x 240 $mm^2$ with a voxel resolution 3.5 x 3.5 x 5.0 $mm^3$, 20 partitions in the second phase encoding direction, it was found that a four shot acquisition offered the best trade-off in terms of image quality, motion sensitivity and SNR, as twice as many signal averages can be obtained in a four shot acquisition compared to an eight shot acquisition.

Nonetheless, the paper recommended that a deblurring algorithm be applied even in the case of an eight shot acquisition, which is the method used in our study, as improvements to image quality were still found. The through-plane blurring observed with an eight shot acquisition using the imaging parameters used for the studies is this thesis is shown in figure 7.4.

*Figure 7.4: Example perfusion data acquired in this thesis. Eight shot acquisition schemes still exhibit through plane blurring, visible in the coronal (top right) and sagittal (bottom right) views.*

### 7.2.3 Methods for theoretical estimation of the PSF

Given the difficulties described above with regards to an empirical measurement of the PSF, it is common to employ methods which estimate the PSF based on sequence parameters or by calculation from the acquired data. There are two reported methods in the literature of estimating the PSF of 3D GRASE sequences.

The first of these has its origins in the Extended Phase Graph (EPG) method of Hennig [75].

#### 7.2.3.1 Extended Phase Graph (EPG) algorithm

The EPG, or coherence pathway diagram, is a technique to predict the echo formation from a train of RF pulses. After every RF pulse, magnetisation is flipped to both the transverse and longitudinal planes which produces a free induction decay (FID), a potential echo formation as well as retaining magnetisation for future RF pulses to refocus.

For the sake of simplicity it is usual to consider one component of the transverse magnetisation only, rather than all of the isochromats fanning out over the transverse plane. This can be plotted on a phase coherence diagram with phase measured on the

ordinal axis and time on the abscissa.

It is beyond the scope of this text to describe the EPG in detail; suffice to say after the application of each RF pulse, the magnetisation splits into three portions:

1. a portion which continues to dephase
2. a portion which is converted to longitudinal magnetisation and does not dephase further
3. a portion for which the phase is reversed, and either continues to dephase or rephase

Whenever one of the lines crosses the zero phase axis, an echo is produced. This formulation enables the prediction of timing and amplitude of stimulated echoes as well as spin echoes. An example EPG with first spin echo and stimulated echo are marked on figure 7.5.

Knowledge of the amplitude of the evolving signal allows for a theoretical calculation of the PSF, as will be described in detail in the Methods section.

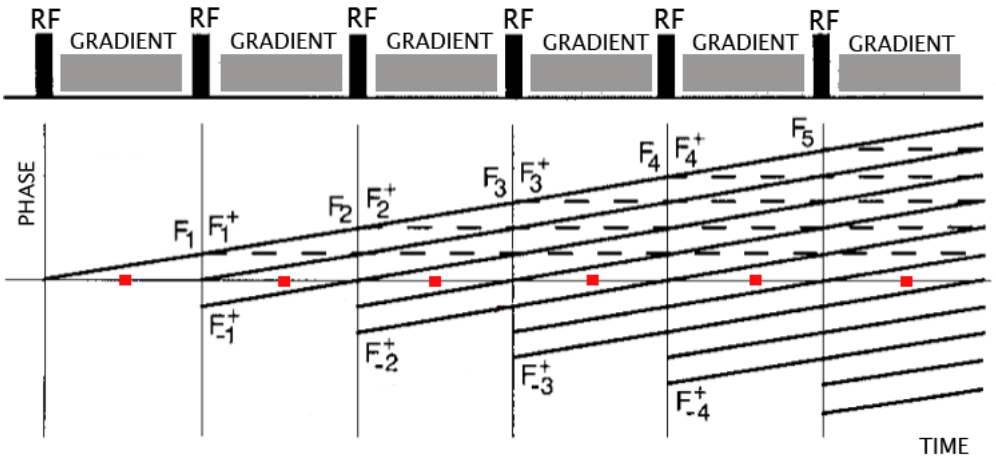


*Figure 7.5: Phase coherence pathway adapted from [18]. $F_n$ represents the dephased state of an isochromat after $n$ dephasing periods induced by the gradient pulse. Spin echoes and stimulated echoes occur at the time the zero phase axis is crossed (red squares) .*

#### 7.2.3.2 PSF by autocorrelation of residuals

A more recent method is that described by Chappell et al [15]. This method relies on multiple ASL measurements, be they either from a single timepoint with multiple

averages, or a multi-timepoint acquisition. The important point is there must be more than one measurement.

These multiple measurements are fitted to the general kinetic model [33] and the residuals to the fit are measured. The mean of the residuals in the x and y directions is subtracted from each voxel to produce a 1D series in the partition direction.

The autocorrelation of this series is then calculated, with the assumption that if there is no blurring the residuals will be random and the autocorrelation function will be a delta function. However, if there is blurring there will be shared information between the residuals and the autocorrelation function will reflect this.

A Lorentzian was fitted to the autocorrelation function, which is the 1D PSF for the sequence. In order to improve robustness, Chappell recommends averaging the PSF across all subjects, as it is sequence, not subject specific.

### 7.2.4 Deblurring using Richardson-Lucy deconvolution

Deblurring an image via deconvolution of the PSF is a common technique from the domain of computer vision and is a well developed field.

The Richardson-Lucy (RL) algorithm is an iterative method for image restoration using Bayes' theorem by treating the real image, degraded image and PSF as probability density functions. The R-L algorithm is a suitable algorithm for image deblurring when there is knowledge of the PSF, and functions effectively in the presence of noise.

If an assumption is made that the system is a linear, shift-invariant one with a position independent PSF, then the relationship between the observed image and the 'real' image may be described by:

$$g(x, y, z) = f(x, y, z) * h(x, y, z) + n(x, y, z) \tag{7.3}$$

where $h(x, y, z)$ is the 3D PSF, $f(x, y, z)$ is the true voxel value, and $g(x, y, z)$ is the

blurred voxel and $n(x, y, z)$ is some additive noise.

This can be written as a summation:

$$g_i = \sum_j h_{ij} f_j \tag{7.4}$$

where $g_i$ is the observed value at location $d_i$ in the image, $h_{ij}$ is the PSF which describes the signal at $i$ which comes from $j$ and $f_j$ is the latent voxel value we wish to recover.

Estimation of the most likely value for $f_j$ given the observed $g_i$ and known $h_{ij}$ leads to the iterative form:

$$f_j^{n+1} = f_j^n \sum_i \frac{g_i}{\sum_j p_{ij} f_j^n} p_{ij} \tag{7.5}$$

where $n$ is the number of iterations and converges to the maximum likelihood solution for $f_j$.

This can be written in terms of convolution as:

$$f^{n+1} = \left( \frac{g}{f^n \otimes h} \otimes h^T \right) f^n \tag{7.6}$$

The R-L equation requires an initial estimate and as long as the first estimate of the restored image is non-negative, the estimations will remain non-negative for all $n$ iterations. The algorithm is sensitive to the initial estimate which also influences the performance. As such, it is usual to provide an initial smooth 'guess' for $f_0$, which also helps avoid the amplification of high frequency noise, as although the R-L algorithm is constrained it is not regularised.

The R-L algorithm terminates when a prescribed number of iterations is reached. The RMSE between the restored image and true image decrease with increasing number of iterations until a minimum is reached; beyond this point the algorithm begins to fit to noise, known as 'overfitting' [76].

## 7.3 Methods

### 7.3.1 Characterisation of the 1D PSF in the partition direction for 3D GRASE

The value of the magnetisation signal at each of the 15 generated echoes (TE = 15ms, 6/8 partial Fourier, flip angle = 130 °) was estimated using an EPG algorithm simulation as described in section 7.2.3.1. The imaging volume was acquired in eight segments, with the split along the first phase encoding direction, i.e. each segment is 64 x 8 x 20 in the x, y and z directions respectively. This was factored into the simulated echo amplitudes by the reduction in the echo train length. In accordance with the assumption that the ASL signal originates from the capillary space, the T1 and T2 times for arterial blood at 3T were used in the calculation (1500 ms and 200 ms respectively).

As a centre-out phase-encoding scheme with 6/8 partial Fourier was employed, it was necessary to reorder the magnetisation decay values according to their partition index. The correspondences between echo number and partition index is shown in figure 7.9. The first five partition indexes were filled with echoes 20, 19, 18, 17 and 16 to mimic the partial Fourier reconstruction.

The 1D PSF in the partition direction was calculated from the MTF described above. The MTF was Fourier transformed, the modulus calculated and zero frequency component shifted to the centre of the spectrum.

### 7.3.2 Simulation study

In order to assess the efficacy of the deblurring algorithm, a simple 1D data vector was created as a digital perfusion phantom. The data vector was 20 elements long to reflect the number of sampled data points in the partition direction. The intensity of the elements were chosen to reflect typical perfusion values for GM and WM, albeit without any PV

effects. The pattern of the values was chosen to simulate the values which might be found for region which is at the interface between the GM and WM. The digital phantom is shown in figure 7.6

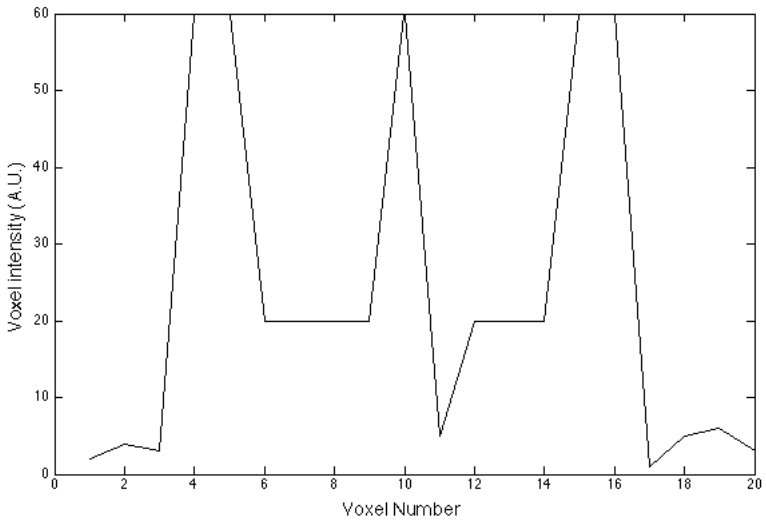


*Figure 7.6: Digital perfusion phantom for testing the deblurring algorithm. Phantom created with voxel intensities to represent typical GM and WM values, with no PV effects.*

The basic aim of this simulation was to verify that, for the simple 1D digital flow phantom, the process of blurring with a known PSF introduced PV effects between the GM and WM voxels by blurring their respective signals, the effect of which could be reversed by application of the deconvolution procedure. This also offered the opportunity to investigate the optimal number of iterations after which to terminate the algorithm.

This vector was convolved with the Lorentzian PSF previously calculated for the 3D GRASE imaging sequence used in this work to simulate the blurring which occurs during acquisition.

The Richardson-Lucy deblurring algorithm was then applied with the known PSF. The Matlab implementation was used with the number of iterations ranging from 5 to 35. The optimal number of iterations was defined as that after which the RMSE converged.

### 7.3.3 Application to in vivo data

In the strictest sense, any deblurring algorithm should be applied to the 'raw data', namely the control and label pairs, as well as to the $M0$ image, should one be present. Applying a deblurring technique directly to the CBF map assumes that the PSF propagates linearly and is unaffected in the difference and ratio of these images.

#### 7.3.3.1 Deblurring correction

In order for the partial volume information derived from anatomical images to be applied to the correct voxel intensity, blurred CBF signals must be reassigned to where they belong. It is for this reason that the deblurring must take place before any correction for tissue fraction effect. Consequently, an investigation of the effect of deblurring CBF maps in isolation from any other form of post-processing was made.

As a proof of concept, the deblurring algorithm was applied to a representative CBF map from a healthy volunteer, using a theoretical PSF calculated from the EPG. The PSF was calculated using this technique as a goal of this thesis was to apply to PV correction techniques to a cohort of single timepoint clinical data, for which only one measurement is available. This makes it unsuitable for calculation of the PSF by autocorrelation of the residuals. The number of iterations used was 25, as indicated as optimal from the simulation study. Whilst our data does not exhibit the same degree of blurring as a one-shot acquisition, there was still an expectation that some degree of 'sharpening' of the data would occur.

#### 7.3.3.2 Tissue fraction effect correction

In order to assess the effect of this additional step of deblurring perfusion images as part of a complete PV correction solution, a comparison was made of the separate PV-corrected GM and WM CBF results obtained with and without deblurring preprocessing. The original and deblurred CBF maps were both PV corrected using linear regression

with a 3D kernel using the procedure described in chapter 5.

The results were investigated on a regional basis by calculation of the mean GM and WM CBF in the regions as defined in section 4.4.1 created from a Freesurfer parcellation. Prior to segmentation into the nine regions, both GM and WM CBF maps were masked to remove voxels with tissue fractions of less than 10% for which PV correction results are unreliable due to the small quantity of tissue in the voxel.

## 7.4 Results

### 7.4.1 PSF determination

#### 7.4.1.1 Phase graph and echo train amplitude

The phase graph calculated for the sequence used is shown in figure 7.7. The population in the different F states (transverse magnetisation) as the echo train develops is shown.

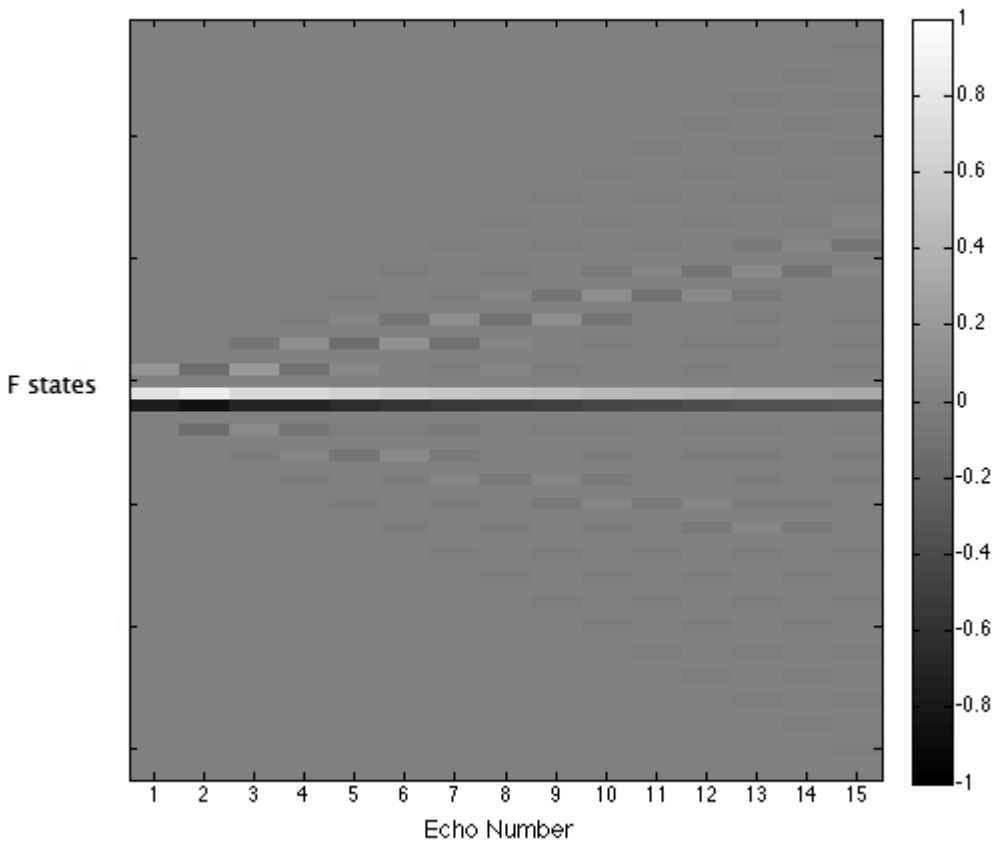


*Figure 7.7: Extended phase graph diagram calculated for the 3D GRASE sequence used in this study. Graph created using Matlab.*

The evolution of the echo train is shown in figure 7.8. The second echo is of greater amplitude than the first due to the fact the second echo has combined spin and stimulated echoes, whereas the first echo has only a spin echo contribution. After the second echo, a smooth decay due to T2 effects is seen.

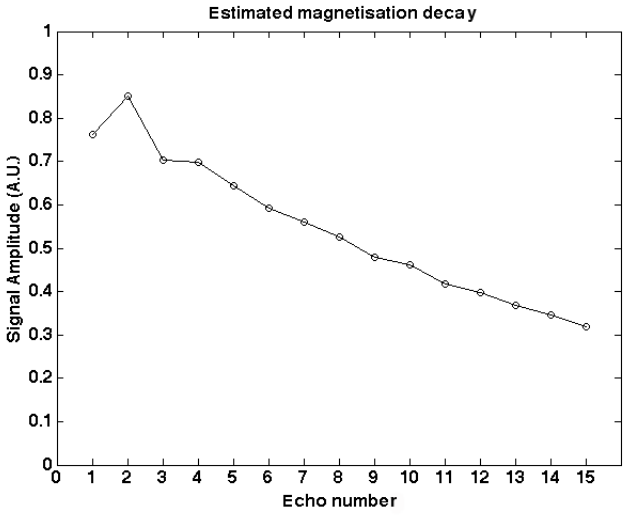


*Figure 7.8: Echo train as calculated using the EPG algorithm over 15 echoes with TE=15ms.*

#### 7.4.1.2 Description of the modulation transfer function (MTF)

The echo train amplitudes obtained in section 7.4.1.1 are reordered according to their partition index in order to characterise the MTF. For example, echo number 1 from figure 7.8 is from the centre of k-space and corresponds to partition 11 due to the centre-out acquisition. This is marked '1' on figure 7.9. Subsequent echoes from 2 to 15 are also marked. As a 6/8 partial Fourier acquisition was used, partitions 1 to 5 were not acquired, so these are filled with the values of echoes 20 to 16, as is the usual practice.

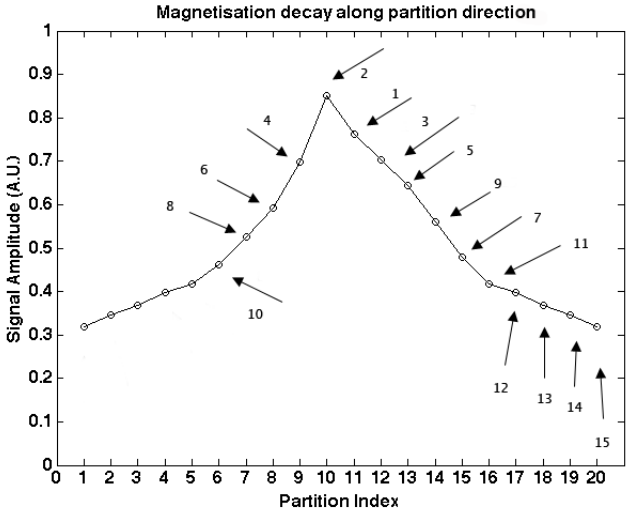


*Figure 7.9: Modulation transfer function calculated from the magnetisation decay depicted in figure 7.8. Partition indices 1 to 5 are filled with 20 to 16 to simulate the partial Fourier reconstruction. Numbered arrows denote the echo number.*

#### 7.4.1.3 Calculated PSF

The FT of the MTF gives the PSF, which is shown in figure 7.10. This was fitted to a Lorentzian function, which gave a FWHM of 1.3 voxels, or 4.9mm.

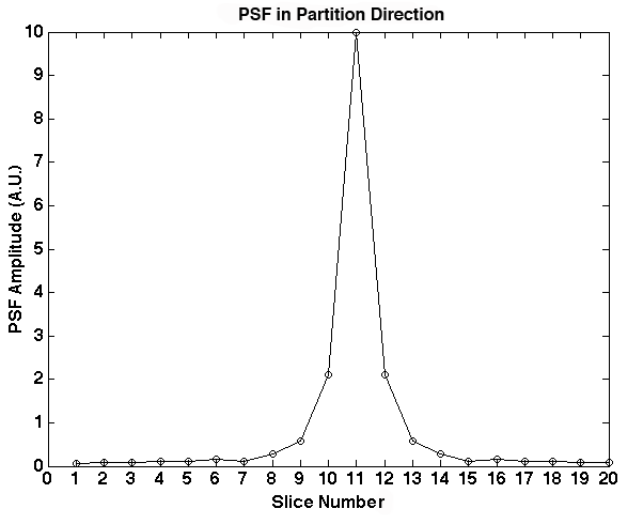


*Figure 7.10: The 1D PSF in the partition direction for this 3D GRASE acquisition. The FWHM is 1.3 voxels.*

### 7.4.2 Simulation study

After blurring using the Lorentzian PSF calculated in section 7.3.1, it can be seen in figure 7.11 that the higher intensity voxels (chosen to represent GM) are diminished to a peak of around 40, whereas the 'WM voxels' are elevated slightly above 20. The mean intensity of the five GM voxels drops to 41.8 after blurring, whereas the mean of the WM voxels rises from 20 to 24.2.

Therefore, the intensity of the 'GM voxels' suffers more modification than for the WM voxels, due to the fact the cortex is usually only one voxel wide at typical ASL resolutions. This means that the signal from the GM voxels is being blurred to WM voxels, whereas the WM voxels will blur to other WM voxels as the WM region is comparatively wide.

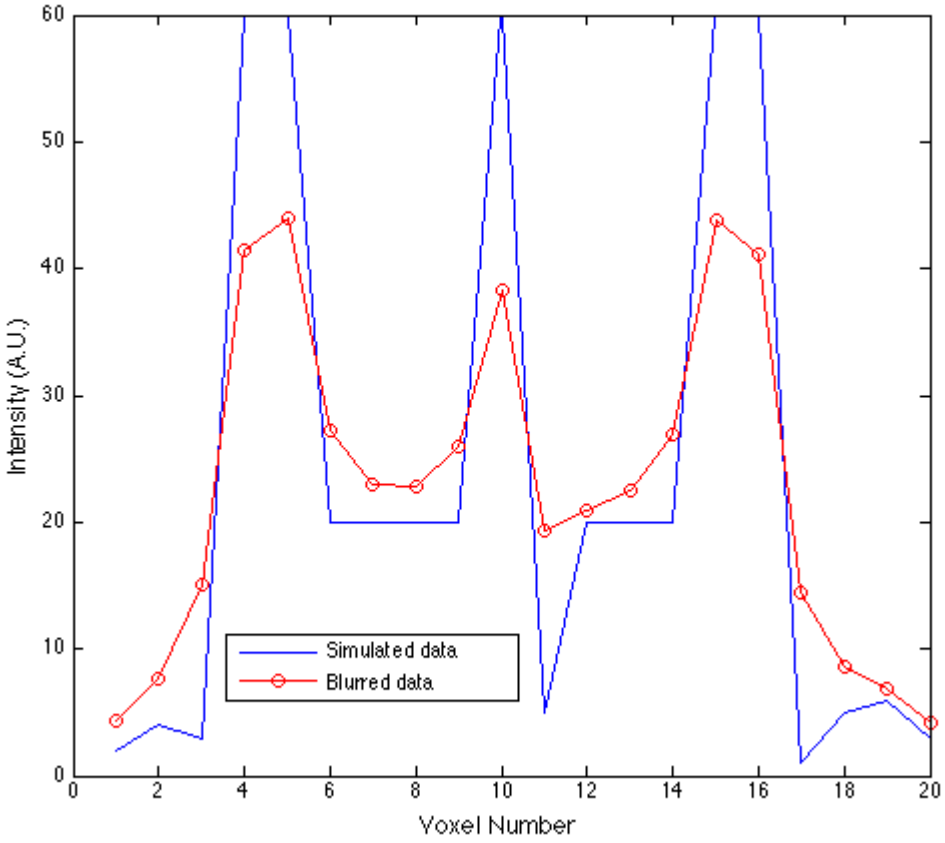


*Figure 7.11: Intensity profile of 1D simulated data (blue) and after blurring with Lorentzian PSF of FWHM = 1.3 voxels (red).*

#### 7.4.2.1 Estimation of optimal number of iterations

The algorithm was initially run with five iterations, and it can be seen in figure 7.12 that the peak values in the profile are not recovered with so few iterations. It was found that the RMSE converges to 0.95 at 25 iterations, and this was used in the subsequent in vivo study.

| No.of iterations | RMSE |
|---|---|
| 5 | 3.7 |
| 10 | 1.5 |
| 15 | 1.1 |
| 20 | 0.98 |
| 25 | 0.95 |
| 30 | 0.95 |
| 35 | 0.95 |

*Table 7.1: RMSE error of deblurred data and data versus number of iterations for the Richardson-Lucy deconvolution algorithm. The RMSE converges at 25 iterations.*

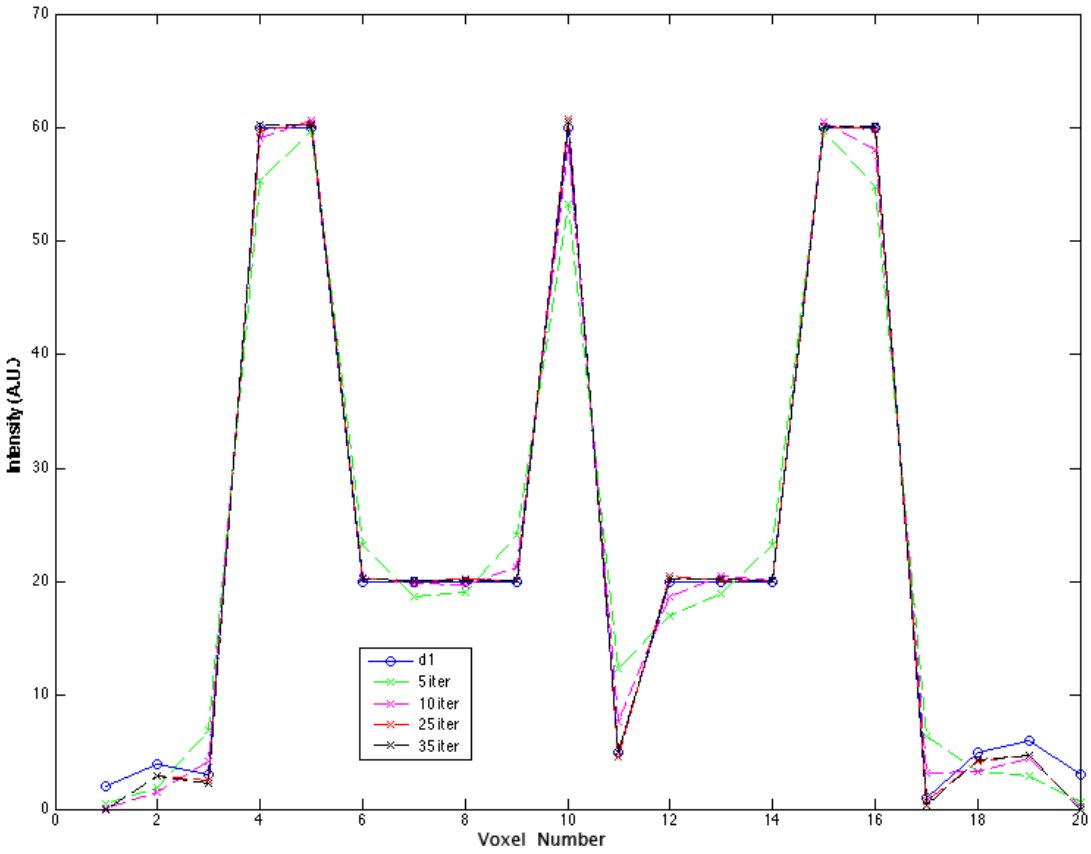


*Figure 7.12: Effect of varying number of iterations of Richardson-Lucy deconvolution algorithm. Twenty five iterations was found to be the optimal number of iterations in terms of smallest RMSE before convergence.*

### 7.4.3 In vivo study

Middle slices of a CBF map from a healthy subject are shown in figure 7.13, before and after deblurring. Whilst the mean of the CBF map is unchanged after deblurring, the

standard deviation has increased; the deblurring procedure clearly increases noise. After deblurring, the image is considerably less smooth. This is a known trade-off of deblurring procedures.

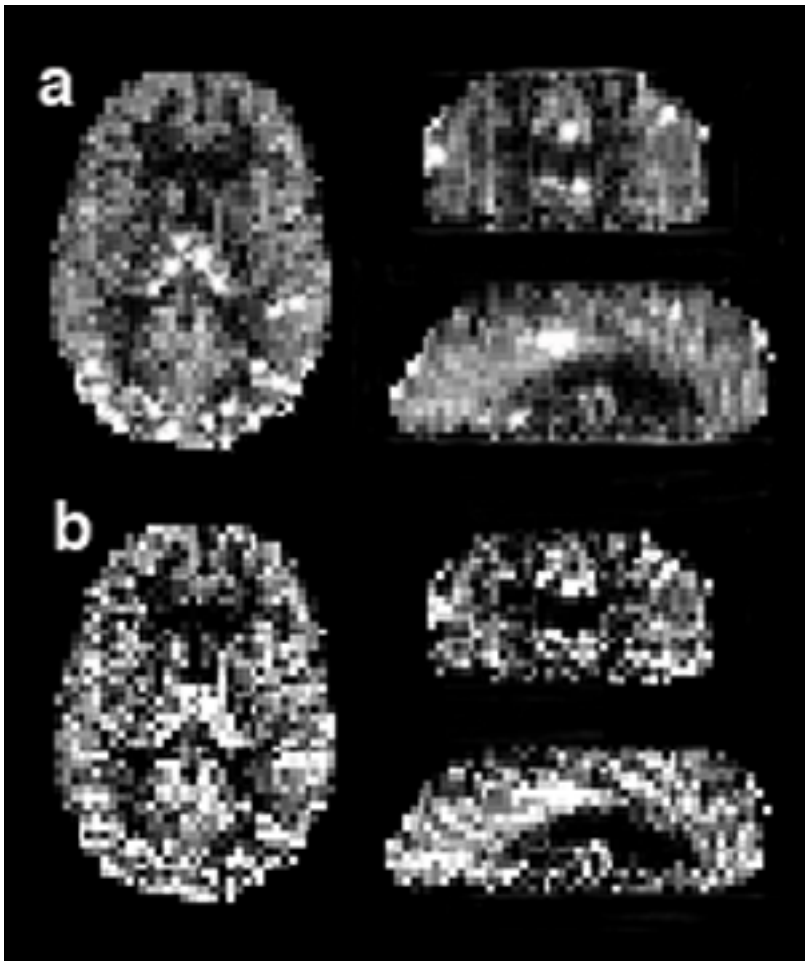


*Figure 7.13: Axial, sagittal and coronal slices from a representative CBF map for (a) original CBF map (b) deblurred CBF map. Richardson-Lucy algorithm used to deblur with 25 iterations.*

| Data | Mean CBF |
|---|---|
| Blurred CBF | $36.6 \pm 21.9$ |
| Deblurred CBF | $36.9 \pm 31.4$ |

*Table 7.2: Mean CBF and S.D. of blurred and deblurred data, measured in ml/100g/min.*

### 7.4.4 Effect of Deblurring and PVC by Linear Regression

PV correction by linear regression using a 3D kernel was performed on both the CBF map and the deblurred CBF map. Mean GM and WM CBF were calculated after removal of

voxels with PV fractions less than 0.1. The results are shown in table 7.3 for the Freesurfer parcellations defined in section 4.4.1.

| | | Mean CBF ± S.D. (ml/100g/min) | |
|---|---|---|---|
| ROI | No voxels in ROI | No deblurring | With deblurring |
| Frontal | 2381 | 54.5 ± 17.1 | 57.0 ± 20.4 |
| Central | 630 | 63.0 ± 16.2 | 66.3 ± 20.1 |
| Parietal | 1683 | 65.2 ± 15.2 | 69.3 ± 19.9 |
| Temporal | 1423 | 57.0 ± 15.7 | 60.5 ± 19.5 |
| Occipital | 704 | 64.8 ± 19.1 | 69.7 ± 24.4 |
| Cingulate | 347 | 60.7 ± 11.5 | 66.2 ± 14.5 |
| Insula | 251 | 48.0 ± 10.9 | 51.8 ± 13.7 |
| Deep GM | 800 | 43.3 ± 21.4 | 49.1 ± 28.3 |
| Hippocampus | 139 | 43.2 ± 24.4 | 52.8 ± 32.4 |
| WM | 9893 | 21.8 ± 9.2 | 19.3 ± 10.1 |

*Table 7.3: Comparison between mean GM an WM CBF after PV correction, with and without deblurring. Difference between blurred and deblurred data signifcant for both GM and WM, Wilcoxon signed rank test p = 0.039. Masked at PVF > 0.1.*

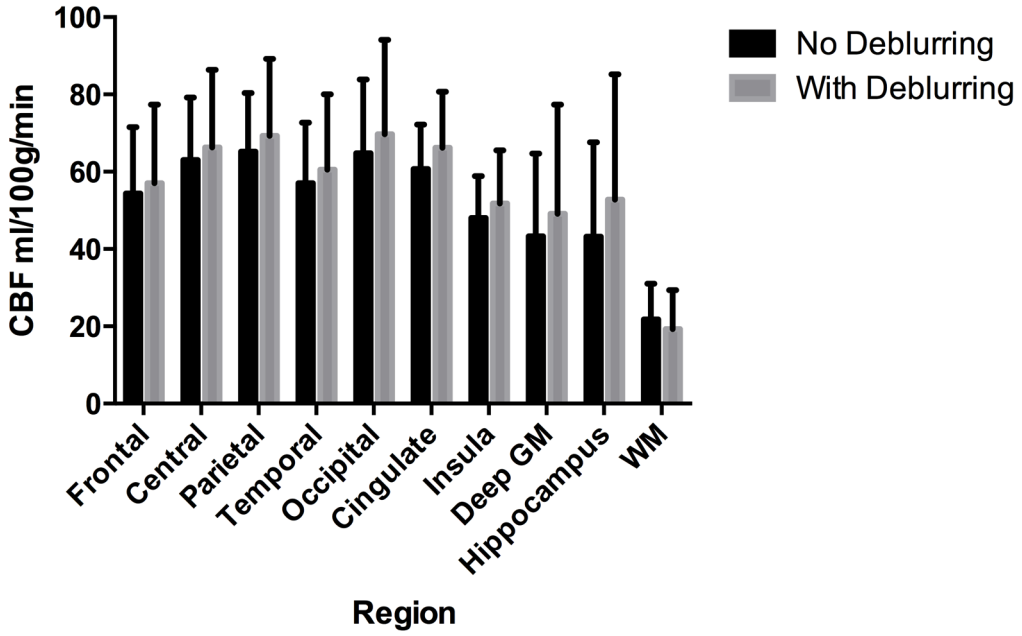


*Figure 7.14: Mean GM CBF in each of the nine GM regions and mean of WM region. Error bars show standard deviation. GM is increased in every region and overal WM decreases with the incorporation of deblurring to the PV correction technique.*

For the CBF map without deblurring, after PVC, the mean GM across all regions was 54.4 ± 17.1 ml/100g/min and WM was 21.8 ± 9.2 ml/100g/min. The deblurred CBF produced a mean GM of 58.8 ± 21.7 and a WM of 19.3 ± 10.1 ml/100g/min after PVC.

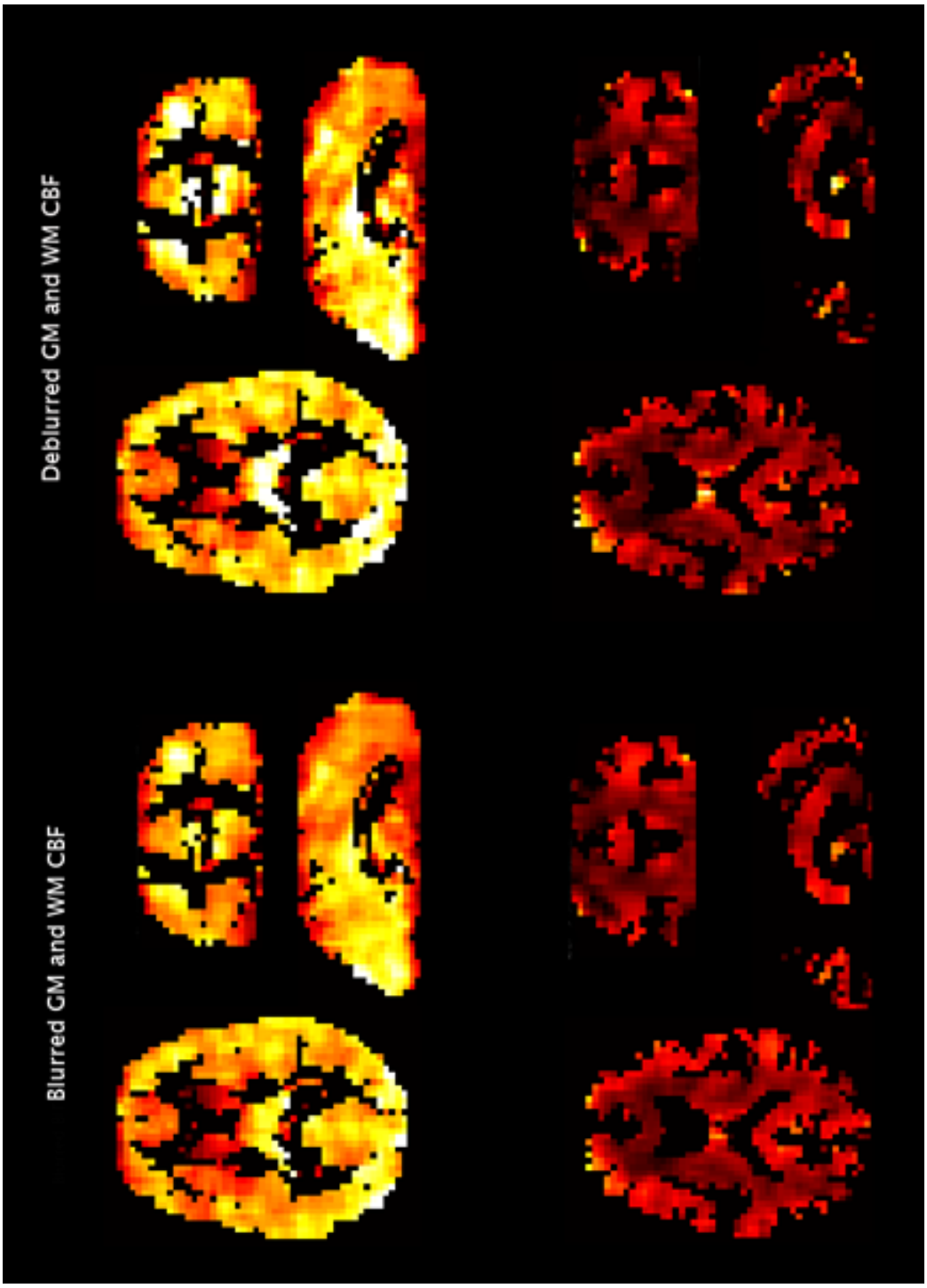


*Figure 7.15: Partial volume corrected GM and WM CBF results for one subject. Deblurred group has had deblurring procedure applied prior to PV correction. Greater CBF values are observed in the deep GM with the application of deblurring.*

Although all GM structures exhibit an increase in perfusion with the inclusion of deblurring, the cingulate and hippocampus show marked increases in perfusion when deblurring is applied. Respectively, the hippocampus and cingulate show a 22% and 9% increase in perfusion. The increased perfusion in the deep GM structures is visible in the deblurred GM CBF images in figure 7.15.

As predicted, WM CBF decreased with deblurring procedures, although the effect is not as dramatic as for GM. This is unsurprising, as the WM is a comparatively large structure and suffers less attenuation as a result. Deblurring causes a consistent increase in the standard deviation of the CBF measurement, suggesting that the deblurring procedure is introducing some noise.

A Wilcoxon signed rank test found the difference to be signicant between the regions with and without deblurring, $p = 0.039$.

## 7.5 Discussion

The hypothesis that blurring due to the PSF contributes to the PVE is based on the assumption that blurring displaces GM and WM signals, causing increased signal mixing. This phenomenon is responsible for suppressing GM and elevating WM CBF values, over and above that which is corrected for as part of the PV correction for tissue fraction. The PV fraction maps obtained from anatomical data carry no information about blurring and are unable to account for it. As such, the expectation is that higher GM and lower WM flow values will be obtained with the inclusion of deblurring as part of the total PV correction method.

This investigation characterised the 1D PSF for an eight shot 3D GRASE acquisition, for the particular sequence parameters used. It is important to recognise that the width of the PSF is a direct consequence of how the echo amplitude decays across k-space. This is influenced by the resolution along all axes, the acquisition bandwidth, and RF pulse duration, to name a few factors. This is the reason that the PSF can differ for sequences,

even using the same number of shots.

The simulation study showed that the Richardson-Lucy deconvolution algorithm is effective at removing signal blurring due to the PSF, although this is sensitive to correct characterisation of the PSF. The simulated data was blurred and deblurred using the same PSF, when in practice, the estimated PSF for a sequence will always be an approximation. This is a potential source of error.

The use of a multi-shot acquisition does reduce the amount of blurring in the partition direction, although we have shown that it is still present and contributing to partial volume effects. For the sequence used here, the FWHM of the PSF was 1.3 voxels, or 4.9 mm, given the resolution of the voxels. This means that the signal from an individual voxel is contributing to the signal in the voxels around it - the blurring due to the PSF is larger than the voxel size of 3.8 mm in the partition direction.

Deblurring the perfusion map prior to PV correction resulted in a mean GM CBF of 60.7 ml/100g/min, compared to 53.4 ml/100g/min when PV correction is performed without deblurring. This suggests that correcting for the tissue fraction effect alone still leads to an underestimation in GM perfusion levels and an overestimation of WM CBF levels. As expected, a decrease in mean WM CBF level was observed, from 21.8 $\pm$ 9.2 to 19.3 $\pm$ 10.1 ml/100g/min. This is not as dramatic as the change in GM CBF, as the WM as a whole is less affected by blurring as it is a much larger region than the GM parcellations. However, an overestimation is still present.

A limitation of this technique is that it is heavily dependent on the correct characterisation of the PSF. It may be possible to estimate the PSF based on the autocorrelation of the residuals from fitting to the general kinetic equation, although this requires more than one measurement. The EPG algorithm is an alternative method used to estimate the PSF, which requires knowledge of the T1 and T2 values of the tissue. Literature values were used for the T1 and T2 of arterial blood and subsequent PSF estimation. The effective relaxation times are known to vary according to the specific sequence used [77], which may affect accuracy of the PSF estimate.

Additionally, the deblurring technique introduces noise into the image, as manifest by an increase in the S.D. for all the ROIs after deblurring. This means that the deblurring technique makes GM and WM flow estimates more accurate, but potentially more noisy. However, this potential problem can be ameliorated by smoothing of the separate GM and WM maps to increase SNR, should it be required.

## 7.6 Conclusion

In order to fully correct for partial volume effects in ASL perfusion imaging using 3D GRASE acquisitions, it is both appropriate and relatively straightforwards to include a deblurring step as part of a complete partial volume correction strategy.

Either Hennig's EPG algorithm or Chappell's autocorrelation of residuals method can be employed for estimation of the 1D PSF in the partition direction. Once characterised, the PSF can be deconvolved from the data, which has the effect of returning GM and WM signal to the appropriate part of the image volume.

PVC performed on deblurred data is more meaningful, as the correction for tissue fraction provided by linear regression using anatomical information is more likely to be accurate. In other words, the spatial location of the perfusion levels corresponds more readily to the anatomical structures causing the perfusion signal to arise, after deblurring. This is manifest by the increase in GM and reduction in WM CBF levels seen with the inclusion of the additional processing step in the form of deconvolution of the PSF.

In conclusion, this chapter has extended the PV correction technique using linear regression for ASL data which only corrects for tissue fraction effect to include the additional pre-processing step of deblurring via deconvolution of the PSF.

# Chapter 8

# Application of PVC to dementia data

This chapter describes the application of the methods developed in earlier chapters as a novel complete solution fo PVC. The method is applied to two challenging, clinical cohorts.

## 8.1 Imaging in neurodegenerative disease

Neurodegenerative disease is typified by progressive dysfunction and neuronal loss and represents a major clinical challenge. The risk of suffering from dementia usually increases with age. In addition, there is a certain degree of neuronal loss associated with 'healthy ageing'. In fact, longitudinal studies show cerebral atrophy rates of 0.5% volume reduction per year in the 65-75 years age group. Rates of volume loss in Alzheimer's Disease (AD) patients is around 2% per year [78].

The cause of the two types of atrophy may be quite different, but in the early stages of disease it is remarkably difficult to differentiate between the two and sophisticated image processing techniques tend to be employed [79].

As well as loss of neuronal tissue, some types of dementia also produce an accumulation of proteins known as amyloid-$\beta$ plaques and neurofibrillary tangles (NFTs). However, these lesions tend not to be readily visible on examination of structural MR images by radiologists. Consequently, structural MRI has limited diagnostic value in detecting

neurodegeneration in its early stages.

A pan-European task force was initiated in 2008 with the goal of arriving at a consensus for a recommended protocol for the diagnosis and management primarily of AD [80]. This committee was concerned with revising previous European Federation of Neurological Societies (EFNS) guidelines with a specific consideration in mind. The question being addressed was, is there new evidence that imaging biomarkers derived from MRI and PET modalities can increase confidence in the clinical diagnosis?

The conclusions reached by the group was that structural imaging should be performed at least once in order to exclude other non-AD pathologies, which may be treatable. However, whilst MRI may be useful to monitor changes over time, it is fluorodeoxy-glucose- (FDG-) PET and single positron emission tomography (SPECT) imaging that have been nominated as imaging modalities most likely to increase confidence in diagnosing dementia.

These imaging modalities are invasive and expensive, and therefore not readily applicable to control populations. However, if new disease modifying treatments are to be the subject of clinical trials, repeatable, cost-effective and non-invasive imaging techniques will be required. If such techniques were available, they could also be employed to screen healthy populations in order to detect pathological changes in pre-symptomatic subjects.

As described in chapter 2, it is the stated aim of the European Cooperation in Science and Technology (eCOST) Arterial Spin Labelling in Dementia (AID) [1] to coordinate 'the development of an alternative and cost-effective tool based on an MRI technique, Arterial Spin Labelling (ASL), to obtain reproducible brain perfusion measurements in dementia patients'. The hope is to replace nuclear medicine techniques as the gold standard for imaging and staging of dementia.

[1] http://www.aslindementia.org

### 8.1.1 ASL as an early stage biomarker of dementia

The coupling of CBF and brain metabolism facilitate the use of brain perfusion as a quantitative biomarker of function. As such, there is great interest in the use of perfusion measurements in the diagnosis and staging of neurodegenerative disease.

There is a large body of work demonstrating the variations in perfusion due to neurodegenerative disease using FDG-PET and SPECT imaging to detect changes in glucose metabolism and perfusion [81]. There is consensus in the literature that functional impairment occurs before advanced neuronal loss, which means that perfusion imaging may potentially detect neurodegeneration before tissue loss has occurred [21]. This would enable identification of patients at risk at an early stage of the disease, paving the way for therapeutic intervention. Moreover, most neurodegenerative diseases exhibit a characteristic pattern of modified perfusion, allowing for a differential diagnosis.

A description of two types of dementia and their signature patterns of perfusion follows. These two are selected for discussion as clinical data from patients populations with these dementias is utilised in this chapter.

#### 8.1.1.1 Alzheimer's Disease

Alzheimer's Disease (AD) is associated with progressive cognitive impairment and is the most common form of dementia, affecting 1 in 5 over the age of 80 and costs the UK £26.3 billion a year [2]. With an ageing global population, the impact of this disease will only increase. There is no effective treatment for AD and it is thought that when patients manifest clinical symptoms, substantial neuronal damage has already occurred [82]. Therefore it is of vital importance that early biomarkers of the disease are developed.

There are a number of studies which have investigated the patterns of brain perfusion in AD and an overview of these is presented in [83]. These studies report a characteristic profile of hypoperfusion which is supported by findings in PET and SPECT studies. This

[2] http://www.alzheimers.org.uk/

pattern consists of hypoperfusion in the parietal, temporal and posterior cingulate cortices. It is also found that the extent of the hypoperfusion is correlated with severity of AD symptoms, which offers evidence that ASL can be used to stage the disease.

It was initially a concern that the pattern of hypoperfusion was in fact merely a consequence of cortical atrophy, which AD is tightly associated with. However, this concern was laid to a rest by a study which corrected for atrophy [53] and found that the same regions of hypoperfusion existed post-correction. Indeed, an important finding was that the extent of regional hypoperfusion was unaltered by atrophy correction, demonstrating a decoupling of structure and function in AD.

#### 8.1.1.2 Frontal Temporal Dementia

Frontal temporal dementia (FTD) is a comparatively rare form of early onset dementia, primarily affecting those in the 45 to 65 years age bracket, although it can also occur earlier or later in life. This can be decades earlier than the onset of sporadic AD and these patients typical present with behavioral problems as the frontal lobe is implicated.

Differential diagnosis between AD and FTD can be difficult to achieve purely on a clinical basis as aspects of FTD can mimic AD, in particular memory impairment. Structural MRI can highlight the differing patterns of atrophy, but as the disease progresses and atrophy encompasses more of the brain, it is difficult to distinguish between the two. Conversely, studies measuring perfusion using PET, SPECT and ASL have shown that the differential diagnosis between FTD and AD is improved as compared to structural MRI alone [21].

The characteristic profile of abnormal perfusion in FTD patients is that of hypoperfusion in the right superior and middle frontal gyri, with normal perfusion levels in parietal and occipital lobes. Again, this pattern is preserved after atrophy correction and correlates well with the observed functional deficits such as poor judgement and problem solving. In some cases, the differing patterns of abnormal perfusion between FTD and AD can be more readily visualised in perfusion images, rather than structural scans, as depicted in figure 8.1 [19].

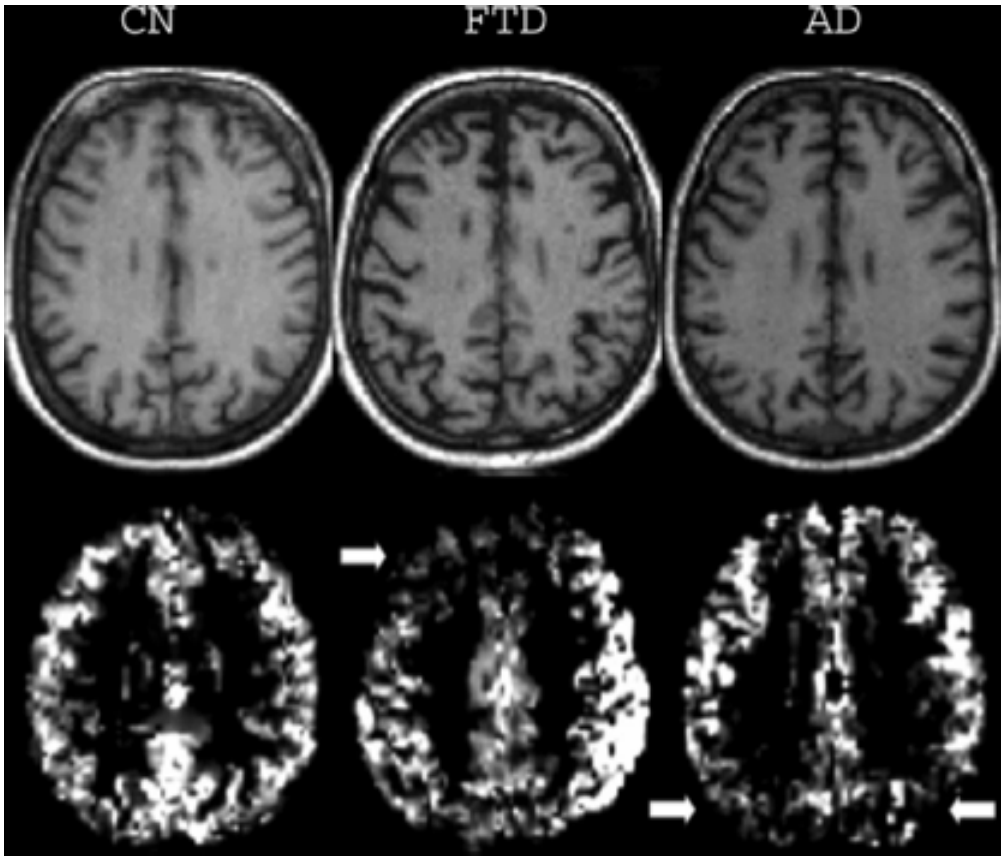


*Figure 8.1: Representative structural and ASL images for a cognitive normal subject (CN), FTD and AD patient. There is an area of reduced perfusion in the frontal lobe for the FTD patient, compared to reduced perfusion in the posterior brain region for the AD patient (marked with arrows). This can facilitate a differential diagnosis. From [19].*

## 8.2 Clinical cohort

All of the previous studies in this thesis have utilised the data of healthy controls. This data came from young people without any evidence of tissue atrophy or perfusion abnormalities. Patient cohorts which exhibit cortical atrophy are more likely to benefit from an improvement in the accuracy of perfusion estimates after PV correction, yet are also more challenging to apply the techniques to, as segmentation algorithms are largely developed for healthy brains. In addition, these patients are less likely to tolerate the scanning procedure in itself particularly well, and are more likely to produce motion artefacts.

Therefore, this chapter tests the methodologies developed throughout this thesis to two

clinical populations, each displaying differing patterns of cortical atrophy. These two groups are referred to as the *GENFI* and *AVID* cohorts.

### 8.2.1 GENFI

GENFI is an acronym for *Genetic Frontal Temporal Dementia Initiative*[3]. Patients from the GENFI cohort are being studied with a view to understanding more about genetic FTD, particularly subjects with mutations in the progranulin (GRN), microtubule-associated protein tau (MAPT) and chromosome 9 open reading frame 72 (C9ORF72) genes. FTD is a strongly inherited disease, with a third of sufferers exhibiting a mutation in one of the three genes above. Previous studies on other genetic dementias were able to show imaging changes before symptom onset; the GENFI study aims to do the same for FTD [84, 85].

The participants to the study were either known carriers of the one of the three gene mutations or possessed a first degree relative who was a known symptomatic carrier.

We have been fortunate enough to be given access to some of this data, although this is a blinded study and the only clinical information known about the patients is their sex. We do not know whether the subjects are symptomatic, or even at risk for FTD. Nonetheless, cortical atrophy is readily apparent in some of the data provided, and as such provides a challenging dataset to apply the PVC techniques developed throughout this thesis.

### 8.2.2 AVID

The AVID data [4] comes from a group of patients who has been diagnosed as suffering from Posterior Cortical Atrophy (PCA). This is a progressive condition in which there is notable tissue loss from posterior regions of the brain and the most common symptom for individuals suffering from PCA is a selective deterioration in higher visual processing and other posterior cortical functions, such as spelling and calculation [20]. PCA is frequently

[3] http://genfi.org.uk

[4] http://www.ucl.ac.uk/drc/research/current-studies/pca

considered to be a variant of AD due to the histopathological finding of amyloid plaques and tau tangles, despite the disparity in which regions display cortical atrophy.

The AVID cohort is involved in a longitudinal study to improve diagnosis and charaterisation of PCA, with a particular focus on visual processing. The aim of the study is to understand what causes this variation on classical Alzheimer's Disease, and to develop strategies which may help to alleviate symptoms. Figure 8.2 shows a structural and FDG-PET scan from a patient suffering from PCA. Note the reduced metabolism in the posterior of the brain on the PET scan and cortical atrophy in the structural scan, and how it differs from the classical presentation of AD.

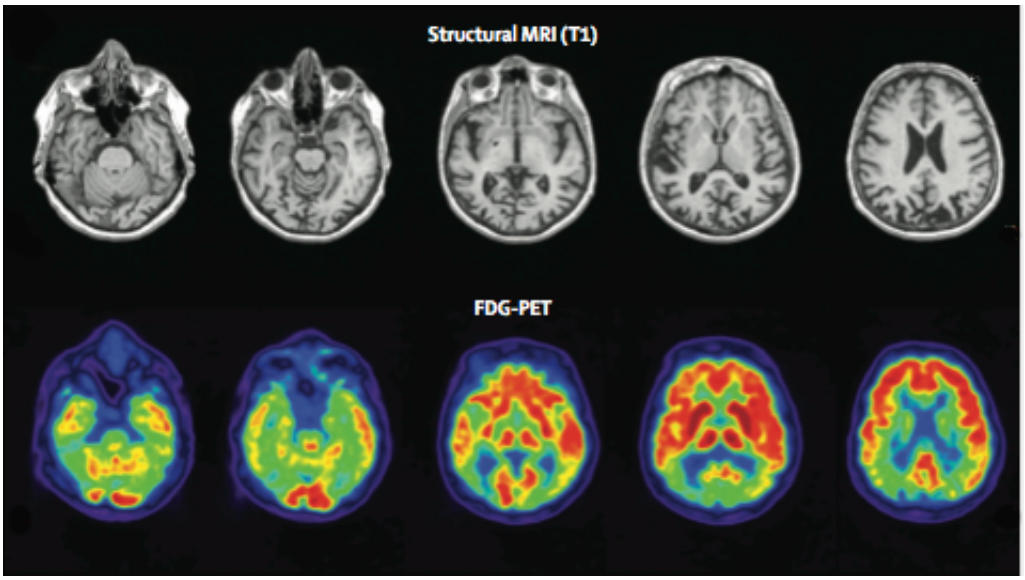


*Figure 8.2: Structural and FDG-PET scan from a PCA patient. Note the presentation of posterior cortical atrophy in the structural scan, and reduced posterior metabolism in the FDG-PET scan. Adapted from [20].*

## 8.3 Methods

The imaging acquisition parameters for the GENFI and AVID studies differ slightly from those used for the previously described control subject studies. Perfusion data were acquired using pulsed ASL (FAIR Q2TIPS) with an 8-segment, background-suppressed 3D GRASE imaging readout. The parameters can be seen in table 8.1.

### 8.3.1 GENFI/AVID data acquisition

| Parameter | Value |
|---|---|
| Matrix | 128 x 128 x 30 |
| Resolution | 1.875 x 1.875 x 4.0 $mm^3$ |
| TI1 | 800 ms |
| TI2 | 2000 ms |
| Turbo factor | 23 |
| Segmented acquisition | 8 segments |
| Background Suppression | 754 ms, 1610 ms |
| Saturation recovery pulses | 1000, 2000, 5000 ms |

*Table 8.1: Summary of perfusion imaging parameters*

Unlike the previous perfusion data, the GENFI and AVID data is acquired on a 64 x 64 matrix but zero-filled to produce a 128 x 128 x 30 resolution. The saturation recovery sequence also differs in that the middle saturation pulses of the series is timed at TR = 2000 ms, rather than 3000 ms. Parameters for the anatomical MPRAGE sequence are listed in table 8.2.

| Parameter | Value |
|---|---|
| Acquisition matrix | 208 x 256 x 256 |
| Resolution | 1.1 x 1.1 x 1.1 $mm^3$ |
| TI | 900 ms |
| TR | 2200 ms |
| TE | 2.9 ms |
| Flip angle | 10 ° |

*Table 8.2: Summary of MPRAGE imaging parameters*

### 8.3.2 Partial Volume Correction

CBF maps were calculated from the perfusion data using the general kinetic model as in equation 2.7. Only one measurement of the control and labelled images was provided, so it was not possible to perform any averaging to improve SNR.

Unfortunately the FRASIER/SEPARATE method for generating PV maps could not be employed as only three timepoints were acquired in the saturation recovery sequence.

Therefore the method for generating the PV maps from anatomical data described in chapter 4 was utilised.

A combined deblurring and tissue fraction PV correction algorithm was employed. Firstly, the PSF was estimated using the Extended Phase Graph Algorithm for the sequence parameters used for these studies and found to have a FWHM of 1.5 voxels. This PSF was used in a Richardson-Lucy deconvolution algorithm to remove the blurring, as described in chapter 7. Secondly, the linear regression method for correction of tissue fraction effect using a 3D 3 x 3 x 3 kernel, as described in chapter 5 was applied to the deblurred data.

Cortical parcellations were created using Freesurfer, which were then downsampled to ASL space and overlaid on the GM CBF map. Voxels with less than GM PVF of 10% were excluded, and a mean value for the 9 Freesurfer regions were calculated.

## 8.4 Results

### 8.4.1 GENFI cohort

The GENFI cohort contains FTD patients, and those potentially at risk of genetic FTD because a first degree relative is a carrier. As the study is blinded, the researchers are unaware of the clinical history of the subjects, which means that there may be some subjects who are 'normal'. As such, it does not make sense to perform any sort of group analysis on the GENFI cohort and the subject results must be considered on their own.

The same post-labelling delay is used in the GENFI/AVID studies as was used for the healthy control studies on young people described in chapters 5 and 6. Due to the blinding on the study, the age of the participants is not known. The post-labelling delay is a parameter which should be adjusted with age, with older subjects requiring a longer delay.

It would seem that the delay used was insufficient for some of the GENFI subjects, and

CBF maps were produced like the one shown in figure 8.3. It can be seen that there is little to no signal in the WM area of the brain. The WM transit time is longer than that to the GM, and either the perfusion weighted image was acquired before the labelled protons had reached the imaging volume, or the signal had decayed away. This makes quantification inaccurate, and is a reminder that sequence parameters must be adapted to suit the application.

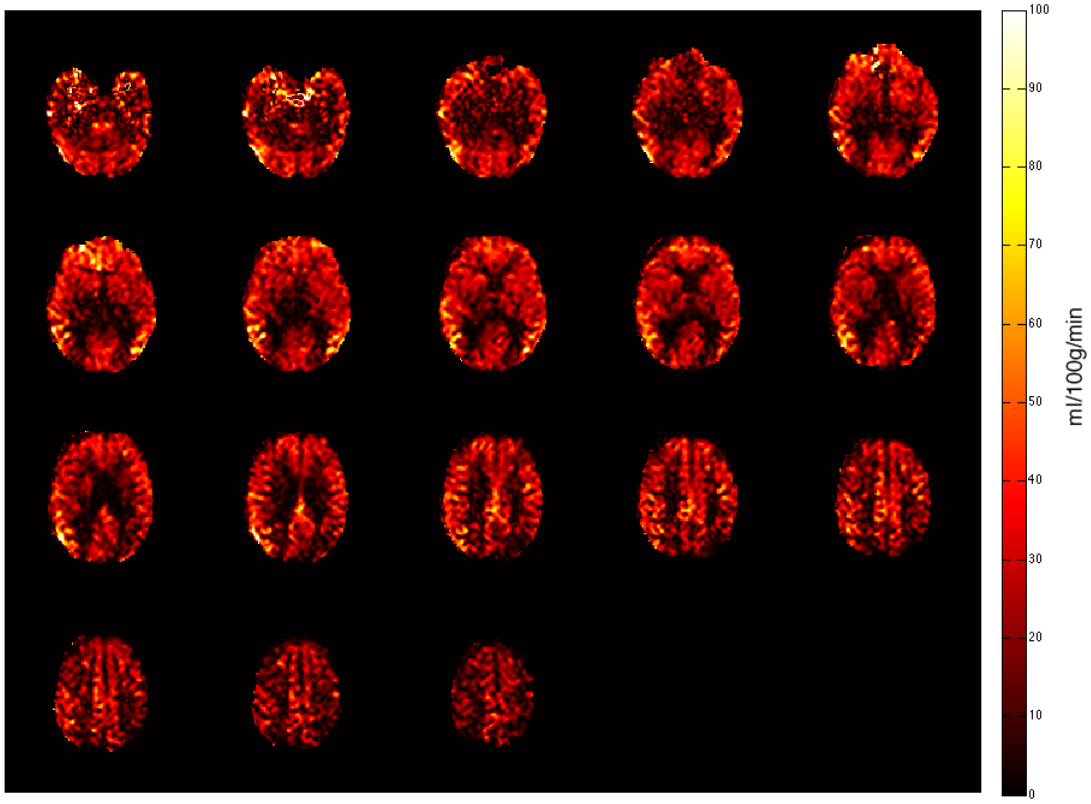


*Figure 8.3: Insufficient post-labelling delay: there is little to no signal in the WM regions. Either the labelled protons have yet to reach the WM, or the signal has decayed before arriving.*

The expectation for the GENFI cohort is that there will be reduced perfusion in the frontal lobe if the subjects are exhibiting FTD. Additionally, it is hypothesised that this pattern will remain after PVC, and that there is a genuine reduction in metabolism, which is not merely a consequence of tissue atrophy.

Figure 8.6 shows the mean CBF and GM CBF after PVC on a regional basis for the six GENFI subjects. Of the six, two subjects stand out from the group. Subjects 01-006 and 01-010 display reduced perfusion in the frontal lobe, relative to the other regions. This

pattern remains after PV correction for both subjects. For subject 01-006 PV correction elevates the CBF in the central lobe most of all, followed by the parietal lobe. This suggests there may be age-related atrophy in these regions and the low perfusion pre-correction is not a genuine metabolic finding. For subject 01-010, overall perfusion is high, with mean regional GM CBF values like those found in healthy subjects (range 56 to 73 ml/100g/min), other than for the frontal lobe, which is 33.3 ml/100g/min before correction and 42.2 ml/100g/min after. (See figure 8.5).

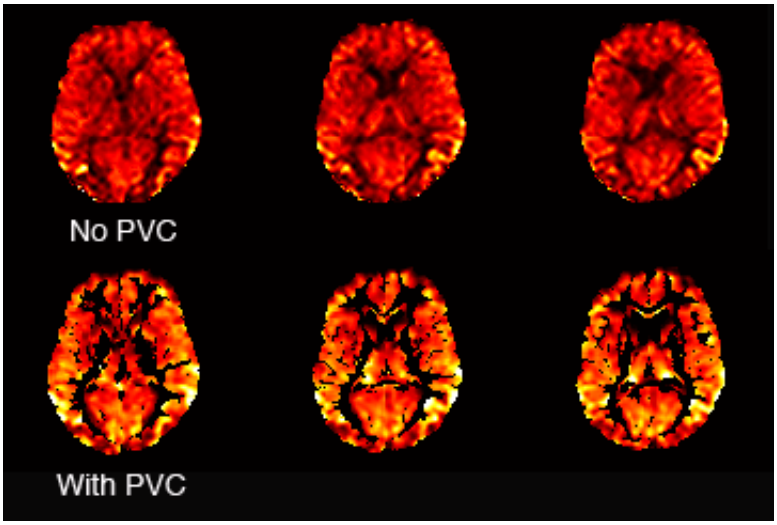


*Figure 8.4: Subject 01-006, top row: CBF prior to PV correction, bottom row, after PV correction. PVC correction elevates perfusion in parietal and central lobes, but no increase is seen in the frontal lobe. GM CBF masked at GM PVF > 0.1.*

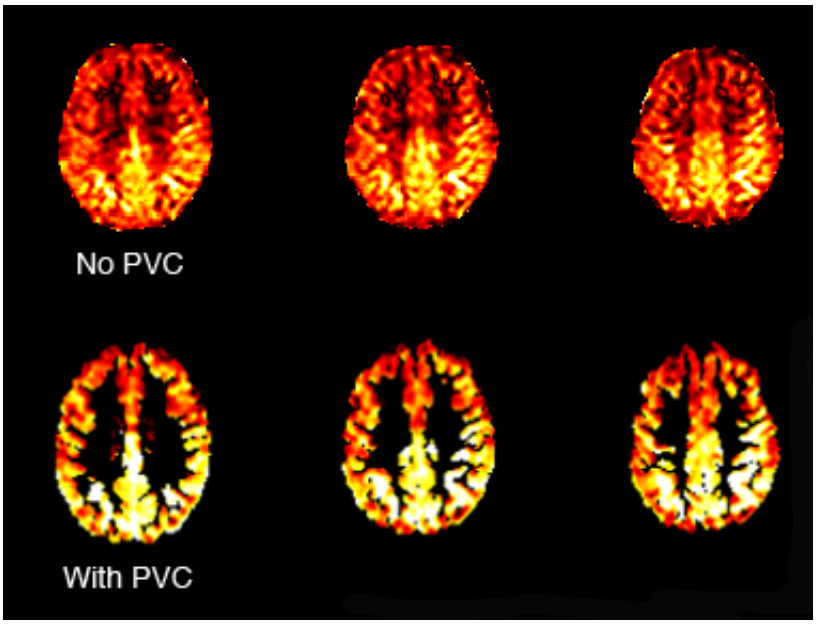


*Figure 8.5: Subject 01-010, top row: CBF prior to PV correction, bottom row, after PV correction. Reduced CBF is seen in the frontal lobe both before and after PV correction. GM CBF masked at GM PVF > 0.1.*

The deep GM and hippocampal regions also showed low perfusion for these subjects, before and after correction. The mean hippocampal GM CBF was 21.3 and 24.4 ml/100g/min before correction and 27.6 ml/100g/min for both subjects after correction, for subjects 01-006 and 01-010 respectively. Both sets of values are incredibly low for GM perfusion which tends to be around 60 ml/100g/min for young healthy subjects. The hippocampal region is small and only contains around 150 voxels, and it is tempting to explain these low results as being unreliable due to the small number of voxels. However, subjects 01-004, 01-009 and 01-019 present with GM perfusion values towards the expected range. These 3 subjects display mean regional GM values like those previously presented for healthy controls. All values are summarised in figure 8.6 and table 8.3.

Subject 01-011 differs from the others, in that there is a consistently low perfusion across all regions prior to PV correction with perfusion around 30 ml/100g/min (other than the hippocampus which is 15.9). The PV correction has a huge effect on the initial perfusion values, with the ratio of corrected to uncorrected perfusion ranging from 1.9 (frontal lobe) to 1.5 (hippocampus). This suggests that the low uncorrected perfusion values are a direct

consequence of tissue atrophy, and post-correction brings this values to a more usual physiological range. This concurs with a PET study carried out by Meltzer et al [43] where it is proposed that the usual reduction in CBF seen in elderly populations is a consequence of tissue atrophy, and that after correction no reduction is seen.

### 8.4.2 AVID cohort

As the AVID subjects are all diagnosed as PCA patients, we expect to see similar patterns of perfusion across the group. Given the PET finding displayed in figure 8.2, the expectation is that we will see reduced perfusion in the occipital lobe, which remains after atrophy correction. Figure 8.9 shows the mean regional CBF and GM CBF for the AVID subjects, which is also given in table 8.4.

In fact, there is only one subject for which the mean occipital lobe perfusion is markedly reduced compared to the other regions, that is subject AV-003, with mean GM CBF 42.7 ml/100g/min in the occipital lobe. Figure 8.7 shows 3 slices from the both the CBF and GM CBF maps. Both maps shows substantial bilateral regions of reduced perfusion in the occipital lobe. Subject AV-004 displays the same pattern of reduced perfusion in the frontal lobes compared to the other regions as the GENFI subjects 01-006 and 01-010. Subject AV-002 displays a mean occipital lobe CBF of 30.7 ml/100g/min before correction and GM CBF of 47.2 ml/100g/min, with a correction ratio of 1.5, compared to ratios of 1.2 - 1.3 for the other regions. This suggests that there is occipital lobe atrophy, but not reduced perfusion. Subjects AV-001, AV-005 and AV-006 show mean occipital lobe GM CBF of 64.8, 54.0 and 59.8 ml/100g/min respectively, which is within healthy parameters.

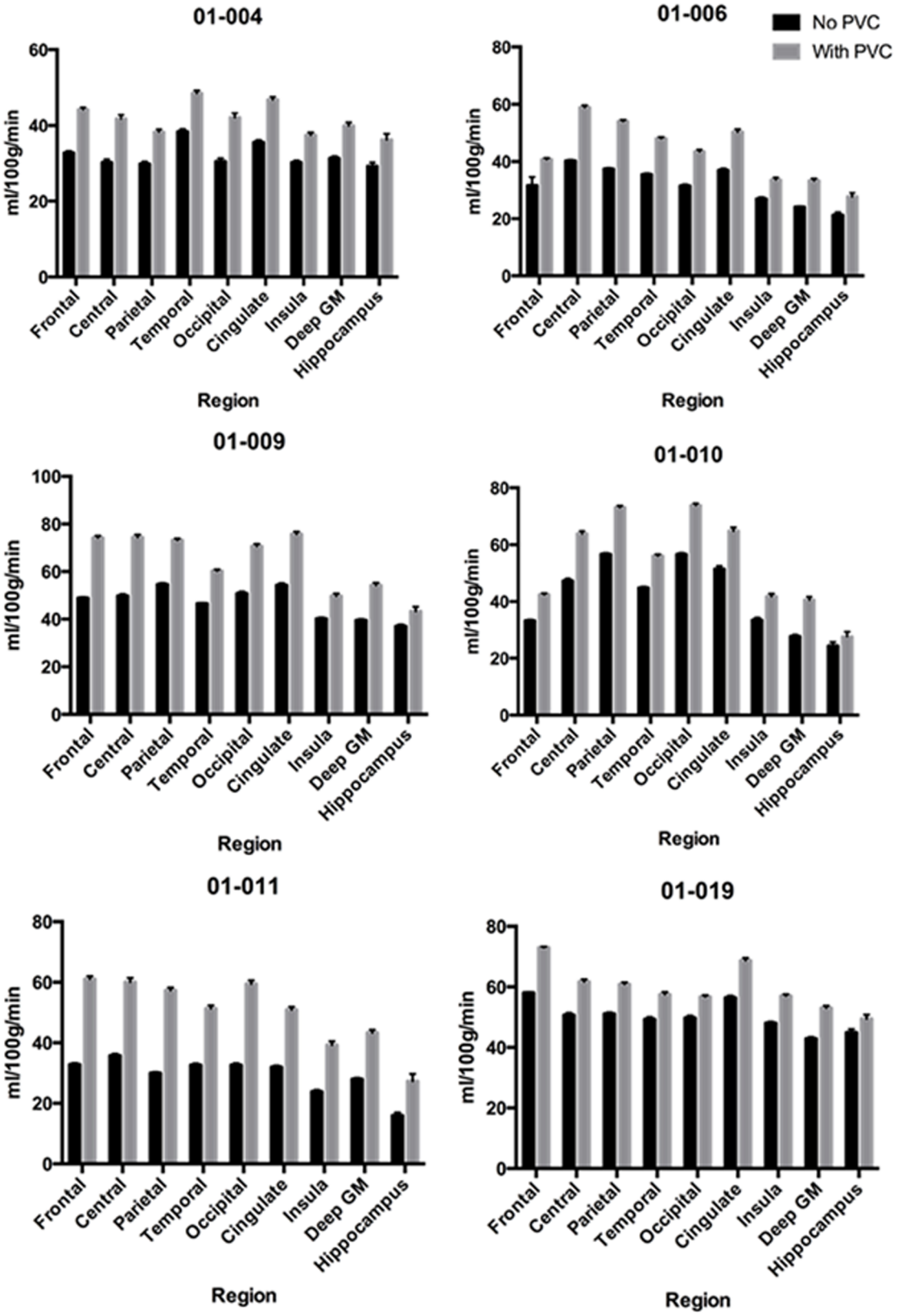


*Figure 8.6: GENFI cohort: GM regions before and after PV correction using a combined deblurring and tissue fraction effect algorithm. Ratio column shows ratio of corrected to uncorrected. All CBF measurements in ml/100g/min, error bars show 95% confidence intervals.*

| | 01-006 | | | 01-004 | | | 01-009 | | | 01-010 | | | 01-011 | | | 01-019 | | |
|---|---|---|---|---|---|---|---|---|---|---|---|---|---|---|---|---|---|---|
| Region | CBF | After PVC | Ratio | CBF | After PVC | Ratio | CBF | After PVC | Ratio | CBF | After PVC | Ratio | CBF | After PVC | Ratio | CBF | After PVC | Ratio |
| Frontal | 31.6 ± 0.3 | 40.8 ± 0.4 | 1.3 | 32.8 ± 0.4 | 44.2 ± 0.6 | 1.3 | 48.9 ± 0.4 | 74.2 ± 0.8 | 1.5 | 33.3 ± 0.4 | 42.4 ± 0.5 | 1.3 | 32.8 ± 0.4 | 61.0 ± 1.0 | 1.9 | 58.0 ± 0.3 | 73.0 ± 0.3 | 1.3 |
| Central | 40.2 ± 0.4 | 58.9 ± 0.7 | 1.5 | 30.3 ± 0.8 | 41.7 ± 1.1 | 1.4 | 49.8 ± 0.7 | 74.4 ± 1.1 | 1.5 | 47.3 ± 0.8 | 63.9 ± 0.9 | 1.4 | 35.7 ± 0.6 | 60.0 ± 1.4 | 1.7 | 50.7 ± 0.7 | 61.7 ± 0.8 | 1.2 |
| Parietal | 37.4 ± 0.4 | 54.0 ± 0.5 | 1.4 | 29.9 ± 0.6 | 38.3 ± 0.7 | 1.3 | 54.6 ± 0.6 | 73.2 ± 0.7 | 1.3 | 56.6 ± 0.5 | 73.1 ± 0.6 | 1.3 | 29.9 ± 0.4 | 57.3 ± 0.9 | 1.9 | 51.1 ± 0.5 | 60.9 ± 0.6 | 1.2 |
| Temporal | 35.4 ± 0.4 | 48.1 ± 0.5 | 1.4 | 38.4 ± 0.7 | 48.5 ± 0.8 | 1.3 | 46.5 ± 0.4 | 60.3 ± 0.6 | 1.3 | 44.8 ± 0.5 | 56.0 ± 0.6 | 1.3 | 32.6 ± 0.5 | 51.3 ± 1.1 | 1.6 | 49.3 ± 0.7 | 56.8 ± 0.4 | 1.2 |
| Occipital | 31.5 ± 0.5 | 43.4 ± 0.7 | 1.4 | 30.5 ± 0.9 | 42.1 ± 1.2 | 1.4 | 50.8 ± 0.8 | 70.6 ± 1.0 | 1.4 | 56.6 ± 0.6 | 73.8 ± 0.7 | 1.3 | 32.6 ± 0.6 | 59.4 ± 1.2 | 1.8 | 49.8 ± 0.7 | 57.5 ± 0.8 | 1.2 |
| Cingulate | 36.9 ± 0.7 | 50.3 ± 1.0 | 1.4 | 35.6 ± 0.6 | 46.8 ± 0.8 | 1.3 | 54.3 ± 0.8 | 75.7 ± 1.1 | 1.4 | 51.5 ± 1.1 | 64.8 ± 1.3 | 1.3 | 31.9 ± 0.5 | 50.9 ± 1.0 | 1.8 | 56.4 ± 0.7 | 68.7 ± 0.9 | 1.2 |
| Insula | 26.9 ± 0.6 | 33.6 ± 0.8 | 1.2 | 30.3 ± 0.5 | 37.4 ± 0.7 | 1.2 | 40.2 ± 0.5 | 49.7 ± 1.1 | 1.2 | 33.6 ± 0.8 | 41.8 ± 1.0 | 1.2 | 23.8 ± 0.6 | 39.2 ± 1.3 | 1.6 | 48.0 ± 0.5 | 57.0 ± 0.6 | 1.2 |
| Deep GM | 24.1 ± 0.3 | 33.3 ± 0.7 | 1.4 | 31.4 ± 0.5 | 39.9 ± 0.9 | 1.3 | 39.5 ± 0.5 | 54.2 ± 1.1 | 1.4 | 27.8 ± 0.6 | 40.6 ± 1.1 | 1.5 | 27.9 ± 0.5 | 43.3 ± 1.0 | 1.6 | 42.9 ± 0.5 | 53.0 ± 0.8 | 1.2 |
| Hippocampus | 21.3 ± 1.0 | 27.6 ± 1.4 | 1.3 | 29.3 ± 1.0 | 36.2 ± 1.6 | 1.2 | 37.0 ± 0.8 | 43.3 ± 1.9 | 1.2 | 24.4 ± 1.3 | 27.6 ± 1.8 | 1.1 | 15.9 ± 1.0 | 27.3 ± 2.4 | 1.7 | 44.9 ± 1.1 | 49.4 ± 1.4 | 1.1 |

*Table 8.3: GENFI cohort: GM regions before and after PV correction using a combined deblurring and tissue fraction effect algorithm. Ratio column shows ratio of corrected to uncorrected. All CBF measurements in ml/100g/min with 95% confidence intervals.*

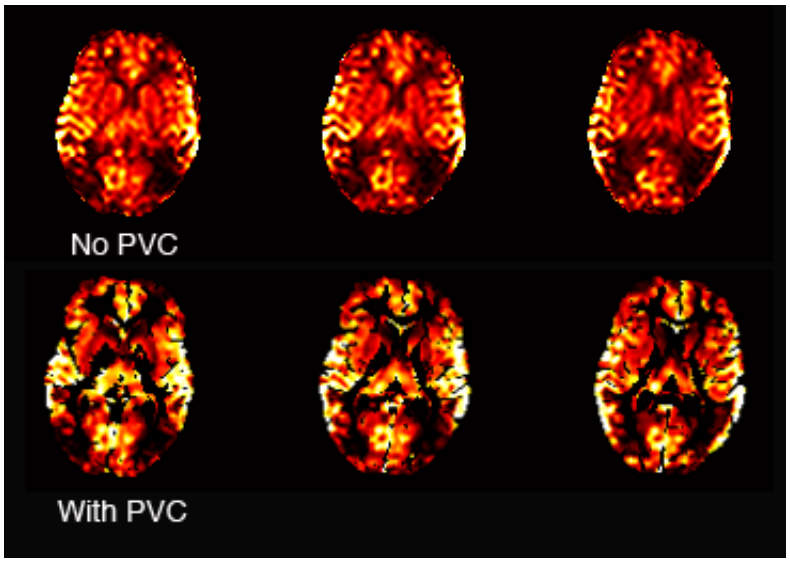


*Figure 8.7: Subject AV-003, top row: CBF prior to PV correction, bottom row, after PV correction. There is substantial reduced perfusion in the occipital lobe which persists after PV correction. GM CBF masked at GM PVF > 0.1.*

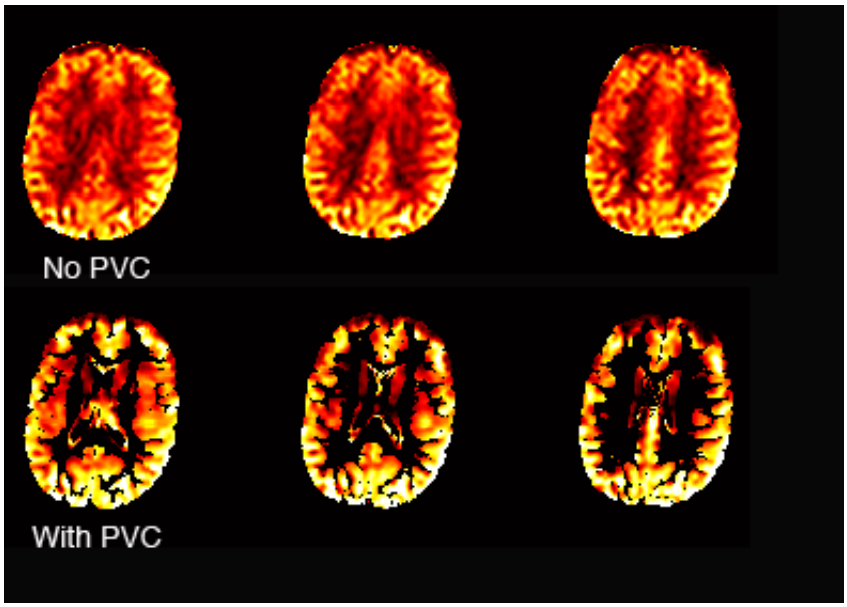


*Figure 8.8: Subject AV-004, top row: CBF prior to PV correction, bottom row, after PV correction. There is reduced perfusion in the frontal lobe compared to other regions, both before and after PVC. GM CBF masked at GM PVF > 0.1.*

## 8.5 Discussion

This is the first study to apply a combined deblurring and tissue fraction correction for PV correction of ASL data to patients groups suffering from dementia. Two separate patient

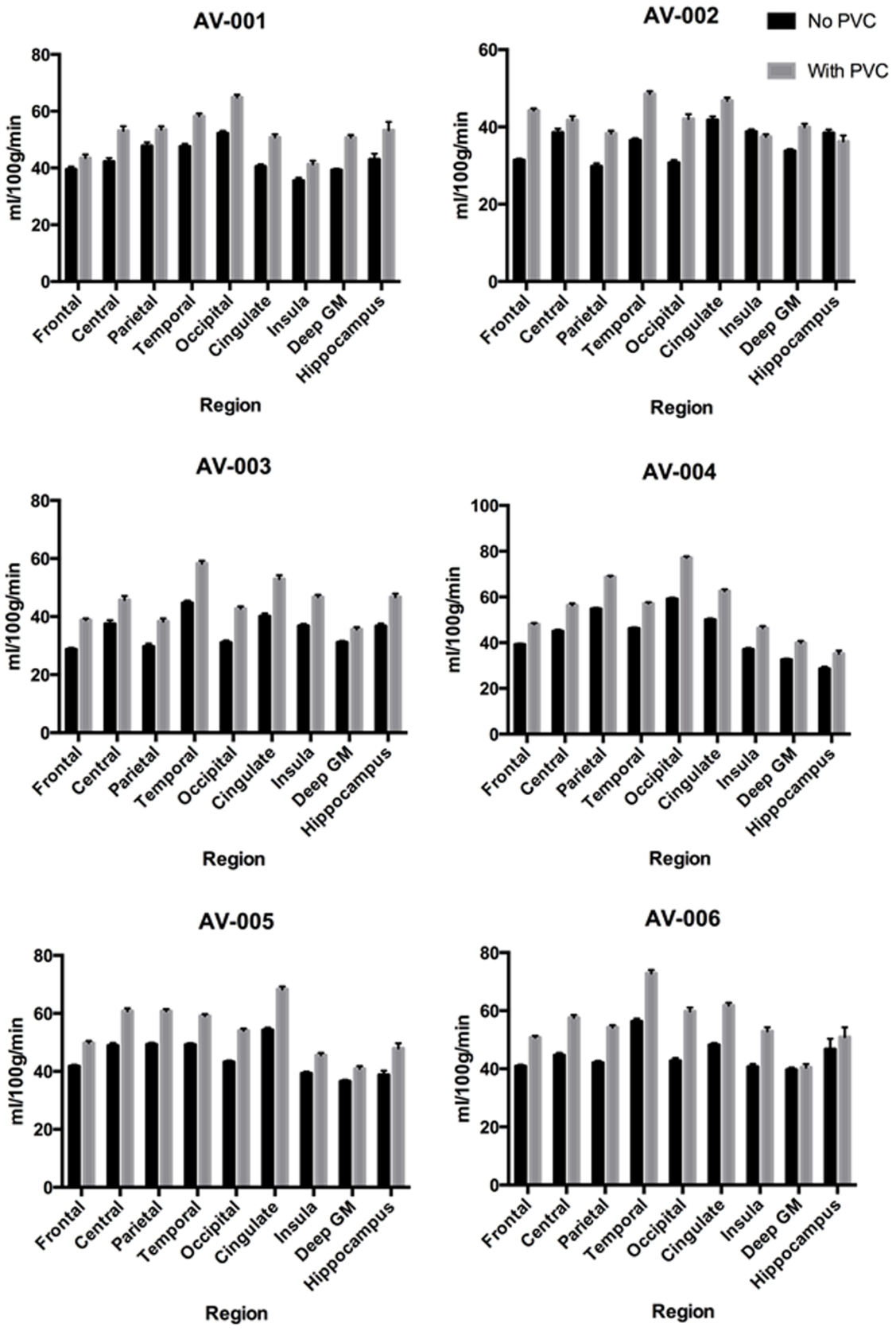


*Figure 8.9: AVID cohort: GM regions before and after PV correction using a combined deblurring and tissue fraction effect algorithm. Ratio column shows ratio of corrected to uncorrected. All CBF measurements in ml/100g/min, error bars show 95% confidence intervals.*

| | AV-001 | | | AV-002 | | | AV-003 | | | AV-004 | | | AV-005 | | | AV-006 | | |
|---|---|---|---|---|---|---|---|---|---|---|---|---|---|---|---|---|---|---|
| Region | CBF | After PVC | Ratio | CBF | After PVC | Ratio | CBF | After PVC | Ratio | CBF | After PVC | Ratio | CBF | After PVC | Ratio | CBF | After PVC | Ratio |
| Frontal | 35.9 ± 1.0 | 43.5 ± 1.3 | 1.2 | 31.4 ± 0.4 | 44.2 ± 0.6 | 1.4 | 28.7 ± 0.5 | 38.3 ± 0.6 | 1.3 | 39.2 ± 0.4 | 48.0 ± 0.6 | 1.2 | 41.8 ± 0.5 | 49.8± 0.7 | 1.2 | 40.9 ± 0.5 | 50.8 ± 0.6 | 1.2 |
| Central | 42.2 ± 1.3 | 53.1 ± 1.6 | 1.3 | 38.5 ± 1.0 | 41.7 ± 1.1 | 1.3 | 37.5 ± 1.3 | 45.7 ± 1.4 | 1.2 | 45.0 ± 0.7 | 56.3 ± 0.9 | 1.3 | 48.9 ± 0.9 | 60.8 ± 1.0 | 1.2 | 44.7 ± 0.8 | 57.6 ± 1.0 | 1.3 |
| Parietal | 47.8 ± 1.2 | 53.5 ± 1.2 | 1.1 | 29.8 ± 0.8 | 38.3 ± 0.7 | 1.3 | 29.7 ± 1.0 | 38.3 ± 1.1 | 1.3 | 54.8 ± 0.5 | 68.7 ± 0.6 | 1.3 | 49.3 ± 0.6 | 60.8 ± 0.7 | 1.2 | 42.1 ± 0.7 | 54.2 ± 0.8 | 1.3 |
| Temporal | 47.6 ± 0.9 | 58.2 ± 1.0 | 1.2 | 36.5 ± 0.6 | 48.5 ± 0.8 | 1.4 | 44.7 ± 0.8 | 58.2 ± 1.0 | 1.3 | 46.2 ± 0.5 | 57.1 ± 0.6 | 1.2 | 49.2 ± 0.6 | 59.1 ± 0.7 | 1.2 | 56.3 ± 1.0 | 72.8 ± 1.2 | 1.3 |
| Occipital | 52.2 ± 0.9 | 64.8 ± 1.0 | 1.2 | 30.7 ± 0.7 | 42.1 ± 1.2 | 1.5 | 31.0 ± 0.8 | 42.7 ± 0.8 | 1.4 | 59.1 ± 0.6 | 77.1 ± 0.7 | 1.3 | 43.2 ± 0.6 | 54.0 ± 0.8 | 1.2 | 42.8 ± 1.0 | 59.8 ± 1.3 | 1.4 |
| Cingulate | 40.5 ± 0.8 | 50.8 ± 1.1 | 1.3 | 41.8 ± 0.9 | 46.8 ± 0.8 | 1.4 | 40.1 ± 1.0 | 52.9 ± 1.3 | 1.3 | 50.0 ± 0.6 | 62.5 ± 0.9 | 1.3 | 54.3 ± 0.8 | 68.3 ± 1.0 | 1.3 | 48.2 ± 0.7 | 61.8 ± 1.0 | 1.3 |
| Insula | 35.6 ± 1.0 | 41.3 ± 1.3 | 1.2 | 38.8 ± 0.6 | 37.4 ± 0.7 | 1.3 | 36.8 ± 0.7 | 46.7 ± 0.8 | 1.3 | 37.0 ± 0.7 | 46.4 ± 0.9 | 1.3 | 39.3 ± 0.6 | 45.6 ± 0.8 | 1.2 | 40.7 ± 1.0 | 52.9 ± 1.4 | 1.3 |
| Deep GM | 39.3 ± 0.5 | 50.7 ± 0.9 | 1.3 | 33.8 ± 0.5 | 39.9 ± 0.9 | 1.2 | 31.1 ± 0.5 | 35.6 ± 0.8 | 1.1 | 32.5 ± 0.5 | 35.1 ± 1.4 | 1.2 | 36.6 ± 0.5 | 40.9 ± 0.9 | 1.1 | 39.7 ± 0.7 | 40.4 ± 1.2 | 1.0 |
| Hippocampus | 43.0 ± 2.0 | 53.3 ± 2.9 | 1.2 | 38.4 ± 0.9 | 36.2 ± 1.6 | 1.2 | 36.7 ± 0.9 | 46.7 ± 1.2 | 1.3 | 28.5 ± 1.0 | 35.1 ± 1.4 | 1.2 | 38.8 ± 1.4 | 47.9 ± 1.8 | 1.2 | 46.8 ± 3.6 | 50.9 ± 3.4 | 1.1 |

*Table 8.4: AVID cohort: GM regions before and after PV correction using a combined deblurring and tissue fraction effect algorithm. Ratio column shows ratio of corrected to uncorrected. All CBF measurements in ml/100g/min with 95% confidence intervals.*

groups were investigated. The first of these is the GENFI cohort, which is a blinded study and potentially contains some healthy subjects who are not suffering from nor are at risk from FTD. It appears that 3 of the 6 subjects analysed are may be healthy or not at risk subjects, as their perfusion 'profile' is like that of a healthy control. One subject presents like an elderly subject, with relatively low perfusion, which is elevated to normal physiological levels after PV correction. The remaining two subjects exhibit reduced perfusion in the frontal lobe before and after PV correction, which suggests that there is a reduction in metabolic activity in this region and shows a decoupling of structure and function. It would be interesting to discover if the hypothesis that this group of six subjects is composed of two FTD patients, one healthy elderly person and two younger healthy subjects is correct.

The second group is a cohort of patients suffering from posterior cortical atrophy which is variant of Alzheimer's disease, with atrophy primarily occurring in the posterior region and affecting visual processing. It was expected that there would be reduced perfusion in the occipital lobe which would remain after PV correction for these subjects, as PET studies have observed a metabolic reduction in AD patients after PVC [45]. This expectation is only met for one subject, with one subject showing a similar pattern of perfusion as a patient from the GENFI cohort, and the others displaying healthy levels of perfusion across the brain after PV correction.

No clinical information was communicated to me about these patients, such as how long they have been diagnosed with PCA and what the severity of their symptoms is. As such, it may be that some of these subjects are early on in the disease trajectory and have yet to show abnormal metabolic changes. A longitudinal assessment of changes in CBF would be very valuable for this group.

## 8.6 Conclusion

This chapter has shown the importance of using PV correction strategies for decoupling structure and function. Whilst this is a small study and a much larger number of subjects is needed for validation, it seems that genuine metabolic changes remain after atrophy correction, whereas age-associated tissue loss does not cause a reduction in cerebral perfusion.

# Chapter 9

# Conclusion

## 9.1 Summary and conclusions

This aim of this thesis was to develop a partial volume correction strategy for ASL images. The partial volume effect is known to significantly degrade the accuracy of perfusion estimates, yet it remains uncommon to account for it. In particular, a strong goal was to incorporate a deblurring technique into the correction strategy, in order to remove the effect of the point spread function, which had not previously been considered in PV correction techniques for ASL data.

A summary of the chapters contained within this thesis and the main conclusions to be drawn from each follows below.

In chapter 5, a novel modification is made to the linear regression method for PVC which reduces spatial blurring and improves quantification. The 3D kernel for linear regression is introduced, which has the effect of reducing the kernel radius whilst maintaining the same volume, and therefore available information. This was proven to reduce the spatial blurring in PV corrected map of GM perfusion and therefore, improve quantification.

A Bayesian PV correction tool is applied to single time point ASL data, for the first time, with the finding that spatial priors are heavily relied upon when few imaging volumes are available which results in an overly smoothed result. The tool was designed for multiple

time point data, where numerous averages are available.

Finally, a comparison is made of the difference between applying PVC methods directly to a CBF map, or to the constituent images, namely the difference and equilibrium magnetisation images. It was found that there is no significant difference in applying the technique directly to a CBF map, rather than separately to the difference and M0 images. This is an important finding as some vendors (GE, for instance) do not provide access the difference and M0 images without a research key. However, the lack of a control image as a registration target could prove problematic.

Chapter 6 presents a new method for creating PV estimates from saturation recovery data acquired using a 3D GRASE readout. This new method is termed *SEPARATE* and uses a voxelwise estimation of the longitudinal relaxation time of GM to improve upon existing estimates of the GM PV fraction in the deep GM. Existing methods such as *FRASIER* utilise a global value for the T1 of GM which results in an underestimation of the concentration of GM in the deep GM regions as the T1 in this region differs from that of the cortex.

Registration and downsampling of high resolution anatomical data to low resolution perfusion space is a major challenge for PV correction methods. The use of saturation recovery data at ASL resolution for PV estimates avoids this problematic step. An investigation of the accuracy in applying *SEPARATE* derived PV maps, compared to maps from high resolution data is undertaken. Fractional segmentation methods are found to introduce less registration error and provide a more consistent GM CBF across the entire PV range.

Chapter 7 introduces the concept of the point spread function (PSF) in ASL imaging and provides a description of its origin from the 3D GRASE sequence. The PSF arises as a consequence of T2 decay throughout the echo train, which leads to blurring of the acquired signal. Segmented acquisition schemes help to minimise this effect, but this chapter shows that the effect is still present, which causes a suppression of GM CBF values, whilst elevating WM CBF, even for an 8-shot scheme.

The width of the PSF is estimated from the extended phase graph algorithm. As simulation study is performed to investigate the the optimal number of iterations to use for a Richardson-Lucy deblurring algorithm. This found is to be 25, after which the error between the ground truth and deblurred digital phantom plateaued.

Conventional partial volume correction strategies for ASL only correct for tissue fraction effect and are unable to remove deblurring due to the PSF. These methods usually make use of PV estimates from high resolution anatomical data, downsampled to perfusion space. These PV fractions maps will be inaccurate unless the perfusion data is pre-processed to remove blurring.

In chapter 8, a complete solution for PVC which incorporates a deblurring component in addition to a correction for tissue fraction effect is applied to two clinical cohorts of dementia patients. We believe this is the first time this has been done. Within this chapter, the importance of choosing appropriate sequence parameters for the population under study is demonstrated. An example is shown of a CBF map produced when an insufficient post-labelling delay has been used, which leads to little or no signal in the WM.

It is shown that reduced perfusion, relative to other regions of the brain, in the frontal lobe remains after PV correction for Frontal Temporal Dementia patients and in the occipital lobes of Poster Cortical Atrophy patients. This is evidence of reduced metabolism in these regions and is a genuine reduction in perfusion. In healthy, elderly subjects, an apparent decrease in perfusion is removed after the application of a PV method.

## 9.2 Summary of significant findings

The significant findings of this thesis are summarised below:

- A 3D kernel for linear regression is introduced and evaluated. This is found to reduce the inherent spatial blurring of the linear regression method for PVC
- The application of Bayesian methods for PVC to single timepoint data was

investigated, and whether Bayesian methods offer any advantage over linear regression techniques when no tissue kinetic information is available. It was found that Bayesian methods rely heavily upon spatial priors to estimate GM and WM CBF when few averages are available, resulting perfusion images which lack gross spatial detail.

- A new method for creating PV estimates from the fractional segmentation of 3D GRASE data using a voxelwise estimation of the T1 of GM is presented. This produces more accurate estimations of the concentration of GM in deep GM regions.

- The PSF for the 3D GRASE sequence used in our studies is estimated using an Extended Phase Graph algorithm. Perfusion maps are deblurred using a Richardson-Lucy deconvolution algorithm. This procedure is shown to reduce blurring even in the case of an 8-shot acquisition scheme for the 3D GRASE data.

- A complete solution for PVC of ASL data is proposed which combines a correction inadequate resolution caused by blurring due to the PSF and tissue signal mixing due to voxel grid size.

## 9.3 Further work

The new method of applying a correction for blurring and tissue fraction effect should be fully validated, as well as a thorough investigation of the validity of applying deblurring techniques to the CBF maps in preference to the raw data. This technique is both dependent on accurate characterisation of the PSF and reliable estimates of PV fraction. It would be useful to perform a simulation study to investigate how estimates of GM CBF deviate from a ground truth when the registration of PV maps is poor, and to fully characterise the impact this has.

The saturation recovery curve acquired during the *SEPARATE* development was comprehensively sampled 31 times, with TR ranging from 100 to 8000 ms. The early

part of the curve which changes rapidly was sampled more densely. An extension to this study would be an investigation to ascertain the optimal sampling interval, in order to strike a balance between sufficient data points to sample the curve and obtain fractional segmentation information, yet few enough that the imaging time is short enough to be acceptable in a clinical environment. Limited conclusions can be drawn from the application of the PVC method to the clinical cohorts described in chapter 8. Both cohorts that were analysed consisted of only 6 subjects, with the GENFI group more than likely containing healthy control data as well as images from FTD patients.

The application of this complete PVC method for ASL data is potentially of great clinical utility in separating cases of actual reduced regional metabolism in patient populations, compared to age-related tissue atrophy producing an apparent decrease in perfusion. This could be validated through assessment of a large patient longitudinal dataset, which could lead to the development of a perfusion-based biomarker for dementia.

# Appendix A

# Publications and Proceedings

**The following publications and proceedings have arisen as a result of this thesis:**

## A.1 Conference Proceedings

"Improved Partial Volume Correction of ASL images using 3D kernels", R.A. Oliver, D.L. Thomas, X.Golay. *British Chapter ISMRM Cambridge 2012*.

"Improved Partial Volume Correction of ASL images using 3D kernels", R.A. Oliver, B.Thomas, D.L. Thomas, X.Golay. *Proc ESMRMB Lisbon 2012, Oral presentation*.

"Comparison of Bayesian and Linear Regression based Partial Volume Correction in single time point ASL MRI", R.A. Oliver, M.A. Chappell, D.L.Thomas, X.Golay. *Proc ISMRM Salt Lake City 2013*.

"Comparison of Bayesian and Linear Regression based Partial Volume Correction in single time point ASL MRI", R.A. Oliver, M.A. Chappell, D.L.Thomas, X.Golay. *Proc ESMRMB Toulouse 2013, Oral presentation*.

"Partial Volume Correction of 3D GRASE ASL images using T1 maps acquired with the same readout scheme", R.A. Oliver, E. De Vita, X.Golay, D.L. Thomas. *Proc ISMRM Milan 2014, Oral presentation summa cum laude*.

## A.2 Papers

"Diagnostic classification of arterial spin labelling and structural MRI in presenile early-stage dementia", Bron EE, Steketee RME, Houston GC, Oliver RA, Achterberg HC, Loog M, Van Swieten JC, Hammers A, Niessen WJ, Smits M, Klein S. *Human Brain Mapping, 35(9), 4916–4931*.

The above paper uses the partial volume correction software developed during this thesis as part of the processing pipeline.

# Bibliography

[1] X. Golay and E. T. Petersen, "Arterial Spin Labeling: Benefits and Pitfalls of High Magnetic Field," *Neuroimaging Clinics of North America*, vol. 16, pp. 259–268, May 2006.

[2] R. B. Buxton, "Introduction to Functional Magnetic Resonance Imaging," pp. 1–479, July 2009.

[3] W.-M. Luh, E. C. Wong, P. A. Bandettini, and J. S. Hyde, "QUIPSS II with thin-slice TI 1 periodic saturation: a method for improving accuracy of quantitative perfusion imaging using pulsed arterial spin labeling," *Magnetic Resonance in Medicine*, vol. 41, no. 6, pp. 1246–1254, 1999.

[4] K. Oshio and D. A. Feinberg, "GRASE (Gradient- and spin-echo) imaging: a novel fast MRI technique.," *Magnetic Resonance in Medicine*, vol. 20, pp. 344–349, Aug. 1991.

[5] B. Fischl and A. M. Dale, "Measuring the thickness of the human cerebral cortex from magnetic resonance images.," *Proceedings of the National Academy of Sciences*, vol. 97, pp. 11050–11055, Sept. 2000.

[6] X. Liang, A. Connelly, and F. Calamante, "Improved partial volume correction for single inversion time arterial spin labeling data," *Magnetic Resonance in Medicine*, vol. 69, pp. 531–537, Apr. 2012.

[7] I. Asllani, C. Habeck, A. Borogovac, T. R. Brown, A. M. Brickman, and Y. Stern, "Separating function from structure in perfusion imaging of the aging brain," *Human*

*Brain Mapping*, vol. 30, pp. 2927–2935, Sept. 2009.

[8] W. Shin, X. Geng, H. Gu, W. Zhan, Q. Zou, and Y. Yang, "Automated brain tissue segmentation based on fractional signal mapping from inversion recovery Look–Locker acquisition," *NeuroImage*, vol. 52, pp. 1347–1354, Oct. 2010.

[9] J. Petr, G. Schramm, F. Hofheinz, J. Langner, and J. van den Hoff, "Partial volume correction in arterial spin labeling using a Look-Locker sequence," *Magnetic Resonance in Medicine*, pp. n/a–n/a, Dec. 2012.

[10] A. Ahlgren, R. Wirestam, E. T. Petersen, F. Ståhlberg, and L. Knutsson, "Partial volume correction of brain perfusion estimates using the inherent signal data of time-resolved arterial spin labeling," *NMR in Biomedicine*, vol. 27, pp. 1112–1122, July 2014.

[11] M. Vidorreta, E. Balteau, Z. Wang, E. De Vita, M. A. Pastor, D. L. Thomas, J. A. Detre, and M. A. Fernández-Seara, "Evaluation of segmented 3D acquisition schemes for whole-brain high-resolution arterial spin labeling at 3T," *NMR in Biomedicine*, vol. 27, pp. 1387–1396, Sept. 2014.

[12] M. Günther, K. Oshio, and D. A. Feinberg, "Single-shot 3D imaging techniques improve arterial spin labeling perfusion measurements," *Magnetic Resonance in Medicine*, vol. 54, no. 2, pp. 491–498, 2005.

[13] J. V. Manjón, J. J. Lull, J. Carbonell-Caballero, G. García-Martí, L. Martí-Bonmatí, and M. Robles, "A nonparametric MRI inhomogeneity correction method," *Medical Image Analysis*, vol. 11, pp. 336–345, Aug. 2007.

[14] S. M. Smith, "Fast robust automated brain extraction," *Human Brain Mapping*, vol. 17, pp. 143–155, Nov. 2002.

[15] M. A. Chappell, A. R. Groves, B. J. MacIntosh, M. J. Donahue, P. Jezzard, and M. W. Woolrich, "Partial volume correction of multiple inversion time arterial spin labeling MRI data," *Magnetic Resonance in Medicine*, vol. 65, pp. 1173–1183, Feb. 2011.

[16] B. A. Thomas, "Improved brain PET quantification using partial volume correction techniques," pp. 1–192, Sept. 2011.

[17] R. A. Lerski and J. D. De Certaines, "II. Performance assessment and quality control in MRI by Eurospin test objects and protocols," *Magnetic resonance imaging*, vol. 11, no. 6, pp. 817–833, 1993.

[18] K. Scheffler, "A pictorial description of steady-states in rapid magnetic resonance imaging," *Concepts in Magnetic Resonance*, vol. 11, no. 5, pp. 291–304, 1999.

[19] A. T. Du, G. H. Jahng, S. Hayasaka, J. H. Kramer, H. J. Rosen, M. L. Gorno-Tempini, K. P. Rankin, B. L. Miller, M. W. Weiner, and N. Schuff, "Hypoperfusion in frontotemporal dementia and Alzheimer disease by arterial spin labeling MRI," *Neurology*, vol. 67, no. 7, pp. 1215–1220, 2006.

[20] S. J. Crutch, M. Lehmann, J. M. Schott, G. D. Rabinovici, M. N. Rossor, and N. C. Fox, "Posterior cortical atrophy," *The Lancet. Neurology*, vol. 11, pp. 170–178, Jan. 2012.

[21] P. Barker, X. Golay, and G. Zaharchuk, *Clinical Perfusion MRI*. Cambridge University Press, Apr. 2013.

[22] I. Asllani, A. Borogovac, and T. R. Brown, "Regression algorithm correcting for partial volume effects in arterial spin labeling MRI," *Magnetic Resonance in Medicine*, vol. 60, pp. 1362–1371, Dec. 2008.

[23] X. Golay, J. Hendrikse, and T. C. C. Lim, "Perfusion imaging using arterial spin labeling.," *Topics in magnetic resonance imaging : TMRI*, vol. 15, pp. 10–27, Mar. 2004.

[24] P. Tofts, *Quantitative MRI of the Brain: Measuring Changes Caused by Disease*. Wiley, 2003.

[25] H. Lu, C. Clingman, X. Golay, and P. C. M. van Zijl, "Determining the longitudinal relaxation time (T1) of blood at 3.0 Tesla," *Magnetic Resonance in Medicine*, vol. 52, no. 3, pp. 679–682, 2004.

[26] J. A. Detre, J. S. Leigh, D. S. Williams, and A. P. Koretsky, "Perfusion Imaging," *Magnetic Resonance in Medicine*, vol. 23, pp. 37–45, Jan. 1992.

[27] D. S. Williams, J. A. Detre, J. S. Leigh, and A. P. Koretsky, "Magnetic resonance imaging of perfusion using spin inversion of arterial water," *Proceedings of the National Academy of Sciences*, vol. 89, no. 1, pp. 212–216, 1992.

[28] K. K. Kwong, J. W. Belliveau, D. A. Chesler, I. E. Goldberg, R. M. Weisskoff, B. P. Poncelet, D. N. Kennedy, B. E. Hoppel, M. S. Cohen, and R. Turner, "Dynamic magnetic resonance imaging of human brain activity during primary sensory stimulation.," *Proceedings of the National Academy of Sciences*, vol. 89, pp. 5675–5679, June 1992.

[29] S. G. Kim, "Quantification of relative cerebral blood flow change by flow-sensitive alternating inversion recovery (FAIR) technique: application to functional mapping.," *Magnetic Resonance in Medicine*, vol. 34, pp. 293–301, Sept. 1995.

[30] R. R. Edelman, D. G. Darby, and S. Warach, "Qualitative Mapping ofCerebral Blood Flow and Functional Localization with Echo-planar MR Imaging and Signal Targeting with Alternating Radio Frequency'," *Radiology*, vol. 192, pp. 513–520, 1994.

[31] W. Dai, D. Garcia, C. de Bazelaire, and D. C. Alsop, "Continuous flow-driven inversion for arterial spin labeling using pulsed radio frequency and gradient fields," *Magnetic Resonance in Medicine*, vol. 60, pp. 1488–1497, Dec. 2008.

[32] D. C. Alsop and J. A. Detre, "Reduced transit-time sensitivity in noninvasive magnetic resonance imaging of human cerebral blood flow," *Journal of Cerebral Blood Flow & Metabolism*, vol. 16, no. 6, pp. 1236–1249, 1996.

[33] R. B. Buxton, L. R. Frank, E. C. Wong, B. Siewert, S. Warach, and R. R. Edelman, "A general kinetic model for quantitative perfusion imaging with arterial spin labeling," *Magnetic Resonance in Medicine*, vol. 40, pp. 383–396, Aug. 2005.

[34] P. Herscovitch and M. E. Raichle, "What is the correct value for the brain–blood partition coefficient for water?," *Journal of Cerebral Blood Flow & Metabolism*, vol. 5, pp. 65–69, Mar. 1985.

[35] E. C. Wong, R. B. Buxton, and L. R. Frank, "Quantitative imaging of perfusion using a single subtraction (QUIPSS and QUIPSS II)," *Magnetic Resonance in Medicine*, vol. 39, no. 5, pp. 702–708, 1998.

[36] F. Q. Ye, J. A. Frank, D. R. Weinberger, and A. C. McLaughlin, "Noise reduction in 3D perfusion imaging by attenuating the static signal in arterial spin tagging (ASSIST).," *Magnetic Resonance in Medicine*, vol. 44, pp. 92–100, July 2000.

[37] P. Mansfield and A. A. Maudsley, "Planar spin imaging by NMR," *Journal of Magnetic Resonance (1969)*, 1977.

[38] A. W. Song, E. C. Wong, and J. S. Hyde, "Echo-volume imaging.," *Magnetic Resonance in Medicine*, vol. 32, pp. 668–671, Nov. 1994.

[39] D. C. Alsop, J. A. Detre, X. Golay, M. Günther, J. Hendrikse, L. Hernandez-Garcia, H. Lu, B. J. MacIntosh, L. M. Parkes, M. Smits, M. J. P. van Osch, D. J. J. Wang, E. C. Wong, and G. Zaharchuk, "Recommended implementation of arterial spin-labeled perfusion MRI for clinical applications: A consensus of the ISMRM perfusion study group and the European consortium for ASL in dementia," *Magnetic Resonance in Medicine*, pp. n/a–n/a, Apr. 2014.

[40] J. Petr, J.-C. Ferre, J.-Y. Gauvrit, and C. Barillot, "Denoising arterial spin labeling MRI using tissue partial volume," in *SPIE Medical Imaging* (B. M. Dawant and D. R. Haynor, eds.), pp. 76230L–76230L–9, SPIE, Mar. 2010.

[41] M. J. P. van Osch, W. M. Teeuwisse, M. A. A. van Walderveen, J. Hendrikse, D. A. Kies, and M. A. van Buchem, "Can arterial spin labeling detect white matter perfusion signal?," *Magnetic Resonance in Medicine*, vol. 62, pp. 165–173, July 2009.

[42] E. Prieto, J. M. Martí-Climent, J. Arbizu, P. Garrastachu, I. Domínguez, G. Quincoces, M. J. García-Velloso, P. Lecumberri, M. Gómez-Fernández, and J. A. Richter, "Evaluation of spatial resolution of a PET scanner through the simulation and experimental measurement of the recovery coefficient," *Computers in Biology and Medicine*, vol. 40, pp. 75–80, Jan. 2010.

[43] C. C. Meltzer, M. N. Cantwell, P. J. Greer, D. Ben-Eliezer, G. Smith, G. Frank, W. H. Kaye, P. R. Houck, and J. C. Price, "Does cerebral blood flow decline in healthy aging? A PET study with partial-volume correction.," *Journal of Nuclear Medicine*, vol. 41, pp. 1842–1848, Nov. 2000.

[44] H. W. Muller-Gartner, J. M. Links, J. L. Prince, R. N. Bryan, E. McVeigh, J. P. Leal, C. Davatzikos, and J. J. Frost, "Measurement of radiotracer concentration in brain gray matter using positron emission tomography: MRI-based correction for partial volume effects," *Journal of Cerebral Blood Flow & Metabolism*, vol. 12, no. 4, pp. 571–583, 1992.

[45] O. G. Rousset, Y. Ma, and A. C. Evans, "Correction for partial volume effects in PET: principle and validation," *Journal of Nuclear Medicine*, vol. 39, no. 5, pp. 904–911, 1998.

[46] M. A. A. Binnewijzend, J. P. A. Kuijer, M. R. Benedictus, W. M. van der Flier, A. M. Wink, M. P. Wattjes, B. N. M. van Berckel, P. Scheltens, and F. Barkhof, "Cerebral Blood Flow Measured with 3D Pseudocontinuous Arterial Spin-labeling MR Imaging in Alzheimer Disease and Mild Cognitive Impairment: A Marker for Disease Severity," *Radiology*, vol. 267, pp. 221–230, Apr. 2013.

[47] I. Boscolo Galazzo, M. A. Chappell, D. L. Thomas, X. Golay, P. Manganotti, and E. De Vita, "Reduced blurring artifacts in 3D-GRASE ASL by integrating new acquisition and analysis strategies," *Proc. Intl. Soc. Mag. Reson. Med. 22(2014)*, vol. 2014, pp. 1–1, Nov. 2013.

[48] E. De Vita, M. Vidorreta, X. Golay, M. A. Fernández-Seara, D. L. Thomas, and

E. Balteau, “Optimised segmentation scheme for high-resolution multi-shot 3D-GRASE pCASL with improved point spread function ,” *Proc. Intl. Soc. Mag. Reson. Med. 22(2014)*, vol. 2014, pp. 1–1, Nov. 2013.

[49] P. van Gelderen, J. A. de Zwart, and J. H. Duyn, “Pittfalls of MRI measurement of white matter perfusion based on arterial spin labeling,” *Magnetic Resonance in Medicine*, vol. 59, no. 4, pp. 788–795, 2008.

[50] K. Erlandsson, I. Buvat, P. H. Pretorius, B. A. Thomas, and B. F. Hutton, “A review of partial volume correction techniques for emission tomography and their applications in neurology, cardiology and oncology,” *Physics in Medicine and Biology*, vol. 57, pp. R119–R159, Oct. 2012.

[51] P. J. Rousseeuw and K. Van Driessen, “Computing LTS regression for large data sets,” *Data mining and knowledge discovery*, vol. 12, no. 1, pp. 29–45, 2006.

[52] A. R. Groves, M. A. Chappell, and M. W. Woolrich, “Combined spatial and non-spatial prior for inference on MRI time-series,” *NeuroImage*, vol. 45, pp. 795–809, Apr. 2009.

[53] N. A. Johnson, G.-H. Jahng, M. W. Weiner, B. L. Miller, H. C. Chui, W. J. Jagust, M. L. Gorno-Tempini, and N. Schuff, “Pattern of Cerebral Hypoperfusion in Alzheimer Disease and Mild Cognitive Impairment Measured with Arterial Spin-labeling MR Imaging: Initial Experience1,” *Radiology*, vol. 234, pp. 851–859, Mar. 2005.

[54] M. J. Donahue, H. Lu, C. K. Jones, R. A. E. Edden, J. J. Pekar, and P. C. M. van Zijl, “Theoretical and experimental investigation of the VASO contrast mechanism,” *Magnetic Resonance in Medicine*, vol. 56, no. 6, pp. 1261–1273, 2006.

[55] E. T. Petersen, T. Lim, and X. Golay, “Model-free arterial spin labeling quantification approach for perfusion MRI,” *Magnetic Resonance in Medicine*, vol. 55, pp. 219–232, Feb. 2006.

[56] V. Popescu, M. Battaglini, W. S. Hoogstrate, S. C. J. Verfaillie, I. C. Sluimer, R. A. van Schijndel, B. W. van Dijk, K. S. Cover, D. L. Knol, M. Jenkinson, F. Barkhof, N. de Stefano, H. Vrenken, and o. b. o. t. M. S. Group, "Optimizing parameter choice for FSL-Brain Extraction Tool (BET) on 3D T1 images in multiple sclerosis," *NeuroImage*, vol. 61, pp. 1484–1494, July 2012.

[57] J. Ashburner and K. J. Friston, "Unified segmentation," *NeuroImage*, vol. 26, pp. 839–851, July 2005.

[58] Y. Zhang, M. Brady, and S. Smith, "Segmentation of brain MR images through a hidden Markov random field model and the expectation-maximization algorithm," *Medical Imaging, IEEE Transactions on*, vol. 20, no. 1, pp. 45–57, 2001.

[59] J. B. Maintz and M. A. Viergever, "A survey of medical image registration," *Medical Image Analysis*, vol. 2, no. 1, pp. 1–36, 1998.

[60] K. Keyvan, M. Dehghani, and K. Kazemi, "Comparison Evaluation of Three Brain MRI Segmentation Methods in Software Tools," *Proc. ICBME 2010*, pp. 1–4, Nov. 2010.

[61] J. V. Hajnal, D. L. G. Hill, and D. Hawkes, *Medical Image Registration*. CRC Press, June 2001.

[62] J. Wang, G. K. Aguirre, D. Y. Kimberg, A. C. Roc, L. Li, and J. A. Detre, "Arterial spin labeling perfusion fMRI with very low task frequency," *Magnetic Resonance in Medicine*, vol. 49, pp. 796–802, Apr. 2003.

[63] M. Inglese, S. Adhya, G. Johnson, J. S. Babb, L. Miles, H. Jaggi, J. Herbert, and R. I. Grossman, "Perfusion magnetic resonance imaging correlates of neuropsychological impairment in multiple sclerosis," *Journal of Cerebral Blood Flow & Metabolism*, vol. 28, pp. 164–171, May 2007.

[64] W. Rashid, "Abnormalities of cerebral perfusion in multiple sclerosis," *Journal of Neurology, Neurosurgery & Psychiatry*, vol. 75, pp. 1288–1293, Sept. 2004.

[65] L. Debernard, T. R. Melzer, S. Van Stockum, C. Graham, C. A. Wheeler-Kingshott, J. C. Dalrymple-Alford, D. H. Miller, and D. F. Mason, "Reduced grey matter perfusion without volume loss in early relapsing-remitting multiple sclerosis," *Journal of Neurology, Neurosurgery & Psychiatry*, vol. 85, pp. 544–551, Apr. 2014.

[66] R. Gonzalez and R. Woods, *Digital Image Processing*. Pearson Education, third ed., May 2008.

[67] W. Shin, H. Gu, and Y. Yang, "Fast high-resolution T1mapping using inversion-recovery look-locker echo-planar imaging at steady state: Optimization for accuracy and reliability," *Magnetic Resonance in Medicine*, vol. 61, pp. 899–906, Apr. 2009.

[68] R. Oliver, E. De Vita, X. Golay, and D. L. Thomas, "Partial Volume Correction of 3D GRASE ASL images using T1 maps acquired with the same readout scheme," *Proc. Intl. Soc. Mag. Reson. Med. 22(2014)*, pp. 1–1, May 2014.

[69] H. Lu, L. M. Nagae-Poetscher, X. Golay, D. Lin, M. Pomper, and P. C. M. van Zijl, "Routine clinical brain MRI sequences for use at 3.0 Tesla," *Journal of Magnetic Resonance Imaging*, vol. 22, no. 1, pp. 13–22, 2005.

[70] M. Quarantelli, K. Berkouk, A. Prinster, B. Landeau, C. Svarer, L. Balkay, B. Alfano, A. Brunetti, J. C. Baron, and M. Salvatore, "Integrated software for the analysis of brain PET/SPECT studies with partial-volume-effect correction," *Journal of Nuclear Medicine*, vol. 45, pp. 192–201, Feb. 2004.

[71] B. A. Thomas, K. Erlandsson, M. Modat, L. Thurfjell, R. Vandenberghe, S. Ourselin, and B. F. Hutton, "The importance of appropriate partial volume correction for PET quantification in Alzheimer's disease," *European Journal of Nuclear Medicine and Molecular Imaging*, vol. 38, pp. 1104–1119, Feb. 2011.

[72] C. Catana, A. Drzezga, W. D. Heiss, and B. R. Rosen, "PET/MRI for Neurologic Applications," *Journal of Nuclear Medicine*, vol. 53, pp. 1916–1925, Nov. 2012.

[73] M. D. Robson, J. C. Gore, and R. T. Constable, "Measurement of the point spread function in MRI using constant time imaging.," *Magnetic Resonance in Medicine*,

vol. 38, pp. 733–740, Nov. 1997.

[74] M. A. Fernández-Seara, Z. Wang, J. Wang, H.-Y. Rao, M. Guenther, D. A. Feinberg, and J. A. Detre, "Continuous arterial spin labeling perfusion measurements using single shot 3D GRASE at 3 T," *Magnetic Resonance in Medicine*, vol. 54, no. 5, pp. 1241–1247, 2005.

[75] J. Hennig, "Echoes—how to generate, recognize, use or avoid them in MRimaging sequences. Part I: Fundamental and not so fundamental properties of spin echoes," *Concepts in Magnetic Resonance*, vol. 3, no. 3, pp. 125–143, 1991.

[76] Q. Wu and F. A. Merchant, *Microscope Image Processing*. Elsevier, Mar. 2008.

[77] G. J. Stanisz, E. E. Odrobina, J. Pun, M. Escaravage, S. J. Graham, M. J. Bronskill, and R. M. Henkelman, "T1, T2 relaxation and magnetization transfer in tissue at 3T," *Magnetic Resonance in Medicine*, vol. 54, no. 3, pp. 507–512, 2005.

[78] M. C. Evans, J. Barnes, C. Nielsen, L. G. Kim, S. L. Clegg, M. Blair, K. K. Leung, A. Douiri, R. G. Boyes, S. Ourselin, N. C. Fox, and Alzheimer's Disease Neuroimaging Initiative, "Volume changes in Alzheimer's disease and mild cognitive impairment: cognitive associations.," *European radiology*, vol. 20, pp. 674–682, Mar. 2010.

[79] K. K. Leung, M. J. Clarkson, J. W. Bartlett, S. Clegg, C. R. Jack, Jr., M. W. Weiner, N. C. Fox, S. Ourselin, and t. A. D. N. Initiative, "Robust atrophy rate measurement in Alzheimer's disease using multi-site serial MRI: Tissue-specific intensity normalization and parameter selection," *NeuroImage*, vol. 50, pp. 516–523, Apr. 2010.

[80] J. Hort, J. T. O'Brien, G. Gainotti, T. Pirttila, B. O. Popescu, I. Rektorova, S. Sorbi, P. Scheltens, and on behalf of the EFNS Scientist Panel on Dementia, "EFNS guidelines for the diagnosis and management of Alzheimer's disease," *European Journal of Neurology*, vol. 17, pp. 1236–1248, Sept. 2010.

[81] M. Ewers, R. A. Sperling, W. E. Klunk, M. W. Weiner, and H. Hampel, "Neuroimaging markers for the prediction and early diagnosis of Alzheimer's disease dementia," *Trends in Neurosciences*, vol. 34, pp. 430–442, Aug. 2011.

[82] G. B. Frisoni, N. C. Fox, C. R. Jack, P. Scheltens, and P. M. Thompson, "The clinical use of structural MRI in Alzheimer disease," *Nature Reviews Neurology*, vol. 6, pp. 67–77, Feb. 2010.

[83] D. C. Alsop, W. Dai, M. Grossman, and J. A. Detre, "Arterial spin labeling blood flow MRI: its role in the early characterization of Alzheimer's disease.," *Journal of Alzheimer's disease : JAD*, vol. 20, no. 3, pp. 871–880, 2010.

[84] J. e. a. Rohrer, "ArticlesPresymptomatic cognitive and neuroanatomical changes in genetic frontotemporal dementia in the Genetic Frontotemporal dementia Initiative (GENFI) study:a cross-sectional analysis," *The Lancet. Neurology*, vol. 14, pp. 253–262, Feb. 2015.

[85] J. D. Rohrer, J. D. Warren, N. C. Fox, and M. N. Rossor, "Presymptomatic studies in genetic frontotemporal dementia," *Revue Neurologique*, vol. 169, pp. 820–824, Oct. 2013.